

ISSTT 2014

The 25th International Symposium
on Space Terahertz Technology



Proceedings

27-30 April 2014 Moscow, Russia

www.isstt2014.hse.ru

**These *Proceedings* include articles submitted by the authors or abstracts
for the Symposium talks with no article submission**

SPONSORS AND SUPPORT

We want to thank the Higher School of Economics of Moscow and SCONTEL, Moscow State Pedagogical University, Terasense and Tydex whose contributions help to make the 25th International Symposium on Space Terahertz Technology, ISSTT2014, possible.



Moscow State
Pedagogical University

Since 1872



Tydex specializes in custom manufacturing of optical components and instruments for research and industry. Tydex develops and produces a wide range of THz products, including Golay Cells, Broad-band Phase Transformers, filters, polarizers, attenuators, windows, lenses, prisms, waveplates, mirrors, beam splitters, spectral splitters and AR coatings.

Visit us on [tydex.ru!](http://tydex.ru)

TeraSense is a leading manufacturer of innovative sub-THz imaging systems for science and industry. We supply and sell portable sub-THz imaging cameras, generators & Ultrafast detectors (response time 300ps). Our sub-THz imaging cameras feature low cost, broad-band frequency range 0.05-0.7 THz, image acquisition rate up to 50 fps.



WELCOME

National Research University Higher School of Economics, Moscow, and Moscow State Pedagogical University welcome you to the 25th International Symposium on Space Terahertz Technology, ISSTT2014, held from April 27 to 30, in Moscow, Russia.

A total of 86 abstracts were accepted. 42 abstracts are scheduled for oral presentations and 37 for poster presentation. There are 7 Invited contributions and 1 Special talk. We would like to thank the Scientific Organizing Committee for the abstracts review.

The Higher School of Economics (HSE) has been founded in 1992 to provide a better education in economy. Since then it has grown to become an internationally very respected research university in the field of economics as well as mathematics. In recent years it has broadened its scope further and was also promoted to the status of a National Research University in July 2013, together with 15 other universities in Russia. One of the expansions of the HSE was the acquisition of the Moscow Institute for Electronics and Mathematics (MIEM), famous for its contributions to the Sputnik program. Hosting the International Symposium on Space THz technology for the first time in Moscow emphasizes the importance that the Higher School of Economics as a research university attaches to advanced technology.

Scientific Organizing Committee

Andrey Baryshev	<i>SRON</i>
Victor Belitsky	<i>Chalmers</i>
Eric Bryerton	<i>NRAO</i>
Thomas Crowe	<i>VDI</i>
Heribert Eisele	<i>University of Leeds</i>
Brian Ellison	<i>RAL</i>
Neal Erickson	<i>University of Massachusetts</i>
Gregory Goltsman (chairman)	<i>Moscow State Pedagogical University</i>
Karl Jacobs KOSMA	<i>University of Cologne</i>
Tony Kerr	<i>NRAO</i>
Teun Klapwijk	<i>Delft University, Moscow State Pedagogical University</i>
Arthur Lichtenberger	<i>University of Virginia</i>
Alain Maestrini	<i>University of Paris, LERMA</i>
Doris Maier	<i>IRAM</i>
Imran Mehdi	<i>JPL/Caltech</i>
Yutaro Sekimoto	<i>NAO (Japan)</i>
Sheng-Cai Shi	<i>Purple Mountain Observatory, CAS</i>
Jan Stake	<i>Chalmers</i>
Christopher Walker	<i>University of Arizona</i>
Wolfgang Wild	<i>ESO</i>
Stafford Withington	<i>Cambridge University</i>
Raymond Blundell	<i>Harvard Smithsonian Institute</i>
Ghassan Yassin	<i>University of Oxford</i>

Local Organizing Committee:

Gregory Goltsman (chair), Teun Klapwijk, Valery Koshelets, Alla Otstavnova, Sergey Ryabchun, Anna Maslennikova, Yury Lobanov, Alexandre Karpov.

Program at a glance

SUNDAY, April 27	MONDAY, April 28	TUESDAY, April 29	WEDNESDAY, April 30
	8:30 Registration & Coffee	9:00 Registration & Coffee	9:00 Registration & Coffee
	9:30 Symposium opening 10:05 Invited Talk	9:30 Invited Talk	9:30 Invited Talk 9:55 Special Talk
	10:30 – 11:30 Session 1 – Systems & receivers	9:55 – 11:10 Session 5 – THz coherent detectors: HEB I	10:10 – 11:10 Session 8 – THz coherent detectors: HEB II & SIS mixers
13:00 Registration	11:30 – 11:45 Coffee & Tea	11:10 – 11:30 Coffee & Tea	11:10 – 11:30 Coffee & Tea
	11:45 – 12:30 Session 2 – Sources I	11:30 – 12:30 Session 6 – Systems & receivers	11:30 – 12:00 Session 9 – Back-ends: readout & signal processing
			12:00 – 12:30 Session 10 – Sources II
13:30 Coffee & Tea	12:30 – 14:00 Lunch	12:30 – 14:00 Lunch	12:30 – 14:00 Lunch
14:00 – 16:30 TERADEC	14:00 Invited Talk	14:00 Invited Talk	14:00 Invited Talk
	14:25 – 15:40 Session 3 – Direct detectors	14:25 – 15:40 Session 7 – Novel devices & measurements	14:25 – 15:25 Session 11 – THz coherent detectors: Schottky mixers
			15:25 – 15:40 Session 12 – Announcements & conference closing
	15:40 – 16:00 Coffee & Tea	15:40 Coffee & Tea	15:40 – 16:00 Coffee & Tea
	16:00 Invited talk	15:40 – 17:40 Poster Session	
17:00 – 19:30 Welcome party in the Main Hall	16:25 – 17:10 Session 4 – Optics		
	17:25 Bus boarding	17:40 Bus boarding	16:10 Bus boarding
	* 18:00 – 20:00 Tour to *Radio Physics Lab and Technological Center of Moscow State Pedagogical University, (optional)	* 18:00 – 19:00 Tour to **IRE (Kotel'nikov Institute of Radio Engineering and Electronics, RAS) (optional)	* 17:00 – 19:00 Tour to *** IKI (Space Research Institute, RAS) (optional)
		19:30 – 23:00 Conference dinner	* 19:00 – 21:00 Entertainment (optional)

Program in detail

Sunday, April 27, 2014

13:00 – 19:30 Registration Desk open, the Main Hall

14:00 – 16:30 TERADEC

17:00 – 19:30 Welcome party, the Main Hall

Monday, April 28, 2014

8:30 – 9:30 Registration

9:30 – 10:05 Symposium opening: Gregory Goltsman, Teunis M. Klapwijk

Chair: Boris Karasik

10:05 – 10:30 Invited Talk: “SAFARI new and improved - extending the capabilities of SPICA’s Imaging Spectrometer” - Dr. Gerhard de Lange, SRON

10:30 – 11:30 Session 1: Systems & receivers I

Paper	Abstract Title	Presenter
1-1	Submillimeter-Wave Radiometer and Spectrometers using Cryogenically Cooled HEMT Amplifier Front-Ends	Goutam Chattopadhyay
1-2	Progress on the upGREAT heterodyne array receivers for the SOFIA telescope	Christophe Risacher
1-3	Development of a Terahertz Superconducting Imaging Array (TeSIA)	Sheng-Cai Shi
1-4	Development of a Total-Power Radiometer comprising a 340 GHz High-Resolution Sideband-Separating Schottky Receiver	Simon Rea

11:30 – 11:45 Coffee & Tea Break

Chair: Doris Maier

11:45 – 12:30 Session 2: Sources I

Paper	Abstract Title	Presenter
2-1	Phase-locking of a 4.7 THz quantum cascade laser based on a harmonic super-lattice mixer	J.-R. Gao, Darren Hayton, D. Pavelyev
2-2	Progress towards a Room-Temperature 4.7 THz Multiplied Local Oscillator Source to Enable Neutral Oxygen Observation	Jose Siles
2-3	A 4.7 quantum-cascade lasers as local oscillator for the GREAT heterodyne spectrometer on SOFIA	Heiko Richter

12:30 – 14:00 Lunch Break

Meeting of ISSTT Steering Committee (continue on Tuesday if necessary)

Chair: Alexej Semenov

14:00 – 14:25 Invited Talk: “SpaceKIDs - The development of Kinetic Inductance Detectors for Space Based Applications” - Dr. Simon Doyle, Cardiff University

14:25 - 15:40 Session 3: Direct detectors

Paper	Abstract Title	Presenter
3-1	A stacked wafer design for hexagonal arrays of TES bolometers	Gerhard de Lange
3-2	A Resonance Cold-Electron Bolometer with a Kinetic Inductance Nanofilter	Leonid Kuzmin
3-3	A planar frequency selective bolometric array at 350 GHz	Alexander Sobolev
3-4	Power Load Dependencies of Cold Electron Bolometer Optical Response at 350 GHz	Mikhail Tarasov
3-5	Response of the antenna coupled TES with High-Frequency Readout to 0.65 THz radiation	Artem Kuzmin

15:40 – 16:00 Coffee & Tea Break

Chair: Sergey Ryabchun

16:00 – 16:25 Invited Talk: “Superconducting Metamaterials” - Dr. Alexey Ustinov, Karlsruhe Institute of Technology

16:25 – 17:10 Session 4: Optics

Paper	Abstract Title	Presenter
4-1	Cryogenic resonator spectrometer for satellite antennas reflectivity investigation at millimeter and terahertz bands	Evgeny Serov
4-2	Capillary quasioptical highpass filter	Artem Chekushkin
4-3	Development of the Wide FoV Cold Optics for Millimeter and Submillimeter Wave Observation	Shigeyuki Sekiguchi

*17:25 – Bus boarding

*18:00 – 20:00 Tour to *Radio Physics Lab and Technological Center of Moscow State Pedagogical University* (optional)

Tuesday, April 29, 2014

9:00-9:30 Registration

Chair: Raymond Blundell

9:30 – 9:55 Invited Talk: “Millimetron: The next FIR/mm Space Observatory” - Dr. Thijs de Graauw, Astro Space Centre of P.N. Lebedev Physical Institute, RAS

9:55 – 11:10 Session 5: THz coherent detectors: HEB I

Paper	Abstract Title	Presenter
5-1	Optimization of the intermediate frequency bandwidth in the THz HEB mixers	Alexey Semenov
5-2	Low Noise Terahertz Mixers made of MgB ₂ Films	Sergey Cherednichenko
5-3	Performance of a 4.7 THz waveguide HEB mixer for SOFIA's upGREAT	Denis Büchel
5-4	MgB ₂ Hot Electron Bolometers Operating Above 20 K	Daniel Cunnane, Boris Karasik
5-5	Performance of twin-slot antenna coupled NbN hot electron bolometer mixers at frequencies ranging from 1.4 to 4.7 THz	Nathan Vercrussen

11:10 – 11:30 Coffee & Tea Break

Chair: Victor Belitsky

11:30 – 12:30 Session 6: Systems & receivers II

Paper	Abstract Title	Presenter
6-1	Testing of 166 to 664 GHz receivers prototypes based on discrete planar Schottky diodes for ICI onboard MetOp-SG	Mostafa Benzazaa
6-2	Scientific Requirements for Next Generation Space Terahertz Astronomy Missions	Igor Zinchenko
6-3	THz photometers for solar flare observations from space	Pierre Kaufmann
6-4	Atmospheric Profiling Synthetic Observation System at THz Wave Band	Qijun Yao

12:30 – 14:00 Lunch Break

Chair: Teunis Klapwijk

14:00 – 14:25 Invited Talk: “Large format, background limited arrays of Kinetic Inductance Detectors for sub-mm astronomy” - Dr. Jochem Baselmans , SRON

14:25 - 15:40 Session 7: Novel devices & measurements

Paper	Abstract Title	Presenter
7-1	Normal Metal HEB Detector with Johnson Noise Thermometry Readout	Boris Karasik
7-2	Photon Statistics for Space Terahertz Astronomy	Hiroshi Matsuo
7-3	Frequency multiplication in a distributed array of SIS junctions	Bhushan Billade
7-4	Terahertz detectors based on the room temperature Nb ₅ N ₆ microbolometers	Jian Chen
7-5	Photothermoelectric Response in Asymmetric Carbon Nanotube Devices Exposed to Sub-THz Radiation	Georgy Fedorov

15:40 Coffee & Tea Break

Chair: Gregory Goltsman

15:40 – 17:40 Poster session

Poster	First name	Last name	Title
1-c - THz coherent detectors: Schottky diodes			
1-b - THz coherent detectors: SIS			
1	Edward	Tong	Wideband Receiver Upgrade for the Submillimeter Array
2	Patrick	Pütz	First mixer prototype results for Band L (455-495 GHz) of CHAI
3	Patrice	Serres	Characterization of the IF output impedance of SIS mixers
4	Parisa	Yadranjee Aghdam	SIS Tunnel Junction's Specific Capacitance Direct Measurement
5	Andrey	Khudchenko	Image Rejection Ratio of 2SB SIS Receivers
6	Hawal	Rashid	Improved Quadrature RF Hybrid for 2SB and Balanced THz Receivers
7	Konstantin	Kalashnikov	Development of Phase Lock Loop based on Harmonic Phase Detector

Poster	First name	Last name	Title
1-a - THz coherent detectors: HEB			
8	Gregory	Gay	Design, fabrication and measurement of a membrane based quasi-optical THz HEB mixer
9	Tatsuya	Soma	Wide RF band mixer-block design for waveguide-type HEB mixer
10	Yury	Lobanov	Development of a 30 THz Heterodyne Receiver Based on a Hot-Electron-Bolometer Mixer
2 -Direct Detectors			
11	Jing	Li	Development of an 8×8 Microwave Kinetic Inductance Detector Array at 850 μm
12	Masato	Naruse	Superconducting on-chip spectrometers at sub-millimeter wavelength
13	Mikhail	Patrashin	Zero bias GaAsSb/InAlAs/InGaAs tunnel diodes for MMW-THz detection
14	Wen	Zhang	Characterization of Ti superconducting transition edge sensors
15	Timothe	Faivre	Experimental study of a Josephson junction based thermometer and its possible application in bolometry
16	Alexander	Shurakov	A Microwave Pumped HEB Direct Detector Using a Homodyne Readout Scheme
3 - Systems & Receivers			
17	Alexander	Shurakov	1200 GHz receiver front-end for Sub-millimetre Wave Instrument for the JUICE mission
18	Olivier	Auriacombe	Laboratory Based Terahertz Spectroscopy for Ice Desportion Studies of the Interstellar Medium
19	Victor	Belitsky	Dual Band MM-Wave Receiver for Onsala 20m Antenna
20	Fabien	Defrance	Heterodyne measurements at 2.6THz of the HEB mixer for the balloon experiment CIDRE
21	Weidong	Hu	The 220 GHz stepped-frequency Imaging Radar
22	-	-	-
23	Grigoriy	Bubnov	Search for New Sites for THz Observations in Eurasia

Poster	First name	Last name	Title
4 - NbN film technology			
24	Sascha	Krause	Deposition of high-quality ultra-thin NbN films at ambient temperatures
25	Alexey	Pavolotsky	Study of NbN ultra-thin films for THz hot-electron bolometers
5 – Sources			
26	Andrey	Kaveev	Terahertz Emission from Silicon Nanostructures Heavily Doped with Boron
27	Ion	Oprea	Monolithically integrated 440 GHz doubler using Film-Diode (FD) technology
28	Zhe	Chen	A Schottky Diode Frequency Multiplier Chain at 380 GHz for a gyro-TWA Application
29	Yoshihisa	Irimajiri	Phase-locking of a 3.1THz quantum cascade laser to terahertz reference generated by a frequency comb
6 – Optics			
30	Arvid	Hammar	Spline Feed Horns for the STEAMR Instrument
31	Bertrand	Thomas	1.9-2.5 THz and 4.7 THz electroformed smooth-wall spline feedhorns for the HEB mixers of the upGREAT instrument onboard SOFIA aircraft
32	Hiroaki	Imada	Condition of Optical Systems Independent of Frequency for Wide Filed-of-View Radio Telescopes
33	Takafumi	Kojima	Design and Loss Measurement of Substrate Integrated Waveguides at Terahertz Frequencies
7 - Back-ends: readout & signal processing			
34	Anton	Artanov	The operation of SIS mixer as up- and down-convertor at low frequencies for frequency multiplexing.
35	Kenichi	Karatsu	Development of Superconducting Low Pass Filter for Ultra Low Noise Measurement System of Microwave Kinetic Inductance Detector

Poster	First name	Last name	Title
8 - Novel devices & measurements			
36	Boon Kok	Tan	A Planar Superconducting Phase Switch for Polarization Modulation
37	Edward	Tong	A Digital Terahertz Power Meter Based on an NbN Thin Film

*17:40 – Bus boarding OR walk to IRE (~15 minutes)

*18:00 – 19:00 Tour to *IRE (Kotel'nikov Institute of Radio Engeneering and Electronics, RAS)* (optional)

19:00 – Bus boarding at IRE or at the Symposium site

19:30 – 22:00 Conference dinner

Wednesday, April 30, 2014

9:00 – 9:30 Registration

Chair: Patrick Pütz

9:30 – 9:55 Invited Talk: “The Greenland Telescope” - Dr. Raymond Blundell , Smithsonian Astrophysical Observatory

9:55 – 10:10 Special Talk “Radioastron” – Dr. Yury Kovalev, Astro Space Centre of P.N. Lebedev Physical Institute, RAS

10:10 – 11:10 Session 8: THz coherent detectors: HEB II & SIS mixers

Paper	Abstract Title	Presenter
8-1	NbN Hot-Electron Bolometer Mixer Operation at 3.8 THz	Ivan Tretyakov
8-2	Superconducting Integrated Receiver with HEB-Mixer	Nickolay Kinev
8-3	High-quality NbN-MgO-NbN SIS junctions and integrated circuits for THz applications	Valery Koshelets
8-4	Fully integrated sideband-separating Mixers for the NOEMA receivers	Doris Maier

11:10 – 11:30 Coffee & Tea Break

Chair: Bertrand Thomas

11:30 – 12:00 Session 9: Back-ends: readout & signal processing

Paper	Abstract Title	Presenter
9-1	SIS Frequency Multiplexers and RF-to-DC converters for Frequency Division Multiplexed TES Read-out	Gerhard de Lange
9-2	Experimental Study of Superconducting Microstrip Travelling-wave Parametric Amplifiers	Wenlei Shan

12:00 – 12:30 Session 10: Sources II

Paper	Abstract Title	Presenter
10-1	High Power Solid-State THz Source Development	Jeffrey Hesler
10-2	4-Pixel Frequency Multiplied Source for High-Resolution heterodyne Array receivers at 1.9 THz	Imran Mehdi

12:30 – 14:00 Lunch Break

Chair: Imran Mehdi

14:00 – 14:25 Invited Talk: “The SubMM Wave Instrument on JUICE” - Dr. Paul Hartogh,

Max Planck Institute for Solar System Research

14:25 – 15:25 Session 11: THz coherent detectors: Schottky mixers

Paper	Abstract Title	Presenter
11-1	Schottky-structures for Space THz Technologies	Oleg Cojocari
11-2	THz Schottky Diode MMICs for Astronomy and the Physics of the Atmosphere	Lina Gatilova
11-3	Sub-millimeter-wave balanced mixers and multipliers at the 5th harmonic	Hugh Gibson
11-4	Schottky diode based components for TeraSCREEN	Hui Wang

15:25 – 15:40 Session 12 (optional): Announcements & conference closing: Gregory Gol’tsman

15:40 – 16:00 Coffee & Tea Break

* 16:10 – Bus boarding

* 17:00 – 19:00 Tour to *IKI (Space Research Institute, RAS)* (optional)

* 19:00 — 21:00 Entertainment (optional)

PROCEEDINGS

Invited Talk

SAFARI new and improved - extending the capabilities of SPICA's Imaging Spectrometer

Gerhard de Lange¹, Peter Roelfsema^{1,2}, Martin Giard³, Francisco Najarro⁴, Kees Wafelbakker¹, Willem Jellema^{1,2}, Brian Jackson¹, Bruce Sibthorpe¹, Marc Audard⁶, Anna di Giorgio⁷, Javier Goicoechea⁴, Matt Griffin⁸, Frank Helmich^{1,2}, Franz Kerschbaum⁹, Michael Meyer¹⁰, David Naylor¹¹, Albrecht Poglitch¹¹, Luigi Spinoglio⁷, Bart Vandenbussche¹²

¹ SRON Netherlands Institute for Space Research, Groningen, The Netherlands, Email: P.R.Roelfsema@sron.nl

² Kapteyn Astronomical Institute, Groningen, The Netherlands; ³ IRAP, Toulouse, France; ⁴ CAB-INTA, Madrid, Spain; ⁵ RAL, Didcot, United Kingdom; ⁶ ISDC, Geneva, Switzerland; ⁷ IFSI, Rome, Italy; ⁸ Cardiff, United Kingdom; ⁹ University of Vienna, Vienna, Austria; ¹⁰ ETH, Zurich, Switzerland; ¹¹ MPE, Garching, Germany; ¹² KUL, Leuven, Belgium

The Japanese SPace Infrared telescope for Cosmology and Astrophysics, SPICA, will provide astronomers with a new window on the universe in the next decade. With a large -3 meter class- cold -6K- telescope, the mission will provide a unique environment optimally suited for instruments that are limited only by the cosmic background itself. SAFARI, the SpicA FAR infrared Instrument SAFARI, is a Fourier Transform imaging spectrometer designed to fully exploit this extremely low far infrared background environment provided by the SPICA observatory.

The SAFARI consortium, comprised of European and Canadian institutes, has established a reference design for the instrument based on a Mach-Zehnder interferometer stage with outputs directed to three extremely sensitive Transition Edge Sensor arrays covering the 35 to 210 μm domain. Thus the baseline instrument provides R~1000 spectral imaging capabilities instantaneously over a 2' by 2' field of view. A number of modifications to the instrument to extend its capabilities are under investigation. With the reference design SAFARI's sensitivity for many objects is limited not by the detector NEP but by the level of broad band background radiation – the zodiacal light for the shorter wavelengths and baffle structures for the longer wavelengths. Options to reduce this background are dedicated masks or dispersive elements which can be inserted in the optics as required. The resulting increase in sensitivity will directly impact one of the prime science goals of SPICA and SAFARI, the evolution of galaxies over cosmic times. With the expected factor of a several better sensitivity as compared to the reference design astronomers will be able to study thousands of galaxies out to redshift 3 and even many hundreds out to redshifts of 5 or 6. Secondly, in the context of the modified approach towards the SPICA mission, changes to the instrument to also accommodate longer wavelength operation -up to 400 μm - is being investigated. Finally elements to increase the wavelength resolution, at least for the shorter wavelength bands, are investigated as this would significantly enhance SAFARI's capabilities to study starformation in our own galaxy.

Session 1: Systems & receivers I

Submillimeter-Wave Radiometer and Spectrometers using Cryogenically Cooled HEMT Amplifier Front-Ends

Goutam Chattopadhyay, Theodore Reck, William Deal*, Paul Stek, and Imran Mehdi

*Jet Propulsion Laboratory, California Institute of Technology
4800 Oak Grove Drive, Pasadena, CA91109, USA*

**Northrop Grumman Corporation, One Space Park, Redondo Beach, CA 90278, USA*

Radiometric and high-resolution spectroscopic studies at submillimeter-wave frequencies play a very important role in the Earth science, astrophysics, and planetary exploration. Its importance is underscored by the key role of heterodyne spectrometers in the ESA cornerstone Herschel Space Observatory, NASA's Microwave Limb Sounder (MLS) instrument on Earth Observation System (EOS) Aura satellite, NASA's Microwave Instrument on the Rosetta Orbiter (MIRO), as well as the ground-based Atacama Large Millimeter Array (ALMA), and airborne Stratospheric Observatory for Infrared Astronomy (SOFIA).

Traditionally, where highly sensitive measurements are the prime requirement, superconductor-insulator-superconductor (SIS) mixer based receivers cooled to 4K temperature were used at the front-end of the submillimeter-wave radiometer and spectrometers. When cryogenic cooling is not an option, Schottky diode based receivers operating at the room temperature were the obvious choice for these applications as there were no amplifiers available at the submillimeter wavelengths. However, InP high electron mobility transistor (HEMT) based amplifiers and mixers are now available at these frequencies. At submillimeter-wavelengths, low noise amplifiers with substantial gain at the front-end will reduce noise contribution from mixers and intermediate frequency (IF) amplifiers. Moreover, power amplification available through these devices would significantly improve local oscillator (LO) efficiencies. Cryogenic cooling of these amplifiers to 20K provides sensitivity similar to SIS mixers. Although the noise temperature of the front-end HEMT amplifier cooled to 20 K might not be as close to the SIS mixers, however, the 20-30 dB gain it will provide at the front of the mixers and IF amplifiers will provide system noise temperatures similar to a SIS based system, without a 4 K cooling system. Moreover, the sensitivity to physical temperature is much less for amplifiers than SIS. The amplifier receivers would still work at higher temperatures, though at a bit higher system noise, unlike the SIS receivers. Moreover, the higher operating temperature makes these amplifier receivers better suited to planetary instruments and earth remote sensing suborbital platforms where available power is scarce.

In the last few years, the development of transistor technologies with maximum device frequency (f_{MAX}) over 1 THz has pushed operating frequencies of amplifiers well into the 700 GHz range. Northrop Grumman Aerospace Systems (NGAS) has developed an ultra-short-gate-length HEMT process which has produced InP HEMT amplifiers working at 700 GHz and beyond. We have evaluated several of these amplifiers in the 300 GHz and 650 GHz band and cooled them to 20K. The amplifier noise temperatures were reduced by a factor of 8 to 10 when cooled to 20K from room temperature.

In this paper, we will discuss the science drivers and progress in the cryogenic HEMT amplifier based heterodyne receivers at submillimeter wavelengths and their potential for future spectroscopic and radiometric instruments.

The research described herein was carried out at the Jet Propulsion Laboratory, California Institute of Technology, Pasadena, California, USA, under contract with National Aeronautics and Space Administration.

Progress on the upGREAT heterodyne array receivers for the SOFIA telescope

C. Risacher^{1*}, R. Güsten¹, J. Stutzki², H-W. Hübers³, A. Bell¹, D. Büchel², I. Camara¹, R. Castenholz¹, M. Choi¹, U. Graf², S. Heyminck¹, C. E. Honingh², K. Jacobs², M. Justen², B. Klein¹, T. Klein¹, C. Leinz¹, P. Pütz², N. Reyes¹, H. Richter³, O. Ricken¹, A. Semenov¹, A. Wunsch¹

¹ Max Planck Institut für Radioastronomie*, Auf dem Hügel 69, 53121 Bonn, Germany,
² KOSMA, 1. Physikalisches Institut des Universität zu Köln, Zülpicher Straße 77, 5093 Köln, Germany,
³ German Aerospace Center (DLR), Institute of Planetary Research, Rutherfordstr. 2, Berlin, Germany

* Contact: crisache@mpifr.de, phone +49-228-525 338

The NASA-DLR airborne observatory SOFIA is about to enter routine observations in 2014, having the German PI instrument (GREAT) as one of its four main instruments. The instrument currently comprises single pixel heterodyne receivers observing in selected ranges in the frequency windows 1.25-2.7 THz. A 4.7 THz single pixel receiver will be commissioned in May 2014.

We present the status of the upGREAT receivers, part of GREAT, which are two medium-size array receivers, operating cooled using closed-cycle pulse tube coolers. The Low Frequency Array (LFA) covers the 1.9-2.5 THz range using dual polarization 7-pixel HEB arrays (hence 14 pixels in total). The second receiver, the High Frequency Array (HFA), will observe the O[I] line at ~4.7 THz using a 7-pixel HEB array.

We present here the progress made in the development of those channels. We will show the preliminary results for the LFA for the frequency range 1.9 to 2.1 THz, where we will use a high power VDI solid state chain that can provide LO power for up to 7 pixels. The DSB receiver noise temperatures for the LFA are expected to be below 1000 K DSB for a 0-4 GHz IF range. For the HFA array, results for the NbN HEB Kosma waveguide mixers selected for the HFA [1] show that DSB mixer noise temperatures of 600-1400K will be achievable for the IF range [0-4 GHz] at 4.745 THz.

Installation and commissioning of the LFA instrument is planned for end of 2014, and mid 2015 for the HFA array.

1. P. Puetz, this conference

Development of a Terahertz Superconducting Imaging Array (TeSIA)

Sheng-Cai Shi&TeSIA Team

Purple Mountain Observatory, Chinese Academy of Sciences

Key Lab of Radio Astronomy, Chinese Academy of Sciences

2 West Beijing Road, Nanjing 210008, China

E-mail: scshi@pmo.ac.cn

The terahertz (THz) regime is the frequency window to be fully explored in astronomy. Dome A in Antarctic, with an altitude of 4093 m and temperature below -80 Celsius degree in winter, is regarded as the best site on earth for astronomical observations in this frequency regime. Currently, China is proposing to build an observatory there, in which Dome A 5m Terahertz Telescope (DATE5) is one of two major telescopes. This talk will present the development of next generation instrument for DATE5, namely terahertz superconducting imaging array (TeSIA).

Development of a Total-Power Radiometer comprising a 340 GHz High-Resolution Sideband-Separating Schottky Receiver

Simon Rea^{*}, Matthew Oldfield^{*}, Ben Rackauskas^{*}, Brian Moyna^{*}, Steve Parkes[†], Martin Dunstan[†] and Alex Mason^{**}

^{*}*Millimetre-Wave Technology Group, RAL Space Science & Technology Facilities Council*

Email: simon.rea@stfc.ac.uk

[†]*University of Dundee*

Email: sparkes@computing.dundee.ac.uk

^{**}*STAR-Dundee Ltd. Email: alex.mason@star-dundee.com*

This abstract presents the recent development of an instrument breadboard comprising a 340 GHz sideband-separating receiver with high spectral resolving capability. Such a receiver configuration is a high-priority option for STEAM-R, a millimetre-wave limb-sounder originally proposed within the scope of ESA's Earth Explorer 7 candidate mission PREMIER. This receiver topology is of interest for atmospheric spectroscopy as wide spectral coverage can be achieved in a single-sideband configuration, thus eliminating issues associated with spectral fold-over in a conventional double-sideband heterodyne receiver. Characterization of the instrument, a total-power radiometer, is complete and deployment at the High Altitude Research Stations Jungfraujoch and Gornergrat (HFSJG) in the Swiss Alps is planned for February 2014.

In addition to the development of the instrument breadboard, the MARSCHALS airborne limb-sounder shall be upgraded with a similar receiver configuration in preparation for deployment in a tropical field campaign in 2015 within scope of the StratoCLIM project. The instrument breadboard is therefore an excellent test-bed for the more complex upgrade of MARSCHALS.

The sideband-separating receiver comprises two key enabling pieces of technology:

- 1: Sub-harmonic Image-Rejection Mixer (SHIRM)
- 2: Wideband Spectrometer v2 (WBS II)

The SHIRM is the key front-end component in the sideband-separating receiver. It comprises two 340 GHz DSB Schottky mixers and relevant passive waveguide elements providing the down-converted upper and lower sidebands in phase-quadrature at the two IF outputs of the device. Sideband separation is completed after passing the IF signals through an external quadrature hybrid. Several SHIRM topologies have been optimized in previous work [1, 2], demonstrating ~20 dB of sideband rejection. The WBS II is a digital-FFT spectrometer which utilizes IQ input sampling to maximize bandwidth. A maximum sampling rate of 3 Gs/s provides up to 3 GHz bandwidth from a single unit. The spectrometer performs a 2048-point complex FFT thus achieving a resolution of order 1-2 MHz depending on sampling rate. Two WBS II units are employed in the instrument breadboard and configured to provide a total of 4 GHz bandwidth. A detailed description of the instrument together with results from the characterization tests and deployment shall be presented at the conference.

References

1. B. Thomas, S. P. Rea, B. Moyna, B. Alderman, D. Matheson, "A 320-360 GHz Sub-harmonically Pumped Image Rejection Mixer using Planar Schottky Diodes" in *IEEE Microwave and Wireless Component Letters*, Vol. 19, No. 2, Feb 2009, pp. 101–103.
2. S. P. Rea, B. Alderman, M. Henry, D. Matheson, Y. Munro, "Progress on the Performance Improvement of Submillimetre-wave Sub-Harmonically Pumped Image-Rejection Schottky Mixers" in *6th ESA Workshop on Millimetre-Wave Technology and Applications and 4th Global Symposium on Millimetre Waves*, 2011, Espoo, Finland.

Session 2: Sources I

Phase-locking of a 4.7 THz quantum cascade lasers based on a harmonic super-lattice mixer

D. J. Hayton¹, A. Khudchenko¹, D.G. Pavelyev², J.N. Hovenier³, A. Baryshev¹, J. R. Gao^{1,3}, T.Y. Kao⁴, Q. Hu⁴, J.L. Reno⁵ and V. Vaks⁶

¹*Netherlands Institute for Space Research SRON, Netherlands*

²*Radiophysics Department, Nizhny Novgorod State University, Russia*

³*Kavli Institute of NanoScience, TU Delft, Netherlands*

⁴*Department of Electrical Engineering and Computer Science, Massachusetts Institute of Technology (MIT), Cambridge, Massachusetts 02139, USA*

⁵*Sandia National Laboratories, Albuquerque, NM 87185-0601, USA*

⁶*Institute for Physics of Microstructures, Russian Academy of Sciences, Nizhny Novgorod 603950, Russia*

For heterodyne spectroscopy in the super-THz (~2-6 THz) there are currently few solid state local oscillator (LO) sources available. Since the introduction of the first THz quantum cascade laser¹ (QCL) much progress has been made in pushing QCLs to higher frequencies, increasing output power and improving the far-field beam profile making the QCL increasingly well suited as a heterodyne LO. QCLs have been demonstrated in THz heterodyne receivers at frequencies up to 4.75 THz² where the astronomically significant neutral atomic oxygen [OI] line is situated.

Since QCLs are not inherently frequency stable, some external frequency stabilization or phase locking must be applied. We previously reported on the phase locking of a 3.4 THz QCL³ based on a superlattice harmonic mixer⁴. Using a similar technique, we can now report on a successful phase locking experiment with a 4.7 THz QCL by using a superlattice harmonic mixer cooled to 10 K. In this configuration, both the harmonic mixer and the QCL are mounted together in a common cryostat and at a common temperature. The QCL used is a single mode, 3rd order distributed feedback laser. A beat signal of 400 MHz between the QCL and a reference is generated by the super-lattice harmonic mixer, where the QCL signal is mixed with the 24th harmonic of the 198 GHz input signal. The latter is the local oscillator signal for the harmonic mixer which is injected through a window in the cryostat from an external solid state source.

Phase locking is observed from a beat signal that is more than 25 dB above the noise level for a 30 kHz resolution bandwidth of the spectrum analyzer. This system also allows for a detailed characterization of the QCL tuning coefficient and linewidth versus applied bias voltage down to low QCL output power.

References

1. R. Köhler, A. Tredicucci, F. Beltram, H. E. Beere, E. H. Linfield, A. G. Davies, D. A. Ritchie, R. C. Iotti, and F. Rossi, *Nature* 417, 156 (2002).
2. J. L. Kloosterman, D. J. Hayton, Y. Ren, T. Y. Kao, J. N. Hovenier, J. R. Gao, T. M. Klapwijk, Q. Hu, C. K. Walker, and J. L. Reno, *Appl. Phys. Lett.* 102, 011123 (2013).
3. D. J. Hayton, A. Khudchenko, D. G. Pavelyev, J. N. Hovenier, A. Baryshev, J. R. Gao, T. Y. Kao, Q. Hu, J. L. Reno, and V. Vaks, *Appl. Phys. Lett.* 103, 051115 (2013).
4. D. G. Pavelyev, Y. I. Koshurinov, A. S. Ivanov, A. N. Panin, V. L. Vax, V. I. Gavrilenko, A. V. Antonov, V. M. Ustinov, and A. E. Zhukov, *Semiconductors* 46, 125 (2012).

Progress towards a Room-Temperature 4.7 THz Multiplied Local Oscillator Source to Enable Neutral Oxygen Observation

Jose V. Siles*, Choonsup Lee, Robert Lin, Goutam Chattopadhyay and Imran Mehdi

NASA Jet Propulsion Laboratory, California Institute of Technology, Pasadena, CA

**Contact: Jose.V.Siles@jpl.nasa.gov*

Oxygen is the third most abundant element in the Universe, and knowledge of the chemistry of oxygen in interstellar clouds and protostellar regions is essential for understanding the formation of stars and the incorporation of key molecules into forming planetary systems. The OI line at 63 um (4.7 THz) together with CII (158 um) are the major coolants of photo-dissociation regions in giant molecular clouds. However, the OI line at 4.7 THz has never been observed with resolutions better than 7 km/s. Leveraging off of the success of the HIFI instrument on-board the Herschel Space Observatory, our objective is to develop the first all-solid-state Schottky diode based broadband frequency multiplied local oscillator source at 4.7 THz able to provide the minimum required output power ($>1 \mu\text{W}$) to drive a Hot Electron Bolometer mixer, and thereby enabling high-resolution ($\lambda/\Delta\lambda > 10^6$, $\Delta\nu < 0.3 \text{ km/s}$) heterodyne spectroscopy of the fine atomic oxygen line at 63 μm . It will be compact, broadband, frequency-agile, tunable, temperature, frequency stable and able to operate at room-temperature.

Our strategy will consist of a X2X3X3X3 multiplication scheme (see Fig. 1) featuring a number of new technologies and novel multiplier concepts to provide frequency multipliers with the necessary enhancements to improve the state-of-the-art by at least a factor of 5 in terms of power and almost a factor of 2 in terms of maximum operation. We will use for the first time GaN based multipliers in the lower stage to increase power handling capabilities, novel on-chip power combining techniques to increase the input/output power of current GaAs multipliers by a factor of up to four, and silicon micromachining techniques to produce waveguide blocks with lithographic precision ($< 1 \mu\text{m}$) in order to make it possible to fabricate waveguide blocks operating up to 4.7 THz. The silicon micromachining technique developed at our group also allows 3D integration by vertical stacking the device wafers (see Fig. 1 –right), which leads to ultra-compact LO sources. The progress on the design and development of the different novel components of this 4.7 THz LO source will be discussed.

At the conclusion of this project we will also provide NASA with multi-pixel capabilities for the entire terahertz region (up to 5 THz), highly demanded for future astrophysics missions such as SOFIA, STO-2, GUSSTO, etc.

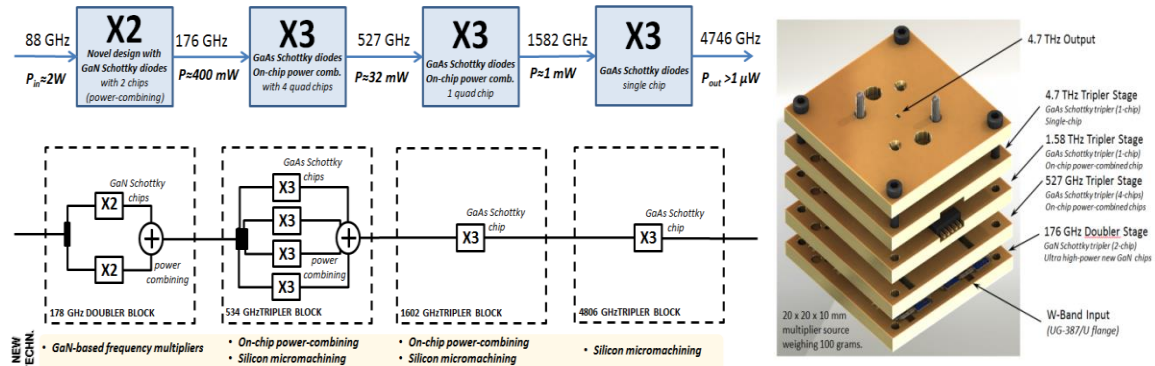


Fig.1. General scheme of the 4.7 THz frequency multiplied LO source.

This work was carried out at the Jet Propulsion Laboratory, California Institute of Technology, Pasadena, CA under a contract with National Aeronautics and Space Administration (NASA). All rights reserved.

A 4.7-THz quantum-cascade laser as local oscillator for the GREAT heterodyne spectrometer on SOFIA

Richter^{1*}, M. Greiner-Bär¹, K. Rösner¹, A. Semenov¹, M. Wienold², L. Schrottke², K. Biermann², T. Grahn², and H.-W. Hübers^{1,3}

¹*Institute of Planetary Research, German Aerospace Center (DLR), Rutherfordstr. 2, 12489 Berlin, Germany*

²*Paul-Drude-Institut für Festkörperelektronik, Hausvogteiplatz 5-7, 10117 Berlin, Germany* ³*Institut für Optik und Atomare Physik, Technische Universität Berlin, Straße des 17. Juni 135, 10623 Berlin, Germany*

Email: heiko.richter@dlr.de

Heterodyne spectroscopy of molecular rotational lines and atomic fine -structure lines is a powerful tool in astronomy and planetary research. It allows for the study of the chemical composition, the evolution, and the dynamical behaviour of astronomical objects such as molecular clouds and star-forming regions. For frequencies beyond 2 THz, SOFIA, the Stratospheric Observatory for Infrared Astronomy, is currently the only platform which allows for heterodyne spectroscopy at these frequencies. One example is the OI fine-structure line at 4.7 THz, which is a main target to be observed with GREAT, the German Receiver for Astronomy at Terahertz Frequencies, on board of SOFIA.

We report on the development of a 4.7-THz local oscillator (LO) for the heterodyne spectrometer GREAT on SOFIA. The LO combines a quantum-cascade laser (QCL) with a compact, low-input-power Stirling cooler. The 4.7-THz QCL is based on a hybrid design and has been developed for continuous-wave operation, high output powers, and low electrical pump powers [1]. Efficient carrier injection is achieved by resonant longitudinal optical phonon scattering. This design allows for an operating voltage below 6 V. The amount of generated heat complies with the cooling capacity of the Stirling cooler of 7 W at 65 K with 240 W of electrical input power [2]. Frequency stabilization is achieved by locking the emission from the QCL to an absorption line of CH₃OH using a pyroelectric detector and a PID control loop [3]. The design of the LO and its performance in terms of output power, frequency accuracy, frequency stability, and beam profile as well as its implementation in GREAT will be presented.

References

1. L. Schrottke, M. Wienold, R. Sharma, X. Lü, K. Biermann, R. Hey, A. Tahraoui, H. Richter, H.-W. Hübers, and H. T. Grahn, “Quantum-cascade lasers as local oscillators for heterodyne spectrometers in the spectral range around 4.745 THz,” *Semicond. Sci. Technol.* 28, 03511 (2013).
2. H. Richter, M. Greiner-Bär, S. G. Pavlov, A. D. Semenov, M. Wienold, L. Schrottke, M. Giehler, R. Hey, H. T. Grahn, and H.-W. Hübers, “A compact, continuous-wave terahertz source based on a quantum-cascade laser and a miniature cryocooler,” *Opt. Express* 18, 10177-10187 (2010).
3. H. Richter, S. G. Pavlov, A. D. Semenov, L. Mahler, A. Tredicucci, H. E. Beere, D. A. Ritchie, and H.-W. Hübers, “Submegahertz frequency stabilization of a terahertz quantum cascade laser to a molecular absorption line”, *Appl. Phys. Lett.* 96, 071112 (2010).

Invited Talk

SpaceKIDs - The development of Kinetic Inductance Detectors for Space Based Applications

S. Doyle,^a A. Baryshev^{b,h}, J. Baselmans^b, A. Bideaud, J. Bueno^b, M. Calvo^c, A. Gomez^d, N. Llombart^e, M. Griffin^a, M. Grim^b, P. Hargrave^a, T. Klapwijk^e, J. Martin-Pintado^d, A. Monfardini^c, H. Steenbeek^f, K. Wood^g, A. Woodcraft^g

^a*School of Physics and Astronomy
Cardiff University
Email: simon.doyle@astro.cf.ac.uk*

^b*SRON Netherlands Institute for Space Research
Email: J.Baselmans@sron.nl*

^c*Institut Neel, CNRS
Universite Joseph Fourier
Email: alessandro.monfardini@neel.cnrs.fr*

^d*Centro de Astrobiologia (CSIC-INTA)
Email: jmartin@cab.inta-csic.es*

^e*Kavli Institute of Nano Science
Delft University of Technology
Email: T.M.Klapwijk@tudelft.nl*

^f*AimValley BV
Email: hsteenbeek@aimvalley.nl*

^g*QMC Instruments Ltd
Email: k.wood@terahertz.co.uk*

^h*Kapteyn Astronomical Institute
University of Groningen
Email: A.M.Baryshev*

The past decade has seen a revolution in the development of Kinetic Inductance Detectors (KIDs) with the technology moving from the concept stage to large format imaging arrays on ground based telescopes observing at mm, sub-mm and optical wavelengths. The simplicity of the KID along with its high sensitivity and natural multiplexing in the frequency domain make it a strong candidate to fulfill the detector role for the next generation of space-based observatories. The SpaceKIDs program is a three-year, European funded project involving five academic institutes and two industrial partners across Europe working to develop KIDs towards the next generation of space based astronomical and Earth observing instruments. The study aims to highlight and address the key issues facing the KIDs deployment as a space based detector, such as optical bandwidth, speed, power consumption and susceptibility to cosmic rays. This presentation will give an overview of the SpaceKIDs project and its relevance to the scientific community along with key results from the project to date.

Session 3: Direct Detectors

Design description of silicon micro-machined cavity coupled far-infrared bolometer array

Gert de Lange, Michael D. Audley, Geert Keizer, Stephen Doherty and Colm Bracken.

Abstract—We give a design description of a novel way to construct bolometer arrays out of pixels that consist of thermally isolated Silicon Nitride islands that are suspended with long and narrow SiN legs on a Si wafer. We use a multi-wafer approach that facilitates the use of extra pixels on underlying wafers that fill the "empty" spaces between adjacent pixels in a top wafer. In this way we can achieve both a low thermal conductivity and a high pixel packing density. The design is especially of interest for far-infrared bolometer arrays for space based astronomy applications that need extremely low thermal conductance, where pixel size easily can be as large as a few millimeters.

Index Terms— Antenna arrays, Bolometers, Infrared detectors, Micromachining.

I. INTRODUCTION

BOLOMETER arrays with a radiation absorber on a thermally isolated Silicon Nitride (SiN) island are widely used as detectors in astronomical observatories, with applications ranging from microwave to x-ray frequencies [1]. A key aspect in this is that a SiN membrane suspended on a Si wafer is very robust, even with the very thin (sub-) micron dimensions of the SiN legs that are used to create the thermal isolation of the island. Clean room processing allows for either wet (with KOH) or dry (Deep Reactive Ion Etching) etching to remove the Si carrier wafer at the position of the island. The responsivity of a bolometer scales as G^{-1} whereas the ultimate Noise Equivalent Power (NEP), determined by thermal fluctuation noise, is proportional to \sqrt{G} , where G is the thermal conductance of the SiN legs. For applications in background limited far-infrared space-based astronomy (like the SPICA SAFARI instrument) a detector NEP of order $10^{-19} W/\sqrt{Hz}$ is required. Translating this into the required dimensions for the SiN legs results in a typical length of the legs of order 500-1000 μm [2], [3]. An example of a single pixel far infrared bolometer is shown in Figure 1 and an example of an array of bolometers is shown in Figure 2. It can be seen in Figure 2 that the absorbing area of the bolometers takes up only a small amount of the footprint of the array. Low NEP bolometer arrays like this have a very low filling factor in the focal plane, contrary to arrays (e.g. in the SCUBA-2 instrument [4]) that act more as a CCD type of filled array.

Manuscript received June 20 2014. This work was supported in part by the TERADEC Centre of Excellence, funded by the Netherlands Organization of Fundamental Research. G. de Lange, M.D. Audley and G. Keizer are with the SRON Netherlands Institute for Space Research, Landleven 12 9747AD Groningen, The Netherlands. (phone: +31 503634051 e-mail: g.de.lange@sron.nl). C. Bracken and S. Doherty are with the NUI Maynooth, Department of Experimental Physics, Maynooth, Co. Kildare, Ireland.

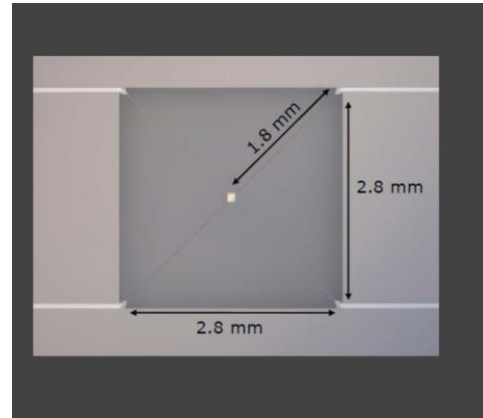


Figure 1 Example of typical low NEP $10^{-19} W/\sqrt{Hz}$ bolometer design. The pixel to pixel spacing in this case would be at least 2.8 mm. The 1.8 mm arrow indicates the length of the SiN legs.

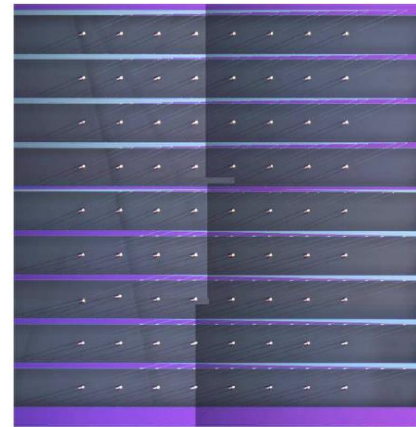


Figure 2 Example of a (wet etched) low NEP far-infrared bolometer imaging array. The light/dark color difference on the left and right side of this picture are due to photographic exposure. The array of light spots are the actual bolometers. As one can see only a small fraction of the area is actually covered by the active bolometers.

To improve the collecting area of the bolometers one typically places a light collecting horn in front of the bolometer array. This horn concentrates the light impinging on the front surface of the horn onto the much smaller bolometer area. With an array of light collecting horns and bolometers with long thin SiN legs, one can therefore build bolometer arrays with very low NEP values. However, the practical limitations to this are the dimensions of the resulting horn and bolometer array. With a typical pixel spacing of 1 to 2 mm (dictated by the required leg length) an array of 100x100 pixels would end up with an array size of say 15-25 cm. This can be prohibitively

large for single wafer processing and the design of cryogenic focal planes. To make better use of the available space in the focal plane we therefore propose to use a stack of bolometer wafers, where each wafer fills part of the empty space that is created by the long SiN legs of an overlying bolometer wafer. In order to optimize the radiation coupling to the individual bolometers, we propose to combine the bolometer wafers with a stack of micro-machined Si wafers that form a non-resonant cavity enclosing the bolometer. In this paper we show some initial design sketches of possible configurations of such an array, together with some initial results on simulations of the radiation coupling to the cavity enclosed bolometer arrays.

II. DESIGN DESCRIPTION OF A SINGLE LAYER CAVITY COUPLED BOLOMETER ARRAY.

Key to the designs described here is the use of Si DRIE etching of the bolometer and cavity wafers. Wet etching restricts the possible configuration of the design to the crystal planes within the wafer, but DRIE etching gives the possibility to etch any desired (vertical) shape within the wafer (see [5] for an application of Si micromachining to fabricate millimeter wave arrays). To illustrate the basic design of the proposed structure we first describe the design of a cavity enclosed single wafer bolometer. As a first step to reduce the pixel spacing we propose to make use of a triangular three leg suspension in a hexagonal packing, instead of a square four leg suspension. The reduction from four to three legs already reduces the thermal conductance and the hexagonal packing and DRIE etching gives the opportunity to have thermally overlapping pixels where a SiN leg of one pixel is placed into the footprint of an adjacent pixel. This is sketched in Figure 3 and Figure 4. For efficient coupling of far infrared radiation to the bolometer it is common to use a reflecting backshort at a distance of $\lambda/4$ behind the bolometer [4]. We propose to use an integrating cavity similar to bolometer designs described in [6] and [7]. A novel approach in this design is to build this cavity by mounting the bolometer wafer on a backing wafer that is etched such that part of the wafer close to the bolometer area is sticking through the bolometer wafer (where slits are etched at the position of the SiN legs). Another wafer with cavity sections and optical feed-throughs to the top surface of this wafer is placed on top to the bolometer and backing wafer. We then have an array of cavity coupled bolometers with optical access via a short section of waveguide or light-pipe. For radiation coupling to the waveguide one can use either a horn array or a Si micro-machined lens array placed in front of the wafer stack.

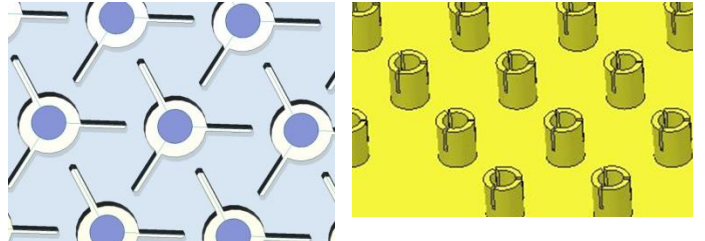


Figure 3 Left: Sketch of a hexagonally packed bolometer array fabricated with DRIE. The blue circles represent the thermally isolated islands that hold the absorber and the temperature sensor. The light blue area is the Si wafer. Electrical wiring to the devices is not shown. Right: The backing wafer where we have extruded the structure vertically in an exaggerated way to show the principle of operation. This backing wafer is made of Si that is fully gold plated

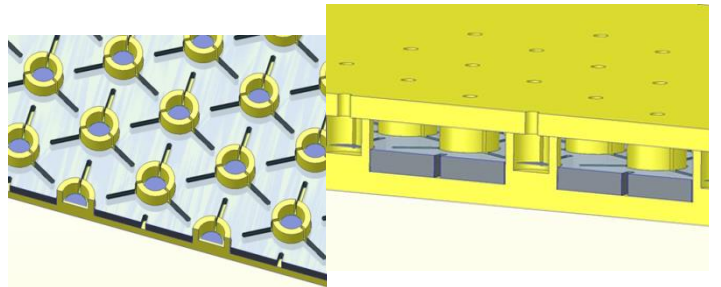


Figure 4 Sketch of a cavity enclosed bolometer array. The left figure shows how the bolometer wafer is placed on the backing wafer, where the lower wafer sticks through the bolometer wafer. Right: the sandwich of wafers including the top wafer (gold plated Si) that closes the cavity, but has an optical feedthrough to couple radiation into the cavity. Since the top wafer is not touching the surface of the bolometer wafer, the gold plated wafer will not short the bias lines of the bolometer wafer. A horn or lens array that is needed to focus the light into the light pipe is not shown.

III. DESIGN DESCRIPTION OF A MULTI-LAYER CAVITY COUPLED BOLOMETER ARRAY

To further enhance the packing density of the bolometers we propose to use the empty space in between the SiN legs. A sketch of this is shown in Figure 5 where the bolometer wafer and a backing wafer are shown.



Figure 5 Left: Bolometer array with extra etched feedthroughs in between the SiN legs. Right: Backing wafer that contains cavities and feedthroughs.

With a stack of multiple wafers we can create a structure as shown in Figure 6 and Figure 7.

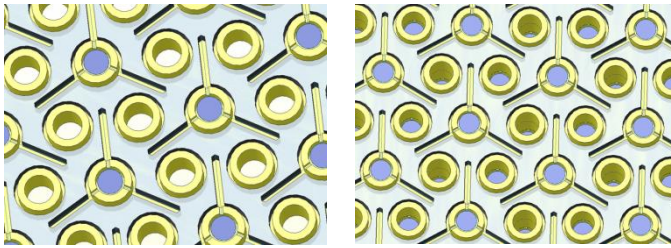


Figure 6 Left: first stage of assembly of a multi-wafer bolometer array. Right: final assembly of the hexagonally packed array. Note that the bolometers are at different depths within the cavity. The top wafer that closes the cavities is not shown.

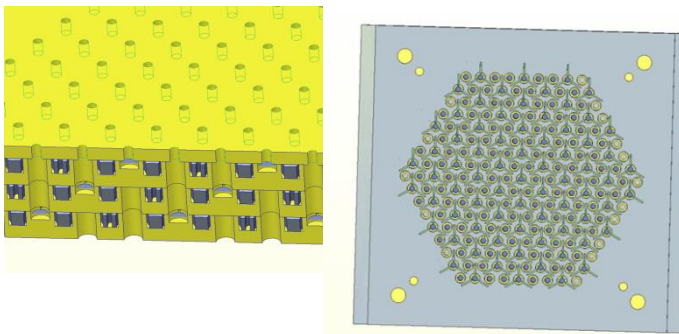


Figure 7 Left: side view of the multi-wafer bolometer design. The yellow wafers are gold plated Si wafers, the grey wafers are the Si wafers that hold the bolometers. Right: final assembly of the hexagonally packed array. The top wafer that closes the cavities is not shown. Details of the bias line connections at the side of the wafers are not shown in this sketch.

The bolometer array now consists of three layers of bolometers and 4 additional backing/topping wafers. If we take a fixed pixel-to-pixel spacing L_{pix} it can be shown that with this identical pixel spacing in a square array and an array as shown in Figure 7, the thermal conductance in the hexagonal array can be about a factor of three lower. For an array of Transition Edge Sensors therefore the phonon noise limited NEP can be reduced by a factor of $\sqrt{0.3}$, for an array that has the same physical dimensions as a square pixel design. If the array size is a design driver the hexagonal design can pack about a factor of 9 more pixels in the same area. This can be of great benefit in reducing the size of large number TES arrays.

IV. SIMULATED DEVICE RESPONSE

In the previous section we have sketched a possible configuration of a cavity enclosed bolometer, without detailing the actual design of the cavity. The absorbing material for far-infrared bolometers with $\lambda/4$ back-shorts generally consists of a thin semi-transparent metal film or mesh with a surface impedance close to 377 ohm (matching the free space impedance). This allows for a 100% coupling efficiency of incoming radiation to the absorber at the resonant wavelength. The general approach for the enclosed bolometers described here is that the cavity is over-moded for the wavelength of interest and is non-resonant, and therefore broadband. We basically propose to build a black-body type cavity with reflecting walls and an absorbing film as discussed by Richards and Winston [6],[7]. The exact position of the film within the cavity is not very critical, which is an

advantage over $\lambda/4$ back-shorts that have to be fabricated with μm accuracy at FIR wavelengths. At very short wavelengths (in a ray-tracing approach) such a cavity can be considered as a highly reflecting cavity with a free standing metal film, where light bounces from surface to surface and loses part of its energy at every pass through the absorbing film. So the radiation in the cavity is either absorbed by the film, or reflected out of the cavity via the entrance aperture. A cylindrical cavity as sketched previously would be possible, but we have simulated the response of square cavities that are terminated by a pyramid. The reason for this is that pyramidal cavities can be etched with an anisotropic KOH etch of Si <100> wafers [8] resulting in reflecting surfaces with extremely low surface roughness. A sketch of an array with pyramidal shaped cavities is shown in Figure 8. In a ray tracing approach the 70.6 degree angle of the etched pyramidal shape causes many reflections within the cavity, contrary to a flat surface or a 90 degree corner cube like reflector.

We have analyzed the pyramidal shaped cavity first with ZEMAX in a ray tracing method, which corresponds to a situation where the incoming light has a much smaller wavelength than the dimensions of the cavity structure. This is the extreme case of a multi-mode approach where a high number of electromagnetic modes is present [9]. As another extreme we have analyzed the structure with the COMSOL EM simulation program, where we use a single mode approach, with only the fundamental TE01 mode being present in the entrance waveguide. In both cases we assume that the surface of the cavity (gold plated Si) is nearly lossless, and the additional apertures in the cavity needed to enclose the SiN legs (see Figure 3) are so small that radiation cannot leak into it. So we assume a cavity with only an entrance light-pipe, reflecting walls, and an absorbing film. Also we do not take into account the coupling mechanism of a horn or lens array to the entrance waveguide, but merely look at the absorption once the light has entered the cavity structure.

TABLE 1 PARAMETERS AND DIMENSIONS USED IN SIMULATING THE ABSORPTION EFFICIENCY OF A CAVITY ENCLOSED BOLOMETER WITH COMSOL.

Parameter	Value
Waveguide Width	100 μm
Waveguide Length	200 μm
Thickness of top wafer	200 μm
Cavity width at widest point	382.84 μm
Absorber Width	200 μm
Absorber Surface Resistance	377 Ω/\square
Absorber thickness	20 nm

We have analyzed several different configurations of pyramidal shaped cavities. Some initial results are shown in Figure 8 and Figure 10. More detailed analysis of this structure will be published elsewhere. An example of a ray-tracing simulation is shown in Figure 8. In this initial simulation the absorber size was equal to the dimension of the waveguide entrance (100x100 μm) and the largest dimension of the cavity was 400x400 μm . Therefore the absorbing film fills only a relatively small area of the cross section of the cavity. Even with this configuration we find that due to the

many internal reflections an absorption efficiency of 85% can be obtained.

An initial result of a COMSOL simulation is shown in Figure 10. The parameters that were used in this simulation are shown in TABLE 1. These numbers are chosen to comply with the restrictions on pixel size and spacing for the development of the far-infrared TES bolometers developed for the SAFARI instrument. The SAFARI instrument has three wavelength bands covering the 30-200 μm wavelength range (2-9 THz). Standard wafer thicknesses of Si wafers, and the capabilities of DRIE etching match well with the required dimensions in these far-infrared wavelengths. In this initial design of the pyramidal cavity we observe that the absorption has a cut-on frequency at 1.5 THz due to the 100x100 μm waveguide, shows a strong resonant behavior between 1.5 to 3 THz and then has a more than 80% coupling efficiency up to 9 THz (where we stopped our simulation) with some notable resonances between 5 and 7 THz. To get rid of these resonances we have further optimized the cavity design by introducing some asymmetry that smears out the resonances. By doing so we are able to get a simulated response of the cavity coupled bolometer over a very wide band running from 2-9 THz, only limited by the cut-on frequency of the waveguide, and the end frequency of our simulation.

V. CONCLUSION

In conclusion we have described the possible configuration of a silicon micro-machined cavity coupled bolometer that can be used in the far-infrared wavelength range. Simulations show that the design can have broadband coupling over a very wide wavelength range. Compared to existing designs that make use of a combination of Si bolometer wafers and Cu reflecting backshorts or cavities, the use of Si micro-machined cavities has several advantages with respect to vertical alignment, packing density, and thermal expansion properties at cryogenic temperatures. A more detailed study on the simulated performance will be published elsewhere.

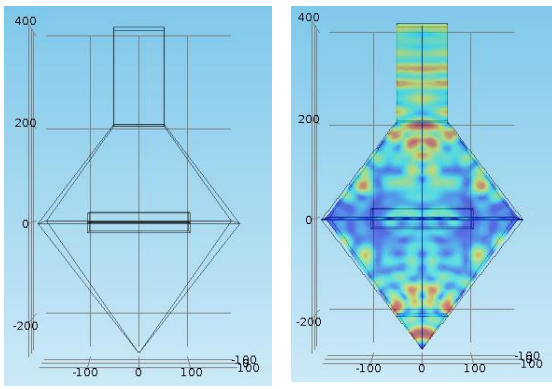


Figure 9 COMSOL modelling of a pyramidal cavity with a thin film absorber. The dimensions in the figures are in μm . On the right the electric field distribution within the cavity at a frequency of 5.3 THz. The waveguide is exited with the fundamental TE01 mode.

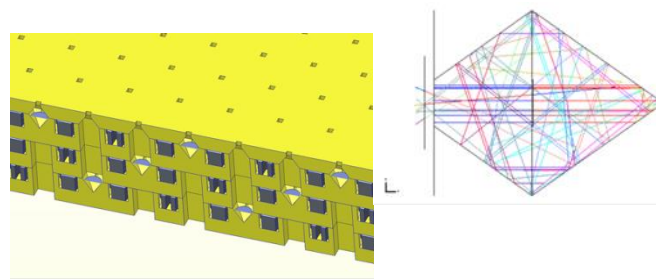


Figure 8 Ray tracing simulations of a pyramidal cavity enclosed bolometer. The ray tracing results for only a few rays are shown and it can be seen that rays that enter the cavity perpendicular to the absorber are reflected many times within the cavity, due to the 70.6 degree angle of the pyramid. Based on simulations with many more rays it is shown that an absorption efficiency of 85 % can be achieved.

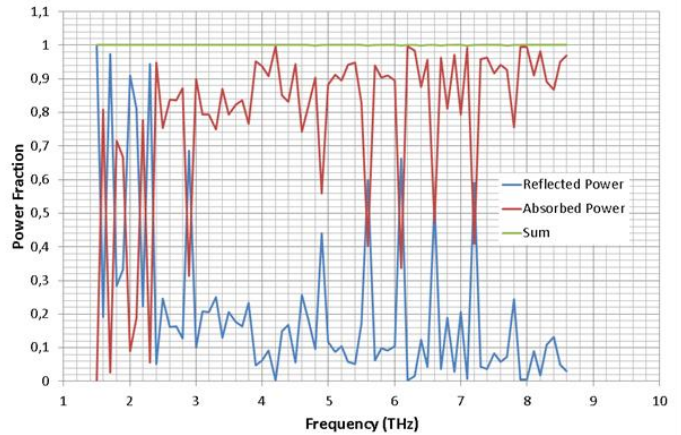


Figure 10 absorbed (red), reflected (blue) and total power (green) of the simulated cavity shown in Fig 9. The absorbed power is measured within the thin film, the reflected power is measured at the input port of the waveguide. The summation is used to cross-check the simulation. The waveguide has a cut-on at 1.5 THz. In the region where the cavity is not very much over-moded, strong resonant behavior is observed.

REFERENCES

- [1] Irwin, K. D. and Hilton, G. C., "Transition-edge sensors," [Cryogenic Particle Detection], C. Enss, Ed., Springer, 81-97 (2005)
- [2] Jackson, B., de Korte, P., van der Kuur, J., Mauskopf, P., Beyer, J., Brujin, M., Cros, A., et al. IEEE Transactions on Terahertz Science and Technology 2(99), 1-10 (2011).
- [3] Michael D. Audley ; Gert de Lange ; Jian-Rong Gao ; Pourya Khosropanah ; Marcel Ridder, et al. Proc. SPIE 8452, Millimeter, Submillimeter, and Far-Infrared Detectors and Instrumentation for Astronomy VI, 84520B (September 27, 2012); doi:10.1117/12.925234.
- [4] Holland W. S. et al., 2013, MNRAS, 430, 2513.
- [5] J.W. Henning, P. Ade, K.A. Aird, J.E. Austermann, J.A. Beall, D. Becker, B.A. Benson, L.E. Bleem, J. Britton, J.E. Carlstrom et al. Proc.SPIE Int.Soc.Opt.Eng. 8452 (2012) 84523A
- [6] P.L. Richards and M. Tinkham, Phys. Rev. 119, 575 (1960).
- [7] D. A. Harper, R. H. Hildebrand, R. Stiening, and R. Winston Applied Optics, Vol. 15, Issue 1, pp. 53-60 (1976)
- [8] G.T.A.
- [9] Kovacs, N.I. Maluf, and K.E. Petersen, "Bulk Micromachining of Silicon," IEEE Proceedings, vol. 86, no. 8, pp. 1536-1551, August 1998
- J.A. Murphy and R. Padman, Infrared Physics, Vol 31, No 3, pp 291-299, 1991.

A Resonance Cold-Electron Bolometer with a Kinetic Inductance Nanofilter

Leonid S. Kuzmin

*Chalmers University of Technology, Sweden, NSTU, N. Novgorod, SINP, MSU, Moscow
Email: kuzmin@chalmers.se*

A novel type of resonance cold-electron bolometer (RCEB) is proposed. In this sensor, the internal resonance is organized by the kinetic inductance of an ultrasmall NbN superconducting nanostrip and the capacitance of the nanoscale SIN (Superconductor-Insulator Normal) tunnel junction. Decisive breakthrough was done by implementation of the CEB with kinetic inductance of superconducting absorber and normal metal traps [1, 2] with proper resonance properties. The kinetic inductance is about 300 times smaller than the geometrical inductance of the same value. This reduction of size gives an opportunity to create nanofilters with a total size considerably smaller than the wavelength. This internal resonance acts as a bandpass filter (instead of external filters) with a bandwidth of 3-50%, something needed for radioastronomy applications [3].

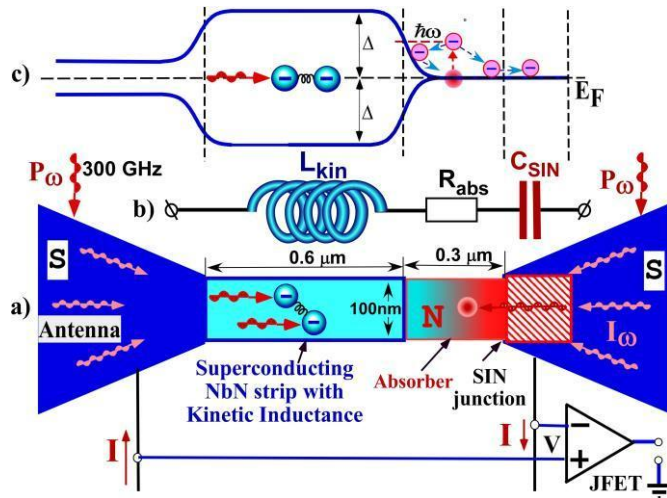


Fig 1. a) Sketch of the Resonance Cold-Electron Bolometer (RCEB) with kinetic inductance of the superconducting NbN strip and capacitance of the SIN tunnel junction as an RF internal filter. b) Equivalent scheme of the bolometer including kinetic inductance L_{kin} , the capacitance of the tunnel junction C_{sin} , and resistance of absorber R_{abs} with typical parameters for 300 GHz; c) Energy diagram of RCEB with $\Delta > hf$.

The NbN protection against escaping hot quasiparticles provides a unique opportunity to create an optimal CEB with only one SIN junction and an Andreev SN contact for thermal protection, in contrast to a classical CEB with two SIN junctions. The well-known problem of hot quasiparticles escaping over the Andreev barrier (Δ) is overcome here by creating a barrier higher than quantum energy $\Delta > hf$ to have working kinetic inductance. Replacing two SIN junctions by one junction, we could use this junction of half the area to keep the same capacitive coupling. Therefore, a single-junction RCEB would have four times less area of junctions (and volume of absorber) in comparison with a two-junction RCEB and should show better noise performance due to the proportionally decreased e-ph noise component.

The RCEB can be effectively used to create multiband elements that are actual tasks in radioastronomy due to the benefit that comes from its ability to use co-located data, and problems with the dramatic increase of the size of the focal plane.

References

1. L.S. Kuzmin, "Cold-Electron Bolometer," in the book: *BOLOMETERS*, ed. A.G.U.Perera, INTECHWEB.ORG, ISBN 978-953-51-0235-9, 2012, pp. 77-106. Available: <http://www.intechopen.com/books/bolometers/cold-electron-bolometers>
2. L. S. Kuzmin, "Superconducting Cold-Electron Bolometer with Proximity Traps", *Microelectronic Engineering*, 69, 309-316 (2003).
3. L. S. Kuzmin, "Resonance Cold-Electron Bolometers with a Kinetic Inductance Nanofilter", submitted to IEEE TST, Sept. 2013

A planar frequency selective bolometric array at 350 GHz

S. Mahashabde*, A. Sobolev†,♣, M. A. Tarasov†,* and L. S. Kuzmin*

Email: sumedh@chalmers.se

*Dept. of Microtechnology and Nanoscience (MC2)

Chalmers University of Technology, Göteborg, Sweden

†Kotel'nikov Institute of Radio Engineering and Electronics, Moscow, Russia

♣Moscow Institute of Physics and Technology (State University), Moscow, Russia

Planar bolometric imaging arrays are becoming increasingly diverse in kind due to their simple design and scalability. Frequency selective bolometric designs [1] have earlier coupled bolometers with frequency selective quasioptical interference filters as compact sub-millimetre radiometers. Here we describe a bolometric focal plane array consisting of the Cold-Electron Bolometer [2] (CEB) integrated in a frequency selective surface (FSS) fabricated on a Silicon substrate with a backshort. This array is formed by a periodic pattern of conducting annular square elements and the two-terminal CEB is embedded directly in the elements' arms. The CEBs impedance has been matched to the FSS which provides resonant interaction with sub-millimetre radiation. A further degree of freedom for the tuning is via varying the thickness of the substrate. We've been able to design the FSS at 350 GHz with peak coupling of more than 90% as is common for FSS based filters. The integrated CEB array has been designed for a photon noise limited performance with cold JFET amplifiers for optical power loads between 15 pW to 80 pW. This design can fit the requirement of balloon-borne CMB missions like OLIMPO. A prototype of such a detector has been fabricated and optical response to blackbody radiation has been measured, indicating responsivity up to 5×10^8 V/W and higher. FSS based structures exhibit narrow bandwidths and we're in the process of optimisation of our imaging array to achieve bandwidth of more than 10% required for OLIMPO telescope. The details of this new concept, together with numerical simulations and optical measurements will be presented.

References

1. Kowitt, M. S., Fixsen, D. J., Goldin, A., & Meyer, S. S. (1996). Frequency selective bolometers. *Applied optics*, 35(28), 5630-5635.
2. L. Kuzmin, Optimization of the hot-electron bolometer for space astronomy, SNED Proc., pp. 145-154, Naples (2001).

Power Load Dependencies of Cold Electron Bolometer Optical Response at 350 GHz

Mikhail A. Tarasov, Valerian S. Edelman, Andrey B. Ermakov, Sumedh Mahashabde, and Leonid S. Kuzmin

Abstract— Cold electron bolometers integrated with twin-slot antennas have been designed and fabricated. Optical response was measured in 0.06-0.6 K temperature range using black body radiation source at temperature 2-15 K. The responsivity of 0.3×10^9 V/W was measured at 2.7 K radiation temperature. The estimated ultimate dark responsivity at 100 mK can approach $S_v = 10^{10}$ V/W and reduces down to 1.1×10^8 V/W at 300 mK for the sample with absorber volume of 5×10^{-20} m³. At high power load levels and low temperatures the changes of tunneling current, dynamic resistance and voltage response have been explained by non-thermal energy distribution of excited electrons. Distribution of excited electrons in such system is of none-Fermi type, electrons with energies of the order of 1 K tunnel from normal metal absorber to superconductor instead of relaxing down to thermal energy kT_e . This effect can reduce quantum efficiency of bolometer from hf/kT_{ph} in ideal case down to single electron per signal quantum in the high power case.

Index Terms—bolometers, nanofabrication, slot antennas, submillimeter wave technology, superconducting devices

I. INTRODUCTION

Cold-electron bolometer with Superconductor-Insulator-Normal metal-Insulator-Superconductor (SINIS) structure has promising predicted performance [1,2]. Under microwave irradiation additional excited electrons with high excess energy provide increase in tunneling current and/or decrease of dc voltage and such response is dependent on applied power and frequency. Usually for theoretical estimations it is assumed that microwave radiation is equivalent to dc heating at the same absorbed power. In such process the electron temperature of absorber is increased over the phonon temperature.

However in normal metal for Terahertz radiation at frequency $f \gg kT/h$ dominates quantum absorption of photons with energy $E=hf \gg kT$ by single electrons [3-6]. In this case the energy distribution of electrons is determined by a balance of processes of photon quantum absorption, electron-electron, electron-phonon, phonon-electron, phonon escape processes, and tunneling of excited electrons in a SIN junction [3,4]. This distribution function is significantly different from

Manuscript received on May 29, 2014. This work was supported in part by the Swedish Space Agency SNSB and Swedish scientific agency Vetenskapsrådet.

M.A.Tarasov and A.B.Ermakov are with the V.Kotelnikov Institute of Radio Engineering and Electronics of Russian Academy of Sciences, 125009 Moscow, Russia (phone: 7-495-6293418; fax: 7-495-6293678; e-mail: tarasov@itec.cplire.ru).

V.S.Edelman is with the P.Kapitza Institute for Physical Problems of Russian Academy of Sciences, Moscow, Russia.

S.Mahashabde and L.S.Kuzmin are with the Chalmers University of Technology, Gothenburg, Sweden.

equilibrium Fermi distribution. Microscopic calculations of tunneling current in clean limit [3,4] for electron-electron and electron-phonon collision integrals show that increase of response is dependent on multiplication of excited electrons with energies $\epsilon \gg kT$ due to electron-electron interactions and reabsorption of nonequilibrium phonons that did not escape from absorber. Multiplication of non-equilibrium electrons leads to increase of current response $\delta I(P)$, in which P – absorbed power, and this multiplication leads to increase in current δI for voltage bias mode. Thus current response δI of SINIS detector can exceed the photon counter limit of e/hf , but still being below the bolometric response limit of e/kT . Studies and optimization of energy relaxation in electron system at low temperatures can help to improve the practical optical response of SINIS detectors.

In our earlier experiments [7,8] we observed voltage response $\delta V(I) = V_{I,P=0} - V_{I,P}$, which shows that there is no thermal equilibrium in electron system. Now we performed detail analysis of new experimental data on IV curves, dynamic resistance, optical response to show absence of equilibrium in electron system and significant tunnel current due to electrons with excess energy.

II. EXPERIMENT

Bolometers containing 3 serial SINIS structures were integrated in twin-slot antennas. Bottom layer of bolometer was made of normal-metal Al absorber 10 nm thick in which superconductivity was suppressed by underlayer of ferromagnetic film [9]. For microwave signal such bolometers were connected in parallel by means of capacitive connection. Dimensions of elements: area of tunnel junctions $0.25 \mu\text{m}^2$, length, width and thickness of normal metal strip between tunnel junctions $1 \times 0.1 \times 0.01 \mu\text{m}^3$, dc resistance of single absorber $\sim 200 \Omega$. Parallel connection for microwave signal makes antenna load of 60Ω . Tunnel junctions parameters were similar to earlier studied in [7,8]. When cooling down to $T < 0.1$ K the resistance ratio $R_d(V=0)/R_n$ (in which $R_d = dV/dI$, R_n - asymptotic normal resistance) approached $R_d/R_n = 15000$, and total resistance of array at 0.1 K approached $R_{d(V=0)} = 400 \text{ M}\Omega$.

Samples were measured in dilution cryostat equipped with pulse tube refrigerator [10]. Additional recondensing stage with liquefying of He gas in a 0.12 liter container allows to keep temperature below 0.1 K during 4-5 hours with compressor shut down. Chip with SINIS receiver was mounted inside copper radiation shield at temperature 0.4-0.45 K, in which inner wall was painted with black absorber containing Stycast® 2850FT.

Silicon chip 0.35 mm thick was attached to sapphire hyperhemisphere 10 mm in diameter that collect radiation to the planar antenna. Lens itself was glued with Stycast® 1266 in copper holder screwed to the dilution chamber. Measurements with RuO₂ thermometer glued to Si plate instead of detector show that its temperature at 0.1 K differs by less than 2-3 mK from mixing chamber temperature measured by LakeShore® thermometer with absolute error below 5 mK.

In front of lens in the bottom of radiation shield it was a hole 5 mm in diameter, which was covered with planar bandpass filters [11] for central frequency of 330 GHz and total passband of 50 GHz. Spectral transmission within 10% accuracy is described by product of two Lorentz lines with halfwidth of 70 GHz. Transmission in the maximum was over 90%. Distance from lens to filter is 2-3 mm, between filters 2 mm, from filter to black body source 2-3 mm.

Radiation source is a black body made of Si wafer covered with NiCr film of square resistance of 300 Ω. Wafer was mounted on heat insulating legs to 1 K pot. Temperature of radiation source was monitored by resistance of a calibrated RuO₂ chip-resistor and heating varied by current through this NiCr film in the range of 0.9-15 K. Dissipated power was up to few milliwatts, time constant for heating/cooling of the order of 0.1 s.

Power received by antenna was calculated using Planck formula for single mode

$$P_{\text{incident}} = \int df \frac{\frac{hf}{kT_R}}{\exp\left(\frac{hf}{kT_R}\right) - 1} * K1 * K2 * K3 \quad (1)$$

in which T_R - radiation source temperature, factors $K1$ and $K2$ accounted for transmission of filters and spectral matching of antenna. For twin-slot antenna we take Lorentz line with half-width of 100 GHz and maximum at 330 GHz. Influence of $K2$ was rather small, below 20%. Multiplier $K3=0.72$ takes into account reflection of sapphire-silicon and sapphire-vacuum interfaces.

III. EXPERIMENTAL IV CURVES AND ESTIMATIONS OF ELECTRON TEMPERATURE

Equivalent electron temperature in normal metal absorber was deduced from dependencies of dynamic resistance $R_d=dV/dI$ and comparison with dV/dT dependence of ideal SIN junction at some effective electron temperature. In Fig. 1a,b presented IV curves for two electron temperatures and calculation according to simple analytic relation (2). IV curve of ideal SIN junction for voltages below the gap of superconductor $V_\Delta=\Delta/e$ (in which Δ — energy gap of superconductor), for single junction can be presented as [12]:

$$I(V,T) = \frac{1}{eR_n} \sqrt{2k\pi T_e e V_\Delta} \exp\left(-\frac{eV_\Delta}{kT_e}\right) \sinh\left(\frac{eV}{kT_e}\right) \quad (2)$$

In our case we have 6 junctions connected in series, so measured values of R_n and V are divided by 6 to fit with model curve. Voltage derivative of current brings dynamic conductivity and inverse value is dynamic resistance. In

experimental curves measured voltage corresponds to $6V_{\text{sin}}$ in which V_{SIN} — voltage across the single SIN junction.

Gap voltage V_Δ in (2) according to BCS theory corresponds to $eV_\Delta=\Delta(0)=1.76*kT_c$ in which T_c — critical temperature. It can be determined from the dependence $R_d(T, V=0)$, which in the temperature range ~ 0.3 – 0.5 K has exponential shape. At higher temperatures it should be accounted also the temperature dependence $\Delta(T)$, and at temperatures below 0.2 K dynamic resistance R_d approaches constant value that is explained by overheating of electron system by external radiation. Value of equivalent T_e can be estimated by fitting with equation (2). In our case using $\Delta=k*2.45$ K we obtained good correspondence of experimental calculated curves in all figures. Small difference can be observed at $V>0.4-0.5$ mV, where resistance is higher compared to calculated one due to electron cooling. In our fitting we use value of Δ that corresponds to $T_c\sim 1.4$ K. In measurements at $T=1.5$ K IV curve is linear and at 1.3 K nonlinearity is clear visible, so T_c is within this range.

If electron system is excited by radiation, then dependence is different from heating of sample, see fig. 1b. There is no more correspondence with simple thermal model. If we take T_e for which $R_d(V=0)$ is the same as in model, then at higher bias current the difference in resistance can be more than 10 times larger. One can see that power response and temperature response are different at 70 mK and coincide at 340 mK (Fig. 2).

Dependencies of responsivity $d\delta V/dP$ on phonon temperature and equivalent electron temperature are presented in Fig. 3a,b for radiation power levels 0.22 pW, 1.35 pW, 2.95 pW, 4.95 pW. When plotted in dependence on electron temperature (b) the shape of dependence is more natural and shows that responsivity is dependent on nonequilibrium electron temperature. When irradiated at 5 pW load the responsivity is reduced by an order of magnitude compared to 0.2 pW power load. When bath is heated to 0.34 K these responsivities become equal for all power loads which means that in this range detector becomes linear, $d\delta V/dP$ is independent on power and is determined by temperature. In this case electron and phonon temperatures are very close, and nearly equal. It means that increase in bath temperature leads to increase of relaxation processes and thermalization of electron system.

Losses in bolometer can be roughly estimated from power to current transfer ratio, or current responsivity. Compare a number of incoming quanta $I_0=5*10^8$ s⁻¹ for 0.1 pW at frequency 330 GHz and number of excited electrons that tunnel due to irradiation $I_S=6*10^8$ s⁻¹ (current increase at this power load). Quantum efficiency $\eta=I_S/I_0=1.2$ is close to unity, which means that one quantum produce just one electron, that is a photon counter mode. There is no multiplication of excited electrons number which was predicted in [4] for bolometric mode of operation. If energy did not escape from electron system, then the number of excited electrons with energies in the range ~ (0.2 – 1) Δ should be 30 times more.

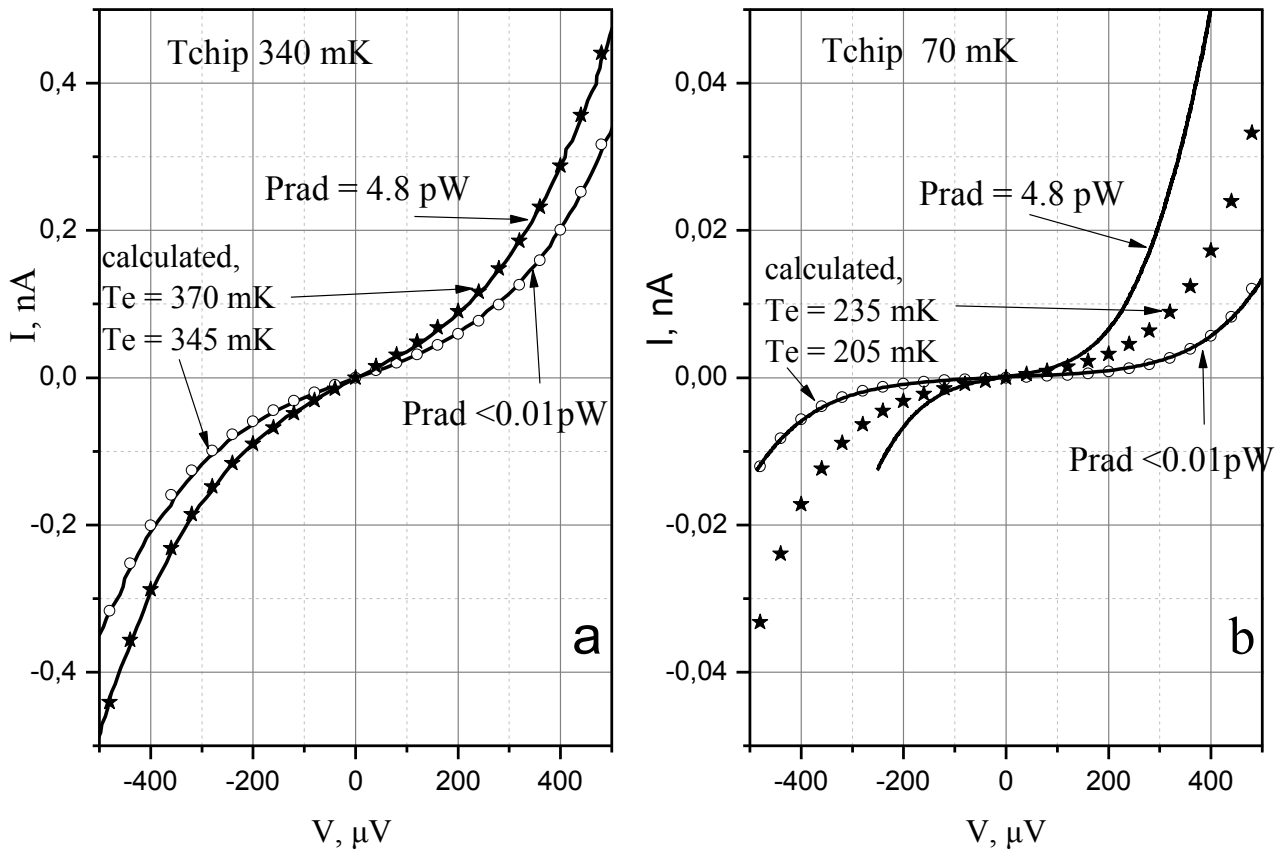


Fig. 1. IV curves of SINIS bolometer at bath temperature 340 mK (a) and 70 mK (b). Solid lines correspond to experimental data obtained at two radiation power levels of 4.8 pW and below 10 fW. Stars and circles – calculated curves for 370 mK and 345 mK (a), and 235 mK and 205 mK (b).

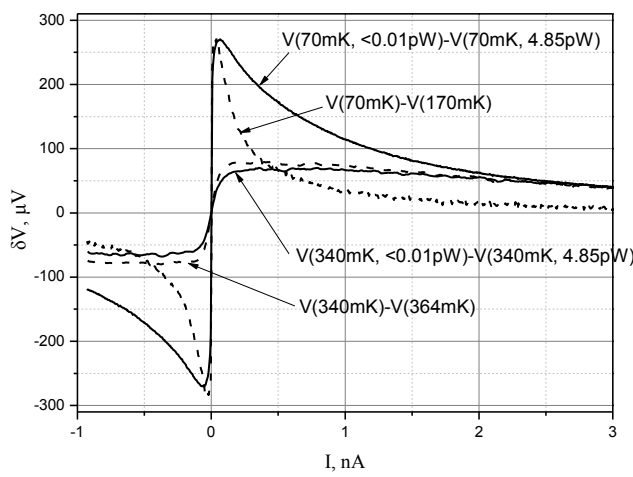


Fig. 2. Voltage response dependencies on dc bias for temperatures 70 mK and 340 mK. Solid lines under 4.85 pW irradiation, dashed- response to equivalent increase in temperature without irradiation.

IV. DISCUSSION

According to estimations [17] the difference of calculated and experimental curves proves the absence of equilibrium in electron system when energy distribution for electrons with energy above the Fermi energy and holes with energy below it does not correspond to Fermi distribution with equivalent electron temperature. These excited electrons can be viewed in two groups: thermalized and athermal. Impact of thermalized electrons can be estimated assuming that their temperature corresponds to calculated for the case when calculated curve tangents experimental at $V=0$, and dynamic resistance of both are equal. In Fig.1b such assumption leads to the electron temperature under irradiation estimation of 235 mK. The impact from athermal electrons can be estimated as a difference between measured and calculated and can be up to 70% of the total response. When temperature increase the relaxation processes speed-up and at 0.34 K the impact from athermal electrons is much less. At the same time impact from thermalized electrons increase, they prevail in tunneling current. As a result the voltage dependence of response approaching the calculated one.

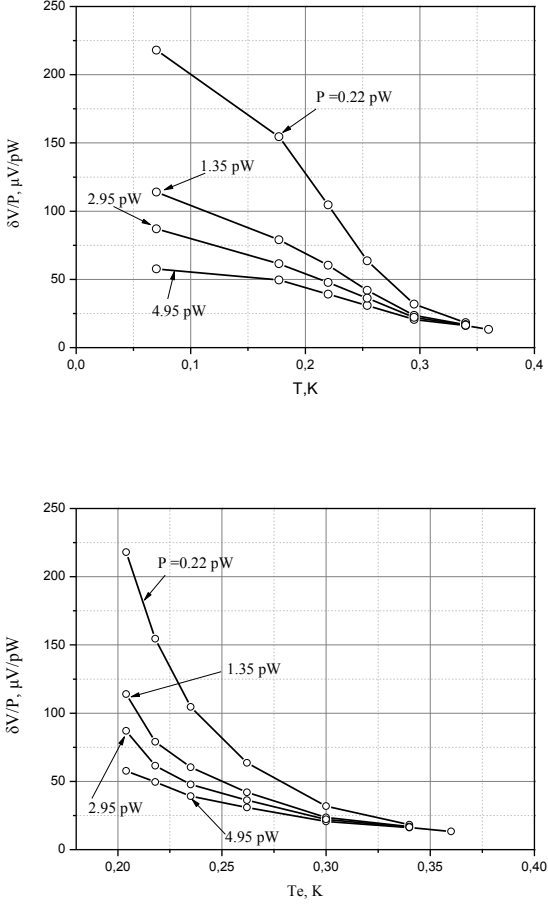


Fig. 3. Responsivity dependence on bath temperature (top panel) and on equivalent electron temperature (lower panel) for radiation power levels 0.22 pW, 1.35 pW, 2.95 pW, 4.95 pW.

Radiation power is collected in a normal metal absorber with dimensions much less compared to the wavelength, so it can be considered as a lumped element. When absorbing the radiation quantum energy $hf/k = 16 \text{ K}$, all this energy is transferred to electron, it forms electron-hole pair with energies from 0 to hf above/below the Fermi energy. The average energy of excited electron and hole is 8 K.

Excited electrons and holes diffuse towards the area of tunnel junctions with diffusion time τ_{diff} , after that transfer into superconducting electrode with time constant τ_{sin} . During this period energy is redistributed due to electron-phonon, phonon-electron, electron-electron, phonon-phonon and phonon escape processes. As a result energy of excited electrons is reduced, their number can increase, some power escape into substrate and superconducting electrodes. Additional tunneling current under irradiation depends on ratio of time constants of these processes. Since all time constants are strongly dependent on excitation energy, the dynamics become very complicated, especially taking into account transition from two-dimensional to three dimensional cases when changing temperature and power. Processes in superconducting electrode will be also ignored; we assume it as a thermal sink.

Microscopic model described in [13] assume that as the result of electron-electron interaction primary electron after each inelastic collision will produce three new quasiparticles: two electrons and one hole. Each of them has $hf/6$ of initial energy. Absorption of one phonon will produce two quasiparticles: one electron and one hole, similar to photon absorption. Spontaneous emission of phonons preserves the number of quasiparticles. Rate of electron-electron collisions that are necessary for multiplication of electrons is an order of magnitude slower compared to electron-phonon relaxation which reduce excitation energy and do not lead to multiplication of quasiparticles. The phonon-electron process can slightly increase bolometer response above the photon counter limit.

Model of thermalization in normal metal is also discussed in [16]. According to this model the most probable process for energy relaxation of electron from energy level of $E=\Delta$ is down to $\Delta/4$ and emerging of phonon with energy $3\Delta/4$. This energy is much higher compared to thermal phonons and we obtain a nonthermal distribution for both phonons and electrons.

First we estimate the diffusion constant for electrons in normal metal:

$$D = \frac{1}{e^2 N \rho} \quad (3)$$

in which $\rho=0.07 \Omega \cdot \mu\text{m}$, $N=2.3 \cdot 10^{10} \mu\text{m}^{-3} \text{ eV}^{-1}$ is electron density at Fermi level, this brings $D=0.004 \text{ m}^2/\text{s}$. Diffusion time for electrons to travel the distance about 1 μm from the middle of absorber to tunnel junction area is $\tau_{\text{diff}}=0.25 \text{ ns}$.

Relation of diffusion constant with speed v mean free path 1 is $D=lv/3$. Taking Fermi velocity $v_F=2 \cdot 10^6 \text{ m/s}$ one can get the mean free path in absorber $l=6 \text{ nm}$. Thickness of absorber in our samples is 10 nm, which is comparable to mean free path. Diffusion time through the thickness of absorber is 0.025 ps.

One more important parameter is a characteristic time for tunneling in SIN junction. Time constant for electrons to escape from normal metal to superconducting electrode is determined by time of many attempts providing close to unity probability to tunnel through the barrier. Transparency of barrier is related to normal resistance of junction. According to [3, 12], if in the bias point differential resistance is close to normal resistance, then tunneling time constant is

$$\tau_{\text{sin}} = N(0)e^2 R_n S t \quad (4)$$

in which N is density of states at Fermi level, R_n is normal resistance of junction, S junction area, t film thickness. For aluminum film 10 nm thick, $R_n S \approx 1000 \Omega \cdot \mu\text{m}^2$, this corresponds to $\tau_{\text{sin}} \approx 40 \text{ ns}$. As a result $\tau_{\text{sin}} \gg \tau_{\text{diff}}$ and distribution of electrons along the normal metal is uniform.

Nonequilibrium condition of system is mainly determined by relation between electron-electron and electron-phonon time constants. The last can be estimated similar to [13, 14] as:

$$\tau_{\text{ep}} = \frac{3 I_0 k^6 N(0)}{\sum E^4} \quad (5)$$

Parameter $I_0=25$, electron-phonon constant $\Sigma=2.3 \text{ nW}/(\mu\text{m}^3 * \text{K}^6)$. For average excitation energy of electrons $E/k=8 \text{ K}$ it corresponds to $\tau_{ep}=0.2 \text{ ns}$, that is comparable to diffusion time. The wavelength of such phonons with energy 8 K and sound speed in aluminum $\sim 5000 \text{ m/s}$ equals to $\lambda_{\text{phonon}} \sim 30 \text{ nm}$ and it is larger compared to film thickness. It means that such phonons propagate at small angles to the boundary between Al absorber and Si substrate and probability of their escape to substrate is rather small. The last stage of electron-phonon interaction producing quasi-Fermi distribution happens at phonon temperature 340 mK or 70 mK with corresponding electron temperatures 370 mK and 235 mK for which electron-phonon power flow in absorber is 280 fW and 28 fW. Actually electrons interact with phonons of the entire volume of Al absorber and Al superconducting electrodes that is 10 times as large, this makes corresponding power flow up to 3 pW and 0.3 pW.

Opposite process of phonon-electron interaction is rather fast, according to [9,14]:

$$\tau_{pe} = \frac{234 N_A n_d k^3}{6 \sum \Theta_D^3 E^2} \quad (6)$$

In which $N_A * n_d$ – atomic density that is for aluminum $6 * 10^{22} \text{ cm}^{-3}$, $\Theta_D=428 \text{ K}$ – Debye temperature. If we take the distribution of energy from electron with initial energy 8 K to electron and phonon with the ratio 1:3, this corresponds to $\tau_{pe}(6 \text{ K})=5 \text{ ps}$.

The dynamics is quite different for electrons in the region of tunnel junctions. For acoustic waves both normal and superconducting electrodes separated by barrier below 2 nm thick is the same material and phonons can escape from normal into superconductor metal in few picoseconds without returning energy to electrons in absorber. Such process is a loss channel for energy that irreversibly escapes to superconductor or substrate. Characteristic time for such escape through the thickness of absorber t_{abs} is $\tau_{\text{escape}}=t_{abs}/v_{\text{sound}}=2 \text{ ps}$.

Phonon relaxation time can be estimated in the case of scattering at boundaries by dividing the characteristic length of our sample about $l_{\text{abs}}=3 \mu\text{m}$ by sound speed

$$\tau_{pp}=l_{\text{abs}}/v_{\text{sound}}=600 \text{ ps.}$$

Redistribution of energy among electrons is governed mainly by electron-electron interaction. Equation for calculating of such time constant τ_{ee} for two-dimensional case corresponding to thin normal absorber taken from [12,14]:

$$\tau_{ee} = \frac{\hbar E_F}{\pi^2 E^2 \ln\left(\frac{E_F}{E}\right)} \quad (7)$$

in which $E_F=11.6 \text{ eV}$ – is Fermi energy. At electron temperature of 8 K this time is $\tau_{ee}=1 \text{ ns}$, that exceeds $\tau_{ep}=0.2 \text{ ns}$ for the same electron energy. For three-dimensional case τ_{ee} is dozens times as much compared to two-dimensional. Value of τ_{ee} becomes equal to τ_{sin} for temperatures in the range (1...1.3) K. Value of τ_{ep} becomes equal to τ_{sin} for electron temperatures $\sim 2 \text{ K}$.

From the above review it is clear that due to complicated combination of electron-electron, electron-phonon, phonon-electron interactions which vary with signal frequency and

power, the energy distribution of electrons is much different from simple Fermi distribution. Nonequilibrium of system is mainly determined by ratio of escape time for electrons due to tunneling τ_{sin} to electron-electron and electron-phonon time constant. Finally, we can pick out two groups of time constants, first is energy independent, it is diffusion time $\tau_{\text{dif}}=0.25 \text{ ns}$, tunneling time $\tau_{sin}=40 \text{ ns}$, phonon escape time $\tau_{\text{esc}}=2 \text{ ps}$, and phonon-phonon time $\tau_{pp}=0.6 \text{ ns}$. Energy dependent time constants are second order dependent $1/E^2$ electron-electron time τ_{ee} and τ_{pe} , and also a fourth order dependent $1/E^4$ electron-phonon constant τ_{ep} . Dependencies are presented in Fig. 4.

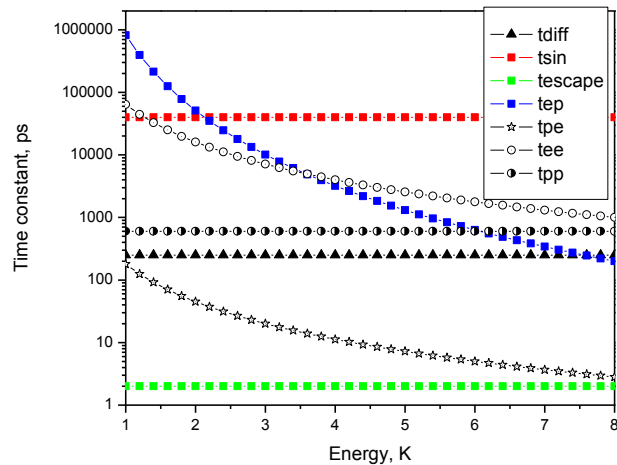


Fig. 4. Time constant dependencies on excitation energy plotted in Kelvins i.e. E/k .

Electron-electron and electron-phonon time constants become equal at energy around 3.7 K, and for lower energies electron-phonon interaction get slower, so electron-electron can become dominating. To increase bolometer efficiency the length of absorber should be increased providing diffusion time τ_{dif} longer compared to τ_{ee} and τ_{ep} , value of τ_{ep} should be increased by using absorber material with lower electron-phonon parameter sigma; resistivity, density, and acoustic impedance of absorber material should be increased as well. According to [3] the optimal resistance of SIN junction should be around $10 \text{ k}\Omega$.

V. VOLTAGE RESPONSE

In our experiments at low bias we observe significant maximum that is not presented in conventional model of SINIS bolometer without strong power load. This maximum is increasing with signal power level that contradicts to eventual explanation by Coulomb blockade that should increase with cooling and reducing of power level. In IV curves current increase is observed compared to the dark IV curve.

We assume that such additional maximum corresponds to direct detection at nonlinearity of SIN junction. At zero bias there is no detection because of IV symmetry for both half-periods of signal and for bias about $50-100 \mu\text{V}$ there is maximum of rectified signal at maximum of nonlinearity.

Contrary to bolometric detection here we have direct detection (rectification) of incoming signal. In Fig.5,6 presented response dependencies measured at black body source temperatures 0.89; 1.8; 2.25; 3.0; 3.6; 4.3; 4.9; 5.5; 6.0; 6.6; 7.2; 8.3; 9.8; 11.2; 12.5 K. Voltage response obtained by subtraction of adjacent IV curves.

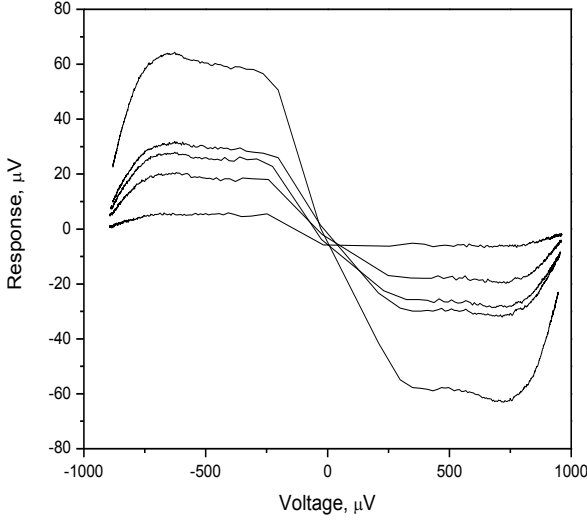


Fig. 5. Voltage response at lower levels of signal in the range 1-4 K. Standard bolometric response observed at about half-gap voltage bias, and at lower bias around quarter gap voltage corresponding to higher nonlinearity appears a direct detector response.

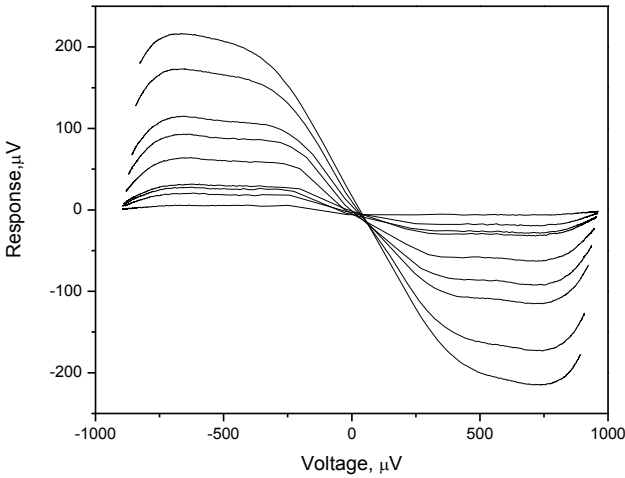


Fig. 6. Voltage response in wider radiation temperature range 1 - 15 K.

Simple calculation of second derivative of IV curve for SIN junction (Fig.7) shows that maximum curvature is presented at lower bias voltages. For comparison in Fig.8 similar dependencies is presented in logarithmic scale for three temperatures of sample. Curvature is increasing by four orders with cooling from 350 mK to 150 mK.

Nonlinearity of SIN junctions was earlier used for heterodyne and direct detection of microwave signals in [18,19], in which were used Pb/Bi/In-oxide-Ag junctions with area of $1.2 \mu\text{m}^2$ and specific capacitance of InOx of $4 \mu\text{F}/\text{cm}^2$.

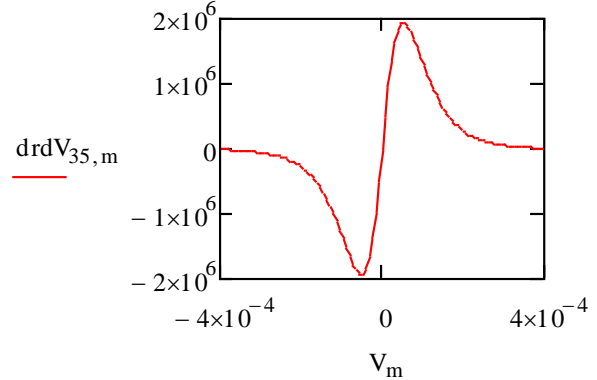


Fig. 7. Second derivative of normalized IV curve at 350 mK.

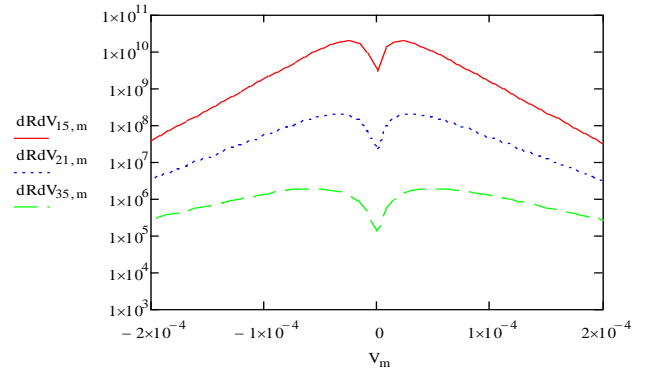


Fig. 8. Curvature dR/dV in logarithmic scale for temperatures 150, 210, 350 mK.

Noise temperature comparable to SIS junctions was demonstrated in such junctions when biased near the energy gap. Specific methods of fabrication for lead and niobium SIN junctions of $0.5 \mu\text{m}^2$ area are described in [20,21]. Noise temperatures down to 140 K were obtained at signal frequencies up to 320 GHz [22]. One more similar structure of SINS type is described in [23], for which the estimation of noise temperature is at the level of 13 K for signal frequency 330 GHz. Direct detectors in mm-wave band with $\text{NEP} = 10^{-15} \text{ W/Hz}^{1/2}$ [24] working at 4.2 K did not found practical applications, but for temperatures below 300 mK they can be competitive with superconducting bolometers. According to [25] the conventional current response at relatively low frequencies can be presented as

$$R_i^{cl} = \frac{d^2I/dV^2}{2*dI/dV} = \frac{S}{2} \quad (8)$$

In nonlinear SIN or SIS junction with responsivity $S/2 > e/\text{hf}$ this expression should be modified to the relation for quantum assisted tunneling

$$R_i^{QM} = \frac{e}{\text{hf}} \left[\frac{I(V+\text{hf}/e) - 2I(V) + I(V-\text{hf}/e)}{I(V+\frac{\text{hf}}{e}) - I(V-\text{hf}/e)} \right] \quad (9)$$

Assuming that shot noise is dominating in such detectors $i_n^2 = 2eIB$ we can estimate the NEP of matched detector as

$$\text{NEP} = \frac{\sqrt{2eIB}}{R_i^{QM}} \quad (10)$$

that can approach in quantum limit maximum value of $\text{NEP} = \text{hf}(2IB/e)^{1/2}$.

In our case at T=100 mK for bias current 0.01 nA and output band 1 Hz this corresponds to 2×10^{-18} W/Hz $^{1/2}$, and comparable to estimations for bolometric response of SINIS structure. In this rough estimations we do not take into account input mismatch $\eta = \frac{4R_{rf}R_s}{(R_{rf}+R_s)^2}$, in which R_{rf} is antenna impedance and R_s is detector impedance. For planar antenna we can take source impedance of 70Ω . Active part of nonlinear detector impedance in quantum assistant tunneling limit is

$$R_{rf} = \frac{2hf/e}{I(V+hf/e) - I(V-hf/e)} \quad (11)$$

contrary to dynamic resistance in bias point for classical detector. This value will be partially shunted by SIN junction capacitance with specific value of about $60\text{ fF}/\mu\text{m}^2$ that is about 10Ω at signal frequency of 350 GHz.

For comparison we can also mention super-Schottky diodes with superconductor-semiconductor junctions Pb-GaAs that were first proposed in [26]. Shape of IV curve and detector response analytic theory for super-Schottky diodes were developed in [27]. Current response can be presented as

$$R_i = \frac{e}{2kT} \frac{\tanh(hf/2kT)}{hf/2kT} \quad (12)$$

This value approaches classical limit $R_{cl}=e/2kT$ for lower frequencies $hf \ll 2kT$ and quantum limit $R_q=e/hf$ for higher frequencies $hf > 2kT$. For T=100 mK the characteristic frequency separating two cases is only 5 GHz.

For our signal at 350 GHz the nonlinearity scale for quantum assisted tunneling corresponds to $dV \sim hf/e = 1.3\text{ mV}$, and energy gap of single Al SIN junction is only 0.2 mV. In this scale we cannot expect quantum detection, but low-frequency components of black body thermal radiation and external RF interferences like mobile telephones and TV stations will be detected and make impact to current as we can see in Fig. 6. Such detector effect can be assumed as significant for frequencies below 50 GHz for bias close to zero and for frequencies below 100 GHz for bias around the gap voltage.

VI. CONCLUSION

For SINIS detectors nonequilibrium in electron system plays the main role in optical response performance. Ultimate parameters can be achieved for maximum multiplication of electrons in absorber due to electron-electron interactions and absorption of nonequilibrium phonons. Time of electron-electron collisions is relatively big at the beginning of such process and diminish multiplication. Nonequilibrium of phonon system is determined by freedom of phonon escaping to superconducting electrode that is fabricated from the same aluminum as absorber. The natural way to increase multiplication and response of detector is using material with lower τ_{ee} , higher τ_{ep} , and higher acoustic mismatch with aluminum, that can be Hafnium. Inversion of sequence of layers with placing absorber above superconductor can also reduce phonon escape to substrate.

REFERENCES

1. L. Kuzmin, On the concept of a hot-electron microbolometer with capacitive coupling to the antenna, Physica B: Condensed Matter, **284-288**, 2129 (2000).
2. L. Kuzmin, Array of cold-electron bolometers with SIN tunnel junctions for cosmology experiments, Journ. of Phys.: Conf. Ser. **97** (2008) 012310
3. I.Devyatov, M.Kupriyanov, Investigation of a nonequilibrium electron subsystem in low-temperature microwave detectors, JETP Lett., v.**80**, No. 10, pp. 646-650 (2004).
4. I.Devyatov, P.Krutitsky, M.Kupriyanov, Investigation of various operation modes of a miniature superconducting detector of microwave radiation, JETPh Lett., v.**84**, No.2, pp.57-61 (2006).
5. A.Semenov, I.Devyatov, M.Kupriyanov, Theoretical analysis of the operation of the kinetic-inductance based superconducting microwave detector, JETP Lett., v.**88**, No.7, pp.514-520 (2008).
6. P. Virtanen, T.T. Hekkila, F.S. Bergeret, and J.C. Cuevas, Theory of microwave-assisted supercurrent in diffusive SNS junctions, Phys. Rev. Lett. **104**, 247003 (2010).
7. M.Tarasov, L.Kuzmin, V. Edelman, et al., Optical response of a cold-electron bolometer array, JETP Lett., v.**92**, No.6, p. 416-420 (2010).
8. M.Tarasov, V. Edelman, L.Kuzmin, P. de Bernardis, S.Mahashabde, Optical response of a cold-electron bolometer array integrated in a 345 GHz cross-slot antenna, IEEE Trans. Appl. Supercond., vol.**21**, no. 6, pp. 3635 (2011)
9. M.A.Tarasov, L.S.Kuz'min, N.S.Kaurova, Thin multilayer aluminum structures for superconducting devices, Instr. and Exp. Techn., Vol. 52, No. 6, pp. 877-881 (2009).
10. V.Edelman, G.Yakopov, A dilution microcryostat cooled by a refrigerator with an impulse tube, Instr. and Exp. Techn., vol.56, № 5, pp. 613-615 (2013).
11. M.A. Tarasov, V.D. Gromov, G.D. Bogomolov, et al., Production and characteristics of grid band-pass filters, Instr. and Exp. Techn., 2009, Vol. 52, No. 1, pp. 74-78 (2009).
12. G. O'Neil, Improving NIS tunnel junction refrigerators: modelling, materials, and traps, Ph.D. Thesis, Univ. Colorado, 2011.
13. J N Ullom, P A Fisher, Quasiparticle behavior in tunnel junction refrigerators, Physica B, vol. 284-288, pp. 2036–2038 (2000).
14. G. C. O'Neil, P. J. Lowell, J. M. Underwood, J. N. Ullom, Measurement and modeling of large area normal-metal/insulator/superconductor refrigerator with improved cooling, Phys. Rev. B 85, 134504 (2012)
15. D.Golubev, L.Kuzmin, Nonequilibrium theory of the hot-electron bolometer with NIS tunnel junction, J.Appl. Phys., vol. 89, No 11, 6464-6472 (2001)
16. W.S. Holland, E.L. Chapin, A. Chrysostomou, et al., 2013, arXiv:1301.3650v1 [astro-ph.IM].
17. M.Tarasov, V. Edelman, S.Mahashabde, L.Kuzmin, Nonthermal optical response of of tunnel structures superconductor-insulator-normal metal-insulator-superconductor, JETPh, vol. 118(145), № 6 (2014).
18. R.Blundell, K.H.Gundlach, A quasiparticleSIN mixer for the 230 GHz frequency range, Int. J. Infrared and MM waves, Vol. 8, No. 12, 1573-1579 (1987).
19. S.Rudner, M.J.Feldman, E.Kollberg, T.Claeson, Superconductor-insulator-superconductor mixer with arrays at millimeter-wave frequencies, J.Appl. Phys., 52, 6372, 1981
20. T.Lehnert, K.H.Gundlach, Fabrication and properties of superconductor-insulator-normal metal tunnel junctions, J.Vac. Sci. Technol., A 10(1), pp. 110-114 (1992).
21. D.Winkler, T.Claeson, High-frequency limits of superconducting tunnel junction mixers, J.Appl.Phys., **62**, 4482 (1987)
22. D.Mailer, A.Karpov, T.Lehnert, K.H.Gundlach, Superconductor-insulator-normal conductor tunnel junctions for frequency mixing around 300 GHz, J.Appl. Phys., 78 (3), pp. 2113-2116 (1995).
23. A.Karpov, D.Maier, J.Blondel, B.Lazareff, K.H.Gundlach, Noise and thermal properties of a submillimeter mixer with the SINS tunnel junction, Int. J. IR & MM Waves, Vol. 16, No. 8, pp. 1299-1315 (1995).
24. H.J.Hartfuss, K.H.Gundlach, Video detection of mm-waves via photon-assisted tunneling between two superconductors, Int. J. IR & MM Waves, Vol. 2, No. 4, pp. 809-827 (1981).
25. P.L.Richards, T.-M.Shen, Superconductive devices for millimeter wave detection, mixing and amplification, IEEE Trans. Electron. Dev., ED-27, No. 10, pp. 1909-1920 (1980).
26. M.Mccoll, M.F.Millea, A.H.Silver, The superconductor-semiconductor Schottky barrier diode detector, Appl. Phys. Lett., Vol. 23, pp. 263-264 (1973).
27. J.R.Tucker, Quantum limited detection in tunnel junction mixers, IEEE J. of Quantum Electronics, QE-15, No. 11, pp. 1234-1258 (1979).

Response of the antenna coupled TES with High-Frequency Readout to 0.65 THz radiation

Artem A. Kuzmin^{1*}, Michael Merker¹, Sergey V. Shitov^{2, 3†}, Nicolay N. Abramov², Matthias Arndt¹, Stefan Wuensch¹, Konstantin Il'in¹, Alexey V. Ustinov^{2, 4} and Michael Siegel¹.

^{1*} *Institut für Mikro- und Nanoelektronische Systeme, Karlsruher Institut für Technology* * Email: artem.kuzmin@kit.edu

² *National University of Science and Technology MISIS, Moscow*

³ *Kotel'nikov Institute of Radio Engineering and Electronics RAS, Moscow*

[†] Email: sergey3e@gmail.com

⁴ *Institute of Physics and DFG-Center for Functional Nanostructures (CFN), Karlsruhe Institute of Technology*

Antenna coupled TES bolometers have a great potential as ultra-low noise terahertz detectors. By decreasing the volume of the sensitive element to nanometer scale and operating temperature to millikelvins, one could reach ultra-low Noise Equivalent Power (NEP) for space astronomy which is limited only by cosmic background [1]. Avoiding influence of excess noises and interference through the biasing lines is a great challenge in this case. The well established method to readout the signal from TES is based on the low-noise DC-SQUID amplifiers. Frequency-division multiplexing (FDM) was suggested as a method for building an array of such bolometers [2]. However the bandwidth of SQUID amplifiers implies restriction for scalability of the readout circuit. This leads to an increase of complexity and cost of the system.

In order to improve the scalability of FDM and avoid low-frequency SQUID amplifiers along with the perfect isolation of the sensitive element from excess noise and unwanted interference, we suggested embedding antenna-coupled TES bolometer into high-Q GHz resonator as a load [3-4] and bias it with RF power applied through weakly coupled transmission line. The readout of THz signal is realized via demodulation of RF bias signal. We called this new type of detectors RF-TES.

To verify the feasibility of the new device concept we fabricated sub-micron sized prototypes of single pixel RF-TES for operation temperature of about 5.0 K. Device was fabricated from magnetron sputtered Nb thin films on sapphire substrate: 10 nm thick Nb for TES bridge ($T_c \sim 5$ K) and 250 nm for resonator ($T_c \sim 8.5$ K). To define the geometry of our TES bridges we used e-beam lithography and ion milling. Since TES doesn't have DC connections we fabricated the witness bridges of the same size as TES to investigate DC transport and thermal properties. Witness bridges were made in same fabrication process and on the same wafer with RF-TES. RF measurements of the device were performed in transport He⁴ Dewar using Network Analyzer. Resonance curves were investigated at different bath temperature and RF power levels. Cratered resonance was observed under certain temperature and bias conditions which were chosen as initial working point for further optical measurement at 0.65 THz. To measure response to THz radiation RF-TES was placed in the focus of the sapphire lens mounted in the detector block inside He⁴ cryostat equipped with LNA and optical window. Results on achieved sensitivity and NEP will be presented and discussed.

References

1. J. Wei, D. Olaya, B. S. Karasik, S. V. Pereverzev, A. V. Sergeev, M. E. Gershenson, *Nature Nanotechnology* vol. 3, pp. 496 – 500, 2008.
2. J. van der Kuur, J. Beyer, M. Bruijn, J.R. Gao et al, *J. Low Temp. Phys.*, vol. 167, issue 5-6, pp.561-567, 2012.
3. S. V. Shitov, *Technical Physics Letters*, Vol. 37, No. 10, pp. 932-934, 2011. Original Russian text published in Pis'ma v Zhurnal Tekhnicheskoi Fiziki,, Vol. 37, No. 19, pp. 88-94 2011. DOI: 10.1134/S1063785011100117.
4. A. A. Kuzmin, S. V. Shitov, A. Scheuring, J. M. Meckbach, K. S. Il'in, S. Wuensch, A. V. Ustinov and M. Siegel, *IEEE Transactions on Terahertz Science and Technology*, Vol. 3, No. 1, pp. 25-31, 2013.

Invited Talk

Superconducting Metamaterials

Alexey V. Ustinov^{1,2,3 †}

¹ Physikalisches Institut, Karlsruhe Institut für Technologie, Wolfgang-Gaede-str. 1,
D-76131, Karlsruhe, Germany

² National University of Science and Technology MISIS, Leninskiy prospekt 4,
Moscow, 119049, Russian Federation

³ Russian Quantum Center, Novaya str., 100, BC "URAL", Skolkovo, Moscow
region, 143025, Russian Federation

[†]Email: ustinov@kit.edu

I will review experimental studies performed within recently established collaboration between German and Russian laboratories jointly working on various aspects of superconducting and quantum metamaterials. The focus of our experiments is on ultra-low loss electromagnetic medium comprised of networks of compact superconducting resonators. The design flexibility of superconducting thin-film resonators and circuits allows for utilizing small structures down to the nanoscale while maintaining low loss properties, very strong and well-controlled nonlinearity, and frequency tunability in the microwave and mm-wave frequency range [1, 2]. This approach opens up an opportunity to develop superconducting metamaterials with non-trivially tailored electromagnetic properties, which can be functionalized as ultra-compact resonant magnetic dipole arrays [3-6], integrated tunable non-reciprocal circuits [7], left-handed transmission lines [8], active emitter arrays, phase modulators, etc. Another interesting spin-off of superconducting metamaterials is going to be on *quantum* metamaterials comprised of arrays of superconducting qubits [9]. This direction is an emerging new field for fundamental studies in quantum optics using microwaves, opening a possibility to explore collective quantum dynamics of artificially tailored two-level systems under very strong coupling with electromagnetic field.

References

1. S.M. Anlage, *J. Opt.*, Vol. 13, p.024001, 2011.
2. S.J. Zmuidzinas, *Ann. Rev. Cond. Matt. Phys.*, Vol. 3, p.169, 2012.
3. P. Jung, S. Butz, S.V. Shitov, A.V. Ustinov, *Appl. Phys. Lett.*, Vol. 102, p.062601, 2013.
4. S. Butz, P. Jung, L.V. Filippenko, V.P. Koshelets, A.V. Ustinov, *Opt. Express*, Vol. 21, p.22540, 2013.
5. S. Butz, P. Jung, L. V. Filippenko, V. P. Koshelets, A.V. Ustinov, *Supercond. Sci. Techn.*, Vol. 9, p.094003, 2013.
6. A. Vidiborskiy, V.P. Koshelets, L.V. Filippenko, S.V. Shitov, A.V. Ustinov, *Appl. Phys. Lett.*, Vol. 103, p.162602, 2013.
7. K.G. Fedorov, S.V. Shitov, H. Rotzinger, A.V. Ustinov, *Phys. Rev. B*, Vol. 85, p.184512, 2012.
8. E.A. Ovchinnikova, S. Butz, P. Jung, V.P. Koshelets, L.V. Filippenko, A.S. Averkin, S.V. Shitov, A.V. Ustinov, *Supercond. Sci. Techn.*, Vol. 26, p. 114003, 2013.
9. P. Macha, G. Oelsner, J.-M. Reiner, M. Marthaler, S. Andre, G. Schoen, U. Huebner, H.-G. Meyer, E. Il'ichev, and A.V. Ustinov, Implementation of a quantum metamaterial, *preprint arXiv:1309.5268*, 2013.

Session 4: Optics

Cryogenic resonator spectrometer for satellite antennas reflectivity investigation at millimeter and terahertz bands

Evgeny A. Serov^{*†}, Vladimir V. Parshin^{*†}, Gregory M. Bubnov^{*†}, and Vyacheslav F. Vdovin^{*†}

^{*}*Institute of Applied Physics of the Russian Academy of Sciences*

Email: serov@appl.sci-nnov.ru

[†]*Nizhny Novgorod State Technical University*

Resonator spectrometer developed at IAP RAS is a precision and high sensitive instrument for investigation of reflectivity of metals and coatings in the millimeter (mm) and terahertz bands. An important application of this instrument is investigation of antennas and thermal shields for space telescopes [1-3]. Until recent time the temperature range of sample was limited by liquid nitrogen boiling temperature (78 K). Reflectivity of metal cooled to this temperature differs from theoretical calculation based on normal skin-effect theory. For real metals and coatings it is a problem to calculate the limit of reflective loss for temperatures close to absolute zero ($T \rightarrow 0$ K), because this value depends on several factors in a complex manner: surface roughness, chemical composition, existence of surface structure and preferential directions. However, this limit is important for designing of cooled detector systems and for other applications. The only confident way to determine this value is experimental measurement.

The new laboratory complex, constructed on the base on resonator spectrometer is a great advancement in the aforementioned direction: it allows investigation of dielectrics and metals at temperature from 4 K to 450 K, in a very wide frequency band 60-500 GHz [4]. In this report we present new experimental results obtained by cryogenic resonator spectrometer.

Reflectivity of metalized films for radiation shields of "Millimetron" space observatory with various metal thicknesses were investigated in the MM band from 4 to 300 K. For the first time reflectivity versus temperature dependence of pure metals (Cu, Al) was investigated in 4-300 K range at several frequencies from 150 to 250 GHz. Experimental results are important for cooled antenna systems design for MM and THz waves detection.

This work is supported by Russian Ministry of Education and Science, Government decree No 220 (contract No 11.G34.31.0029).

References

1. Vladimir Parshin, C.G.M. van't Klooster, E.A. Serov, "Antenna Reflectors Reflectivity at 100 - 350 GHz and 80K", in *Proceedings of 30th ESA Antenna Workshop on Antennas for Earth Observation, Science, Telecommunication and Navigation Space Missions*. ESA/ESTEC Noordwijk, The Netherlands May 27- 30, 2008, pp. 353-356.
2. Vladimir Parshin, Evgeny Serov, C.G.M. van 't Klooster, Paolo Noschese, "Resonator technique for reflectivity measurements. Results for measurements at high temperatures", in *Proceedings of 5th ESA Workshop on Millimetre Wave Technology and Applications & 31st ESA Antenna Workshop*, ESTEC, The Netherlands , 2009, pp. 593-600.
3. V.V. Parshin, E.A. Serov, C.G.M. van't Klooster. "Precise Measurements of Materials and Media in the mm/sub-mm Ranges" in *Proceedings of 6th European Conf. on Antennas and Propagation (EuCAP 2012)*, Prague, Czech Republic, 2012, CM01.9.
4. V.V. Parshin, E.A. Serov, G.M. Bubnov, V.F. Vdovin, M.A. Koshelev, and M.Yu. Tretyakov, "Cryogenic Resonator Complex" in *Radiophysics and Quantum Electronics*, vol.56, 2013, in press.

Capillary quasioptical highpass filter

Valerian S. Edelman, Mikhail A. Tarasov, Artem M. Chekushkin

Abstract— A series of capillary matrix highpass filters with different diameters and lengths of capillaries has been fabricated and experimentally studied. Transmission was measured in the frequency range of 150-550 GHz. For inner diameter of capillary of 0.54 mm and length of 3 mm the attenuation of such filter was over 40 dB at frequencies below 200 GHz. At frequencies above 350 GHz attenuation was below 5 dB.

Index Terms— Below cut-off circular waveguide, cryogenic systems, high-pass filters, millimeter and submillimeter waves,

I. INTRODUCTION

THE terahertz radiation is a region of the spectrum between far infrared and microwaves (0.1–10.0 THz). Detectors for balloon and space projects should operate at temperatures below 1K. For calibration of sensitive bolometers using black-body radiation source we need band-depending filters for cryogenic setup Fig.1.

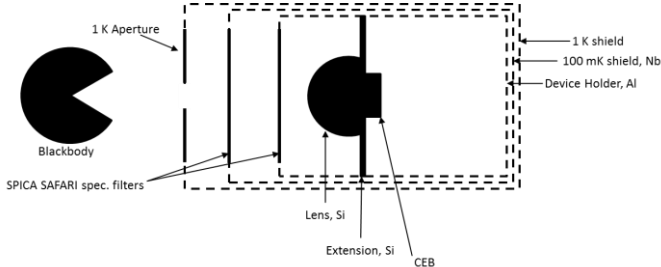


Fig. 1 Example of setup for cryogenic calibration of bolometer (CEB), two filters (SPICA SAFARI filters), black body source and 1 K aperture)

At the different temperatures black body radiation source has spectral maximum at different frequencies Fig.2. And level of out-of-band radiation can be more than in the required band (1).

$$P = \frac{8 \cdot f \cdot h}{2 \cdot \pi \cdot \left(\exp\left(\frac{2 \cdot h \cdot f}{k \cdot T}\right) - 1 \right)} \quad (1)$$

In this case for correct calibration it is necessary to have high suppression at the frequencies below signal. Such filter should have a sharp cut-off frequency.

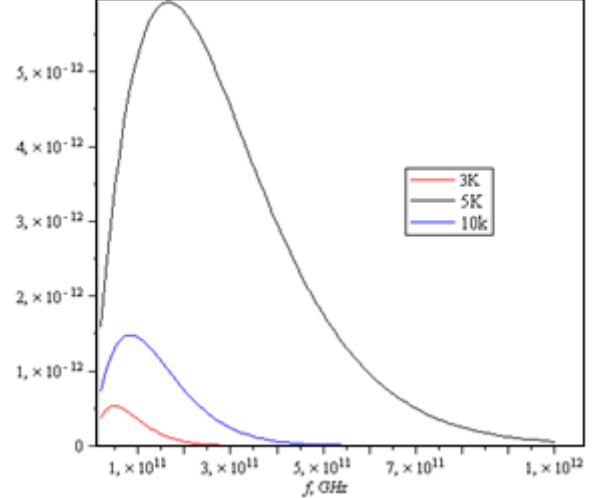


Fig. 2 Radiation spectra of black body source at temperatures 3 K, 5 K, 10 K.

II. THEORY

There are different types of high pass filters. One of them is a metal mesh filter [1]. High-quality filters are fabricated of several layers of mesh filters. Multi-mesh filters are rather expensive and difficult in fabrication. And such filters still have some disadvantages, like Wood anomaly -loses due to substrate mode; and losses at edges of metal film due to skin effect.

Another type is a waveguide filter. The specifications of below cut-off circular waveguides were studied in detail in [2]. The suppression of the long-wave part of radiation in this filter can be rather high. Another important advantage of the below cut-off circular waveguide as a filter is the sharpness of the transmission cut-off. In this case characteristics of the filters can be chosen within wide range by varying the diameters and lengths of waveguides. The amplitude of the wave propagating in waveguide is (2)

$$|\vec{E}|(Z) = |\vec{E}_0| \exp(i\gamma Z) \quad (2)$$

where Z is the coordinate along the waveguide, \vec{E} is the intensity of the electric field at point Z , \vec{E}_0 is the intensity of the electric field at the initial point, and γ is the propagation constant, described as (3).

$$\gamma = \frac{2\pi}{\lambda_{cr}} \sqrt{\left(\frac{\lambda_{cr}}{\lambda}\right)^2 - 1} \quad (3)$$

In the case when $\lambda < \lambda_{cr}$ we have ordinary propagating wave, but if $\lambda > \lambda_{cr}$ then the propagation constant will be

M. A. Tarasov is with the V.Kotelnikov Institute of Radio Engineering and Electronics RAS

V.S.Edelman is with the P.Kapitza Institute for Physical Problems RAS

A. M. Chekushkin is with the V.Kotelnikov Institute of Radio Engineering and Electronics RAS (e-mail: boudko@gmail.com)

imaginary and incoming wave will be exponentially attenuated inside waveguide. These properties allow fabricating filter with a very sharp cut-off frequency, high suppression of radiation below cut-off frequency and uniform transmission.

III. FABRICATION AND CONSTRUCTIONS

Single below-cutoff circular waveguide as a high-pass filter was studied earlier in [2], in which was obtained attenuation of 6-12 dB in the pass-band and attenuation of 30-60 dB in the stop-band. Such filter requires input and output horns and adapters (Fig.3) if using in quasi-optical systems and makes construction rather complicated, of big size, with nonuniform spectral characteristics.

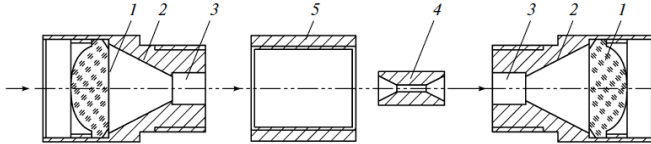


Fig.3 Filter construction: 1- Polyethylene lenses (13mm diameter), 2- Waveguide horns, 3- Apertures for sleeve, 4- Sleeve (internal diameter: 1.5, 1.2, 0.48, 0.4, 0.24 mm), 5- Metal coupling for fastener.

Matrix of many capillaries each like element (4) in Fig.3 can operate as a high-pass filter at millimeter and submillimeter waves without additional adapters. At lower frequencies each capillary can be viewed as a below-cutoff circular waveguide. Array of capillaries do not need any adapters, they are thin and can be inserted in any quasi-optical beam-guide. They can be alternative to perforated plates (grids) that should be arranged as 4-6 parallel layers and this pseudo high pass filter is rather a bandpass filter with a bandwidth of about one octave [3]. Industrial manufacturers of multimesh terahertz filters such as QMC Instruments [4] and TYDEX [5] do not offer high performance highpass filters that are required for cryogenic radiation sources intended for calibration of superconducting bolometers.

We fabricated series of capillary matrix filters with different diameters and lengths of capillaries. Fabrication consists of following steps: electroplating of stainless with Ni or nickel-copper capillaries, filling short piece of 10 mm inner diameter tube with as many capillaries as possible, soldering of such package with tin-lead alloy, electroerosion cutting pieces of 1, 2, 3, 4 mm long, final cleaning in ultrasonic bath. Fig.4

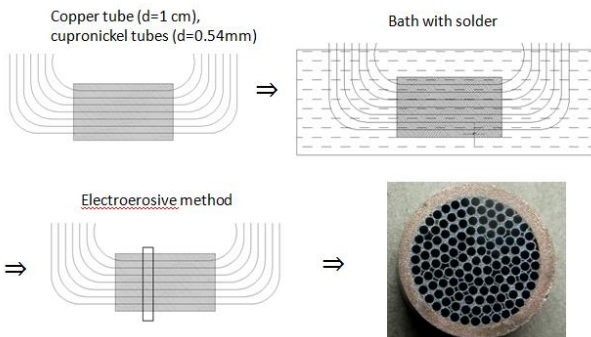


Fig. 4 The main steps in filter fabrication.

IV. MEASUREMENTS

Filters were placed in the waist of a quasioptical gaussian beam-guide comprising Backward Wave Oscillator (BWO) radiation source, modulator, corrugated horn, four teflon lenses (focal length 20 cm and 40 cm), and Goley cell detector. Fig.5 Transmission was measured in the frequency range 150-550 GHz. BWO is not uniform radiation source. Due to that we measured the filter transmission at each spectral point by dividing transmitted signal with filter by transmission of blank aperture.

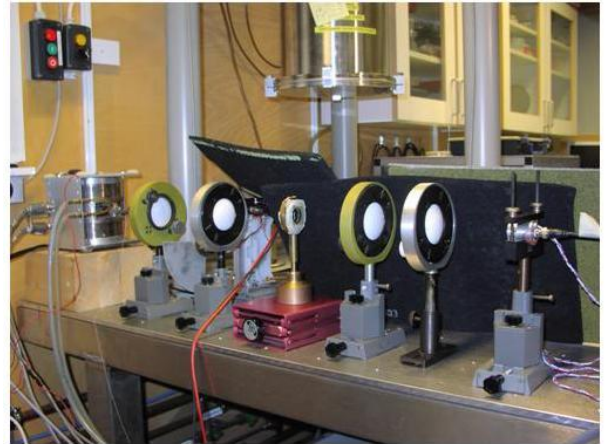


Fig. 5 Measurement setup: 1-BWO, 2,4 –teflon lenses, 5-HPF under test, 6 -Golley cell detector.

V. RESULTS AND DISCUSSIONS

For inner diameter of capillary of 0.54 mm and length of 3 mm the attenuation of such filter was over 40 dB at frequencies below 200 GHz. At frequencies above 350 GHz attenuation does not exceed 5 dB Fig.6.

Theoretical transmission at operating range determined by ratio of open area $S(\text{open})$ to the whole area of filter $S(\text{whole})$. In our filter this ratio should be about 60%. Experimental results measured in configuration of Fig. 5 showed 33%. This difference could be explained with nonideal optical beam shape. We use Gaussian beam and put our filter in the waist of beam, but after that Gaussian beam will not spread in the same condition. Beam at the output is wider. If we take the whole output beam this value approaches theoretical value of 0.33.

If we return to theory [3], we can compare our filter with very similar [6]. But they have some differences. For [6] it is a band-pass filter. Fig.7, contrary to our case of high-pass filter. In [6] it was essentially an array of round holes (0.29 mm dia.) drilled in a 1-mm-thick Cu plate. The waveguide structure provides an extremely sharp cut-off below $f=620$ GHz. This filter type is important for controlling the blackbody power in the Wien limit, where the spectral density of the radiation power decreases exponentially with

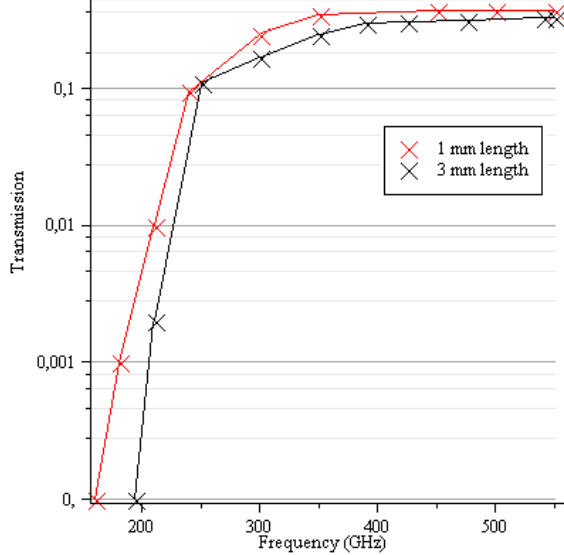


Fig. 6 Experimental results for 1 mm and 3 mm length of filters.

frequency. This filter could be compared with cross-shaped band-pass filter.[7]. The key question in this geometry is distance between crosses or circles. The main advantage in our filter is uniform transmission above cutoff frequency, low cost and simple fabrication.

VI. CONCLUSION

A novel type of sharp highpass filter of terahertz and subterahertz electromagnetic radiation based on frequency selectivity properties of below cut-off circular waveguide, is developed. Experimental results show that the filters provide a sharp cut-off in the transmission band with the efficient radiation suppression below the transmission band. The filter transmission in the pass band was at a level of 30–40%. Small size allows using such filters at cryogenic measurement setup.

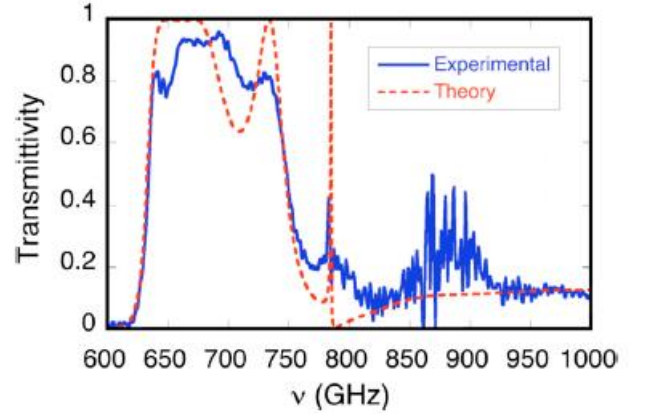


Fig.7 Transfer function of the frequency selective surface filter in comparison with theory of [3]. A noisy bump around 900 GHz is due to a large data error in the vicinity of the Fourier transform spectrometer beamsplitter node. [4]

REFERENCES

- [1] P. A. R. Ade, G. Pisano, C. Trucker, S. Weaver, "A review of metal mesh filters," in *Millimeter and Submillimeter Detectors and Instrumentation for Astronomy III*, vol.6275, 2006
- [2] V. S. Syzranov, A.S. Ermolov, S.P. Lebedev and V.N. Murzin, "Designing and studying waveguide filters of terahertz and subterahertz frequency ranges," in *Instruments and Experimental Techniques*, vol. 55, no. 6, pp. 673–679, 2012.
- [3] Chao-Chun Chen, "Transmission of microwave through perforated flat plates of finite thickness," *IEEE Trans. Microwave Theory Tech.*, vol. MTT-21, Jan. 1973
- [4] <http://www.terahertz.co.uk/>
- [5] <http://www.tydexoptics.com/>
- [6] B. S. Karasik, R. Cantor, "Demonstration of high optical sensitivity in far-infrared hot-electron bolometer," *Appl. Phys. Lett*, vol. 98, May 2011.
- [7] K. D. Moller, K. R. Farmer, D.V.P. Ivanov, O. Sternberg, K. P. Stewart, P. Lalanne, "Thin and thick cross shaped metal grids" *Infrared Physics and Technology*, vol. 40, pp.475-485, 1999.

Design of a Compact Cold Optics for Millimeter Wave Observations

Shigeyuki Sekiguchi, Tom Nitta, Kenichi Karatsu, Yutaro Sekimoto, Norio Okada, Toshihiro Tsuzuki, Shingo Kashima, Masakazu Sekine, Takashi Okada, Shibo Shu, Masato Naruse, Agnes Dominjon, Takashi Noguchi, Hiroshi Matsuo

Abstract—An optics which we have developed for 220 GHz observations is a compact cold re-imaging one from a telescope focal plane with $F/\# = 6$ to a detector plane with $F/\# = 1$ at 100 mK. It employs two high refractive lenses, high purity alumina ($n=3.1$) and silicon ($n=3.4$). To reduce the incident stray light into the detector, a cold nested baffle composed of 4 reflectors with the same spherical shape has been developed. The stray light power is simulated to be $0.2 \mu\text{W}$ which corresponds a quarter of that of a without-baffles case. The total transmittance of three kinds of IR blocking filters is 0.78 at the observation frequency, and less than 10^{-10} above 6 THz. Thermal flow power into the detector, including the stray light power, is about $0.7 \mu\text{W}$. The cold optics with an 600 pixels MKID camera has been cooled down to 100 mK.

Index Terms—compact cold optics, high refractive lens, millimeter-wave astronomy

I. INTRODUCTION

Wide field-of-view (FoV) observation is crucial to survey large area of astronomical sources such as distant galaxies, which helps us to understand the process of galaxy formation [1]. To realize the wide FoV, it is necessary to develop a telescope, focal-plane array detectors, and a re-imaging optics to couple them. One of such wide FoV telescopes is planned [2], and we have been developing aluminum based MKID camera [3]–[5].

In this paper, a re-imaging cold optics which connected with a 600-pixels MKID camera we have developed is demonstrated.

This work was supported by MEXT/JSPS KAKENHI Grant Numbers 21111003, 25247022, 24111712. This work was also supported by a Grant-in-Aid for JSPS Fellows (No. 25001164).

S. Sekiguchi is with Department of Astronomy, The University of Tokyo, Hongo, Bunkyo-ku, Tokyo, 113-8654, Japan and also with Advanced Technology Center, National Astronomical Observatory of Japan, Mitaka, Tokyo, 181-8588, Japan (e-mail: shigeyuki.sekiguchi@nao.ac.jp).

T. Nitta is with JSPS Research Fellow, Kojimachi, Chiyoda-ku, Tokyo, 102-8472, Japan and also with Advanced Technology Center, National Astronomical Observatory of Japan, Mitaka, Tokyo, 181-8588, Japan.

K. Karatsu, N. Okada, T. Tsuzuki, A. Dominjon, T. Noguchi, H. Matsuo are with Advanced Technology Center, National Astronomical Observatory of Japan, Mitaka, Tokyo, 181-8588, Japan.

Y. Sekimoto is with Advanced Technology Center, National Astronomical Observatory of Japan, Mitaka, Tokyo, 181-8588, Japan and also with Department of Astronomy, The University of Tokyo, Hongo, Bunkyo-ku, Tokyo, 113-8654, Japan.

S. Kashima is with JASMINE Project Office, National Astronomical Observatory of Japan, Mitaka, Tokyo, 181-8588, Japan.

M. Sekine, T. Okada, S. Shu are with Department of Astronomy, The University of Tokyo, Hongo, Bunkyo-ku, Tokyo, 113-8654, Japan and also with Advanced Technology Center, National Astronomical Observatory of Japan, Mitaka, Tokyo, 181-8588, Japan.

M. Naruse is with Graduate School of Science and Engineering, Saitama University, Saitama, Saitama, 338-8570, Japan.

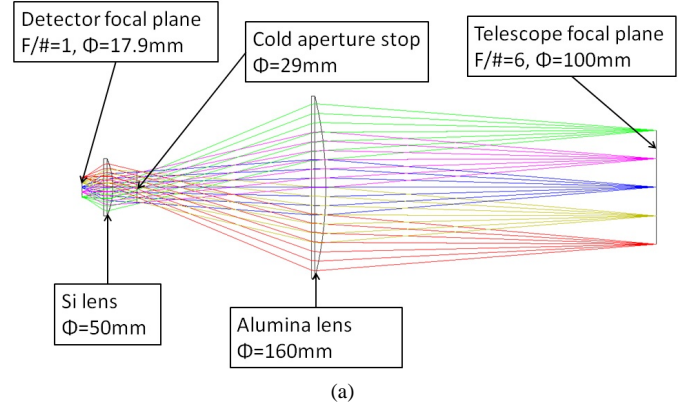


Fig. 1. (a) Ray tracing image of optics calculated with ZEMAX.

For the optics, a refractive optics is adopted because it is more compact than a reflective optics such as SCUBA2 [6] and AzTEC [7]. The requirements is follows;

- 1) To connect a 100 mm diameter $F/\# = 6$ focus of a telescope with a telecentric $F/\# = 1$ focus for the MKID camera. An MKID camera optimized for the $F/\# = 1$ focus has a 99% coupling with less than 5 degree tilted beam.
- 2) Reduction of infrared radiation and stray light to cool down the MKID camera. Stray light in the observation frequency becomes a noise source of the detector.
- 3) Total transmittance of IR blocking filters at 200 - 250 GHz is as high as possible.
- 4) A cold aperture stop exists below 4 K to terminate side lobes of the MKID camera. It also reduces the stray light through the vacuum window into the MKID camera.
- 5) Bath temperature of the MKID camera is kept to less than 150 mK. To satisfy this condition with twice as large as the optical system (a 200 diameter $F/\# = 6$), the thermal loading to this optics is less than $3 \mu\text{W}$.

II. DESIGN

A. Optical design

A refractive optics at 220 GHz with silicon and alumina lenses, which have high refractive indices and low dielectric loss tangents in millimeter wave band [8], was designed. We have developed sub-wavelength structure anti-reflection (AR) coating on the silicon and alumina lenses [8]. Another AR coating using mixed epoxy was also applied for silicon lens

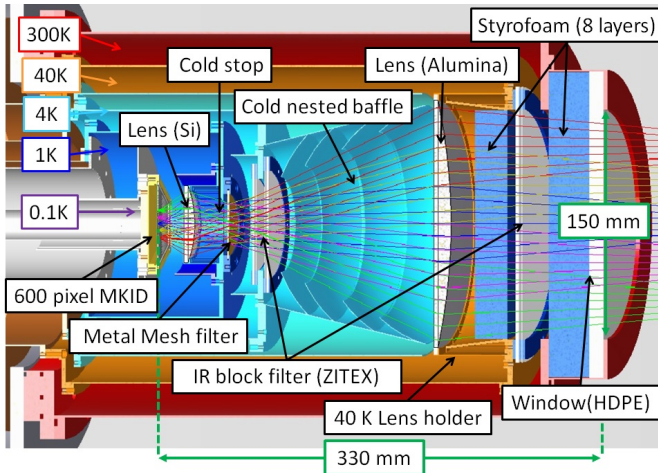


Fig. 2. Schematic drawing of the compact cold optics.

array coupled with the 600-pixels MKID [8]. A ray tracing image with ZEMAX software [9] is shown in Fig. 1. The beam patterns were calculated and the side lobe level is less than -12 dB at all positions. The Strehl ratio is larger than 95 % at all positions. This optics has 6.6 arcminutes FoV when it is installed in a $F/\# = 6$ focus of a 10 m telescope. It is scalable for wider FoV with larger lenses. It is also planned to install this optics and the MKID camera on Nobeyama 45 m telescope.

B. Mechanical design

A schematic drawing of the refractive cold optics is shown in Fig. 2. Alumina and silicon lenses are mounted at 40 K and 1 K stages, respectively. A cold aperture stop is provided at 1 K. Three kinds of infrared (IR) blocking filters; ZITEX coated PTFE filters [10]; radio-transparent multi-layer insulation (RT-MLI) [11] using Styrofoam 8 layers; and a metal mesh filter [12], are mounted at 300 K, 40 K, 4 K, and 1 K. Transmittance of these filters are measured with a Fourier transform spectrometer (FTS) [13]. ZITEX coated PTFE filter has the cutoff frequency at 6 THz, Styrofoam 8 layers at 1 THz, and metal mesh at 300 GHz. The averaged transmittance of superimposed filters is confirmed 0.78 in 200 GHz - 250 GHz and less than 10^{-10} at over 6 THz.

Cold baffles reduce the incident stray light into the MKID camera. A cold nested baffle is mounted at 4 K and three flat baffles are installed at 1 K, 4 K and 40 K, respectively. The nested baffle consists of 4 spherical reflectors with the same radius of curvature (80 mm). They reflect stray light on outside of the baffle. Inside of the nested baffle except for the reflective surface and the flat baffles set 1 K and 4 K are coated with an absorber. The stray light power coming from outside vacuum window into the detector focal plane is $0.2 \mu\text{W}$, which is simulated with LightTools [14]. The baffles reduce 74% stray light power than without-baffles model.

A lens holder has 32 divisions whose structure is similar to a thermal clamp [15]. Divisions of the lens holder play a role in a spring which reduces the pressure applied to lens. 32 divisions lens holders are adopted to reduce applied pressure

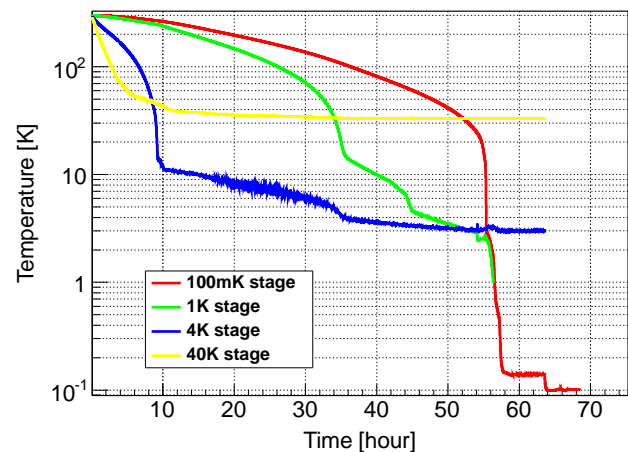


Fig. 3. Cooling time of the optical system. Red line shows the detector temperature and it was cooled down to 100 mK.

less than 1/1000 yield stress of the lenses [16]. To reduce magnetic field into the detector, two kinds of magnetic shields, mumetal (A4K) and a superconducting coating, are mounted at 4 K, 1 K, and 100 mK stage, respectively.

These components have scalability for twice as large as the optical system.

C. Thermal design

We calculated incident power into 100 mK stage. The thermal sources are radiation, which come from outside of vacuum window including stray light, IR blocking filters, and radiation shields of refrigerator, and conduction from readout cables. The total thermal flow power is $0.7 \mu\text{W}$, which is enough below the refrigerator cooling power.

Optical loading power into one pixel detector is also calculated with assumption of a ground-based telescope at a good observing site, Antarctica [17]. The area of each pixel is assumed with 2.11 mm^2 , which corresponds to a pixel size of the silicon lens array [18]. The total loading power to each pixel of MKID camera is 42 pW . Large loading power is caused at the vacuum window, the styrofoam layers, and the alumina lens.

III. CRYOGENIC EXPERIMENT

All optical components with the 600-pixels MKID camera were installed with the 100 mK dilution refrigerator. The temperatures of all stages were monitored, as shown in Fig. 3. The MKID camera on the focal plane was cooled down to 100 mK in 64 hours whose temperature was consistent with the thermal calculation. High yield of around 95% of the MKID has been achieved. The hot-cold response of the MKIDs was confirmed.

IV. CONCLUSION

A compact refractive cold optics with silicon and alumina lenses has been developed for the 220 GHz band. With a stray light simulation, we confirmed that the with-baffles model

decreases 74% incident stray light power compared to the without-baffles model. The 600-pixels MKID camera was cooled down to 100 mK and ~95% yield was achieved. This optical system is scalable for other frequencies and larger FoV. The technology of this cold optics is applicable for a proposed optical system with wide FoV of 1 degree for a 10 m telescope at 850 GHz [19], and a 20,000 pixel MKID camera has been designed for the optical system [3].

ACKNOWLEDGMENT

The authors would like to thank S. Saitou with Advanced Technology Center, National Astronomical Observatory of Japan (NAOJ) for helping in the design of the lens holders and O. Tajima with Institute of Particle and Nuclear Studies, High Energy Accelerator Research Organization (KEK) for advising on RT-MLI.

REFERENCES

- [1] A. W. Blain, I. Smail, R. Ivison, J.-P. Kneib, and D. T. Frayer, "Submillimeter galaxies," *Phys. Rep.*, vol. 369, no. 2, pp. 111–176, 2002.
- [2] T. A. Sebring, R. Giovanelli, S. Radford, and J. Zmuidzinas, "Cornell Caltech Atacama Telescope (CCAT): a 25 m aperture telescope above 5000 m altitude," in *Proc. SPIE*, vol. 6267, p. 62672C, 2006.
- [3] Y. Sekimoto, T. Nitta, K. Karatsu, M. Sekine, S. Sekiguchi, T. Okada, S. Shu, T. Noguchi, M. Naruse, K. Mitsui *et al.*, "Developments of wide field submillimeter optics and lens antenna-coupled MKID cameras," in *Proc. SPIE*, vol. 9153, p. 91532P, 2014.
- [4] M. Naruse, Y. Sekimoto, T. Noguchi, A. Miyachi, T. Nitta, and Y. Uzawa, "Development of crystal Al MKIDs by molecular beam epitaxy," *J. Low Temp. Phys.*, vol. 167, no. 3-4, pp. 373–378, 2012.
- [5] M. Naruse, Y. Sekimoto, T. Noguchi, A. Miyachi, K. Karatsu, T. Nitta, M. Sekine, Y. Uzawa, T. Taino, and H. Myoren, "Optical Efficiencies of Lens-Antenna Coupled Kinetic Inductance Detectors at 220 GHz," *IEEE Trans. THz Sci. Technol.*, vol. 3, pp. 180–186, 2013.
- [6] E. Atad-Ettedgui, T. Peacocke, D. Montgomery, D. Gostick, H. McGregor, M. Cliff, I. J. Saunders, L. Ploeg, M. Dorrepaal, and B. van Venrooij, "Opto-mechanical design of SCUBA-2," in *Proc. SPIE*, vol. 6273, p. 62732H, 2006.
- [7] G. Wilson, J. Austermann, T. Perera, K. Scott, P. Ade, J. Bock, J. Glenn, S. Golwala, S. Kim, Y. Kang *et al.*, "The AzTEC mm-wavelength camera," *Mon. Not. R. Astron. Soc.*, vol. 386, no. 2, pp. 807–818, 2008.
- [8] T. Nitta, S. Sekiguchi, Y. Sekimoto, K. Mitsui, N. Okada, K. Karatsu, M. Naruse, M. Sekine, H. Matsuo, T. Noguchi *et al.*, "Anti-reflection Coating for Cryogenic Silicon and Alumina Lenses in Millimeter-Wave Bands," *J. Low Temp. Phys.*, vol. 176, pp. 677–683, 2014.
- [9] ZEMAX, <https://www.zemax.com/home>.
- [10] K. Yoon, P. Ade, D. Barkats, J. Battle, E. Bierman, J. Bock, J. Brevik, H. Chiang, A. Crites, C. Dowell *et al.*, "The Robinson Gravitational Wave Background Telescope (BICEP): a bolometric large angular scale CMB polarimeter," in *Proc. SPIE*, vol. 6275, p. 62751K, 2006.
- [11] J. Choi, H. Ishitsuka, S. Mima, S. Oguri, K. Takahashi, and O. Tajima, "Radio-transparent multi-layer insulation for radiowave receivers," *Rev. Sci. Instrum.*, vol. 84, no. 11, p. 114502, 2013.
- [12] P. A. Ade, G. Pisano, C. Tucker, and S. Weaver, "A review of metal mesh filters," in *Proc. SPIE*, vol. 6275, p. 62750U, 2006.
- [13] H. Matsuo, A. Sakamoto, and S. Matsushita, "FTS measurements of submillimeter-wave atmospheric opacity at Pampa la Bola," *Publ. Astron. Soc. Japan*, vol. 50, no. 3, pp. 359–366, 1998.
- [14] LightTools, <http://optics.synopsys.com/lighttools/>.
- [15] M. Sugimoto, Y. Sekimoto, S. Yokogawa, T. Okuda, T. Kamba, H. Ogawa, K. Kimura, T. Nishino, K. Noda, and K. Narasaki, "Thermal link for cartridge-type cryostat," *Cryogenics*, vol. 43, no. 8, pp. 435–439, 2003.
- [16] K. E. Petersen, "Silicon as a mechanical material," *Proc. IEEE*, vol. 70, no. 5, pp. 420–457, 1982.
- [17] S. Ishii, M. Seta, N. Nakai, S. Nagai, N. Miyagawa, A. Yamauchi, H. Motoyama, and M. Taguchi, "Site testing at Dome Fuji for submillimeter and terahertz astronomy: 220GHz atmospheric-transparency," *Polar Sci.*, vol. 3, no. 4, pp. 213–221, 2010.
- [18] T. Nitta, K. Karatsu, Y. Sekimoto, M. Naruse, M. Sekine, S. Sekiguchi, H. Matsuo, T. Noguchi, K. Mitsui, N. Okada *et al.*, "Close-Packed Silicon Lens Antennas for Millimeter-Wave MKID Camera," *J. Low Temp. Phys.*, vol. 176, pp. 684–690, 2014.
- [19] T. Tsuzuki, T. Nitta, H. Imada, M. Seta, N. Nakai, S. Sekiguchi, and Y. Sekimoto, "Design of wide-field Nasmyth optics for a submillimeter camera," in *Proc. SPIE*, vol. 9153, p. 91532U, 2014.

Invited Talk

Millimetron: The next FIR/mm Space Observatory

Thijs de Graauw,
on behalf of the Millimetron team,

Astro Space Centre of P.N. Lebedev Physical Institute, Moscow, Russia

Millimetron is an approved mission for a FIR/mm space observatory with a 10-m deployable antenna. It will enable the scientific community to make observations with unprecedented sensitivity and angular resolution. Observations in these bands are indispensable for our understanding the early stages of the Universe, galaxy formation and star formation. The observatory will have two observing modes: as a single-dish telescope and as an element of a Space-Earth interferometer. The antenna will be cooled to a temperature less than 10K while the instrument compartment is to be cooled down to 4 K. With state of the art detector technology (MKID arrays and HEB mixer arrays), it will provide extraordinary performance for imaging and spectroscopic observations in terms of sensitivity and angular resolution. Millimetron will be launched into a L2 orbit.

In this talk I will present the status of the program, the main characteristics of the Millimetron observatory and its instruments with the associated scientific objectives of the mission.

Session 5: THz coherent detectors: HEB I

Optimization of the intermediate frequency bandwidth in the THz HEB mixers

A. Semenov¹, H. Richter¹, H.-W. Hübers^{1,2}, D. Petrenko³, I. Tretyakov³, S. Ryabchun³, M. Finkel³, N. Kaurova³, G. Gol'tsman³, C. Risacher⁴, O. Ricken⁴, R. Güsten⁴

¹*Institute of Planetary Research, German Aerospace Center, Rutherfordstraße 2, 12489 Berlin, Germany*

Email: alexei.semenov@dlr.de

²*Institut für Optik und Atomare Physik, Technische Universität Berlin, Hardenbergstraße 36, 10623 Berlin, Germany*

³*Department of Physics, Moscow State Pedagogical University, M. Pirogovskaya 29, 119992 Moscow, Russian Federation*

⁴*Max-Planck-Institut für Radioastronomie, Auf dem Hügel 69, 53121 Bonn, Germany*

We report on the studies of the intermediate frequency (IF) bandwidth of quasi-optically coupled NbN hot-electron bolometer (HEB) mixers which are aimed at the optimization of the mixer performance at terahertz frequencies. Extension of the IF bandwidth due to the contribution of electron diffusion to the heat removal from NbN microbolometers has been already demonstrated for NbN HEBs at subterahertz frequencies. However, reducing the size of the microbolometer causes degradation of the noise temperature. Using in-situ multilayer manufacturing process we succeeded to improve the transparency of the contacts for electrons which go away from microbolometer to the metallic antenna. The improved transparency and hence coupling efficiency counterbalances the noise temperature degradation. HEB mixers were tested in a laboratory heterodyne receiver with a narrow-band cold filter which allowed us to eliminate direct detection. We used a local oscillator with a quantum cascade laser (QCL) at a frequency of 4.745 THz [1] which was developed for the H-Channel of the German Receiver for Astronomy at Terahertz frequencies (GREAT). Both the noise and gain bandwidth were measured in the IF range from 0.5 to 8 GHz using the hot-cold technique and preliminary calibrated IF analyzer with a tunable microwave filter. For optimized HEB geometry we found the noise bandwidth as large as 7 GHz. We compare our results with the conventional and the hot-spot mixer models and show that further extension of the IF bandwidth should be possible via improving the sharpness of the superconducting transition. The cross characterization of the HEB mixer was performed in the test bed of GREAT at the Max-Planck-Institut für Radioastronomie with the same QCL LO and delivered results which were consistent with the laboratory studies.

References

1. see presentation H. Richter

Low Noise Terahertz Mixers made of MgB₂ Films

Sergey Cherednichenko^{*}, Stella Bevilacqua^{*}, Evgenii Novoselov^{*}, Hiroyuki Shibata[†] and Yasuhiro Tokura[†].

^{*} Department of Microtechnology and Nanoscience (MC2) Chalmers University of Technology, SE-41296 Göteborg, Sweden Email: serguei@chalmers.se

[†] NTT Basic Research Laboratories
Morinosato, Atsugi, Kanagawa 243-0198, Japan

Mixers based on Hot-Electron Bolometers (HEB) are used for low noise detection in radio astronomy at frequencies above 1THz as e.g. in [1]. The majority of HEB mixers are made of very thin superconducting NbN films, where a short electron-phonon interaction time (10 ps at 10 K) and a short phonon escape time (40 ps for 5nm) insures a gain bandwidth (GBW) of about 3-4 GHz. In some cases, for very short length NbN HEBs, the GBW can be extended to 7-9 GHz. The critical temperature of the used NbN films is about 9-11 K, and hence, there is no much choice as to cool the devices to 4K or even below. Obviously, there is an interest if other materials can be utilized for the HEB mixers with a competitive or even superior performance with a possibility of operation at high temperatures.

In ref [2] we demonstrated that a short electron energy relaxation time can be achieved in thin magnesium deboride (MgB₂) films ($T_c > 20\text{K}$). Later [3, 4], a low noise temperature (600 K) and a wide GBW (3.4 GHz) was reported for MgB₂ HEB mixers at 600 GHz.

In this contribution we will report on the MgB₂ HEB mixer performance above 1 THz, where a wide noise bandwidth has been achieved. We will also discuss the progress and challenges in fabrication of high quality and very thin MgB₂ films using a method of Physical Chemical Vapor Deposition.

References

1. S. Cherednichenko et al, "Hot-electron bolometer terahertz mixers for the Herschel space observatory," *Review of Scientific Instruments*, vol. 79, no. 3, pp. 034501–10, Mar. 2008.
2. S. Cherednichenko et al, "Terahertz mixing in MgB microbolometers," *Appl. Phys. Lett.*, vol. 90, no. 2, p. 023507-3, Jan. 2007.
3. S. Bevilacqua et al., "Low noise MgB terahertz hot-electron bolometer mixers," *Appl. Phys. Lett.*, vol. 100, no. 3, p. 033504-3, Jan. 2012.
4. S. Bevilacqua et al., "Study of IF Bandwidth of MgB2 Phonon-Cooled Hot-Electron Bolometer Mixers," in *IEEE Transactions on Terahertz Science and Technology*, 3 (4) s. 409-415.

Performance of a 4.7 THz waveguide HEB mixer for SOFIA's upGREAT

P. Pütz^{1*}, K. Jacobs¹, D. Büchel¹, M. Schultz¹, C. Risacher², H. Richter³, O. Ricken², H.-W. Hübers³, R. Güsten², J. Stutzki¹, and C. E. Honingh³

¹*KOSMA, Universität zu Köln, Zülpicher Str. 77, 50937 Köln, Germany*

²*Max-Planck-Institut für Radioastronomie, Auf dem Hügel 69, 53121 Bonn, Germany*

³*Institute of Planetary Research, German Aerospace Center (DLR), Rutherfordstr. 2, 12489 Berlin, Germany*

* Contact: puetz@ph1.uni-koeln.de, +49 221 470 3484

We present the heterodyne performance characterisation of a waveguide-technology HEB mixer at 4.7 THz. The HEB mixer was developed for the upGREAT focal plane array extension of the German Receiver for Astronomy at Terahertz frequencies (GREAT), which currently is in operation on SOFIA. The High Frequency Array (HFA) at 4.7 THz will consist of 7 pixels and will be combined with the 14 pixel Low Frequency Array (LFA) at 1.9-2.5 THz, using similar waveguide mixers [1].

The HEB mixer is designed and fabricated at KOSMA, with the device utilizing normal metal planar circuitry including a waveguide antenna, transmission lines and beamlead structures for DC and RF contact [2]. New for our HEB device is the combination of in-house deposited NbN for the superconducting microbridge and a 2 µm thin silicon substrate, which is shaped from SOI wafers using MEMS front- and backside processes. The broadband RF coupling measured with an FTS shows an excellent match with the circuit design. With a QCL local oscillator operating at 4.745 THz, near the frequency of the [O I] line of astronomical interest, we measure an uncorrected noise temperature Trec (Raleigh-Jeans) of 1200 K at 250 MHz IF using a HDPE dewar window with 73% transmission and a 88 % signal transmission 13 µm thick Mylar beamsplitter in horizontal polarization and an evacuated signal path to the calibration blackbodies. The 3 dB IF noise roll-off is 3.3 GHz, which is a significant increase in comparison to our previous NbTiN HEBs on silicon nitride membranes.

The waveguides are fabricated from a CuTe alloy by stamping techniques in the KOSMA in-house workshop. The achieved accuracy, e.g. of the 48 µm by 24 µm waveguides, is 1 µm. The waveguide mixer uses a smooth-wall spline profile feedhorn, optimized and manufactured at Radiometer Physics GmbH. Our measurements confirm the excellent quality of the beam pattern of the mixer, which is important for a focal plane array [3].

The heterodyne characterisation of the KOSMA mixer was performed in the (up)GREAT consortium test bed at the MPIfR using a QCL based local oscillator developed by the DLR-PF for the GREAT H-Channel [4].

References

1. see presentation C. Risacher
2. P. Pütz, C. E. Honingh, K. Jacobs, M. Justen, M. Schultz and J. Stutzki, Terahertz hot electron bolometer waveguide mixers for GREAT, A&A 542 L2 (2012) doi: 10.1051/0004-6361/201218916
3. see presentation T. Bertrand
4. see presentation H. Richter

MgB₂ Hot Electron Bolometers Operating Above 20 K

D. Cunnane^{*}, J. H. Kawamura^{*}, B. S. Karasik^{*}, M. A. Wolak[†] and X. X. Xi[†]

^{*}*Jet Propulsion Laboratory
California Institute of Technology
Email: Daniel.P.Cunnane@jpl.nasa.gov*
[†]*Department of Physics
Temple University, Philadelphia 19122, USA*

Terahertz high-resolution spectroscopy of interstellar molecular clouds greatly relies on hot-electron superconducting bolometric (HEB) mixers. Current state-of-the-art receivers use mixer devices made from ultrathin ($\sim 3\text{-}5$ nm) films of NbN with critical temperature $\sim 9\text{-}11$ K. Such mixers have been deployed on a number of ground based, suborbital, and orbital platform including the HIFI instrument on the Hershel Space Observatory. Despite its good sensitivity and well-established fabrication process, the NbN HEB mixer suffers from the narrow intermediate frequency (IF) bandwidth $\sim 2\text{-}3$ GHz and is requires operation at near-liquid helium temperature. As the heterodyne receivers are now trending towards “high THz” frequencies, the need for a larger IF bandwidth becomes more pressing since the same velocity span at 5 THz becomes 5-times greater than at 1 THz.

Our work is focusing on the realization of HEB mixers using ultrathin (8-20 nm) MgB₂ films. They are prepared using a Hybrid Physical-Chemical Vapor Deposition (HPCVD) process yielding ultrathin films with critical temperature ~ 38 K. This is a major advantage over previous experiments [1] of HEB devices using this material. The expectation is that the combination of small thickness, high acoustic phonon transparency at the interface with the substrate, and very short electron-phonon relaxation time may lead to IF bandwidth ~ 10 GHz or even higher. Currently films are passivated using a thin MgO layer which is deposited ex-situ via sputtering. Micron-sized spiral antenna-coupled HEB mixers have been fabricated using MgB₂ films as thin as 10 nm. Fabrication was done using UV lithography and Ar Ion milling, with E-beam evaporated Au films deposited for the antenna. Measurements have been carried out on these devices in the DC, Microwave, and THz regimes.

The devices are capable of mixing signals above 30 K indicating that operation may be possible using a cryogen-free cooling system which may be the greatest impact of these devices on the future THz heterodyne receivers for space. We will report the results of the measurements taken to indicate the local oscillator power requirements, the IF bandwidth, IF impedance, and noise temperature of these devices. We will also discuss the procedures necessary to mature this technology to the point of practical field receiver as well as discuss trade-offs and advantages associated with this novel material for HEB mixers.

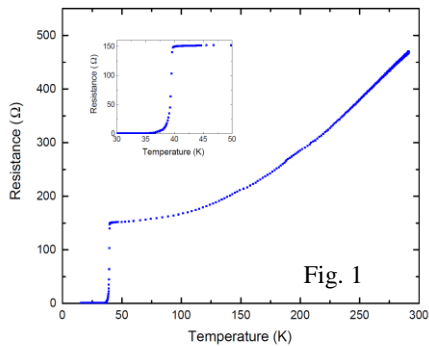


Fig. 1

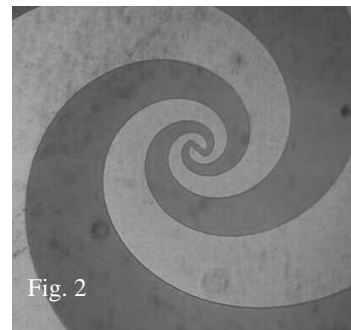


Fig. 2

REFERENCES

1. S. Bevilacqua et al., “Study of IF Bandwidth of MgB₂ Phonon-Cooled Hot-Electron Bolometer Mixers,” *IEEE Trans. THz Sci. Technol.* 3, pp. 409-415, July 2013.

Performance of twin-slot antenna coupled NbN hot electron bolometer mixers at frequencies ranging from 1.4 to 4.7 THz

N. Vercruyssen^{1,2}, D. J. Hayton², Wei Miao³, Wen Zhang³, S.C. Shi, and J. R. Gao^{1,2}

¹*Kavli Institute of Nanoscience, Delft University of Technology, Delft, The Netherlands*

²*SRON Netherlands Institute for Space Research, Utrecht/Groningen, The Netherlands*

³*Purple Mountain Observatory and Key Lab of Radio Astronomy, Nanjing, People's Republic of China
email: N.Vercruyssen@tudelft.nl*

For astronomical observations at frequencies beyond 1 THz, heterodyne detection with NbN hot electron bolometer (HEB) mixers is preferable. In this research we improve the coupling of incoming radiation to the HEB using twin-slot antennas. Our experiments focus on the performance of our antenna designs with frequencies at interesting molecular emission lines corresponding to 1.4, 1.9, 2.7, and 4.7 THz. We make detailed analysis of the performance of the 1.4 THz HEB and demonstrate an excellent measured receiver noise temperature T_{rec} of 480 K with a noise bandwidth of 3 GHz.

Incoming radiation is coupled to the superconducting bridge quasi-optically. Often this is done by a spiral antenna, which is convenient because of its large bandwidth. Using a twin-slot antenna should in principle offer a better coupling efficiency, because it has the same linear polarization as the LO source (QCL). In practice however, the performance of twin-slot antenna at frequencies has been below expectations. We demonstrate improved antenna coupling at high frequencies beyond 1 THz. We compare the spectral response and noise temperature of twin-slot coupled HEBs with design frequencies at the molecular lines at 1.4, 1.9, 2.67, and 4.7 THz. Furthermore we make a detailed analysis of the performance of 1.4 THz HEBs, including the frequency response and the dependence on the resistance and geometry of the bridge.

Session 6: Systems & Receivers II

Testing of 166 to 664 GHz receivers prototypes based on discrete planar Schottky diodes for ICI onboard MetOp-SG

M. Benzazaa¹, B. Thomas¹, H. Gibson¹, M. Brandt¹, A. Walber¹, J. Ceru¹, M.G. Perichaud², T.Narhii², and V. Kangas²

¹Radiometer Physics GmbH, Birkenmaastrasse 10, 53340 Meckenheim, Germany Email: benzazaa@radiometer-physics.de

²European Space Agency, ESTEC, Keperlaan 1, 2201 Noordwijk, The Netherlands. Email: Ville.Kangas@esa.int

The ESA MetOp Second Generation (MetOp-SG) Programme is proposed by ESA/Eumetsat and follow-on to the current, first generation series of MetOp satellites for meteorological observations. Ice Cloud Imager is one of five instruments for the MetOp-SG. RPG has developed five receiver channels covering the frequencies for ICI (183, 243, 325, 448 and 664 GHz) + 2 additional frequencies (166 and 229 GHz) required for some of the MWS and MWI channels. All constitutive mixers and multipliers have been manufactured, and use Schottky diodes devices from two European diode manufacturers (TCL and ACST). The RF measurements have been successfully done over -20°C to +45°C operating temperatures and various LO pumped powers in order to assess the optimal LO range.

The 183 and 243 GHz receivers show Double Side Band mixer noise temperature between 450-550K and Conversion Loss of approx. 5 dB, over a 0,5-8 GHz IF range. The 325 GHz channel shows DSB noise temperature of approx. 900K and CL between 6-7 dB over an IF range of 0.5 -9 GHz. The 448 GHz channel shows DSB noise temperature <1100K and CL < 7dB, over an IF range of 0.5-9 GHz. Finally, the 664 GHz channel shows DSB noise temperature <2000K and CL < 9dB, between 1.6 GHz and 9 GHz of IF range. These results are for room temperature operation. RF results show global compliance to the ICI requirements, and are for most of them at the state-of-the-art.

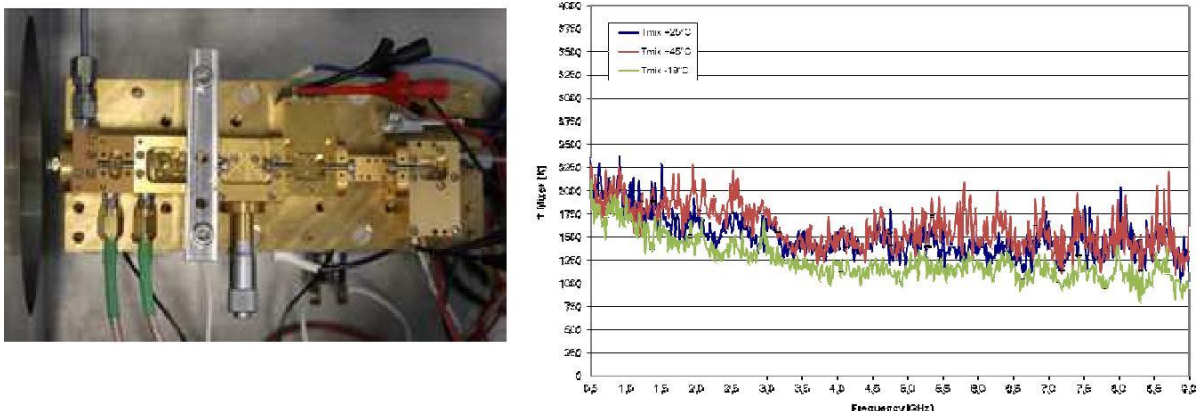


Fig.1. Top: vacuum RF test chamber developed to test receiver in the -20 to +45°C range (left), and 664 GHz receiver under test (right). Bottom: DSB mixer conversion losses measurements of 664 GHz (left) and noise temperature (right) over this temperature range.

Scientific Requirements for Next Generation Space Terahertz Astronomy Missions

Igor I. Zinchenko

*Institute of Applied Physics
Russian Academy of Sciences
Email: zin@appl.sci-nnov.ru*

After the success of *Herschel* and *Planck* new space missions with significantly improved characteristics for terahertz astronomy are planned, in particular *Spica* and *Millimetron*. Here we review topical scientific tasks for terahertz astronomy and corresponding requirements to the frequency coverage, angular resolution, spectral resolution and sensitivity of such missions. The tasks include galactic and extragalactic research, in particular star formation, galactic structure, astrochemistry, exoplanets, etc. Capabilities of different missions for performing these tasks are compared.

THz photometers for solar flare observations from space

Pierre Kaufmann^{1,2}; Rogério Marcon^{3,4}; André Abrantes⁵; Emilio C. Bortolucci²; Luis Olavo T. Fernandes^{1,2};
 Grigory Kropotov⁶; Amauri S. Kudaka¹; Nelson Machado⁵; Adolfo Marun⁷; Valery Nikolaev⁶; Alexandre Silva⁸;
 Claudemir S. da Silva⁹; Alexander Timofeevsky⁶

¹*Escola de Engenharia, CRAAM, Universidade Presbiteriana Mackenzie, São Paulo, SP, Brazil*

²*Centro de Componentes Semicondutores, Universidade Estadual de Campinas, Campinas, SP, Brazil*

Email: pierrekau@gmail.com

³*Instituto de Física Gleb Wataghin, Universidade Estadual de Campinas, Campinas, Brazil*

⁴*Observatório Solar "Bernard Lyot", Campinas, SP, Brazil*

⁵*Propertech Ltda., Jacareí, SP, Brazil*

⁶*Tydex, LLC, Saint Petersburg, Russia*

⁷*Complejo Astronómico El Leoncito, CONICET, San Juan, Argentina*

⁸*Dept. of Electrical and System Engineering, University of Pennsylvania, Philadelphia, USA*

⁹*Neuron Ltda., São José dos Campos, SP, Brazil*

The concept, fabrication and performance of a double THz photometers system is presented. It is the first detecting system conceived to observe solar flare THz emissions on board of stratospheric balloons. An innovative optical setup allows observation the full solar disk and the detection of small burst transients at the same time. The system, named SOLAR-T, has been fabricated, integrated to data acquisition and telemetry modules for this application. The tests included the whole system performance, on ambient and low pressure and temperature conditions. One artificial Sun setup was developed to simulate actual observations and testing sensitivities. SOLAR-T uses two Golay cell detectors preceded by low-pass filters made of rough surface primary mirrors and membranes, 3 and 7 THz band-pass filters, and choppers. SOLAR-T photometers can detect small solar bursts (tens of solar flux units) with sub second time resolution. It is intended to provide data on the still unrevealed spectral shape of the mysterious THz solar flares emissions. The experiment is planned to fly on board of two long-duration stratospheric balloon flights over Antarctica and Russia in 2014-2016.

Atmospheric Profiling Synthetic Observation System at THz Wave Band

Qijun Yao^{1,2}, Dong Liu^{1,2}, Zhenhui Lin^{1,2}, Wenying Duan^{1,2}, Jing Li^{1,2}, Zheng Lou^{1,2}, Shengcai Shi^{1,2}, Hiroyuki Maezawa³, and Scott Paine⁴

¹*Purple Mountain Observatory, CAS, China*

²*Key Lab of Radio Astronomy, CAS, China*

³*Osaka Prefectural University, Japan*

⁴*Harvard-Smithsonian Center for Astrophysics, USA*

In this paper, we will introduce a dual-THz-band SIS (Superconductor- Insulator-Superconductor) heterodyne radiometer system which is under developing for the atmospheric profiling synthetic observation system project (APSOS). This THz system is intended to have a durable and compact design to meet the challenging requirements of remote operation at Tibetan Plateau. The system as well as its major components such as antenna tipping, quasi-optics, cryogenics, SIS mixers and FFTS backend will be discussed thoroughly. Some scientific simulation focusing on the atmospheric profiling componets at THz bands will also be investigated.

Keywords — THz, SIS mixer, Radiometer, Atmospheric profiling.

Invited Talk

Large format, background limited arrays of Kinetic Inductance Detectors for sub-mm astronomy

J.J.A. Baselmans^{*}, P.J. de Visser^{\$}, S.J.C. Yates^{**}, J. Bueno^{*}, R.M.J. Jansen^{***}, A. Endo^{\$}, D. J. Thoen^{\$}, A.M. Baryshev^{#**}, L. Ferrari^{**}, T.M. Klapwijk^{\$,&}

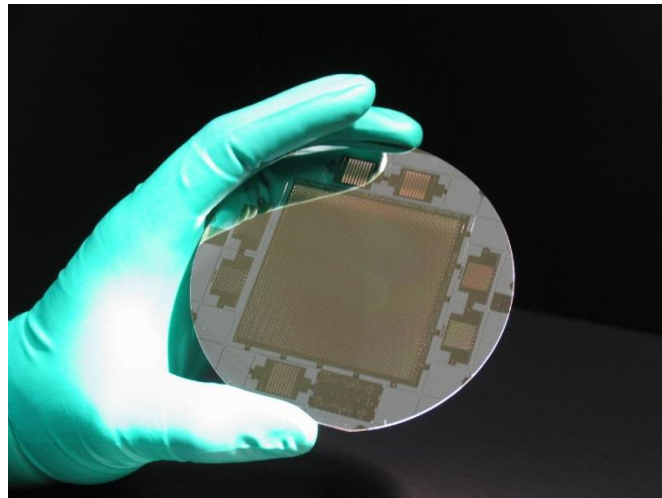
^{*}SRON, Sorbonnelaan 2, 3584CA Utrecht, The Netherlands ^{**}SRON, Landleven 12, 9747AD Groningen, The Netherlands

^{\$}Kavli Institute of Nanoscience, Faculty of Applied Sciences, Delft University of Technology, Lorentzweg 1, 2628CJ Delft, The Netherlands

[#]Kapteyn Astronomical Institute, P.O. Box 800, 9700 AV Groningen, The Netherlands [&]Physics Department, Moscow State Pedagogical University, Moscow, 119991, Russia

Email : J.Baselmans@sron.nl

Kinetic Inductance detectors have held a promise for the last decade to enable very large arrays, in excess of 10.000 pixels, with background limited sensitivity for ground- and Space Based sub-mm observatories. First we present the development of the detector chips of the A-MKID instrument: These chips contain up to 5400 detector pixel divided over up to 5 readout lines for the 350 GHz and 850 GHz atmospheric windows. The individual detectors are lens antenna coupled KIDs made of NbTiN and Aluminium that reach photon noise limited sensitivity at sky loading levels in excess of a few fW per pixel using either phase readout or amplitude readout. The ability to use phase readout is crucial as it reduces the requirements on the readout electronics of the instrument. Cross coupling between the KID resonators was mitigated by a combination of numerical simulations and a suitable position encoding of the readout resonance frequencies of the individual pixels. Beam pattern measurements are performed to demonstrate the absence of any cross talk due to resonator-resonator cross coupling. Second we present experiments on individual lens-antenna coupled detectors at 1.5 THz that are made out of aluminium. With these devices we have observed, as a function of the irradiated power at 1.5 THz, the crossover from photon noise limited performance to detector-limited performance at loading powers less than 0.1 fW. In the latter limit the device is limited by intrinsic fluctuations in the Cooper pair and quasiparticle number, i.e. Generation-Recombination noise. This results in a sensitivity corresponding to a NEP = $3.8 \cdot 10^{-19}$ W/V(Hz).



A 100 mm wafer with in its center a 5400 pixel array of background limited NbTiN-Al antenna coupled KIDs. Clearly visible are the 10 bond pads used to connect the 5 lines that connect to 1080 pixels each.

Session 7: Novel devices & measurements

Normal Metal HEB Detector with Johnson Noise Thermometry Readout

Boris S. Karasik

*Jet Propulsion Laboratory
California Institute of Technology
Email: boris.s.karasik@jpl.nasa.gov*

Next generation submillimeter telescopes will require more sensitive detectors for spectroscopy and imaging. Several advanced concepts have been pursued in the recent years with the goal to achieve a detector Noise Equivalent Power (NEP) of the order of 10^{-20} - 10^{-19} W/Hz $^{1/2}$ that corresponds to the photon noise limited operation of the future space borne far-IR spectrometers under an optical load $\sim 10^{-19}$ W. Our recent work has been focusing on the hot-electron Transition-Edge Sensor (TES) where a much lower thermal conductance than in a SiN membrane suspended TES has been achieved. This is due to the weak electron-phonon (e-ph) coupling in a micron- or submicron-size hot-electron Ti TES. Using this approach, the targeted low NEP values have been confirmed via direct optical measurements [1]. The kinetic inductance detector [2] and quantum capacitance detector [3] demonstrated recently a similar sensitivity as well.

We see nevertheless the possibility to push the state-of-the-art even further. Increase of the operating temperature and the saturation power, and simplification of the array architecture are believed to be important areas of improvement not only for the ultrasensitive detectors but also for far-IR detectors intended for use in photometers and polarimeters where the background is higher (NEP = 10^{-18} - 10^{-16} W/Hz $^{1/2}$). Recently, graphene has emerged as a promising material for hot-electron bolometers (HEB) due to its weak e-ph coupling, very small volume of a single-atom thick sensing element and strong Drude absorption of far-IR radiation. Since the monolayer graphene has a temperature independent resistance its readout is problematic. In recent works [4, 5], Johnson Noise Thermometry (JNT) has been employed as the readout technique.

In this paper, we give a detailed analysis of the expected sensitivity and operating conditions in the power detection mode of a hot-electron bolometer made from a few μm^2 monolayer graphene flake which can be embedded into either a planar antenna or waveguide circuit via NbN (or NbTiN) superconducting contacts with critical temperature ~ 10 K. The most recent data on the strength of the e-ph coupling are used in the present analysis and also the contribution of the readout noise into the NEP is explicitly computed. The readout scheme utilizes the JNT allowing for Frequency-Domain Multiplexing (FDM) using resonator coupling of HEBs. In general, the resonator bandwidth and the summing amplifier noise make a significant effect on the overall system sensitivity. The analysis shows that the readout contribution can be reduced to that of the bolometer phonon noise if the detector device is operated at 0.1 K and the JNT signal is read at about 10 GHz where both the Johnson noise and the microwave photon mediated thermal conductivity weaken greatly. Beside the high sensitivity, this bolometer does not have any hard saturation limit and thus can be used for imaging with arbitrary contrast. By changing the operating temperature the bolometer sensitivity can be fine tuned to the background noise in a particular application. Using a quantum noise limited kinetic inductance parametric amplifier [6], 100s of graphene HEBs can be read simultaneously without saturation of the system output and deterioration of the sensitivity. We will also compare the expected performance of graphene with several conventional normal metal materials for HEB (e.g., W, TiN, Pd). A relative simplicity of the normal metal HEB compared to the TES version (no need in bias, tuning of critical temperature, and dc SQUID amplifiers) can make this approach an attractive alternative for the low-background far-IR arrays.

References

1. B. S. Karasik and R. Cantor, "Optical NEP in hot-electron nanobolometers," *Appl. Phys. Lett.* 98, 193503 (2011).
2. P. J. de Visser et al., "Fluctuations in the electron system of a superconductor exposed to a photon flux," *arXiv:1306.4238 [cond-mat.supr-con]*.
3. P. M. Echternach et al., "Photon shot noise limited detection of terahertz radiation using a quantum capacitance detector," *Appl. Phys. Lett.* 103, 053510 (2013).
4. K. C. Fong and K. C. Schwab, "Ultrasensitive and wide-bandwidth thermal measurements of graphene at low temperature," *Phys. Rev. X* 2, 031006 (2012).
5. A. C. Betz et al., "Hot electron cooling by acoustic phonons in graphene," *Phys. Rev. Lett.* 109, 056805 (2012).
6. B. H. Eom et al., "A wideband, low-noise superconducting amplifier with high dynamic range," *Nat. Phys.* 8, 623 (2012).

Photon Statistics for Space Terahertz Astronomy

H. Matsuo

*Advanced Technology Center,
National Astronomical Observatory of Japan
Email: h.matsuo@nao.ac.jp*

Photon counting technology in terahertz frequency region will open a new field in astronomy that used photon statistics as an observational tool. Electromagnetic wave has been treated as either stream of independent photons in shorter wavelengths or as radio wave in longer wavelengths. However in far-infrared wavelengths or terahertz frequencies, both characteristics of the photon and the wave appear. Photons in this wavelength region are usually bunched, whose photon statistics tell us the physical states of emission sources, such as thermodynamic temperature when the source is in equilibrium.

When one make use of the bunched photon measurements on two telescopes, one can measure their intensity correlation, as demonstrated by the Hanbury-Brown and Twiss (HBT) experiment for the intensity interferometry. Photon counting detectors would further improve the interferometer technology and realize high sensitivity aperture synthesis interferometry for future space programs, which can be named as Photon Counting Terahertz Interferometry (PCTI).

The technology is based on the intensity correlation which is the same as in HBT, and by using fast photon counting detector, it would be possible to achieve high time resolution better than one wavelength passing, which can be used as the phase information of intensity fluctuation. Furthermore, the element telescopes can be independent and number of elements is not limited and very long baseline interferometry could be realized.

Detector technology based on superconducting tunnel junction detector is proposed. Their fast quantum response to terahertz photons enables wide bandwidth measurements to be used to obtain the phase information of the intensity fluctuation. Series connected junctions coupled with high-impedance and low noise amplifiers can be use to count each photon signal with enough signal-to-noise ratio when leakage current of junction is less than an order of pico-ampere.

With the ultimate sensitivity under low-background condition in space, PCTI would image a few hundred Kelvin sources with micro-arcseconds angular resolution using baseline length of several thousand kilometers in far-infrared wavelengths.

References

1. H. Matsuo, "Requirements on Photon Counting Detectors for Terahertz Interferometry", *Journal of Low Temperature Physics* 167, pp. 840–845 (2012).
2. H. Matsuo, "Fast and High Dynamic Range Imaging with Superconducting Tunnel Junction Detectors", *Journal of Low Temperature Physics*, (2014), DOI 10.1007/s10909-013-1022-3

Frequency multiplication in a distributed array of SIS junctions

Bhushan Billade^{*}, Alexey Pavolotsky[†] and Victor Belitsky[†]

^{*}
*Onsala Space Observatory,
 Chalmers University of Technology, Sweden*
 Email: bhushan.billade@chalmers.se

[†]*Group for Advanced Receiver Development (GARD), Chalmers University of Technology, Sweden*

We report the experimental study of the off-chip detection of frequency multiplication in a distributed array of Superconductor-Insulator-Superconductor (SIS) junctions. A test device consisting of a series array consisting sixty eight Nb/Al-AlOx/Nb tunnel junctions was designed for this study, and was fabricated using in-house Nb thin-film technology.

The test device with SIS array was optimized for the study of second harmonic generation in 182–192 GHz output frequency band. The SIS array was excited with microwave radiation at 3 mm band using a quasi-optically coupled Gunn oscillator and the output response of the device was studied using a double sideband SIS mixer operating in 163 – 211 GHz range with 4–8 GHz. The Josephson-effect for both the SIS multiplier and the detector mixer was carefully suppressed using magnetic field. We observed very sharp second harmonic spectral signals, due to frequency multiplication by the SIS array. We also observed distinct multi-photon process in the SIS array tunnel junction response to the applied microwave signal, and the amplitude of the multiplied signal shows dependence on the bias voltage of the SIS array. We observed that the output power of the multiplied signal increases linearly with the power of the pumping signal up to certain level and then saturates. Increasing the input power beyond this level results in the heating of the chip. When the output of the test device was connected to the LO port of the SIS-mixer, an increase of 10 – 20% in the SIS -mixer dark current was observed when the SIS mixer was voltage biased in the middle of first photon step below the gap voltage. The device, although far from providing sufficient power to pump a practical SIS mixer, may be considered as a first experimental step towards SIS frequency multipliers.

Noise in Nano Bolometers: Terahertz Detectors at Room Temperature and at 77K

Stella Bevilacqua, Aurel Bergfalk, and Sergey Cherednichenko

*Department of Microtechnology and Nanoscience (MC2)
Chalmers University of Technology, SE-41296 Göteborg, Sweden
Email: stellab@chalmers.se*

The diversity of THz detectors is as wide as the range of applications for THz waves. Requirements for the detectors vary and so do the detectors. Extremely high sensitivities ($NEP < 10^{-18} \text{ W/Hz}^{0.5}$) for the cosmic microwave background and extragalactic observations can only be achieved with the detector cooling below 1K. Whereas, simplicity and robustness are required for generic THz detectors in a lab. Security imaging needs THz detectors in large arrays, preferably at ambient temperature operation or with compact and lightweight cooling. Until recently, such characteristics as good sensitivity ($NEP < 1 \text{ nW/Hz}^{0.5}$), high speed (< 1 ms), potential for integration in arrays (solid state technology), room temperature operation have been demonstrated only with Schottky barrier diodes. Si FET detectors have also shown a good performance below 1THz. In our previous work we demonstrated [1, 2] that with a micro- and nano- meter scale bolometers based on $\text{YBa}_2\text{Cu}_3\text{O}_7\text{-x}$, (YBCO) thin films, an NEP of $200 \text{ pW/Hz}^{0.5}$ is achievable at room temperature, with a response rate as short as a few nanoseconds (2-5 ns).

In this contribution we will report on the YBCO nano bolometers as small as 100nm. It leads to a large increase in the responsivity ($> 100 \text{ V/W}$) for frequencies from 100GHz to 2THz. As the responsivity grows, the nano bolometers become more sensitive to the external electrical disturbances, which can be confused with intrinsic noise in the device. We will discuss the noise properties of the YBCO nano bolometers, their optical characterization, as well as some of their application for the gas spectroscopy and prospects of the array integration.

References

1. S. Cherednichenko et al., "A room temperature bolometer for coherent and incoherent detection," *IEEE Trans. Terahertz Science and Technology*, v.1, n.2, pp.395-402, Nov. 2011
2. S. Bevilacqua et al, "Fast room temperature THz bolometers," in Proc. 38th International Conference on Infrared, Millimeter and Terahertz Waves (IRMMW-THz), 1-6 Sept. 2013, DOI: 10.1109/IRMMW-THz.2013.6665544.

Terahertz detectors based on the room temperature Nb₅N₆ microbolometers

X. C. Tu, L. Xu, Q. K. Mao, C. Wan, L. Kang, B. B. Jin, J. Chen*, and P. H. Wu

Research Institute of Superconductor Electronics (RISE)

Nanjing University, Nanjing 210093, China

*Email: chenj63@nju.edu.cn

Terahertz (THz) detectors based on the room-temperature (RT) microbolometers consisting of a Nb₅N₆ thin film microbridge and a dipole planar antenna are reported. Due to the high temperature coefficient of the resistance(TCR), which is as high as -0.7% K⁻¹, of the Nb₅N₆ thin film, such an antenna-coupled microbolometer is quite suitable for detecting THz signals. Previously, THz detectors working at 0.1 THz have been reported [1]. Here, the properties at 0.22-0.33 THz will be presented.

The microbolometers consist of a gold dipole planar antenna and a microbridge, which is the core element and is made of properly patterned Nb₅N₆ thin film. To effectively couple the applied THz power onto the Nb₅N₆ microbridge, a resonant dipole antenna is used. The dipole antenna is inserted into a 120 μm by 210 μm stub, which is also used to connect to the bias circuits. The software named HFSS is used to carry out numerical simulations for this antenna structure and to optimize the sizes. In the process of Nb₅N₆ microbolometer chip fabrication, a SiO₂/Si (100) combination substrate is used, where SiO₂ with 100 nm thick, is deposited by thermal oxidation on Si(100) substrate with high resistivity ($\rho > 1000 \Omega\cdot\text{cm}$). Such a combination is chosen because of its low loss at lower band of THz frequencies and ease of fabricating an air-bridge, underneath the Nb₅N₆ microbridge. Then, we used radio frequency (RF) magnetron sputtering to deposit a Nb₅N₆ film (120 nm thick) on the substrate. The film was patterned into microbridges using photolithography and reactive ion etching (RIE). The dipole antenna was then integrated with the Nb₅N₆ microbridge by depositing a 5-nm-thick aluminum film firstly, a 220-nm-thick gold one later, and then pattern the antenna into the right shape and size as designed by the software. Finally, an air-bridge, which reduces the effective thermal conductance of the substrate to further enhance the responsivity, was formed under the Nb₅N₆ microbridge by etching 1 μm of the Si part of the SiO₂/ Si (100) combination substrate.

The DC responsivity at RT, calculated from the measured current-voltage (I-V) curve of the Nb₅N₆ microbolometer, is about -760 V/W at the bias current of 0.19 mA. A typical noise voltage as low as 10 nV/VHz yields a low noise equivalent power (NEP) of 1.3×10^{-11} W/VHz at modulation frequency above 4 kHz. The best RF responsivity at 0.28 THz, characterized using a normal measuring method for the infrared devices, is about 580 V/W, with the corresponding NEP being 1.7×10^{-11} W/VHz. In order to further test the performance of Nb₅N₆ microbolometer, we constructed a quasi-optical type receiver by attaching it to a hyperhemispherical silicon lens and the result shows that the best responsivity of the receiver is about 320 V/W at 0.24 THz, which corresponding the NEP of 3.1×10^{-11} W/VHz.

Using above detectors, an active imaging system at 0.22 THz has been constructed using a Cassegrain reflector with the diameter of 30 cm. The special resolution of about 1.41 cm is obtained. Also, this work could offer a candidate to develop a large scale focal plane array (FPA) with simple technique and low costs. The details will be discussed in the presentation.

Acknowledgements

This work was supported by the National Basic Research Program of China ("973" Program) (No. 2014CB339800), the National High Technology Research Program of China ("863" Program) (No. 2011AA010204) and the National Natural Science Foundation of China (Nos. 11227904). Also, it was partially supported by the Fundamental Research Funds for the Central Universities and Jiangsu Key Laboratory of Advanced Techniques for Manipulating Electromagnetic Waves.

References

1. L. Kang et. al., "A room temperature Nb₅N₆ microbolometer for detecting 100 GHz radiation" 20th ISSTT, Charlottesville, 20-22 April 2009, P7E.

Photothermoelectric Response in Asymmetric Carbon Nanotube Devices Exposed to Sub-THz Radiation

G. Fedorov^{1,2,3}, A. Kardakova^{1,2}, I. Gayduchenko^{1,2,3}, B.M. Voronov¹, M. Finkel¹, T.M. Klapwijk^{1,4}, and G. Goltsman^{1,2}

¹ Physics Department, Moscow State Pedagogical University, Moscow, 119991, Russia

Email: gefedorov@mail.ru

²Department of General Physics, Moscow Institute of Physics and Technology (State University),

9, Institutsky Lane, Dolgoprudny, 141707, Russia

³National Research Centre, Kurchatov Institute, 1, Kurchatov Sq., Moscow, 123182, Russia

⁴ Kavli Institute of Nanoscience

Delft University of Technology, 2600 AA Delft, Netherlands

This work reports on the voltage response of asymmetric carbon nanotube devices to sub-THz radiation at the frequency of 140 GHz. The devices contain CNT's, which are over their length partially suspended and partially Van der Waals bonded to a SiO₂ substrate, causing a difference in thermal contact. Different heat sinking of CNTs by source and drain gives rise to temperature gradient and consequent thermoelectric power (TEP) as such a device is exposed to the sub-THz radiation. Sign of the DC signal, its power and gate voltage dependence observed at room temperature are consistent with this scenario. At liquid helium temperature the observed response is more complex. DC voltage signal of an opposite sign is observed in a narrow range of gate voltages at low temperatures and under low radiation power. We argue that this may indicate a true photovoltaic response from small gap (less than 10meV) CNT's, an effect never reported before.

While it is not clear if the observed effects can be used to develop efficient THz detectors we note that the responsivity of our devices exceeds that of CNT based devices in microwave or THz range reported before at room temperature. Besides at 4.2 K notable increase of the sample conductance (at least four-fold) is observed.

Our recent results with asymmetric carbon nanotube devices response to THz radiation (2.5 THz) will also be presented.

Invited Talk

The Greenland Telescope

R. Blundell

Abstract — The Greenland Telescope will consist of the ALMA North America prototype antenna, repurposed and modified to operate in the Arctic environment, with the principal scientific goal of imaging the Super Massive Black Hole at the heart of the M87 Galaxy. Many of the major antenna components and subsystems are currently undergoing modification or redesign at numerous facilities, worldwide. We expect to collect and reassemble these into a working telescope in the northeastern US during 2014 and 2015, and conduct science verification and commissioning during the winter 2015 – 2016. These tests will include Very Long Baseline Interferometry.

Index Terms —mm and sub mm wavelength instrumentation, radio telescope facilities, Very Long Baseline Interferometry.

I. INTRODUCTION

The potential use of millimeter wavelength Very Long Baseline Interferometry for the highest angular resolution observations of astronomical objects is well documented [1]. Several pioneering observations have been made, both on quasars used for calibration, and on astronomical objects of particular interest. Indeed, a number of radio observatories are working towards the development of the Event Horizon Telescope with the express purpose of studying in great detail SgrA*, the Super Massive Black Hole (SMBH) at the center of the Milky Way – one of only a few candidate objects large enough to enable detailed observations from the ground. Another such object is the SMBH at the center of M87, where greater mass relative to SgrA* results in a longer dynamical timescale accessible to observations constructed by Earth rotation. The Greenland Telescope will be located at 72 degrees north, close to the peak of the Greenland ice sheet, in order to provide the longest north-south baselines toward M87 when coupled to the Atacama Large Millimeter Array in northern Chile. It will also provide a key link between telescope facilities in Europe and the US; and will thus enable the longest baselines in the east-west direction, and hence the highest angular resolution. Furthermore, since the number of telescope facilities that can operate at millimeter and submillimeter wavelengths is limited, it will provide significantly improved imaging capability over the current array, which includes a maximum of 9 locations: The Plateau de Bure Interferometer (France); The IRAM 30 metre (Spain);

The Submillimeter Telescope (Arizona); The Large Millimeter Telescope (Mexico); The Combined Array for Research in Millimeter-wave Astronomy (California); The Submillimeter Array (Hawaii); ALMA and/or the Atacama Pathfinder EXperiment (northern Chile); the South Pole Telescope for southern sources (Antarctica); and the MIT Haystack observatory at the longest wavelengths.

Besides enabling the highest angular resolution astronomical observations, the chosen location, at 72.5 degrees north, is also at high altitude with sufficiently transparent skies to offer the potential of submillimeter single-dish astronomy observations – which may even extend into the Terahertz regime.

II. THE ANTENNA

The antenna, the ALMA North American prototype, was awarded via an open call for proposals, to the Smithsonian Astrophysical Observatory in 2011 by the National Science Foundation Division for Astronomical Sciences, for the express purpose of studying the Super Massive Black Hole at the center of the M87 Galaxy. Being an ALMA prototype, it was originally designed to operate from the high altitude site at Chajnantor in the Atacama Desert of northern Chile. In this environment it was specified to an exacting set of requirements to operate efficiently from centimeter wavelengths to about 0.3 mm. However, it was never



Fig. 1. The ALMA North American prototype antenna before disassembly at the Very Large Array Site, New Mexico, August, 2011.

Manuscript received June 14, 2014

R. Blundell is with the Smithsonian Astrophysical Observatory, Cambridge, MA 02138, USA.

intended to operate under the extreme weather conditions that exist in the Arctic. As a result, numerous modifications and design changes are required in order to transform it for Arctic operation. Many of these modifications have been completed with guidance provided largely by our partner institute, the Academia Sinica Institute for Astronomy and Astrophysics of Taiwan. These include reworking the elevation bearings, the replacement of the azimuth bearing, the design and fabrication of a 6-point antenna base support to better enable an even distribution of the antenna load to a wooden raft and snow foundation, which is currently under design in consultation with the Cold Regions Research and Engineering Laboratory (CRREL) – the site recently selected for initial assembly and testing of the refurbished antenna. Other elements that have required significant redesign, or substantial rework include the electronics enclosures to house power systems, cryogenic compressors, and HVAC equipment; and the carbon fiber back up structure, which was repaired and modified to accept electrical wiring required to power a new reflector panel de-icing system that was never envisioned in the original design. The antenna drive motors / gearboxes, and the hexapod drive system that is used to position the secondary mirror, were redesigned for the Arctic environment. The quadrupod was replaced as it had been damaged during the ALMA acceptance testing of the prototype antenna. Insulating panels will be added to the main mechanical structure of the antenna. Additional insulation will be added to the receiver cabin, along with an improved thermal control system, and access to the cabin will be modified to better enable operations in the extreme Arctic environment.

III. THE SITE

The site, Summit Station, Greenland is a dry arctic environment ideally suited to millimeter, and submillimeter astronomical observations. It is potentially feasible to conduct observations in the supra-terahertz windows during the winter months, when the precipitable water vapor drops to about 0.25 mm for 10% of the time. Furthermore, at 72.5 degrees north and 38.5 degrees west, Summit Station is the ideal location to

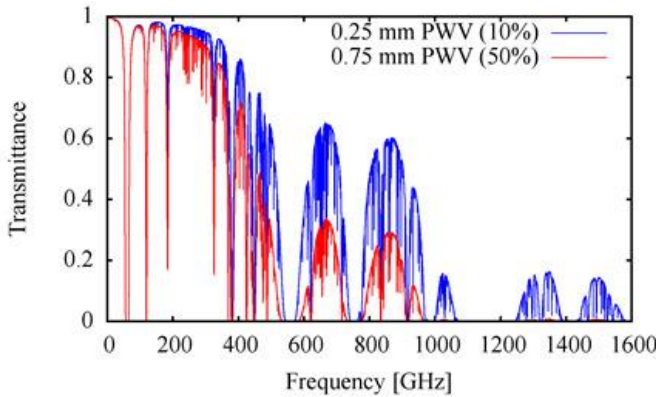


Fig. 2. Expected median and best decile atmospheric transmission versus observing frequency during the October – May observing season at Summit Station.

enable the longest baseline interferometry to ALMA in northern Chile, and provide the required additional, essential, link in the coupling of telescopes in northern Europe to those in the western US to better enable quality imaging. With reference to Fig. 3, even though M87 only reaches a maximum elevation angle of about 30 degrees, corresponding to two air masses, the quality of the atmosphere above the site makes Summit Station a viable proposition for VLBI observations at 345 GHz during the winter months.

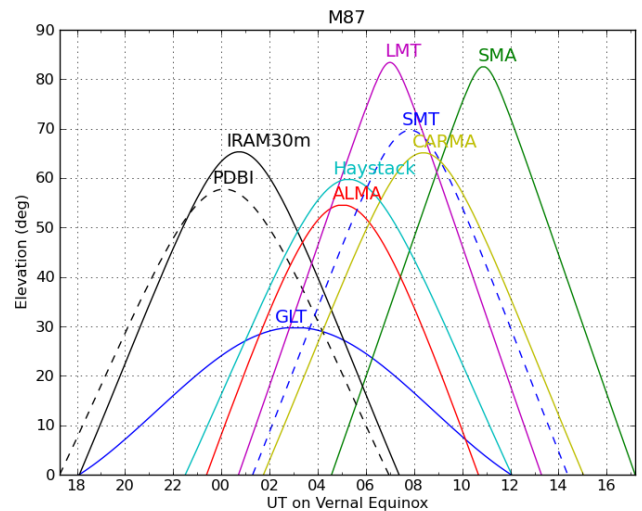


Fig. 3. Common visibility of M87 from millimeter and potential submillimeter VLBI stations.

The Summit Station facility was established by the US National Science Foundation (NSF) in 1989, and has been in year-round use since 2003. The scientific activity of the station includes the European Greenland Ice Core Project (GRIP), and the US Greenland Ice Sheet Project 2 (GISP2), which combined form the longest paleo-environmental record in the northern hemisphere, and atmospheric studies which rely on clean air and clean snow. The siting of a large telescope facility at Summit Station is viewed as an opportunity for the clean air, clean snow science to move away from the Station, which has been in active use for more than 20 years; and plans are being developed to enable such a move. Ideally, these activities would continue a few km to the south of the current Summit Station, close enough to the GRIP and GISP2 records, but sufficiently distant from the telescope, power generation equipment, ski-way used for aircraft access, and other scientific activities of which there are many during the summer months.

Access to the site is generally via LC-130, either from Thule Air Base or Kangerluusuaq, and fuel and cargo are hauled to the site once a year via the Greenland Inland Traverse (GrIT), operated by CH2M HILL Polar Services and CRREL in collaboration with the NSF. The GrIT, made up of a series of purpose-built sleds pulled by tractors equipped for Arctic operation, typically leaves Thule in early April and covers the 1,100 km distance to Summit Station in about 3 weeks. Each tractor can pull up to 80 tons, and they are used in parallel when climbing steep inclines, or in tandem on the descent. In order to reduce antenna assembly effort at the site,

we are planning to ship in the largest possible subassemblies consistent with safe passage and capacity of the traverse.

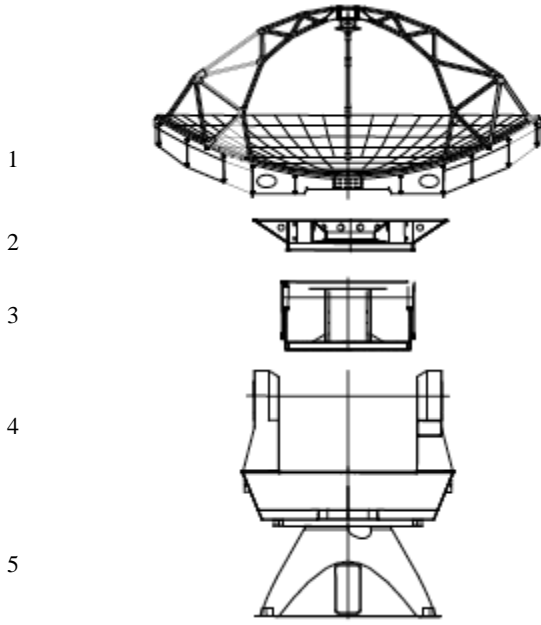


Fig. 4. The antenna may be broken down into large subassemblies to reduce assembly at the top of the Greenland Ice Sheet: 1) Reflector, 2) Reflector support cone, 3) Receiver cabin, 4) Yoke support, 5) Base.

IV. INSTRUMENTATION

The antenna will be equipped with single pixel receivers for the standard millimeter/submillimeter VLBI: 86 GHz, 230 GHz, and 345 GHz. In addition, and depending on the evolution of the science requirements, the antenna will be equipped with a variety of other heterodyne receivers, either single pixel or multi pixel, operating throughout the traditional submillimeter atmospheric windows from 230 GHz, potentially up to 1.5 THz. Bolometric array receivers have proven to be very successful in star formation studies and the search for high red shift galaxies at the APEX telescope and Herschel Space Observatory, and we anticipate similar instrumentation to be developed for the Greenland Telescope.

Several groups, worldwide, are currently focusing on a new class of receiver technology, which will enable arrays of detectors to be fabricated with reasonable spectral resolution ($R \sim 3,000$). We recently began a collaboration with colleagues at the University of Cambridge to develop the CAMbridge Emission Line Surveyor (CAMELS) [2] that will demonstrate on-chip spectrometer technology for mm-wave astronomical observations. ‘On-chip’ spectrometers use a bank of narrow-band electrical filters, integrated onto the detector chip, which perform spectral channelization at signal frequency. This technology has a number of attractive features, including compactness and ruggedness compared with grating and FTS spectrometers, and the ability to realize systems with wide instantaneous bandwidths. On-chip spectrometers fabricated using Kinetic Inductance Detectors (KIDs) are expected to enable the construction of large format imaging arrays in which each pixel is also capable of wide-band, medium resolution, spectroscopy. This is a potentially revolutionary

technology for galactic surveys, Cosmic Microwave Background (CMB) studies, for the detection and identification of high red shift objects, and for Earth observation and atmospheric science.

CAMELS will cover the frequency range 103-114.7 GHz at a resolution of $R \sim 3000$, and will be tested first during the commissioning phase of the Greenland Telescope. It will target $^{12}\text{CO}(1-0)$ and $^{13}\text{CO}(1-0)$ line-emission from galaxies at redshifts $z < 1$ and will map emission at kPc scales in the nearest galaxies. A key aim of the project is to explore the operational issues associated with making science-grade observations using on-chip spectrometers, including flux- and frequency- calibration, and coping with different sky backgrounds and observing strategies. The full bandwidth will be divided between two pairs of detectors, each with 256 channels. One pair will cover the 103-109.8 GHz frequency range, the other will cover 109.8-114.7 GHz. Observing conditions in the two sub-bands are very different, and will allow us to investigate the detection of bright objects against a high background at the edge of the atmospheric window, and faint sources against a low background in the window centre. A pair of pixels will be provided at each frequency to allow for sky chopping.

The key technologies being developed in support of this project are:

A. Optical Coupling Schemes for W-Band:

Aluminium (Al) is commonly used for the sensing regions of KIDs where the optical photons break Cooper pairs. Simulation work performed at Cambridge has shown that the frequency of the optical signal must be well in excess of the pair-breaking frequency of the superconductor for pair-breaking to occur. In the case of Al, the pair-breaking frequency is 90GHz at 100 mK, making it a borderline absorber at the frequencies we are interested in. The group is therefore investigating β -phase Ta as a sensing material, which has a lower pair-breaking frequency (<70GHz) and a resistivity more compatible with that of the NbN used for the resonators. The coupler geometries currently under investigation are discussed in [1].

B. Filter-Bank Technology:

Key to the operation of an on-chip spectrometer is the design of the filter-bank at both the system and element level. At the element level bandpass filters, based on half-wavelength loop-resonators, have been developed which have demonstrated the required R -values in simulation. At the system-level, a statistical framework for analysing the astronomical performance of a filter-bank, given the system level design, (filter shape, overlap, number etc.) has been developed based on maximizing the Fisher criteria.

C. Multichannel Readout:

Readout of a KID requires generating a comb of probe tones, then monitoring the change in amplitude and phase after transmission through the resonator arrays. We are currently planning a solution based on the combination of fast ADC/DAC cards and GPU cards as processors.

V. SCHEDULE

Many of the major antenna components are currently being refurbished to enable reliable under in the harsh Arctic climate, a number of other components are being replaced, and several antenna subsystems are still in the design phase. As noted above, we recently selected the Cold Regions Research and Engineering Laboratory at Hanover (New Hampshire) as the site for antenna reassembly and test, and anticipate the arrival of significant sections of the antenna: base support, azimuth bearing, yoke, receiver cabin, back up structure support cone, back up structure support, and quadrupod during the summer. In a parallel effort, we are working with staff at CRREL to prepare a site plan consistent with the requirement that the antenna be fully assembled, debugged, and tested before shipping to Greenland.

Tests to be performed at CRREL include photogrammetry and holography to set and verify the reflector surface, and optical pointing and tracking. We will also test the de-ice system and a new hexapod system to support and position the secondary mirror assembly. Following assembly and verification of performance, the antenna will be equipped with single pixel heterodyne receivers, working at 86 and 230 GHz, in order to perform on sky tests, including first light single dish science verification observations, which will be followed by a series of VLBI test observations.

We have also begun to work with the NSF and subcontractors to define the infrastructure required to support the telescope and telescope operations at Summit Station, close to the peak of the ice sheet. While it seems entirely possible that, with little new infrastructure, the current station could support the additional staff required to assemble, test, and operate the telescope. A telescope control area, increased laboratory facilities, and additional power generation will be

required, as well as a well-engineered snow foundation capable of providing a stable platform to enable astronomical observations with the telescope.

According to the current schedule, we anticipate that the infrastructure required to support and operate the telescope will be in place to enable telescope construction to begin during summer of 2018, which should make first light science observations possible from Summit during winter 2018 – 2019.

VI. ACKNOWLEDGEMENT

The author thanks Greenland Telescope team members at the Smithsonian Astrophysical Observatory and the Academia Sinica Institute for Astronomy and Astrophysics of Taiwan, and Dr. Patrick Haggerty of the NSF for their support in this work. The author also thanks Professor Stafford Withington, Dr. Chris Thomas, and other CamELS team members at the Cavendish Laboratory, Cambridge. Finally, the author thanks Dr. S. N. Paine for kind permission to reproduce Fig. 2 and Dr. Todd R. Hunter of the National Radio Astronomy for kind permission to reproduce Fig. 3.

REFERENCES

- [1] “Imaging an Event Horizon: submm-VLBI of a Super Massive Black Hole”, Doeleman, S., et. al., Astro210: The Asreonomy and Astrophysics Decadal Survey, Science White Paper, no. 68.
- [2] “The CAMbridge Emission Line Surveyor”, C. N. Thomas, S. Withington, R. Maiolino, D.J. Goldie, E. de Lera Acedo, J. Wagg, R. Blundell, S. Paine and L. Zeng. Proceedings of the 24th International Symposium on Space Terahertz Technology, Groningen, 2013.

Session 8: THz coherent detectors: HEB II & SIS mixers

Noise Temperature and Noise Bandwidth of Hot-Electron Bolometer Mixer at 3.8 THz

Ivan Tretyakov^{1*}, Sergey Seliverstov¹, Philipp Zolotov¹, Natalya Kaurova¹, Boris Voronov¹, Matvey Finkel¹, and Gregory Goltsman^{1,2}

¹*Moscow State Pedagogical University, Moscow*

²*National Research University Higher School of Economics, Moscow*

*Email: ivantretykov@mail.ru

We report on our recent results of double sideband (DSB) noise temperature and bandwidth measurements of quasi-optical hot electron bolometer (HEB) mixers at local oscillator frequency of 3.8 THz. The HEB mixers used in this work were made of a NbN thin film and had a superconducting transition temperature of about 10.3 K. To couple terahertz radiation, the NbN microbridge (0.2 μm long and 2 μm wide) was integrated with a planar logarithmic-spiral antenna. The mixer chip was glued to an elliptical Si lens clamped tightly to a mixer block mounted on the 4.2 K plate of a liquid helium cryostat. The terahertz radiation was fed into the HEB device through the cryostat window made of a 0.5 mm thick HDPE. A band-pass mesh filter was mounted on the 4.2 K plate to minimize the direct detection effect [1]. We used a gas discharge laser irradiating at 3.8 THz H₂O line as a local oscillator (LO). The LO power was combined with a black body broadband radiation via Mylar beam splitter. Our receiver allows heterodyne detection with an intermediate frequency (IF) of a several gigahertz which dictates usage of a wideband SiGe low noise amplifier [2]. The receiver IF output signal was further amplified at room temperature and fed into a square-law power detector through a band-pass filter. The DSB receiver noise temperature was measured using a conventional Y-factor technique at IF of 1.25 GHz and band of 40 MHz. Using wideband amplifiers at both cryogenic and room temperature stages we have estimated IF bandwidth of the HEB mixers used.

The obtained results strengthen the position of the HEB mixer as one of the most important tools for submillimeter astronomy. This device operates well above the energy gap (at frequencies above 1 THz) where performance of state-of-the-art SIS mixers starts to degrade. So, HEB mixers are expected to be a device of choice in astrophysical observations (ground-, aircraft- and space-based) at THz frequencies due to its excellent noise performance and low LO power requirements. The HEB mixers will be in operation on Millimetron Space Observatory.

References

1. J. J. A. Baselmans, A. Baryshev, S. F. Reker, M. Hajenius, J. R. Gao, T. M. Klapwijk, Yu. Vachtomin, S. Maslennikov, S. Antipov, B. Voronov, and G. Gol'tsman, *Appl. Phys. Lett.*, 86, 163503 (2005).
2. Sander Weinreb, Life Fellow, IEEE, Joseph C. Bardin, Student Member, IEEE, and Hamdi Mani, "Design of Cryogenic SiGe Low-Noise Amplifiers", *IEEE Transactions on Microwave Theory and Techniques*, 55, 11, 2007.

Superconducting Integrated Receiver with HEB-Mixer

N.V. Kinev^{*}, L.V. Filippenko^{*}, R.V. Ozhegov[†], K.N. Gorshkov[†], G.N. Gol'tsman[†] and V.P. Koshelets^{*}

^{*}Kotel'nikov Institute of Radio-engineering and Electronics of RAS, Moscow, Russia

Email : nickolay@hitech.cplire.ru

[†]Moscow State Pedagogical University, Moscow, Russia

Email : ozhegov@rplab.ru

Detectors in THz range with high sensitivity are very essential nowadays in different fields: space technology, atmospheric research, medicine and security. The most sensitive heterodyne detectors below 1 THz are the SIS-mixers due to its extremely high non-linearity and low noise level. Nevertheless, their effective range is strongly limited by superconducting gap Δ (about 1 THz for NbN circuits). Above 1 THz the detectors based on HEB (hot electron bolometers) are more effective [1]; their operation frequency is not limited from above and can be up to 70 THz [2]. HEBs can perform as both direct and heterodyne detectors (mixers). All HEB-mixers are used with external heterodyne, most useful are synthesizer with multipliers, quantum cascade lasers or far infrared lasers and backward-wave oscillators.

Superconducting integrated receiver (SIR) is based on implementation of both SIS-mixer and flux flow oscillator (FFO) acting as heterodyne at single chip [3]. Such receiver has been successfully applied at TELIS balloon-borne instrument for study of atmospheric constituents [4] and looks as very promising device for other THz missions including space research. Thus, there is a task to expand its operating range to higher frequencies. The frequency range of the SIR the operation is limited by both the SIS-mixer and the FFO maximum frequencies. The idea of present work is implementation of the HEB as a mixer in the SIR instead of the SIS traditionally used. We introduce the first results of integrating the HEB-mixer coupled to planar slot antenna with the FFO on one chip. For properly FFO operation the SIS harmonic mixer is used to phase lock the oscillator. The scheme of the SIR based on the HEB-mixer is presented in fig. 1.

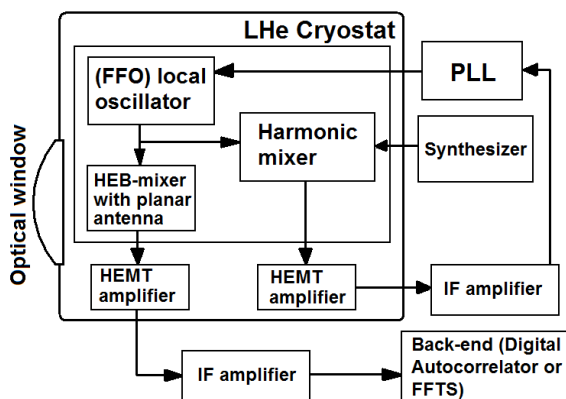


Fig.1. Block-diagram of the superconducting integrated receiver based on hot electron bolometer

We have demonstrated the principal possibility of integration of both the HEB-mixer and the flux-flow oscillator on a single chip and succeed with sufficient power coupling for properly receiver operation. We measured the direct response of the HEB coupled to the antenna at THz frequencies by the FTS setup and noise temperature of the receiver with standard Y-factor measuring technique. The SIR operating range 450-620 GHz was achieved with the best uncorrected noise temperature of about 1000 K. One should note that it is still quite low frequencies for effective operation of the HEB-mixer; therefore we expect to obtain the better results for frequencies above 700 GHz (up to 1.2 THz). Another additional task is to increase the FFO frequencies by using NbTiN electrodes instead of NbN; currently we are working on this issue.

This work was supported by the RFBR grant, the Ministry of Education and Science of Russia and Russian Academy of Sciences.

References

1. D. Semenov, H.-W. Hubers, J. Schubert, G. N. Gol'tsman, A. I. Elantiev, B. M. Voronov, E. M. Gershenson, *Design and performance of the lattice-cooled hot-electron terahertz mixer*, J. Appl. Phys. 88, 6758, 2000.
2. Maslennikov S. N., Finkel M. I., Antipov S. V. et al. *Spiral antenna coupled and directly coupled NbN HEB mixers in the frequency range from 1 to 70THz*. Proc. 17th international symposium on space terahertz technology. Paris, France: 2006.—may. Pp. 177 – 179.
3. V.P. Koshelets, S.V. Shitov. *Integrated Superconducting Receivers*. Supercond. Sci. Technol. Vol. 13. P. R53-R59. 2000.
4. Gert de Lange, Dick Boersma, Johannes Dercksen et.al. *Development and Characterization of the Superconducting Integrated Receiver Channel of the TELIS Atmospheric Sounder*. Supercond. Sci. Technol. vol. 23, No 4, 045016 (8pp). 2010.

High-quality NbN-MgO-NbN SIS junctions and integrated circuits for THz applications

Pavel N. Dmitriev^{*}, Maxim E. Paramonov^{*}, Kirill I. Rudakov^{*†}, and Valery P. Koshelets^{*}

^{}The Kotelnikov Institute of Radio Engineering and Electronics, Russian Academy of Science,
Mokhovaya St. 11, bldg 7, 125009, Moscow*

Email: valery@hitech.cplire.ru

*[†]Moscow Institute of Physics and Technology,
Institutskii per., 9, 141700 Dolgoprudny, Moscow Region, Russia*

Superconductor - insulator-superconductor (SIS) mixers based on NbN films are considered as a promising replacement for conventional Nb SIS mixers for realization of low-noise heterodyne terahertz receivers due to high gap frequency of up to 1.4 THz. In order to realize wideband and low-noise mixers, high current density and high-quality SIS junctions as well as extremely low-loss transmission lines are required.

New technique for fabrication of high-quality SIS tunnel junctions based on epitaxial NbN films with MgO barrier has been developed. NbN films have been deposited on single-crystal MgO substrates placed on the water-cooled substrate-holder. The NbN films are dc magnetron sputtered from a 5-inch diameter high purity Nb target in a reactive mixture of argon and nitrogen, leading to good thickness uniformity on 3-inch diameter substrates. Since deposited NbN films has cubic lattice structure with a lattice constant very similar to those for single-crystal MgO substrates it was possible to obtain single-crystal NbN films even at deposition at ambient temperature [1, 2]. The single-crystal NbN films deposited on an MgO single-crystal substrate in this work show a high transition temperature ($T_c = 16.1$ K) and reasonably low resistivity ($\rho = 80 \mu\Omega\text{m}^2\text{cm}$).

The tunnel barrier was created by oxygen plasma oxidation of extremely thin Mg layer ($d = 1.5$ nm) deposited on the NbN electrode by DC sputtering. The plasma oxidation process is similar to well-known nitridization process that was successfully used for fabrication of high current density NbN-AlN-Nb SIS junctions [3]; such process provides both better current density control compare to traditional rf sputtering of the MgO target [1, 2] and perfect junction quality. As a result the NbN/Mg-MgO/NbN junctions with gap voltage $V_g = 5.2$ mV and quality barrier parameter $R_j(2\text{mV})/R_n > 40$ have been fabricated. Such junction parameters are very promising for development of the Josephson oscillators and superconducting integrated receivers [4] for frequencies well above 1 THz.

To design integrated circuits one should know the parameters of the films composed the integrated circuits (e.g. - London penetration depth, the effective dielectric constant, etc.). Comprehensive studies of the electrical parameters of superconducting microwave structures made with different materials of the wiring electrode (Nb, Al, NbN, and NbTiN) have been performed and compared to numerical calculations in order to determine the various microwave parameters of these integrated structures.

The work was supported in part by the RFBR, the grant НШ-4871.2014.2, and the Ministry of Education and Science of the Russian Federation.

References

1. Akira Kawakami, Zhen Wang, and Shigehito Miki, "Low - loss Epitaxial NbN/MgO/NbN Tri1ayers for THz Applications", IEEE Trans. Appl. Supercond. **11**, p. 80, (2001)
2. Akira Kawakami, Yoshinori Uzawa, and Zhen Wang "Development of epitaxial NbN/MgO/NbN-superconductor-insulator-superconductor mixers for operations over the Nb gap frequency", Applied Physics Letters, 83, p. 3954 (2003)
3. M.Yu. Torgashin, V.P. Koshelets, P.N. Dmitriev, A.B. Ermakov, L.V. Filippenko, and P.A. Yagoubov, "Superconducting Integrated Receivers based on Nb-AlN-NbN circuits" "IEEE Trans. on Appl. Supercond.", vol. 17, pp.379- 382, 2007
4. V.P. Koshelets, S.V. Shitov, "Integrated Superconducting Receivers" Superconductor Science and Technology, vol 13, pp. R53-R69, (2000).

Fully integrated sideband-separating Mixers for the NOEMA receivers

D. Maier, J. Reverdy, L. Coutanson, D. Billon-Pierron, C. Boucher and A. Barbier

Abstract—Sideband-separating mixers with wide IF band have been developed for the NOrthern Extended Millimeter Array. The development of a planar IF coupler chip made it possible to design fully integrated sideband-separating mixers for two of the four bands of the interferometer.

Index Terms—Superconductor-insulator-superconductor (SIS) mixer, sideband-separating mixer, integrated mixer, wide IF band

I. INTRODUCTION

THE Plateau de Bure observatory run by the Institut de RadioAstronomie Millimétrique in the French Alpes will be upgraded during the next years to become the NOrthern Extended Millimeter Array (NOEMA). This largest millimeter project in the northern hemisphere consists of doubling the number of antennas from six to twelve, extending the baseline and installing new state-of-the-art dual polarization receivers with four frequency bands, providing each two approximately 8 GHz wide IF bands per polarization by employing sideband separating mixers. Table 1 gives an overview over the four frequency bands of the new NOEMA receivers compared to the current PdBI receivers.

Table 1: Comparison of the four frequency bands of the NOEMA receivers and the PdBI receivers.

Band	PdBI			NOEMA		
	Fr. range [GHz]	Mix. type	IF Band [GHz]	Fr. range [GHz]	Mix. type	IF Band [GHz]
1	83–116	SSB	4–8	72–116	2SB	3.872–11.616
2	129–174	SSB	4–8	129–179	2SB	3.872–11.616
3	200–268	SSB	4–8	200–276	2SB	3.872–11.616
4	277–371	1SB	4–8	275–373	2SB	3.872–11.616

Because of the atmospheric conditions on-site, Band 4 is of lowest priority for the project, so that in a first phase no new development will be started for this band. Instead the current PdBI mixers will be used. These are sideband-separating mixers with an IF band of 4–8 GHz initially developed for the ALMA Band 7 cartridge [1], but with only one IF output being further processed.

Bands 1 to 3 however will make use of IRAM's more recent mixer developments consisting of sideband-separating mixers with wide IF band. Bands 1 and 2 will even be equipped with fully-integrated sideband-separating mixers.

Manuscript received June 13, 2014. This work was supported in part by the European Union through the Radionet program.

D. Maier, J. Reverdy, L. Coutanson, D. Billon-Pierron, C. Boucher and A. Barbier are with the Institut de RadioAstronomie Millimétrique, Saint Martin d'Hères, France (corresponding author: +33476824916; fax: +3347682515938; e-mail: maier@iram.fr).

II. IF COUPLER CHIP FOR 2SB MIXERS

Sideband-separating SIS mixers are nowadays commonly used in radioastronomical receivers, in order to suppress atmospheric noise in the image band. Most of these mixers use waveguide structures for the realization of the 90° RF coupler, the LO couplers and the in-phase LO splitter, which allows these elements to be integrated together with the two DSB mixers into one E-plane splitblock. The 90° IF coupler on the other hand has not yet been integrated with the RF components, but is still a stand-alone unit in today's mixers, regardless whether a commercially available or a custom-made coupler is used. Mostly these couplers are based on nonhomogeneous dielectric broadside coupled striplines, which makes it impossible to integrate them into the commonly used E-plane splitblock.

Therefore we developed a completely planar IF coupler chip. It makes use of Nb striplines deposited onto a quartz substrate. In order to achieve a very low gain imbalance over the whole IF band of 4 to 12 GHz, three coupling sections are employed. The middle section consists of a Lange-type coupler, where the classically used bonding wires have been replaced by microstrip bridges separated from the underlying Nb lines by an SiO₂ layer. This Lange coupler is inserted between two sections of coupled microstrip lines as can be seen from the schematical layout shown in Fig. 1.

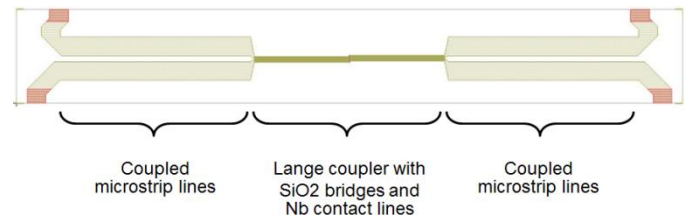


Fig. 1. Layout of the IF coupler chip.

The coupling sections have been optimized using Sonnet [2] yielding 20 μm and 10 μm for the finger width and spacing of the Lange coupler, respectively, and 540 μm and 160 μm for the width and the spacing of the coupled lines, respectively. The lengths of the coupling sections are each 5.49 mm. The distance between the two inputs of the chip have been matched to the distance between the two IF outputs of our existing 230 GHz 2SB mixer (see below), i.e. 16.7 mm, whereas the pitch of the two outputs had been chosen to be 18 mm to provide enough space for the IF amplifiers to be connected directly to the IF coupler.

The simulation results of the coupler chip are shown in Fig. 2. The gain and phase imbalances of the optimized chip are

better than ± 0.3 dB and 1° , respectively, and both input reflection and isolation are better than -20 dB.

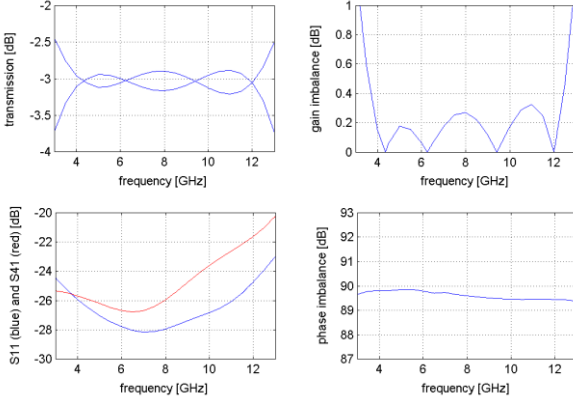


Fig. 2. Simulated performance of the IF coupler chip.

III. BAND 3 MIXER

The newly developed IF coupler has been tested with our 230 GHz 2SB mixer developed within the European project AMSTAR+ [3], [4] and installed since autumn 2011 in EMIR (**E**ight **M**ixer **R**eceiver), the receiver of IRAM's 30m antenna at Pico Veleta in Spain [5]. A photograph of one half of the E-plane splitblock of this mixer is shown in Fig. 3 on the left-hand side. With this mixer the coupler is used as a standalone unit in a dedicated housing (see Fig. 3, right). It replaces the so far used IF coupler based on nonhomogeneous dielectric broadside coupled striplines and developed for the use at cryogenic temperatures [6].



Fig. 3. Left: Photo of one half of the E-plane splitblock of the Band 3 sideband-separating mixer integrating RF coupler, LO splitter, LO couplers and DSB mixers. Right: Complete 230 GHz 2SB mixer with newly developed IF coupler.

The 2SB mixer has been fully characterized by measuring its noise temperatures and image rejections in an IF band of 3.8 to 12 GHz with steps of 100 MHz and for LO frequencies between 210 and 270 GHz. The results are shown in the plots in Fig. 4. The obtained noise temperatures lie approximately between 40 and 60 K over the whole band of 200 to 268 GHz and the image rejections are almost always better than -10 dB with an average value around -18 dB.

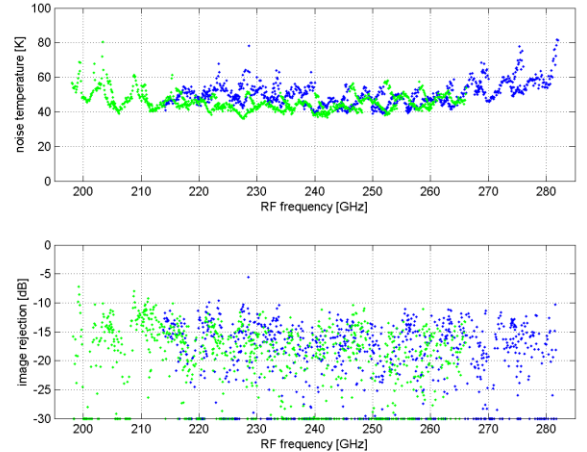


Fig. 4. Measurement results of the 230 GHz 2SB mixer. Above: Noise temperatures as a function of the RF frequency. Below: Image rejections as a function of the RF frequency. LSB measurements are shown in green, USB measurements are plotted in blue.

IV. BAND 2 MIXER

So far only backshort tuned single sideband mixers have been employed at IRAM in this frequency range [7]. Therefore a completely new sideband-separating mixer had to be designed for the NOEMA receivers.

A. 2SB mixer assembly

A coupler/mixer block integrating now not only RF coupler, LO splitter, LO couplers and DSB mixer blocks, but also the IF coupler has been designed as an E-plane splitblock (see Fig. 5). All RF components of this block have been optimized using CST Microwave Studio [8]. The results are shown in Fig. 6-Fig. 8.



Fig. 5. One half of the E-plane splitblock of the Band 2 sideband-separating mixer.

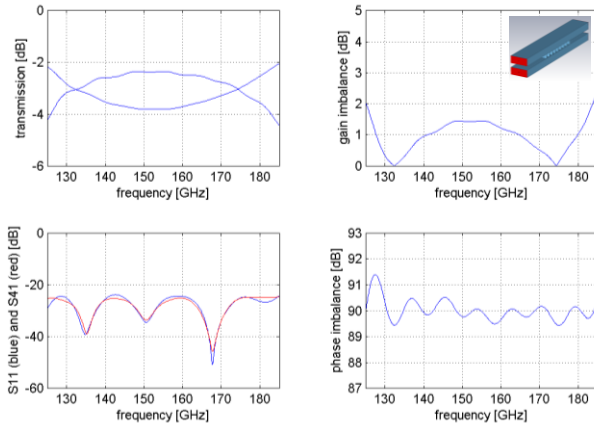


Fig. 6. Simulated performance of the Band 2 90° rf coupler.

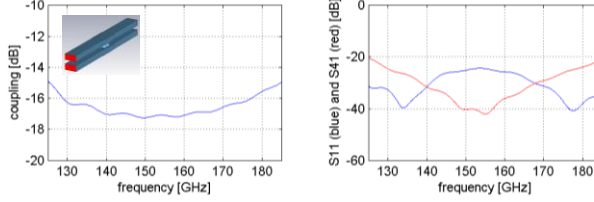


Fig. 7. Simulated performance of the Band 2 LO coupler.

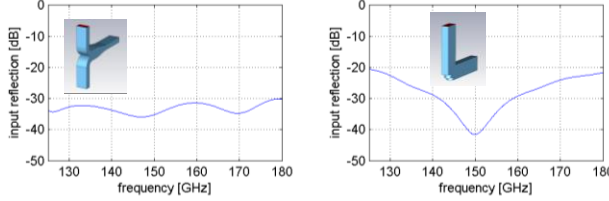


Fig. 8. Simulated performances of the Band 2 in-phase LO splitter (left) and the h-plane bend (right).

B. DSB Mixer

The DSB mixer employs superconductor-insulator-superconductor (SIS) tunnel junctions integrated in a superconducting circuit on a quartz substrate. The layout of one individual mixer chip with a size of $0.4 \times 3.5 \times 0.08 \text{ mm}^3$ is shown in Fig. 9. These devices are fabricated by IRAM's SIS group [9], [10].

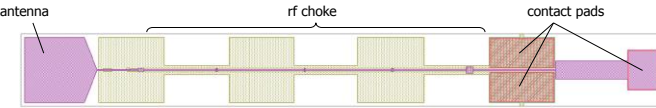


Fig. 9. Layout of the Band 2 mixer chip.

The mixer chip is placed in a channel perpendicular to the waveguide axis and stretches partly across the waveguide as shown in Fig. 10, left. The incoming radiation is coupled to the chip through a full-height waveguide to microstrip transition consisting of a suspended stripline structure at the end of the chip (see Fig. 9 on the left). This structure has been optimized using CST Microwave Studio [8] resulting in a slightly capacitive antenna impedance of around 50Ω shown in the Smith chart in Fig. 10 on the right.

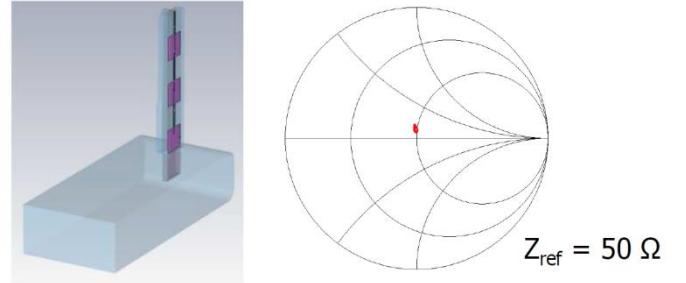


Fig. 10. Full-height waveguide to microstrip transition. Left: Mixer chip placed in the waveguide. Right: Antenna impedance for frequencies between 129 and 179 GHz.

The mixing element consists of a series array of three Nb-Al/AlOx-Nb junctions, each junction having an area of $1.7 \times 1.7 \mu\text{m}^2$ and the normal state resistance of the array being 20Ω . Two of the three junctions are placed on an island structure as shown in Fig. 11 on the right-hand side, which adds a small series inductance to the capacitive junction array. The residual capacitance of the structure is tuned out by means of a parallel inductance realized as coplanar waveguide followed by a large capacitance providing a virtual ground for RF frequencies (see Fig. 11, left, and Fig. 12). Behind the capacitance, the rf choke consisting of alternating coplanar waveguide sections and capacitances blocks the rf signals and only lets pass the IF signal. The circuit is completed by the $\lambda/4$ -wavelength transformer which matches the impedance of the junction array with its tuning structure to the antenna impedance shown in Fig. 10 on the right.

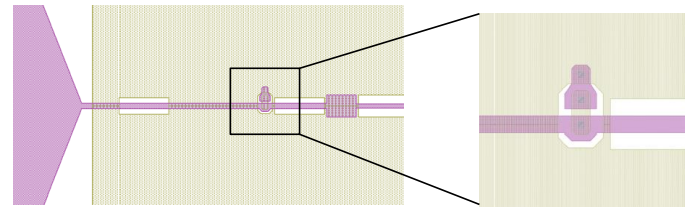


Fig. 11. Tuning structure and SIS junction array.

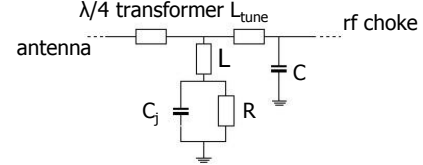


Fig. 12. Schematic view of the tuning structure.

The achieved embedding impedance of the junction is shown in the Smith chart in Fig. 13, left, for frequencies between 129 and 179 GHz. It is quite close to the junction's RF impedance, so that the achieved coupling to the junction is better than 98% (see Fig. 13, right).

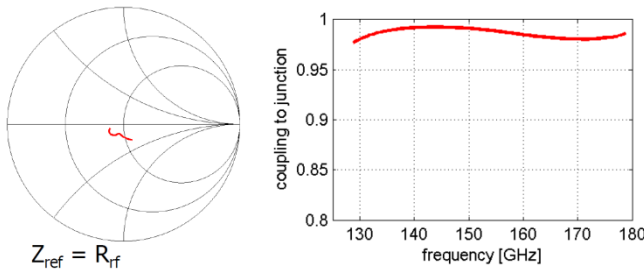


Fig. 13. Left: Embedding impedance of the junction for frequencies between 129 and 179 GHz. The Smith chart has been normalized to the junction's RF impedance. Right: The coupling to the junction is better than 98%.

C. Measurement results

Characterization of the fully integrated sideband-separating mixer showed very good performances with noise temperatures between 30 and 50 K over the whole band of 129 to 179 GHz and image rejections around -15 dB with only a few points lying above -10 dB. The obtained noise temperatures and image rejections measured in the IF band of 3.8 to 12 GHz with steps of 100 MHz and for LO frequencies between 134 and 174 GHz are shown in Fig. 14.

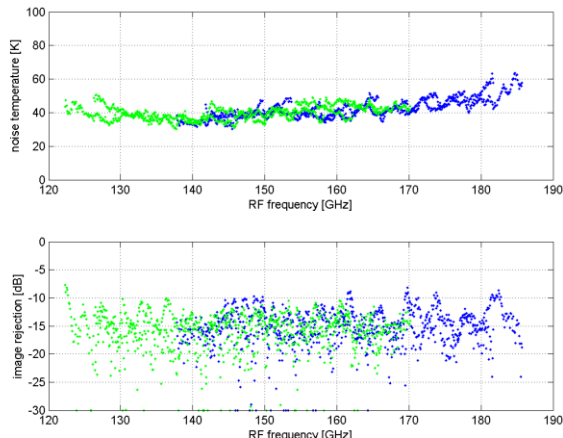


Fig. 14. Measurement results of the fully integrated 150 GHz 2SB mixer. Above: Noise temperatures as a function of the RF frequency. Below: Image rejections as a function of the RF frequency. LSB measurements are shown in green, USB measurements are plotted in blue.

V. BAND 1 MIXER

The NOEMA Band 1 sideband-separating mixer is a further development of the 100 GHz mixer employed in EMIR (Eight Mixer Receiver) at IRAM's 30 m antenna at Pico Veleta [11], [12]. Just as for the Band 2 2SB mixer the RF coupler, LO splitter, LO couplers, both DSB mixers and the IF coupler have been integrated into one unit and realized as an E-plane splitblock. And since the frequency range has been expanded, now starting at 72 GHz compared to formerly 82 GHz, all RF waveguide components have been redesigned to account for this new frequency range using CST Microwave Studio [8]. The simulated performances of these components are shown in Fig. 15-Fig. 17.

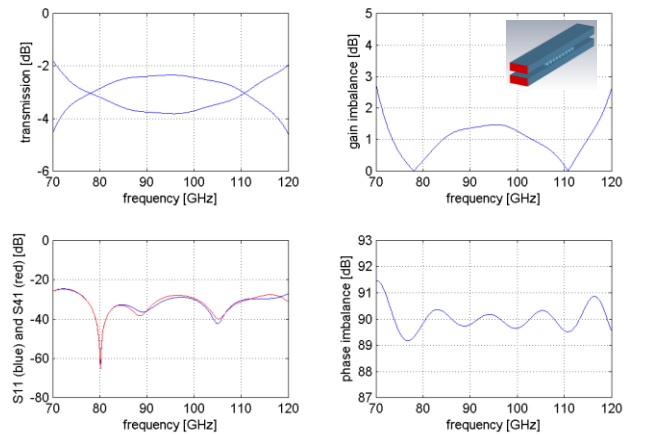


Fig. 15. Simulated performance of the Band 1 90° rf coupler.

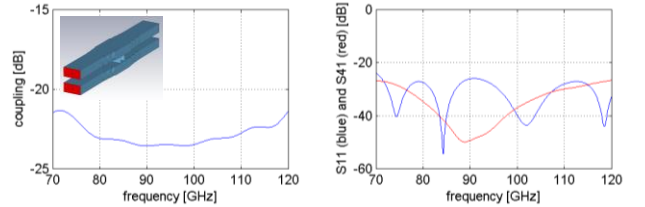


Fig. 16. Simulated performance of the Band 1 LO coupler.

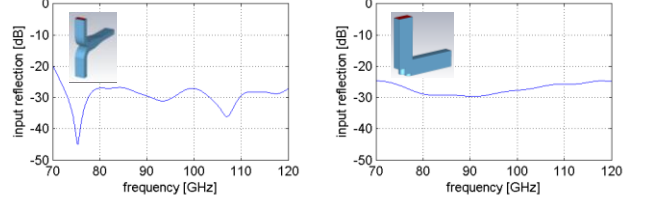


Fig. 17. Simulated performances of the Band 1 in-phase LO splitter (left) and the h-plane bend (right).

However, simulations of the mixer chip showed that it should work down to 72 GHz, so that no new mixer design was necessary.

One half of the E-plane splitblock of the new Band 1 mixer with mounted mixer chips, IF coupler and waveguide loads is shown in Fig. 18.



Fig. 18. One half of the E-plane splitblock of the Band 1 sideband-separating mixer.

Tests of the new fully-integrated 100 GHz sideband-separating mixer showed not only very good performances of noise temperatures around 30 K and image rejections around -15 dB over the extended frequency range of 72-116 GHz (see Fig. 19), but also that the mixer can indeed operate for frequencies between 70 and 122 GHz, i.e. it has a bandwidth of around 55 %.

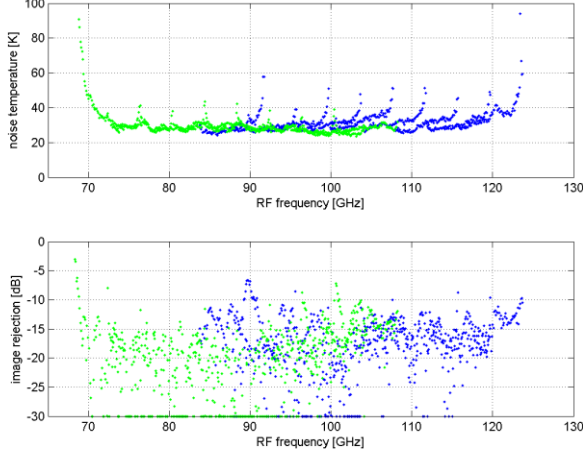


Fig. 19. Measurement results of the fully integrated 100 GHz sideband-separating mixer. Above: Noise temperatures as a function of the RF frequency. Below: Image rejections as a function of the RF frequency. LSB measurements are shown in green, USB measurements are plotted in blue.

VI. CONCLUSIONS

Wide-IF band sideband-separating mixers have been developed for the Bands 1 to 3 of the NOEMA receivers. The development of a planar IF coupler chip made it possible to design fully-integrated sideband-separating mixers for Bands 1 and 2. All mixers show state-of-the-art performances with very good noise temperatures and image rejections around -15 dB.

The first new NOEMA antenna equipped with these developments will be delivered in autumn 2014.

REFERENCES

- [1] D. Maier, A. Barbier, B. Lazareff, and K.F. Schuster, "The ALMA Band 7 Mixer," in *Proc. 16th ISSTT*, Göteborg, Sweden, pp. 428-431, 2005
- [2] Sonnet Software, 100 Elwood Davis Road Syracuse, NY 13212
- [3] D. Maier, "230 GHz sideband-separating mixer array," in *Proc. 20th ISSTT*, Charlottesville, USA, pp. 14-18, 2009
- [4] D. Maier, J. Reverdy, D. Billon-Pierron, and A. Barbier, "Upgrade of EMIR's Band 3 and Band 4 Mixers," in *Proc. 22th ISSTT*, Tucson, USA, pp. 197-200, 2011
- [5] M. Carter, B. Lazareff, D. Maier, J.-Y. Chenu, A.-L. Fontana, Y. Bortolotti, C. Boucher, A. Navarrini, S. Blanchet, A. Greve, D. John, C. Kramer, F. Morel, S. Navarro, J. Peñalver, K.-F. Schuster, C. Thum, "The EMIR multi-band mm-wave receiver for the IRAM 30-m telescope," *Astronomy & Astrophysics*, vol. 538, pp. 13, 2012
- [6] I. Malo-Gomez, J.D. Gallego-Puyol, C. Diez-Gonzales, I. López-Fernández, C. Briso-Rodriguez, "Cryogenic Hybrid Coupler for Ultra-Low-Noise Radio Astronomy Balanced Amplifiers", *IEEE MTT-57*, pp. 3239-3245, 2009
- [7] A. Navarrini, A.L. Fontana, D. Maier, P. Serres, and D. Billon-Pierron, "Superconductor-Insulator-Superconductor Mixers for the 2 mm Band (129-174 GHz)," *Journal of Infrared, Millimeter, and Terahertz Waves*, vol. 35, pp. 536-562, 2014
- [8] CST Microwave Studio, Bad Nauheimer Str. 19, D-64289 Darmstadt, Germany
- [9] I. Péron, P. Pasturel, and K.F. Schuster, "Fabrication of SIS junctions for space borne submillimeter wave mixers usisng negative resist e-beam lithography," *IEEE Trans. on Applied Superconductivity*, vol. 11, pp. 377-380, 2011
- [10] N. Krebs, A. Barbier, D. Billon-Pierron, S. Halleguen, M. Schicke, and K.F. Schuster, "Fabrication of Sub-Micrometer SIS Junctions for Radio Astronomy," *IEEE Trans. on Applied Superconductivity*, vol. 17, pp. 191-193, 2007
- [11] D. Maier, D. Billon-Pierron, J. Reverdy, M. Schicke, "100 GHz sideband separating mixer with wide IF band," in *Proc. 18th ISSTT*, Pasadena, USA, pp. 260-263, 2007
- [12] D. Maier, D. Billon-Pierron, J. Reverdy, M. Schicke, "100 GHz sideband separating mixer with wide IF band: First Results," in *Proc. 19th ISSTT*, Groningen, The Netherlands, pp. 93-96, 2008

Session 9: Back-ends: readout & signal processing

SIS Frequency Multiplexers and RF-to-DC converters for Frequency Division Multiplexed TES Read-out

G. de Lange

**SRON Netherlands Institute for Space Research, P.O. Box 800,
9700 AV Groningen, the Netherlands
Email: g.de.lange@sron.nl*

Frequency Division Multiplexing (FDM) is used for the read-out of large pixel number arrays of far-infrared and X-ray Transition Edge Sensors (TES). Within FDM a pixel within a TES array is AC biased with a unique MHz-frequency signal (with frequency spacing of order 10 KHz), where the frequency selection is achieved with high-Q superconducting filters. The resistance change of several bolometers, caused by the incoming radiation, is monitored simultaneously with a SQUID read-out. Because of the limited dynamic range of the SQUID, a limited amount of pixels (~ 100) can be read-out by a single SQUID. For large arrays of TES bolometers therefore many parallel channels of AC-biasing, SQUID feedback and SQUID read-out and biasing are necessary. The wiring harness that is necessary to run between 300 K and cryogenic temperatures is a limiting factor in the development of large pixel number arrays.

In order to reduce the wire count within the harness, we propose a novel use of SIS devices in the read-out of TES arrays. In this read-out scheme the SIS devices are used as GHz to MHz frequency up- and down converters. With frequency up- and down-conversion many parallel channels of a few MHz wide (where each channel would require separate wiring), can be stacked in series on carriers at GHz frequencies. These GHz signals can be sent over a single coaxial line. Furthermore we propose to use the SIS devices as RF-to-DC converters that can supply the DC-biasing and flux-offset to the SQUID. In the proposed scheme tens of thousands of TES pixels can be read-out over a single coaxial line.

We will present the read-out scheme, and discuss the feasibility and operating conditions of SIS devices as GHz-to-MHz frequency converters and RF-to-DC converter.

Experimental Study of Superconducting Microstrip Travelling-wave Parametric Amplifiers

Wenlei Shan^{*}, Ji. Yang^{*}, Masakazu Sekine[†], Yutaro Sekimoto[†], Takashi Noguchi[†]

^{*}Purple Mountain Observatory, Chinese Academy of Sciences

[†]National Astronomical Observatory of Japan

The emerging superconducting travelling wave parametric amplifiers¹ (STWPA) bring an opportunity of realizing heat-free cryogenic microwave amplifiers that are essential for future large format mm/sub-mm superconducting heterodyne array receiver, in which there are large amount of in-plant IF amplifiers in the frontend operating at cryogenic temperature². Besides the merit of no heat generation, STPAs are also believed to have lower noise than HEMT amplifiers and reasonable bandwidth (>1 GHz) that partly meets the requirement of molecular line observation. A travelling wave parametric amplifier in form of CPW has been demonstrated at 0.3 K¹.

We have designed, fabricated and tested STWPAs based on microstrip line structure. The reasons for using microstrip line instead of CPW are threefold: (1) the microstrip STPAs are more compact than CPW ones because the travelling wave is slower in microstrip by a factor of 5 using a typical set of design parameters; (2) it is practical to achieve 50 characteristic impedance by using microstrip, so that the standing waves trapped in the transmission line can be prevented and flat gain in the working frequency band can be expected; and (3) crosstalk in a microstrip meander line is weak, while it is often a problem in a CPW meander line. The meandering STPA that we designed for this study is about 18 cm long, equivalent to 60 wavelengths at 3 GHz, as shown in Fig.1. The conductive strip is in general 1.5 m wide but is perturbed by 3 m- wide sections located at every one-sixth wavelength to prevent the 3rd harmonic generation. The conducting strip and the ground plane are both 30 nm NbTiN thin films and the dielectric layer is 50 nm SiO₂. The T_c of NbTiN is about 13 K and the resistivity at room temperature is about 130 cm. In order to measure loss and evaluate nonlinearity of the microstrip line, testing chips containing capacitively coupled microstrip resonators are also fabricated and tested.

Testing chips and STWPA devices have been measured at liquid helium temperature. The transmission loss of the 60 wavelength long microstrip line results to be about 1 dB at 3 GHz and it shows apparent dependence on temperature at 4 K, roughly one-third of T_c. The loss of pump power along the amplifier weakens the nonlinearity of the overall transmission line and thus should be minimized by reducing the temperature. When a strong pump power of about -15dBm and a weak signal are applied, four-photon mixing phenomenon can be observed. By switching on and off the pump, we estimated the parametric amplification of signal is about 4 dB. Increase in the pump power can enhance the nonlinearity of the device and therefore increase the parametric gain. However there is a maximum pump power of about -15 dBm for these samples, above which the transmission line abruptly turns to a lossy state. The original state cannot be recovered by reducing the pump power back to that value prior to the trigger point, and an irreversible dependence of the transmission line loss on the pump power was observed.

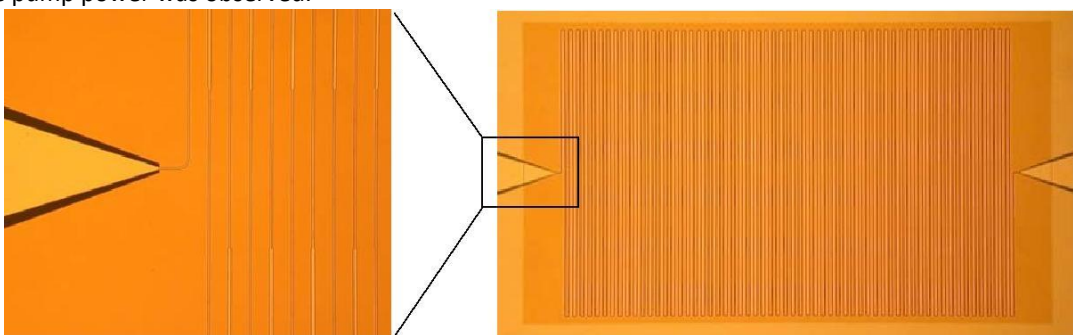


Fig.1 A microstrip line traveling wave parametric amplifier of size 1.5mm x 2.4mm. left panel shows an enlarged part.

References

1. Byeong Ho Eom, Peter K. Day, Henry G. LeDuc and Jonas Zmuidzinas, "A wideband, low-noise superconducting amplifier with high dynamic range," *Nature Physics*, 8, 623-627, 2012.
2. Wenlei Shan, Shengcui Shi, and Ji Yang, "An integrated SIS multibeam receiver for terahertz astronomical observation," the 23th ISSTT, Tokyo, Japan, 2012.

Session 10: Sources II

High Power Solid-State THz Source Development

Steven A. Retzloff, Jeffrey L. Hesler, and Thomas W. Crowe

Virginia Diodes Inc.
Email: hesler@vadiodes.com

This talk will describe recent work at Virginia Diodes on high power THz sources. In particular, one focus has been on the development of high power varactor multipliers in the 50-250 GHz range for use in driving THz multipliers covering 1-3 THz. Careful thermal design to remove heat from the diodes has allowed for unprecedented output power from multiplier chains without the need for power combining, e.g. 2 W at 55 GHz and 175 mW at 220 GHz.

One application for this high drive power has been to allow the integration of the THz multipliers into the cryogenic Dewar alongside the HEB mixer, thus simplifying the coupling of LO power to the mixer and reducing losses. The high power drive multipliers are placed outside the Dewar, and then a waveguide vacuum feed-thru and a thermal break are used to couple the power into the THz multipliers mounted on the cold-stage. By generating excess drive power the losses in the waveguide feed-thru can be overcome, allowing for the proper drive of the THz multipliers. One example of such a system is shown in Fig. 1 below, and more examples will be discussed at the workshop.

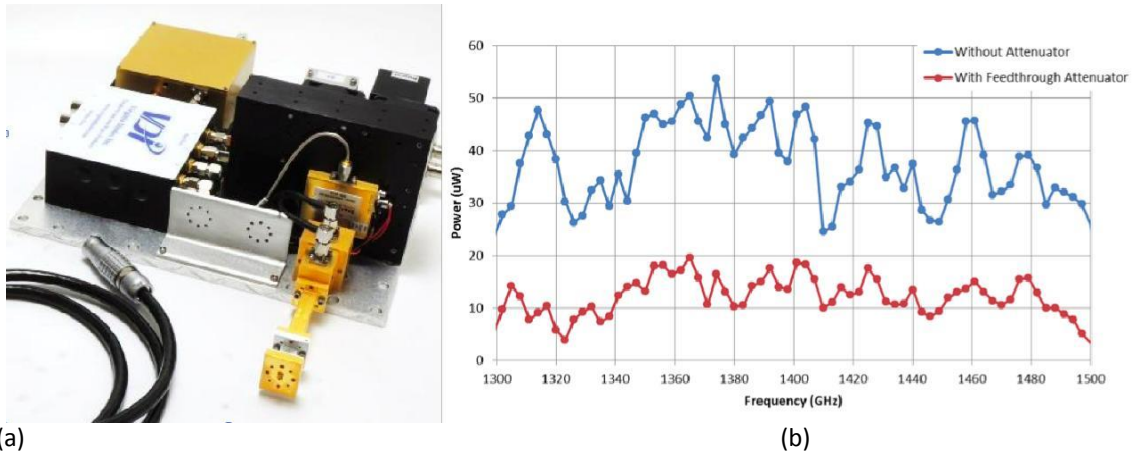


Fig. 1. (a) Photograph and (b) measured output power from a 1.3-1.5 THz source. The power is measured at ambient with and without an attenuator between the varactor drivers and the THz multipliers.

4-Pixel Frequency Multiplied Source For High-Resolution Heterodyne Array Receivers at 1.9 THz

Imran Mehdi, José V. Siles, Robert Lin, Choonsup Lee, Peter J. Bruneau,
Erich Schlecht, Jon Kawamura and Paul Goldsmith

¹NASA Jet Propulsion Laboratory, California Institute of Technology, Pasadena, CA

*Contact: Imran.Mehdi@jpl.nasa.gov

There are many key tracers of the interstellar medium and the process of star formation in the submillimeter region of the spectrum. Many of these, including C+, N+, CO, and H₂O have been successfully observed with the Herschel HIFI instrument, which was a single-pixel system. The goal now is to develop and demonstrate focal plane arrays that can image extended sources in a reasonable observation time frame. This will provide a major enhancement of capability for high spectral resolution imaging of submillimeter lines with SOFIA and future suborbital and space platforms.

We report on a compact 4-pixel frequency multiplied LO source to enable high-resolution heterodyne receivers at 1.9 THz (see Fig. 1). It consists of a X3X2X3X3 multiplier configuration featuring a 2-way coax power divider to split the signal generated by a Ka-band synthesizer, two Ka-band 30-dB gain power amplifiers with 1-Watt output power. This is followed by two 2-way Ka-band waveguide splitters to divide the power into four signal branches (one per pixel), four 105-120 GHz Schottky diode based frequency triplers based on a novel on-chip power-combined topology providing around 20-25 % efficiency. The final two stages consist of a 225-GHz 4-pixel doubler module with a ~25 % efficiency. Final stage consists of four x9 multiplier blocks consisting of a biasable 650 GHz tripler chip plus a biasless 1.9 THz tripler. Initial test of the LO subsystem showed an output power greater than 5 μ W from each pixel when operated at room temperature.

This work will directly benefit the development of future instruments for NASA's.

Stratospheric Observatory for Infrared Astronomy (SOFIA) and sub-orbital platforms, such as the Stratospheric Terahertz Observatory (STO-2).

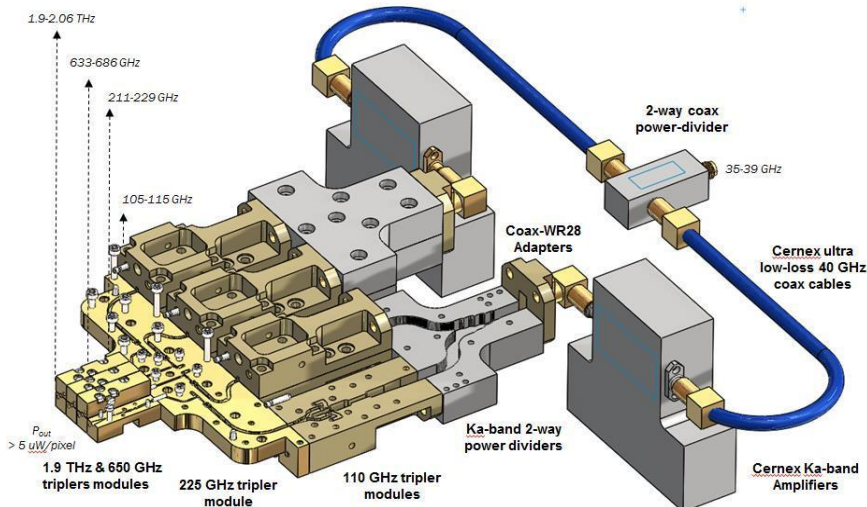


Fig. 1. General CAD scheme of the compact 4-pixel 1.9 THz source.

This work was carried out at the Jet Propulsion Laboratory, California Institute of Technology, Pasadena, CA under a contract with National Aeronautic and Space Administration.

Invited Talk

The Submm Wave Instrument on JUICE

Paul Hartogh * and the SWI team

**Max Planck Institute for Solar System Research*
Email: hartogh@mps.mpg.de

The Submillimetre Wave Instrument (SWI) is one of the scientific instruments on the JUpiter ICy moon Explorer (JUICE), [1-3]. JUICE is the first Large Class mission (L1) of the European Space Agency (ESA). SWI's primary scientific objectives are to investigate the middle atmosphere of Jupiter and the atmospheres and exospheres of the Galilean satellites. SWI will contribute to the understanding of the circulation regime in Jupiter's stratosphere as a function of latitude and altitude, how the various atmospheric regions are dynamically coupled, and how the energy originating in Jupiter's interior vertically propagates to the upper layers to be radiated in space. In this sense SWI complements NASA's Juno mission. Io's volcanic atmosphere will be studied through lines of SO₂, SO, NaCl, and perhaps other species. Water vapour and its sources and sinks will be observed in Ganymede's, Callisto's and Europa's atmospheres. Water isotopes and atmospheric properties like temperature and wind profiles will be derived for Ganymede's and Callisto's atmospheres from highly resolved simultaneous observations of at least two water lines. Depending on the final hardware design the water ortho-to-para ratio (OPR) will be derived and provide information together with the isotopic ratios about the formation region of the water ice the moons are made of. Furthermore thermophysical properties of the Galilean satellite surfaces will be measured by radiometric observations.

In the baseline configuration SWI consists of two tunable submm wave receivers operating from 530 to 625 GHz. Alternatively one receiver may cover the frequency range of 1080 and 1275 GHz. The latter solution is for instance required for the OPR determination, allows higher spatial resolution and extended altitude coverage in Jupiter's stratosphere and the detection of additional isotopes therein. The antenna of SWI has a diameter of 30 cm and will be movable by ± 76 and ± 4.3 degrees along and cross track respectively. Two low power consumption and low mass wideband high resolution Chirp Transform Spectrometers (CTS) with 1 GHz bandwidth and 100 kHz spectral resolution are foreseen and complemented by 2 autocorrelation spectrometers (ACS) with 5 GHz bandwidths and 20 MHz spectral resolution. The total mass/power of the instrument design is < 10 kg/50W.

The definition phase (A/B1) for SWI started in April 2013 and will last until end of March 2015. ESA requires the achievement of Technology Readiness Level (TRL) 5 until end of this phase. The JUICE implementation phase is planned to start in April 2015 followed by the launch of the satellite in summer 2022.

This presentation will give an overview of the scientific objectives and the present technical status of SWI.

References

1. <http://sci.esa.int/juice/50073-science-payload/>
2. <http://sci.esa.int/juice/50068-science-objectives/>
3. <http://sci.esa.int/juice/49837-juice-assessment-study-report-yellow-book/#>

Session 11: THz coherent detectors: Schottky mixers

Schottky-structures for Space THz Technologies

Presented by Oleg Cojocari

*ACST GmbH, Hanau, Germany
www.acst.de
Email: oleg.cojocari@acst.de*

A novel fabrication process, so-called “Film-Diode (FD) process” has been developed at ACST GmbH for fabrication of discrete and monolithically-integrated Schottky-based structures. The process aims to achieve ultimate performance at millimeter (MM) and Sub-millimeter (SubMM) wavelengths. Excellent performance was realized in several MM/SubMM modules. Achieved results represent European state-of-the-art performance at these frequencies. Most of developed structures are included in an ESA preliminary reliability study for space qualification concerning MetOP SG mission.

This talk shall give a short overview on developed FD-process, fabricated Schottky-structures, and achieved performance.

This work has mainly been performed in collaboration with RPG GmbH, ASTRIUM SAS, and ESA in frames of several ESA contracts. The Authors acknowledge all officers, engineers, and technical stuff, which contributed to this work, for excellent work and successful collaboration.

THz Schottky Diode MMICs for Astronomy and the Physics of the Atmosphere

L.Gatilova^{1&2}, J.Treuttel¹, F. Yang^{1&3}, T. Vacelet¹, C. Goldstein⁴, Y.Jin², A. Maestrini^{1&5}

¹*Observatoire de Paris - LERMA,*

²*CNRS - Laboratoire de Photonique et de Nanostructures,*

³*University of South West, Nanjing, China*

⁴*Centre National d'Etudes Spatiales,*

⁵*Université Pierre et Marie Curie – Paris 6*

Among different technologies available to build THz and sub-THz devices for radio-astronomy, Schottky diodes play a crucial role. In particular planar Schottky diodes on thin GaAs membrane remain key elements of submillimetre-wave mixers and frequency multipliers dedicated to the instrumentation for astrophysics, planetology, the science of the atmosphere and experimental physics.

We report on a 310-360 GHz frequency doubler that LERMA has designed as a demonstrator for the local oscillator of the Submillimeter Wave instrument on JUICE (JUpiter ICy moons Explorer - ESA). This multiplier features 4 anodes in a balanced configuration monolithically integrated on a 59m-thick GaAs membrane circuit connected to a split waveguide-block by metallic beam-leads. The LERMA-LPN circuits have been tested at RF with a 20-45 mW source provided by Radiometer Physics GmbH (RPG). A conversion efficiency of about 15-22% has been measured in the 310-360 GHz band, in very good agreement with simulations. A lifetime test is underway at LERMA since mid-December 2013. After more than 3 weeks of continuous operations at 45mW input, the circuit shows no sign of aging. The design and fabrication process of LERMA-LPN 310-360 GHz frequency doubler will be presented at the conference.

In addition, LERMA-LPN discrete anti-parallel diodes have been tested at RF by RPG on a 448 GHz and a 664 GHz sub-harmonic mixer and with an IF LNA in the 0.5-9 GHz band. The following table shows the measured results [1].

RF Frequency	T_mixer_DSB	G_mixer_DSB	P_LO
448 GHz	~1200K	~ -8dB	1.2 mW
664 GHz	~1550K	~ -8dB	2.3 mW

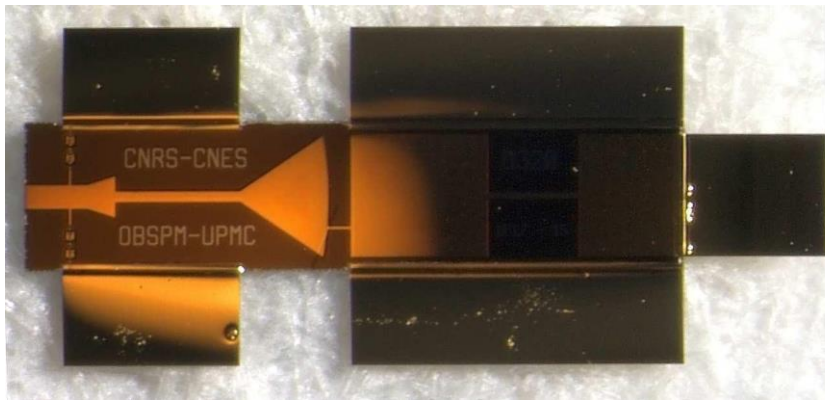


Fig. 1. LERMA-LPN GaAs Schottky diode based 320-340 GHz frequency doubler MMIC circuit.

References

1. Bertrand Thomas, Radiometer Physics GmbH., private conversation, December 2013

Sub-millimeter-wave balanced mixers and multipliers at the 5th harmonic

Hugh J.E. Gibson¹, Achim Walber², Bertrand Thomas²

¹ Gibson Microwave Design EURL France ²RPG Radiometer Physics GmbH Meckenheim, Germany

Abstract— Balanced 3rd harmonic multipliers and mixers have been successfully realized for many years using anti-parallel and series-connected Schottky diodes respectively. It is in principal possible to use the same techniques to make sub-millimeter wavelength devices using the 5th harmonic as the design should be similar. This work will discuss the problems involved with the designs of a WR2.2 wideband balanced 5th harmonic mixer at 500 GHz and a WR2.2 balanced quintupler multiplier also at 500 GHz. Simulations and test results are shown. The efficiencies of 5th harmonic devices are understandably significantly lower than 3rd harmonic devices, but the 5th harmonic allows an attractive, direct way to 500 GHz from the relatively easy 100 GHz where MMICs are nowadays readily available.

Index Terms— Quintupler, Harmonic-mixer, 5th harmonic, WR2.2

I. INTRODUCTION

NARROW-BAND multipliers and mixers at the 5th harmonic have been available for many years but there are very few wideband designs or designs with reasonable conversion efficiencies. The problem of 5th harmonic generation and filtering is similar in both harmonic mixers and multipliers, so there is much in common between the two design concepts. Section II will review a multiplier design and section III will review a harmonic mixer design. The use of commonly available European diodes is a key to both designs. ACST GmbH Germany and Teratech Ltd UK have made custom-designed diodes for RPG and GMD with special high-frequency features which are critical to the successful realization of conventional mixers and also to these 5th harmonic designs at 500 GHz. Both multiplier and mixer

Gibson Microwave Design EURL (GMD) was founded in 2009 and is based in Antony 92160, France. GMD is a one-man company and provides significant design assistance. Contact gibson@radiometer-physics.de

Radiometer Physics GmbH, Meckenheim, Germany have been involved in millimeter-wave instrumentation and radiometers for nearly 40 years. Now majority owned by Rohde & Schwarz, it provides sub-millimeter support for R&S instrumentation as well as retaining its own radiometer and sub-millimeter instrumentation, including instrumentation for space missions. Contact info@radiometer-physics.de or visit www.radiometer-physics.de

Advanced Compound Semiconductor Technologies (ACST GmbH) is a spin-off company from TU Darmstadt. ACST produces high frequency diode technology for mixers, multipliers and photodiodes. Contact contact@acst.de or www.acst.de for further details.

Teratech Components Ltd is a spin-off company from the Millimeter wave technology group at the STFC Rutherford Appleton Laboratory UK. Teratech provides high frequency diode technology for Schottky mixers and multipliers. Contact sales@teratechcomponents.com or visit www.teratechcomponents.com for further details.

designs use pairs of Schottky diodes in predominantly balanced, varistor mode configuration. This has many advantages, including suppression of even harmonics and (for the multiplier) isolation between input and output ports.

The general aim of this paper is to provide some background information on successful wideband 5th harmonic designs and the problems encountered, as there is very little in press about such attempts. Many people have considered such 5th harmonic designs but very few have published data. We hope to cover the design issues and present data of working devices. The performance of these designs is considerably worse than 3rd harmonic designs but we found it interesting that wideband 5th harmonic designs are indeed possible and also to compare performance with 3rd harmonic designs and measurements.

II. MULTIPLIER (QUINTUPLER)

Efficient x5 multiplier designs require very specific impedances at the input, output and idler circuits which are not easy to synthesize. Providing these impedances for the idlers and coupling circuits is a major challenge and is considerably more difficult than for a 3rd harmonic design. Most previous efficient x5 multiplier designs have used series connected devices or HBVs (Heterostructure Barrier Varactor). Various groups have successfully made narrow-band designs, including Chalmers University [7] and University of Virginia [8]. In contrast, we want to concentrate on making full waveguide-band devices.

We have used anti-parallel diodes because they generally have less severe impedances than a pair of series-connected diodes, which is beneficial for a wideband design, even though the overall efficiency may not be as high. Anti-parallel diodes are also widely available for sub-harmonic mixer use and generally have lower parasitic reactance than series-connected designs and are also slightly easier to solder.

Our x5 multiplier design is based on an existing x3 multiplier. A key part of the design is the efficient blocking of the strong 3rd harmonic in both input and output circuits. For a WR2.2 full-band design, this requires a filter with steep rejection below 300 GHz (highest 3rd harmonic frequency), but passing 325 GHz (lowest 5th harmonic frequency). Such a filter is tricky to realize and many different types were tried. Low loss is critical, as is simplicity. The solution finally chosen for the RF output is to use a shorted-stub type bandpass filter, with capacitive loading on the resonators.

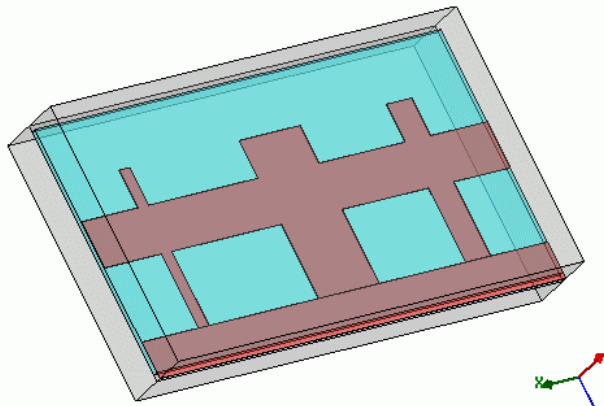


Fig. 1. 3D model of the 5th harmonic shorted-stub bandpass filter.

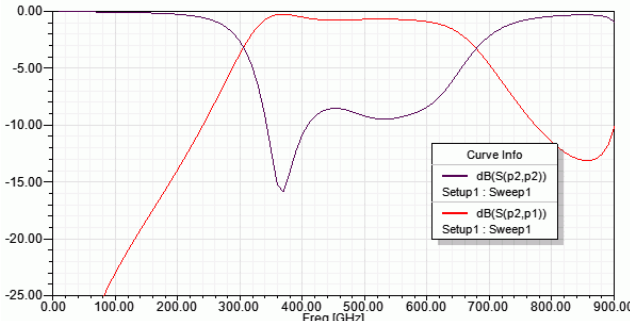


Fig. 2. S-parameter plot (dB scale) of the 5th harmonic bandpass filter.

The filter is further optimized to suit the impedances of the multiplier. The design is low loss, simple and small. It succeeds in passing the 5th harmonic, while terminating the 3rd harmonic with a low impedance with short electrical length which improves efficiency and gain flatness.

For the input circuit, a simpler filter based on low-pass hammer-head filters and stubs is used.

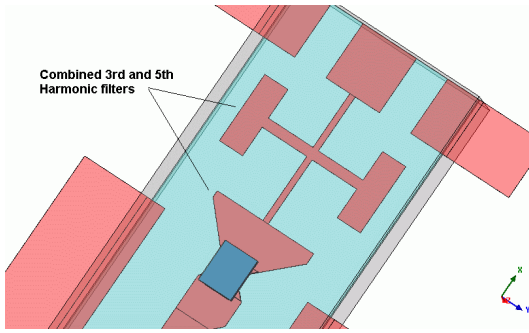


Fig. 3. RF input filter design, with wideband LPF rejection.

Again, it is paramount to block unwanted harmonics as near to the diode as possible to limit the electrical path-length of reflections, which can cause large dips in the multiplier efficiency.

The final design is quite similar to an earlier HBV narrowband quintupler [1] which can be found in the literature.

The simulation uses the conventional approach of pairing a linear structure simulator and a non-linear harmonic-balance

simulator. The entire device is simulated with no division of frequencies, and exported as a single S-parameter block so that the complex interactions of the many harmonics could be correctly simulated within the harmonic balance simulator up to the 7th harmonic.

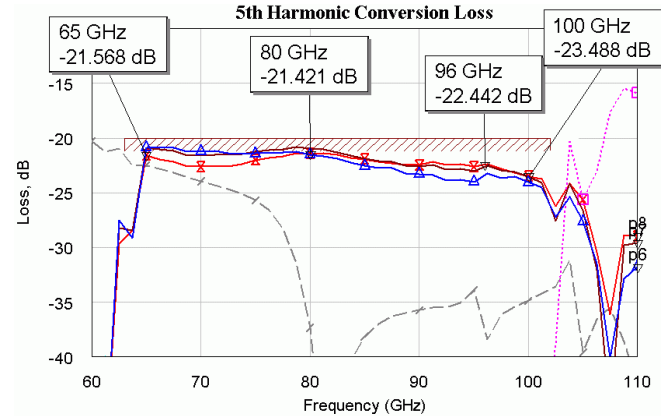


Fig. 4. Simulation of the 5th harmonic multiplier. The thick curves are conversion efficiencies with varying input powers. The pink dotted line is the unwanted 3rd harmonic at the output and the grey dashed line is the 3rd harmonic leaking back into the input.

Fig 4 shows the simulation results of the multiplier. The unwanted 3rd harmonic signal (pink, dotted) is successfully rejected below input frequencies of 100 GHz (i.e. 500 GHz, or top of the WR2.2 band) as required. The conversion efficiency is not strongly dependent on LO power and the conversion plot is remarkably flat. For good efficiency, it is important to use high LO pump powers, and the diode current conduction angle should be quite large.

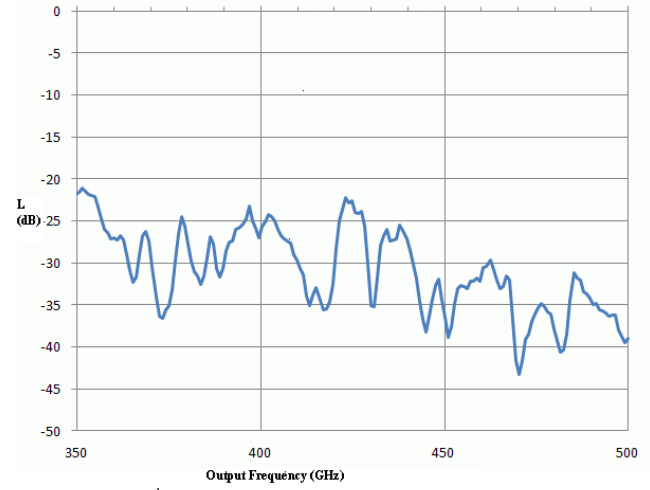


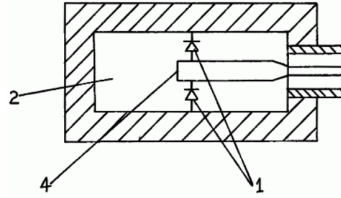
Fig. 5. Measured 5th harmonic multiplier conversion loss (dB).

The 5th harmonic multiplier was fabricated and measured by RPG. Fig 5 shows the measured (uncorrected) conversion loss (dB scale) against output frequency (GHz). The measurement and simulation are in reasonable agreement but there are rapid variations in power, in excess of 10 dB which is unaccounted for in the simulation. Some of this is undoubtedly output mismatch and has a characteristic periodic structure. Nevertheless, a useful multiplier design was successfully achieved with moderate efficiency over the entire WR2.2

band, which was easily pumped from a wideband 100 GHz source.

III. MIXER (USING 5TH HARMONIC)

Balanced mixer designs are possible at odd harmonics, using a “cross-bar” mixer. This design is typically used for fundamental balanced mixer designs [2][3] as it has high intrinsic isolation from input and output due to the arrangement of the diodes.



The small insert shows the general arrangement, with the diodes (1) in series across a rectangular TE10 waveguide (2) but appearing in anti-parallel to the coaxial TEM input line (4).

Cross-bar mixers also work well at higher odd harmonics [6] but the higher harmonics are of course not isolated from the input, so extra filters need to be used. Even-harmonics are generated in the output waveguide (but no odd harmonics). The opposite happens (odd harmonics only) on the input circuit. The simplicity of this design has some shortcomings; Because the diode is effectively the waveguide coupler, there is no opportunity to filter out the even harmonics before the waveguide, and the position of the diodes in the waveguide dictates a minimum length of input transmission line before input-filter components can be used (because of the length of the waveguide backshort).

We have previously made mixers at the 3rd harmonic using the cross-bar concept with good results [4] and others have at the 7th harmonic [6] so it seemed appropriate to adapt this design to try it at the 5th harmonic. Suitable series-connected diodes were available from two European sources, Teratech Ltd (UK) and ACST GmbH (Germany) both with very low parasitic capacitances and small size. An example of the Teratech “SC1” is shown below in Fig 6.

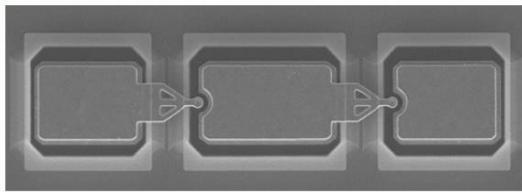


Fig. 6. Scanning Electron Microscope image of an “SC1” diode pair [ref?]

The design requires considerable filtering on the input circuit to reflect the unwanted harmonics close to the diodes. A combination of radial stubs, hammerhead and special photonic-bandgap filters [4] [5] are used to achieve the wideband filtering. The final design is similar to Fig 7. Considerable time is required for optimization of the various filters to achieve the desired results. Waveguide impedance transformations and filtering are also optimized in the output waveguide using stepped transformers and custom size cutoff waveguide. One can also see in Fig 7 that it is not possible to easily fit filters close to the diode, where they would be ideally situated.

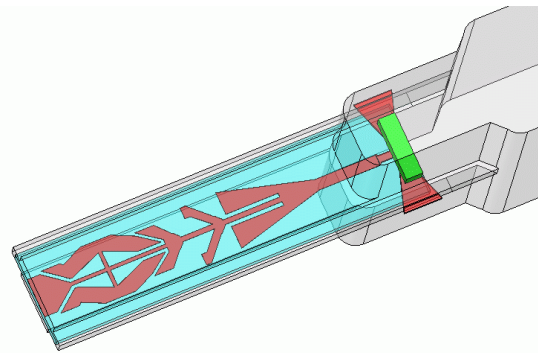


Fig. 7. 3D model of a generic 5th harmonic mixer for the WR2.2 band.

Very high accuracy in the 3D model and simulation are required to achieve results that are realistic at the 5th harmonic. The harmonic balance simulator must be capable of accurately simulating the multiple combination of mixing products. The APLAC HB solver in Microwave Office (AWR Corp) is used for these simulations.

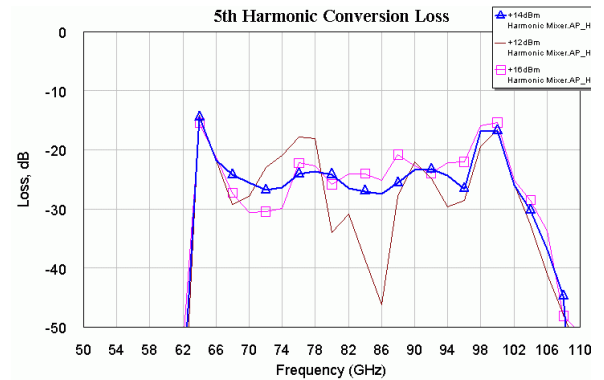


Fig. 8. Simulation of Conversion loss of 5th harmonic mixer (dB) against LO input frequency. Plots show different input LO powers: Blue +14dBm, Brown +12dBm and Pink +10dBm.

The simulated WR2.2 Mixer conversion efficiency (dB) is plotted in Fig 8 against LO input frequency. The mixer is quite flat from 65 to 100GHz input frequency (325 – 500GHz at 5th harm) but is quite sensitive to the LO power level.

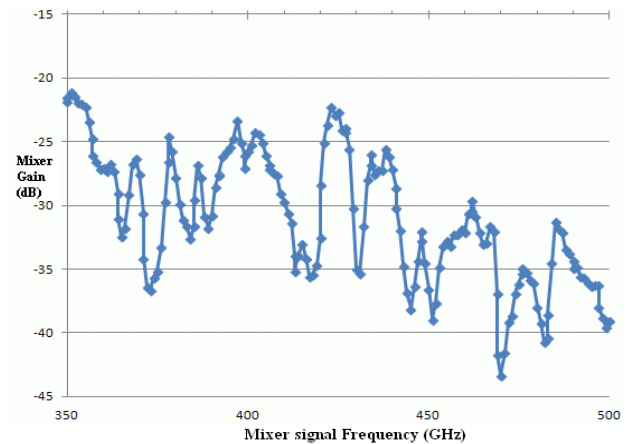


Fig. 9. Measured Conversion Loss (dB) against RF output frequency (GHz)

The measured conversion efficiency in Fig 9 is quite similar to the simulation, with the exception of a drop off in performance above 450 GHz which needs further investigation. There is also more variation in the conversion than the simulation but the overall performance is generally as predicted.

IV. CONCLUSIONS

Wideband varistor-type Quintupler (5^{th} harmonic multipliers) can be designed using anti-parallel Schottky diode pairs but efficiencies are expected to remain around 1%. The input match is good, but high pump power is necessary to produce the best efficiencies and flattest response. Biasing high harmonic devices (mixers and multipliers) seems to be of limited value, as a fast ‘snap’ turn-on is essential for efficient, high harmonic generation.

For multiplier designs using anti-series diodes (or HBVs) input impedance match seems to be the main limitation (being both high-Z and reactive). HBVs are usually very narrow band (5%), but can be relatively efficient.

Using anti-parallel diodes allows an easier impedance match and varistor-type multiplier designs but overall efficiency is lower.

Harmonic mixers at the 5^{th} harmonic, using cross-bar technology work well, but conversion efficiency is dependent on the level of 5^{th} harmonic generated, which can be quite variable with frequency.

Designs for wideband multipliers and mixers are possible, but the design effort required is very considerable compared to 3^{rd} harmonic designs. Control of the strong lower (3^{rd}) harmonic reflections is critical for a flat response and in some cases, small amounts of attenuator damping are necessary to achieve a flat conversion efficiency response.

ACKNOWLEDGMENT

The devices mentioned are realized with the skill of the RPG workshops, including fine machining of the metal blocks by Benjamin Elsner and Peter Krahe and the small Schottky diode mounting skills of Achim Walber. The devices would also not be possible without the availability of suitable diode devices from Oleg Cojocari at ACST GmbH and Byron Alderman at Teratech Ltd.

REFERENCES

- [1] M. Ingvarson, A. Oleson, J. Stake “Design and analysis of 500GHz heterostructure barrier varactor quintuplers” 14th International Symposium on Space Terahertz Technology (ISSTT) 2003 Tucson AZ. USA
- [2] B. Thomas, A. Maestrini, J Gill, C. Lee, R. Lin, I.Medhi, P de Maagt. “A Broadband 835-900GHz Fundamental Balanced Mixer on Monolithic GaAs Membrane Schottky Diodes” IEEE Transactions on Microwave Theory and Techniques Vol 56 No.7 July 2010 .
- [3] N. Erickson “A Schottky-Diode Balanced Mixer for 1.5THz” 19th International Symposium on Space Terahertz Technology (ISSTT) 2008 Groningen NL.
- [4] H. Gibson, A. Walber, R. Zimmerman, B. Alderman, O. Cojocari “Harmonic Mixers for VNA extenders to 900GHz” 21st International Symposium on Space Terahertz Technology (ISSTT) 2010, Oxford UK.
- [5] Q. Xue, K. Shum, C.H. Chan “Novel 1-D Microstrip PBG Cells” IEEE Microwave and Guided wave letters Vol 10 No.10 October 2000
- [6] D. Schneiderbanger, C. Kneuer, M. Sterns, R. Rehner, S. Martius, L-P Schmidt “A 75-110 GHz Seventh-Harmonic Balanced Diode Mixer in a Novel Circuit Configuration” Proceedings of European Wireless Technology Conference (EuWiT) 2008
- [7] M. Ingvarson, A. Ø. Olsen, J. Stake “Design and analysis of 500GHz heterostructure barrier varactor quintuplers” Proceedings of the 14th International Symposium on Space Terahertz Technology (ISSTT) 2003
- [8] Q. Xiao, Y. Duan, J.L. Hesler, T. W. Crowe “A 5mW and 5% efficiency 210GHz InP-based heterostructure barrier varactor quintupler” IEEE Microwave and Wireless Components Letters Vol 14 Issue 4 April 2004

Schottky diode based components for TeraSCREEN

Hui Wang¹, Manju Henju¹, Matthew Oldfield¹, Jeff Powell² and Byron Alderman^{1&2}

¹*Science and Technology Facilities Council, Rutherford Appleton Laboratory, UK*

²*Teratech Components Ltd, UK*

TeraSCREEN is an EU FP7 Security project aimed at developing and demonstrating in a live border control environment a safe, privacy respecting, high throughput security screening system which automatically detects and classifies potential threat objects concealed on a person. This will significantly improve both efficiency and security at border checks. TeraSCREEN will develop passive and active operation at several millimeter and submillimeter-wave frequencies to achieve this. The system developed will demonstrate, at a live control point, the safe automatic detection and classification of objects concealed under clothing, whilst respecting privacy and increasing current throughput rates. This innovative screening system will combine multi-frequency, multi-mode images taken by passive and active subsystems which will scan the subjects and obtain complementary spatial and spectral information, thus allowing for automatic threat recognition. This technology was developed for applications in Earth observation and astronomy and is now of increasing interest in ground based applications. The TeraSCREEN project will be an important demonstrator of this technology migrating into the commercial sector.

This paper will describe the development work at RAL on the 4th harmonic mixer operating at 360GHz for both active and passive subsystem, likewise the frequency multiplier sources up to 360GHz for the active subsystem. These components are all based on the Schottky diode technology. Simulation and measurement results of these components will be presented at the conference.

The TeraSCREEN project has received research funding from the European Union Seventh Framework Programme under grant agreement n° 312496

References

1. TeraSCREEN: Multi-frequency multi-mode Terahertz screening for border checks (312496) - <http://fp7-terascreen.com/>

Poster Session

papers and abstracts are given according to the order in the Program-in-Detail

1-b - THz coherent detectors: SIS

Wideband Receiver Upgrade for the Submillimeter Array

Cheuk-yu Edward Tong, Raymond Blundell, Chih-Chiang Han, Tse-Jun Chen, Wei-Chun Lu, and Ming-Jye Wang

Abstract— The Submillimeter Array (SMA), a radio interferometer of eight 6-meter telescopes on Mauna Kea, Hawaii, has embarked on a wideband system upgrade, replacing its original SIS receivers with wideband receivers, which double the instantaneous bandwidth. The new SMA receivers are based on distributed superconducting tunnel junction arrays, comprising three SIS junctions connected in series. The use of a series junction array reduces the impact of the geometrical capacitance of the SIS junctions and increases the linearity range of the receiver, both of which are important for wide IF design. We here report on the design and performance of the upgraded SMA receivers. Wideband 200 and 300 GHz receivers have been installed in all eight antennas of the Array, and they are being used for routine astronomical observations.

Index Terms—Distributed mixers, superconductor-insulator-superconductor (SIS) mixers, submillimeter receivers, ultra-wide-band receivers.

I. INTRODUCTION

THE Submillimeter Array (SMA) is a radio interferometer comprising of eight 6-meter radio telescopes on Mauna Kea, Hawaii, operated by the Smithsonian Astrophysical Observatory (SAO) in partnership with the Institute of Astronomy and Astrophysics of Academia Sinica (ASIAA), Taiwan. Since its official dedication in 2003, the SMA has been making radio astronomical observations with high spatial and spectral resolution in the atmospheric windows between 200 and 420 GHz.

The instrument suite of the SMA was conceived in the early 1990s. It was based on Double-Side-Band (DSB) mixers, and the two sidebands are separated in the digital backend, using phase switching techniques. The total bandwidth capacity of the digital correlator is 4 GHz from each sideband. In an effort to improve the throughput of the array, we decided, a few years ago, to increase its instantaneous operating bandwidth. This system upgrade calls for front-end receivers with much wider bandwidth and a much faster digital correlator. The increased bandwidth improves the total

power (or continuum) sensitivity of the instrument. Furthermore, it also increases the flexibility for spectral line observation.

The wideband instrumentation is to be supported by a wideband digital correlator, which is being developed in house, using open source FPGA boards designed by the Coalition for Astronomical Signal Processing and Electronics Research (CASPER) with inputs from a 5 GSample per second Analog-Digital Convertor. The new digital backend, the SMA Wideband Astronomical ROACH2 Machine (SWARM), will add multiple frequency slices, each of 2 GHz wide to provide full IF coverage from 4 – 12 GHz. The front-end receiver upgrade would involve the use of a new generation of superconducting receivers based on distributed superconducting tunnel junction arrays [1, 2]. In this report, we will present the design and performance of the upgraded SMA receivers.

II. SERIES-CONNECTED SIS MIXERS

The first generation of Superconductor-Insulator-Superconductor (SIS) mixer for the SMA employs a single SIS junction [3, 4]. The IF bandwidth of such a mixer is dictated by the resistor-capacitor (RC) network formed by the load resistance of the mixer and the total capacitance from the junction and parasitic capacitance introduced by the tuning network [5]. Since the load resistance is typically 50 ohm, reducing the mixer output capacitance is the key to increasing the IF bandwidth. By using N series connected junctions, the contribution of the junction capacitance is reduced by a factor of N . Furthermore, with more junctions in series, the impedance level of the mixer is also increased, reducing the need for lower impedance elements. This, in turn, reduces the parasitic capacitance of the tuning network. Therefore, although the IF bandwidth of a series-connected distributed SIS mixer does not rise linearly with N , it still offers significant improvement in bandwidth as more junctions are cascaded.

A second advantage for the series-connected mixer is the increased dynamic range. As the IF bandwidth is increased, the power output of the SIS mixer also rises. It is well known that saturation effect in SIS mixers is caused by output signal compression [6]. The wider IF bandwidth, therefore, should be accompanied by a higher power handling capacity of the mixer, which scales with N^2 . Consider an SIS mixer terminated by an ambient load ($T_{amb} \sim 300$ K) and its DSB noise temperature, T_{DSB} , is ~ 100 K. Assume further that the

Manuscript received June 1, 2014.

C.-Y. E. Tong and R. Blundell are with the Harvard-Smithsonian Center for Astrophysics, Cambridge, MA 02138, USA. (e-mail: etong@cfa.harvard.edu, rblundell@cfa.harvard.edu).

C.-C. Han, T.-J. Chen, W.-C. Lu and M.-J. Wang are with Academia Sinica Institute of Astronomy & Astrophysics, Taipei, Taiwan. (e-mail: cchan@asia.sinica.edu.tw, tjchen@asia.sinica.edu.tw, wlu@asia.sinica.edu.tw, and mingjye@asia.sinica.edu.tw)

DSB conversion gain, G_{DSB} , is 0 dB and the IF bandwidth, B_{IF} , is 20 GHz. Thus, the IF power output of the mixer is given by

$$P_{IF} = G_{DSB} * k(T_{amb} + T_{DSB})B_{IF} \quad (1)$$

Given that $P_{IF} \sim 10$ pW, the IF voltage swing around the bias point is ~ 70 μ V rms across the 50-ohm load. Since we are dealing with noise like signal in radio astronomy, the peak-to-peak voltage swing is roughly 6 times the rms value, which represents $\pm 3\sigma$ of the Gaussian distribution. At an LO frequency of 242 GHz, the width of the photon step in a single SIS junction is 1 mV, which is only ~ 2.5 times the peak-to-peak voltage swing. Clearly, mixer compression would not be negligible. That is why we have chosen to use a 3-junction array, which would improve the ratio of the photon step width to the peak-to-peak IF voltage swing to > 7 across the RF band.

The disadvantage of using a series array is the increased LO power requirement, which also scales with N^2 . At the same time, the output impedance level scales with N . As a result, devices with higher critical current density and of slightly bigger areas are desirable. A discussion of the properties of series connected SIS mixer is given in [7].

III. DISTRIBUTED TUNING IN SERIES SIS ARRAY

The wideband SIS mixer chips are fabricated in the fabrication facility of ASIAA in Taipei [8]. A photo of the distributed mixer for the new SMA 300 GHz wideband receiver is given in Fig. 1. The junctions are shown in more details in the insert. The junctions are 1.5 μ m in diameter and are spaced 8 μ m apart. The first 2 junctions are located on an island, which forms the central conductor of a coplanar waveguide (CPW) with characteristic impedance of ~ 50 -ohm. The inter-connecting CPW between the junctions add a considerable amount of inductance to the mixer circuit, such that no extra inductance is needed to tune the geometrical capacitance of the junction. In this sense, the tuning of the series-connected SIS junction array is distributed in nature.

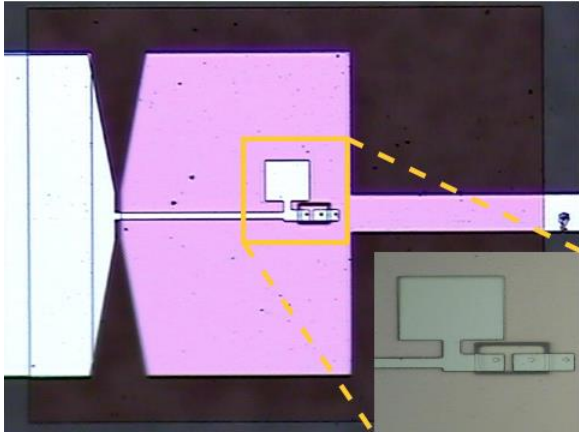


Fig. 1 Photo of a distributed mixer chip used in the upgraded SMA 300 GHz receiver. The insert shows the 3-junction series array in more details. The junctions are 1.5 μ m in diameter. Note the absence of any external tuning inductance to the junction array. The inductance is distributed in the inter-connecting lines between the junctions.

We have also found evidence of extra spreading inductance in the junction array [9]. This spreading inductance is caused by a “current crowding effect” [10] as part of the RF current bends to enter the 1.5 μ m diameter junction from the 6 - 8 μ m wide CPW. The situation is depicted in Fig. 2. Since the extra current path is incurred in a CPW, which has higher characteristics impedance compared to that of microstrip, the added spreading inductance can be quite substantial. HFSS simulation shows that the spreading inductance is as much as 15% of the inductance introduced by the CPW lines connecting a pair of series junction array.

Referring to Fig. 1, a capacitance is put in parallel to the junction array to offset the higher total inductance in the distributed 3-junction array. Located between the junction array and the quarter wave microstrip transformer, which links it to the waveguide feed point of the mixer, this added capacitor helps to mitigate the effects of the extra circuit inductance.

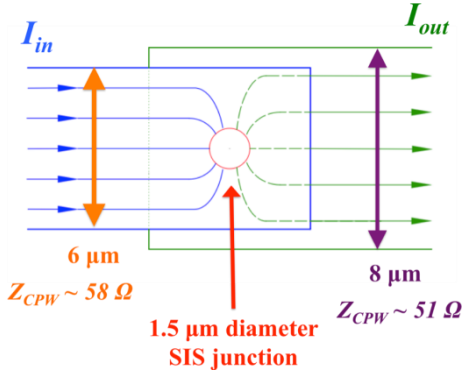


Fig. 2 Effect of “current crowding” in series connected SIS junction array. The additional RF current path introduces spreading inductance to both the input and output CPW lines to the junction.

IV. PERFORMANCE OF THE RECEIVER

The design and performance of the upgraded 200 GHz receivers for the SMA has been reported previously [7, 11]. We here focus on the performance of the 300 GHz receivers.

As stated above, the diameter of the individual SIS junction in the array is 1.5 μ m. The critical current density of the device is about 7 kA/cm². For the 3-junction array, the normal state resistance is in the range of 55 – 60 Ω , such that the ωCR product is ~ 4.5 . The total IF output capacitance, including capacitances from both the junction and the tuning circuit, is ~ 0.18 pF. The expected IF bandwidth is 17 GHz, for a 50- Ω IF load impedance [5].

The mixer is connected to a wideband isolator that provides isolation between 4 and 14 GHz [12]. Its insertion loss is < 1.2 dB, with the highest value found at the top end of the band. The isolator is followed by a low noise cryogenic amplifier, which has a typical noise temperature of 4 – 8 K over the frequency range of 4 – 16 GHz [13].

The current – voltage (I - V) characteristics of the junction array in the presence of optimal magnetic field is plotted in Fig. 3. The sub-gap leakage resistance is ~ 500 Ω , yielding a leakage resistance ratio of only 8.5. When compensated for the series resistance from the 2-point measurement setup, the gap

voltage is found to be 8.1 mV with no magnetic field and 7.9 mV when operated with optimal magnetic field around the second null. The photon step, induced by a Local Oscillator (LO) at 300 GHz, is observed to be quite flat, indicating very high output impedance. The isolator is, therefore, indispensable. The receiver power outputs at an IF of 10 GHz in response to both ambient and cold input loads are also plotted in Fig. 3. At a bias voltage of about 6.5 mV, a Y-factor of 2.51 was recorded, corresponding to a DSB receiver noise temperature of 65 K. The estimated DSB conversion loss at this setting is around 0 dB.

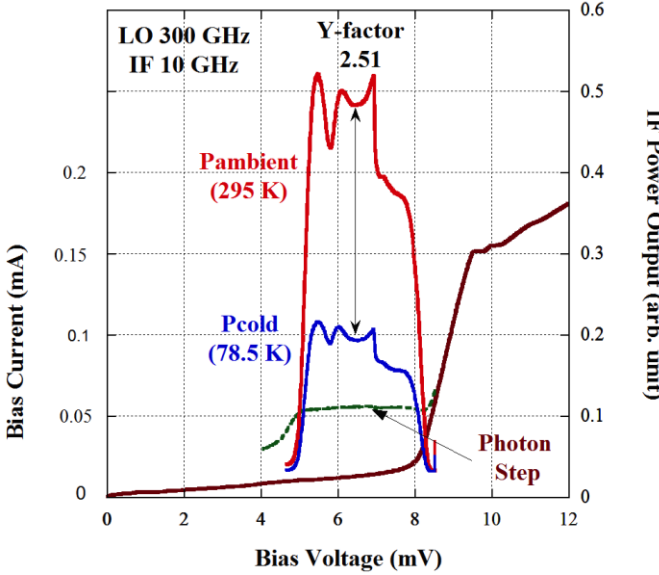


Fig. 3 Current-Voltage (I-V) and Power-Voltage (P-V) curves of SMA 300 GHz mixer (Batch SAO300-2-2 #F1-29). The I-V curve was measured with a 2-point setup, and the added series resistance to the bias circuitry is $3.2\ \Omega$. This device exhibits a sub-gap leakage resistance to normal state resistance ratio of 8.5. When driven by an LO at 300 GHz, flat photon step was observed. A Y-factor of 2.51 was recorded at a bias voltage of around 6.5 mV at an IF of 10 GHz.

The receiver noise temperature as a function of IF for a number of LO frequencies is displayed in Fig. 4. The sensitivity is quite flat for IF between 4 – 12 GHz, rising slightly above 12 GHz. This is mostly due to the higher insertion loss and poorer insertion loss of the wideband isolator. In spite of this, significant degradation of noise temperature does not set in until the IF rises close to 16 GHz. This demonstrates that the receiver presents a wide IF bandwidth as designed. The best noise temperature is obtained with LO frequencies of 300 and 324 GHz, around the center of the SMA band of 255 – 350 GHz. Sensitivity roll-off is observed towards the RF band edges but noise temperature remains below 100 K over the IF of 4 – 12 GHz IF. Note that the RF bandwidth would improve if devices with lower sub-gap leakage resistance were available, as this would improve the conversion loss at the band edges. Alternatively, a higher critical current density of the SIS array would also help. At the present current density, the expected percentage RF bandwidth is $\sim 1/\omega CR$ or about 22 % [13].

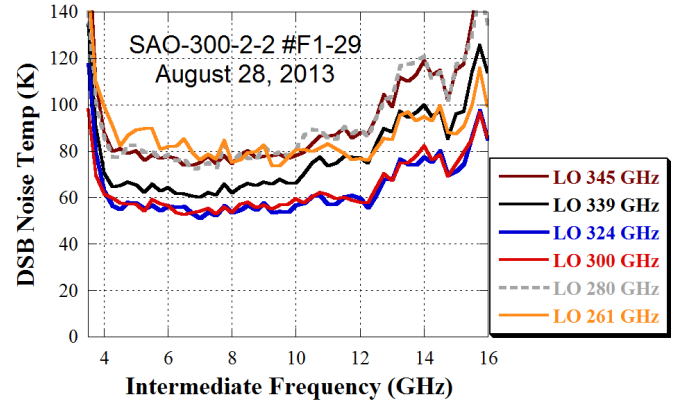


Fig. 4 Double-side-band (DSB) receiver noise temperature as a function of IF for different LO frequencies measured in the laboratory in Cambridge.

All 300 GHz SMA receivers have been upgraded with this new generation of wideband receiver in 2013, following the upgrade of the 200 GHz receivers in 2012. Both the 200 and 300 GHz receivers are being used for routine astronomical observations. Although the full capability of these new wideband receivers will not be available before the operation of the new digital backend, SWARM, SMA users can now access the higher IF using the Bandwidth Doubler feature of the SMA. Fig. 5 shows a 10 GHz wide spectrum obtained with the new receivers. In this observation, the Local Oscillator of the receiver was fixed at 337 GHz. The Bandwidth Doubler mode was used to map a 2 GHz wide spectrum from the 4-12 GHz IF to the SMA correlator in a sequential manner. Since both sidebands are recovered in the SMA correlator, one can use the new receivers to observe a pair of spectral lines that are separated by up to 27 GHz in the 300 GHz band.

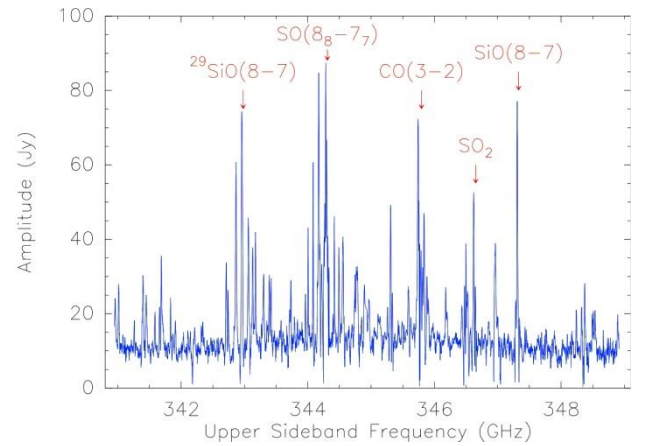


Fig. 5 Upper sideband spectrum of Orion BN/KL for a single baseline taken in a test observation in Dec. 2013. With a local oscillator frequency of 337 GHz, the 4-12 GHz portion of the receiver IF is stepped in frequency, 2 GHz at one time for processing by the SMA correlator. The four spectra are merged to produce this figure. During this observation, the weather was quite poor (~ 4 mm PWV) and the source was not very high in the sky. Integration time per 2 GHz spectrum is about 20 minutes.

V. CONCLUSION

A second generation of wideband receivers for the SMA has been commissioned. These receivers are based on a series-connected 3-junction SIS array which offers wide IF bandwidth of up to 16 GHz, and higher dynamic range to ensure good linearity for both observation and calibration. These receivers offer competitive sensitivities and they are being used in routine astronomical observations. Once the new SMA digital backend is in full operation by late 2014, these receivers will provide 4 – 12 GHz IF coverage in double-sideband operation. Future expansion of the digital backend would extend its coverage to 16 GHz.

REFERENCES

- [1] C.-Y.E. Tong, R. Blundell, K.G. Megerian, J. A. Stern, S.-K. Pan, and M. Popieszalski, "A distributed lumped-element SIS mixer with very wide instantaneous bandwidth," *IEEE Trans. Appl. Supercond.*, vol. 15, pp. 490-494, June 2005.
- [2] C.-Y. E. Tong, P.K. Grimes, A. Barbier, K. Schuster, and M.-J. Wang, "Design and performance of a 3-junction series distributed SIS mixer for wide IF applications," *IEEE Trans. Appl. Supercond.*, vol. 23, p. 1400404, June 2013.
- [3] R. Blundell, C.-Y.E. Tong, D.C. Papa, R.L. Leombruno, X. Zhang, S. Paine, J.A. Stern, H.G. LeDuc, and B. Bumble, "A wideband fixed-tuned SIS receiver for 200-GHz operation," *IEEE Trans. Microwave Theory & Tech.*, vol. 43, pp. 933-937, Apr. 1995.
- [4] C.-Y. E. Tong, R. Blundell, S. Paine, D.C. Papa, J. Kawamura, X. Zhang, J.A. Stern, and H.G. LeDuc, "Design and characterization of a 250-350 GHz fixed tuned superconductor-insulator-superconductor receiver," *IEEE Trans. Microwave Theory & Tech.*, vol. 44(9), pp. 1548-1556, Sept. 1996.
- [5] C.-Y.E. Tong, R. Blundell, K.G. Megerian, J.A. Stern, and H.G. LeDuc, "Quantum-limited mixing in a transformer-coupled SIS resonator for the 600 GHz frequency band," in *Proc. 13th Int'l. Symp. Space THz Tech.*, pp. 23-32, Harvard Univ., Cambridge, MA, pp. 23-32, Mar 2002.
- [6] M. J. Feldman and L. R. D'Addario, "Saturation of the SIS detector and the SIS mixer," *IEEE Trans. Magn.*, vol. 23, pp. 1254–1258, 1987.
- [7] C.-Y. E. Tong, P. Grimes, R. Blundell, M.-J. Wang, and T. Noguchi, "Wideband SIS receivers using series distributed SIS junction array," *IEEE Trans. THz Sci. & Tech.*, vol. 3, pp. 428-432, July 2013.
- [8] M.-J.Wang, H.W. Cheng, Y. H. Ho, and C. C. Chi, "Low noise Nb-based SIS mixer for sub-millimeter wave detection," *J. Phys. Chem. Solids*, vol. 62, p. 1731, 2001.
- [9] C.-Y. Tong, L.-Z. Zeng, M.-J. Wang, C.-C. Han, T.-J. Chen, and W.-C Lu, "Effect of spreading inductance on an SIS mixer based on series-connected SIS junction array," presented at the *14th Int. Superconductive Electronics Conf.*, paper PD-13, Cambridge, MA, July 2013.
- [10] J. Zmuidzinas, H.G. LeDuc, J.A. Stern, and S.R. Cypher, "Two-junction tuning circuits for submillimeter SIS mixers," *IEEE Trans. Microwave Theory & Tech.*, vol. 42, pp. 698 – 706, April 1996.
- [11] C.-C. Han, M.-J. Wang, T.-J. Chen, W.-C. Lu, C.-Y.E. Tong, "A 220 GHz low noise superconducting receiver with wide instantaneous operating bandwidth," *Microwave Conference Proceedings (APMC), 2012 Asia-Pacific*, pp. 427-429, Dec. 2012.
- [12] Cryogenic isolator model, CWJ1015KIBZFM, from Quinstar Corp., USA.
- [13] Cryogenic low noise amplifier model, LNF-LNC4_16A, from Low Noise Factory, Sweden.
- [14] A.R. Kerr, "Some fundamental and practical limits on broadband matching to capacitive devices, and the implications for SIS mixer design," *IEEE Trans. Microwave Theory & Tech.* vol. 43, pp. 2-13, Jan. 1995.

First mixer prototype results for Band L (455-495 GHz) of CHAI

Patrick Pütz, S.Widdig^{*}, S.Fathi^{*}, J.W.Kooi[◊], D.Russel[‡], M.Schultz^{*}, M.P.Westig^{*}, K. Jacobs^{*}, U.U. Graf^{*}, C.E.Honingh^{*}, J.Stutzki^{*}

^{*}KOSMA, I. Physikalisches Institut, Universitaet zu Koeln, Zuelpicher Strasse 77, 50937 Koeln, Germany

[◊]California Institute of Technology, 1200 E California Blvd, Pasadena, CA 91125, United States

[‡]Jet Propulsion Laboratory, 4800 Oak Grove Dr, Pasadena, CA 91011, United States

Email: swiddig@ph1.uni-koeln.de, fathi@ph1.uni-koeln.de

The Cerro-Chajnantor-Atacama-Telescope (CCAT) Heterodyne Array Instrument (CHAI) is a focal plane instrument containing 2 cartridges of heterodyne mixers at 2 frequency bands (Band L and Band H) that will be developed as a mapping instrument for the future CCAT telescope. Each of sub-arrays will consist of 64 (goal 128) pixels. In the current baseline design the arrays will be populated with balanced waveguide SIS mixers with a lateral pixel-footprint of 10mm x 10mm.

We will report measurements of a prototype mixer for 455-495GHz that fits the array footprint, with a balanced Si-chip that contains a RF 90°-hybrid and the 2 SIS mixers, integrated in one block with an IF Wilkinson power combiner and 2 bias T's on an alumina substrate. To suppress the Cooper pair tunneling in the SIS mixers, small (1mm³) permanent magnets are implemented. The GPPO IF mixer output connector is connected via a short coaxial cable with the GPPO input of a miniature (13.7 x 5 x 22.4 mm³) LNA based on SiGe MMIC technology with a bandwidth of 1-8 GHz and a noise temperature of approximately 8K, at a dissipation of 10mW of DC-power.

Measured noise temperatures, using a 92% transmission HDPE windows and a Gunn-multiplier local oscillator source, are around 100K at an operating temperature of 4.5K over an IF bandwidth of 1-6 GHz. We will present a detailed evaluation of the usefulness of this mixer as an array pixel

Characterization of the IF output impedance of SIS mixers

P. Serres, A. Navarrini, Y. Bortolotti and O. Garnier

Abstract— We report on the development of a measurement setup to characterize the IF output impedance of a SIS mixer. The measurement method and the details of the test setup are described.

Index Terms—SIS mixer, IF impedance, DSB and SSB tuning, VNA measurements.

I. INTRODUCTION

MODERN low noise Superconductor-Insulator-Superconductor (SIS) receivers for mm- and sub-mm radio astronomy operate over very wide instantaneous Intermediate Frequency (IF) bands. For example, the current generation of the IRAM Plateau de Bure Interferometer (PdBI) mm-wave dual polarization receivers is being upgraded for the NOEMA (Northern Extended Millimeter Array) project [1] from backshort-tuned Single Side Band (SSB) mixers delivering one 4 GHz wide IF band (across 4-8 GHz) [2]-[3] to Sideband Separating (2SB) mixers delivering two ~8 GHz wide IF bands (across ~4-12 GHz) [4]-[5].

A cryogenic isolator is often used at the single IF output of a SSB mixer (or at each of the two IF outputs of the 2SB mixer) to decouple the SIS mixer IF output impedance from the input impedance of the following IF cryogenic low noise amplifier (LNA): by employing an IF isolator matched to $50\ \Omega$ in a SSB receiver chain, a constant $50\ \Omega$ impedance is presented at the LNA input independently of the output impedance of the SIS mixer and, at the same time, a constant $50\ \Omega$ impedance is presented at the mixer output independently of the input impedance of the LNA. This allows the LNA, which is typically optimized to deliver minimum noise on a $50\ \Omega$ input, to operate at its optimum input impedance and the SIS mixer to be optimized to provide best receiver performance (simulated using Tucker's theory of quasi-particle mixing [6]) when its IF output is connected to a $50\ \Omega$ load. In short, the optimization of the performance of a SIS receiver chain can be optimized more easily by decoupling mixer and LNA through an isolator.

However, isolators have large mechanical size and non-negligible insertion losses which contribute to increase the receiver noise temperature. Removing the isolator from the

chain is essential for the development of closely packed receivers in a focal plane array, for which a miniaturized footprint on their RF and IF sections is required. Moreover, the direct connection of SIS mixer with cryogenic amplifier through a suitable network, offers potential for improvement of the receiver performance.

The IF output impedance of a SIS mixer, Z_{IF} , depends on several parameters, among which the RF embedding impedance of the SIS junctions, the bias condition, and the Local Oscillator (LO) pumping level. Such IF output impedance plays an important role in the performance of a receiver chain and must be known accurately to allow optimization of the receiver performance across its RF and IF bands. This is particularly true when the SIS mixer and following IF low noise amplifier are directly connected without isolator. Therefore, the design of modern wide IF band SIS receiver can strongly benefit from experimental data on the SIS mixer IF output impedance, which can be used for verification and optimization of the following cryogenic IF receiver section.

Here, we describe a measurement system to characterize the IF impedance of SIS mixers, present experimental results, and compare electromagnetic simulations combined with three-port Tucker's theory of quasi-particle SIS mixing with laboratory data. The SIS junction, biased at three different voltages of its unpumped IV characteristic, is used to obtain three known calibration impedances that allowed calibrating the measurement up to the on-chip SIS junction plane (including the SIS junction specific capacitance).

II. TEST SETUP OF SIS MIXER IF IMPEDANCE WITH A VNA

A. Synoptic diagram of measurement setup

A synoptic diagram of the measurement setup, utilizing a Vector Network Analyzer (VNA) and an SIS mixer cooled at 4 K inside a cryostat, is shown in Fig. 1. The synoptic shows the reference measurement plane situated at the on-chip SIS junction. The commercial VNA in its base configuration (Agilent PNAx N5244A 43.5 GHz) would not have enough dynamic range to measure the reflection coefficient of the SIS mixer at IF frequencies, Γ_{IF} (or equivalently Z_{IF}). Indeed, the incident power at the VNA output must be very low, of order -85 dBm, to avoid SIS mixer saturation. If the base VNA configuration were used, a coupler internal to the VNA system would replace the combination of circulator and low noise amplifier (LNA) shown in Fig. 1: the coupler would inject a fraction of the power reflected back from the mixer into the

All authors are with IRAM (Institut de RadioAstronomie Millimétrique), 300 rue de la piscine, 38406 Saint Martin d'Hères, France (P. Serres, phone :+33476824915 ; fax : +33476515938 ; e-mail: serres@iram.fr).

return-wave VNA receiver. However, the combination of the high-noise of the return-wave VNA receiver with the loss of power due the internal coupler would strongly reduce the detectable signal. The combination of circulator plus amplifier allows at the same time to couple the required power to the return-wave VNA receiver with minimum loss while masking its noise. The bandpass filter situated after the LNA reduces the noise bandwidth and suppresses higher harmonics.

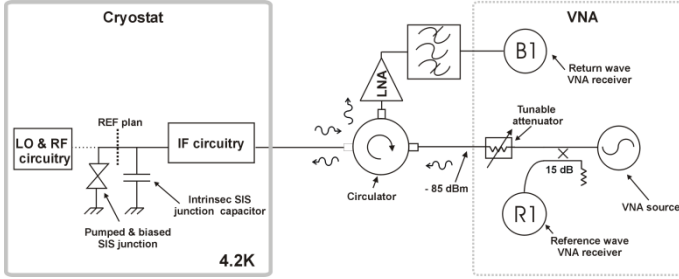


Fig. 1. Synoptic of SIS mixer IF impedance measurement system. The cryostat and the VNA are shown on the left and on the right sides, respectively. In the middle, the paths of the incident and backward waves from the VNA, as well as the connections of the circulator with the cryostat and the VNA are shown.

B. Measurement calibration

One of the main challenges in vector network measurements at cryogenic temperatures is the calibration. To avoid calibration uncertainties related to changes of electrical lengths and of impedance discontinuities upon cooling, we have used the properties of the IV characteristic of the SIS junction at 4.2 K to generate the necessary calibration standards: the junction was biased in three different regions of its IV curve to obtain impedances close to the three classical SOLT standards (see Fig. 2): Open Circuit (OC), Short Circuit (SC) and Load. In choosing the SIS junction as calibration kit, the measurement reference plane is necessarily located at the SIS junction itself. Thus, the calibration procedure calibrates out all IF circuitry of the measurement setup (IF coaxial cables, SIS mixer external IF circuit, bias-T etc.) including the on-chip SIS mixer intrinsic capacitance and inductance. This procedure does not require to thermally cycle and open the cryostat to locate and measure three different calibration standards.

C. Backshort-tuned SSB SIS mixer

We carried out measurements across the 4-8 GHz IF band of the IRAM 3 mm band backshort-tuned Single Side Band (SSB) SIS mixers currently installed on the PdBI antennas. The mixer backshort allows to reject the image side band (typical gain ratios $G_I/G_S \sim 10$ dB), thus reducing the contribution of the atmospheric noise in the image band and improving the system sensitivity during spectroscopic observations.

The SIS mixer chip used in the measurements is based on two junctions in series, with an equivalent gap voltage at ~ 5.6 mV. The electrical distance between the two junctions is very small compared to the wavelength and are considered to be located on the same plane (the reference plane).

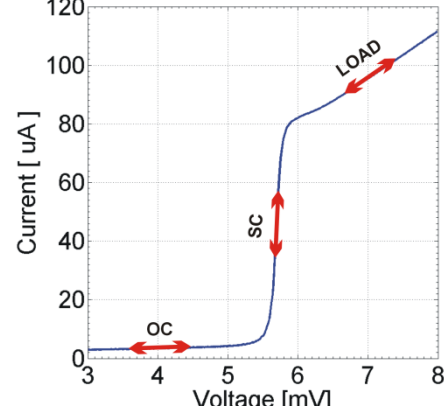


Fig. 2. In blue, the I(V) curve of the SIS junction situated on the mixer chip. The red double arrows show the three different impedance defining the three SOLT (OC, SC, LOAD) calibration standard.

D. SIS IF impedance measurement bench

The IRAM test setup for characterizing the IF impedance of the SIS mixer is shown in Figs. 3 and 4. The mixer is placed inside a laboratory wet cryostat (from Infrared Lab Inc.) in thermal contact with the 4.2 K stage cooled by liquid helium.

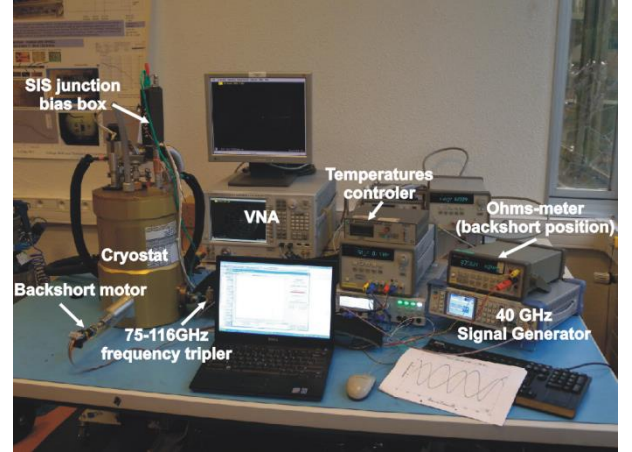


Fig. 3. Overview of the measurement bench showing the VNA, the cryostat to cool down the SIS mixer at the physical temperature of 4.2 K, the backshort motor to tune such SSB mixer in LSB or USB, the SIS junction bias box, the SIS mixer Local Oscillator which is realized by a 40 GHz signal generator combined with tripler and WR10 mechanical attenuator. The system is fully controlled with a computer.

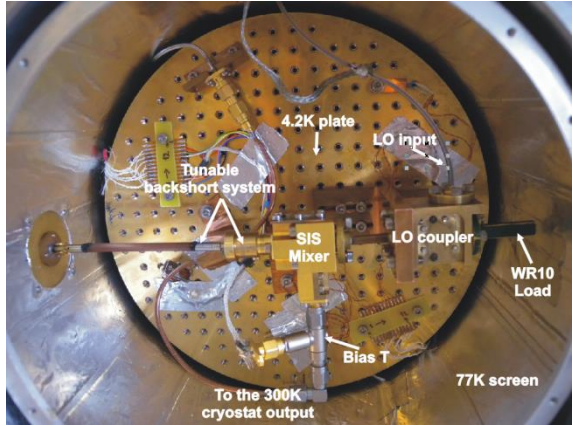


Fig. 4. The cryostat component arrangement is shown. The SIS mixer, located at its center, has a waveguide input connected to a waveguide LO coupler, terminated to a WR10 waveguide load on the signal path, through a WR10 stainless steel waveguide. A WR10 stainless steel waveguide allows to inject the LO signal generated outside the cryostat. The backshort mechanism is connected to a fiberglass rod and controlled from outside the cryostat. The IF SMA output of the SIS mixer is connected to the cryostat IF output through coaxial cables (copper and stainless steel types) through a commercial bias-T.

REFERENCES

- [1] *The Northern Extended Millimeter Array (NOEMA)*. IRAM web pages: <http://www.iram.fr/GENERAL/NOEMA-Phase-A.pdf>
- [2] D. Maier, S. Devoluy, M. Schicke, K. F. Schuster, "230 GHz SSB SIS mixer for band 3 of the new generation receivers for the Plateau de Bure interferometer," *16th International Symposium on Space Terahertz Technology*, pp. 33-36, Chalmers, Sweden, May 2-4, 2005.
- [3] A. Navarrini, A. L. Fontana, D. Maier, P. Serres, D. Billon-Pierron, "Superconductor-Insulator-Superconductor Mixers for the 2 mm Band (129-174 GHz)," *Journal of Infrared, Millimeter, and Terahertz Waves*, Vol. 35, Issue 6-7, pp. 536-562, 2014.
- [4] D. Maier, D. Billon-Pierron, J. Reverdy, M. Schicke, "100 GHz Sideband Separating Mixer with Wide IF band: First results," *Proceedings of the 19th International Symposium on Space Terahertz Technology*, Groningen, The Netherlands, April 28-30, 2008, p.93-96.
- [5] D. Maier, J. Reverdy, D. Billon-Pierron, A. Barber, "Upgrade of EMIR's Band 3 and Band 4 Mixers for the IRAM 30 m Telescope," *IEEE Trans. THz Sci. Tech.*, Vol. 2, No 2, March 2012, p. 215-221.
- [6] J.R. Tucker, "Quantum limited detection in tunnel junction mixers", *IEEE J. Quantum Electron*, 6, p. 1234-1258, 1979.
- [7] J.R. Tucker and M.J. Feldman, "Quantum detection at millimetre wavelengths", *Rev. Mod. Phys.*, 57, 1055-1113, 1985.

SIS Tunnel Junction's Specific Capacitance Direct Measurement

Parisa Yadranjee Aghdam, Hawal Rashid, Vincent Desmaris, Alexey Pavolotsky, Victor Belitsky

Abstract—The need for operating frequencies well into THz region with higher sensitivity and wider bandwidth pushes superconductor-insulator-superconductor (SIS) technology towards junctions with more transparent barrier and higher current densities. Obtaining accurate knowledge of the specific capacitance, which is related to the transparency of the junctions, leads to a precise design of the tuning circuitry. Previously, characterization of the SIS junction's specific capacitance involved complex measurements providing data relying on various model fitting. Herein, we present the characterization of the specific capacitance by directly measuring the impedance of the SIS tunnel junction at microwave frequencies (~3 GHz).

Index Terms—SIS junction, S-parameter measurements, specific capacitance.

I. INTRODUCTION

Superconductor-Insulator-Superconductor (SIS) mixers have been the workhorse in radio astronomy receivers. SIS mixers with Nb/Al-AlO_x/Nb trilayer are commonly recognized for their lowest noise performance at operating frequencies below Nb gap frequency (c.a. 700GHz) [1]. An SIS junction is characterized by its intrinsic capacitance (C) being in parallel with the nonlinear tunnel resistance (R). The linear part of R in which the junction is biased above the gap is called the normal resistance (R_n). The R_nA product where A is the SIS junction area, defines the SIS junction Q-factor value and if it is reduced the junction operation band could be increased [2]. Additionally, the R_nA value is a measure of the transparency of the barrier; the lower the R_nA value the higher the critical current density of the junction [3]. Since the tunnel barrier in the Nb/Al-AlO_x/Nb trilayer is formed by the thermal oxidation of the Al layer, the non-uniformity of the insulator's thickness becomes more significant at thinner tunnel barriers. Therefore, at very low barrier thicknesses, the junction quality degrades which manifests itself in an increase of the sub-gap region's resistance and additional shot noise [4]. Since it is neither possible to uniquely define a uniform barrier thickness, nor assign a relative permittivity (ϵ_r) to the barrier's insulator (AlO_x), the junction capacitance is determined as a function of R_nA product. Its value can be measured from the DC IV characteristics of the junction and using prior knowledge of the junction area. Thus, the specific capacitance (C/A) is

semi-empirically predicted to be inversely proportional to R_nA [2]. However, experiments have shown that at very low barrier thicknesses, the specific capacitance deviates from estimated values. Furthermore, depending on the trilayer deposition techniques, inconsistent values of specific capacitance have been reported. Therefore, there is a clear demand for the method to accurately measure the capacitance.

So far, the most commonly used methods to estimate the specific capacitance were based on analysis of Fiske steps [5], SQUID structures [6] or McCumber parameter [7]. In these methods, the capacitance is calculated by indirect measurement of its effects, e.g. resonance. Thus, the estimated value is accompanied with high uncertainty levels that depend not only on the accuracy of the aforementioned measurements, but also on the assumptions made in the employed models.

In another method, escape rate from the tilted washboard potential is studied while microwave signal is applied to the junction [8]. In this method, aka time-resolved measurement, quite high accuracy is reported. However, for the SIS junctions with R_nA in the range of interest, this calls for measurements at 100 GHz and above thus technically challenging.

In this paper, we present a method for characterization of the specific capacitance, which uses S-parameters direct measurements and analysis of the junction. Since on practice, the impedance of the junction is often very small compared to the 50 Ω impedance of a microwave measurement system and stray impedances, the reflection coefficient from the junction is rather masked by a very large mismatch. However, nowadays, the progress in the measurement equipment and calibration techniques allows this type of measurements to be performed at satisfactory accuracy level. In this paper, the measurement and calibration method is discussed and initial results are presented.

II. JUNCTION FABRICATION AND DC CHARACTERIZATION

The Nb/Al-AlO_x/Nb SIS junctions were fabricated in-house [9] with R_nA product of 30 Ω·μm². A superconducting microstripline of 50 Ω on a high-resistivity Si substrate mounted into a fixture, connects the junction to the SMA connector. The junctions with various sizes were fabricated, from which the resulting R_nA value and device areas were estimated. From the semi-empirical relation (1) and (2), the approximate value of the specific capacitance (C_s) and the junction capacitance (C) can be predicted.

$$C_s = [0.3 / \ln(R_nA)] \quad (1)$$

$$C = C_s A \quad (2)$$

Manuscript received June 13, 2014. The authors are with the Group for Advanced Receiver Development (GARD), Chalmers University of Technology, Gothenburg, Sweden (e-mail: parisa.aghdam@chalmers.se).

III. ONE-PORT MEASUREMENTS

A voltage biased SIS junction equivalent circuit is represented as a resistance (R) in parallel with the junction capacitance (C). Accordingly, the admittance of the junction can be shown as in (3). The S-parameter (S_{11}) can be measured with a Vector Network Analyzer (VNA). The S_{11} is now converted to Y_{11} , see (4).

$$Y_{11} = [1/R + jC\omega] \quad (3)$$

$$Y_{11} = Y_0[(1 - S_{11}) / (1 + S_{11})] \quad (4)$$

IV. MEASUREMENT SETUP

The first challenge in the measurement of the SIS junction's impedance is the calibration. The temperature gradient through long stainless steel cables would alter the length and propagation characteristics of the cables. Consequently, a de-embedding method on top of the ambient temperature calibration is required to exclude the aforementioned effects.

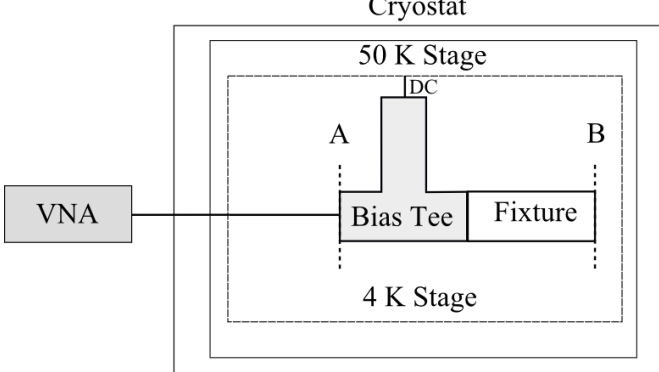


Fig. 1. Cryogenic measurement setup with two thermal stages. A) Room-temperature calibration plane. B) The DUT's reference plane

V. CALIBRATION

Amongst calibration methods for one-port setups, the Short-Open-Load (SOL) can calibrate out the unwanted effects and move the reference plane of the measurements to the DUT's plane. However, this requires three cooling cycles in addition to the DUT measurement. Herein, we have improved time efficiency by an insignificant compromise of the calibration accuracy. In this calibration method [10], short-open-load calibration is performed at room temperature at the A plane shown in Fig. 1. A short circuit standard, which replicates the DUT geometry is fabricated by removing the AlO_x layer, the top and bottom electrodes are shortened. This short circuit calibration unit is cooled down to 4K. Exploiting the Direct Fixture Compensation (DFC) feature of the Rhode & Schwarz ZVA40, the measurements reference plane is moved to the DUT's. Also, it should be noted that this calibration method, which uses DFC, is considered to have decent accuracy only if the setup is lossless.

VI. MEASUREMENT RESULTS

At the first iteration of the measurements, thin film capacitors with known capacitance values were measured to assess the accuracy of the measurements. Later, an SIS junction with the estimated capacitance of $\sim 0.9 \text{ pF}$ was measured, see Fig. 2.

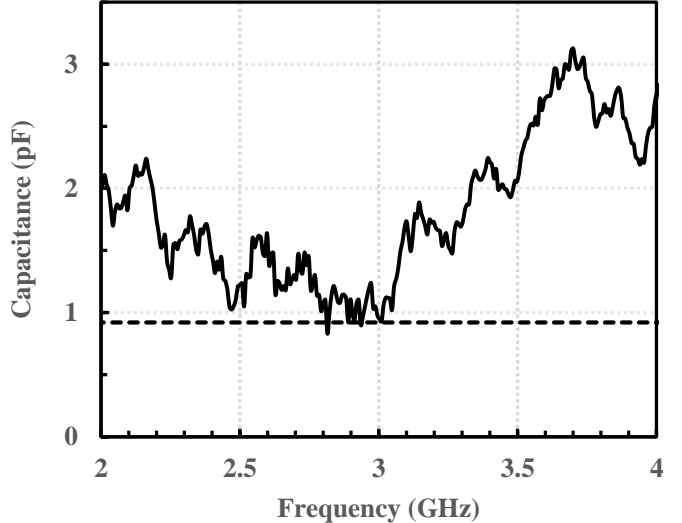


Fig. 2. Capacitance of a SIS junction (solid line) and its estimated value (dashed line) shows a good agreement in the middle of the band.

VII. CONCLUSION

In this paper we have proposed a new measurement method for the specific capacitance of SIS junction. Developing such measurement method for a complex device parameter such as SIS junctions' specific capacitance requires extensive studies and comparison of the measurements and models. Then, the measurement uncertainties can be approximated and the device parameter can be determined. The uncertainties of this measurement method can mainly stem from the losses. This can be improved by employing new techniques which are not dependent on using terminated lossless transmission line definition for input impedance.

REFERENCES

- [1] B. Billade, A. Pavolotsky, V. Belitsky, "An SIS Mixer With DSB Noise Temperature at 163 – 211 GHz Band," vol. 3, no. 4, pp. 416–421, 2013.
- [2] V. Belitsky, S. W. Jacobsson, S. A. Kovtonjuk, E. L. Koliberg, and A. B. Ermakov, "100 GHz Mixer with Vertically Integrated (stacked) SIS Junction Array," *Int. J. Infrared Millimeter Waves*, vol. 14, no. 5, pp. 949–957, 1993.
- [3] J. A. Stern and H. G. LeDuc, "Characterization of NbN films and tunnel junctions," *IEEE Trans. Magn.*, vol. 27, no. 2, pp. 3196–3199, Mar. 1991.
- [4] R. Teipen, "Influence Of Junction-Quality And Current Density On HIFI Band 2 Mixer Performance," *Proc. 14th Int. Symp. Space THz Technol.*, 2003.
- [5] D. D. Coon and M. D. Fiske, "Josephson ac and Step Structure in the Supercurrent Tunneling Characteristic," *Phys. Rev.*, vol. 138, no. 3A, pp. A744–A746, May 1965.
- [6] F. Deppe, "Determination of the capacitance of nm scale Josephson junctions," *J. Appl. Phys.*, vol. 95, no. 5, p. 2607, Feb. 2004.
- [7] H. H. Zappe, "Minimum current and related topics in Josephson tunnel junction devices," *J. Appl. Phys.*, vol. 44, no. 3, p. 1371, Oct. 1973.
- [8] G. Sun, J. Chen, Z. Ji, W. Xu, L. Kang, P. Wu, N. Dong, G. Mao, Y. Yu, and D. Xing, "Time-resolved measurement of capacitance in a Josephson tunnel junction," *Appl. Phys. Lett.*, vol. 89, no. 8, p. 082516, 2006.
- [9] A. B. Pavolotsky, D. Dochev, and V. Belitsky, "Aging- and annealing-induced variations in Nb/Al-AlO_x/Nb tunnel junction properties," *J. Appl. Phys.*, vol. 109, no. 2, p. 024502, 2011.
- [10] H. Rashid, D. Meledin, V. Desmaris, A. Pavolotsky, and V. Belitsky, "Superconducting 4.8 GHz Hybrid Assembly for 2SB Cryogenic THz Receivers," *Int. Symp. Sp. Terahertz Technol.*, 2013.

Image Rejection Ratio of 2SB SIS Receivers

A.V. Khudchenko^{1*}, R. Hesper², A.M. Baryshev^{1,2}, F.P. Mena³, J. Barkhof²

¹*Netherlands Institute for Space Research, Groningen, The Netherlands*

²*NOVA/Kapteyn Astronomical Institute, University of Groningen, The Netherlands*

³*Electrical Engineering Department, Universidad de Chile, Santiago, Chile*

Email: A.Khudchenko@sron.nl

A number of sub-mm sideband-separating (2SB) SIS (superconductor-insulator-superconductor) receivers have been developed in the past few years [1-6]. ALMA Bands 3 to 8 are equipped with receivers of this type. Image Rejection Ratio (IRR) is one of the key parameters of any 2SB mixer. Achieving IRR better than 10dB in total RF band is a challenging technical problem [1-4].

We have developed a 2SB SIS receiver for the frequency range 600-720 GHz (ALMA Band 9) [5] and found that IRR dependence on frequency is strongly determined by standing waves in the RF waveguide structure, which are caused by reflections from the SIS mixers and the RF absorption load. Analyzing results of different 2SB receivers [2-5] we find similar periodic structures in the IRR pattern.

Reduction of these standing waves, without modifying the RF and IF hybrids and SIS mixers, leads to significant improvement of IRR level. In this report we present an effective method to estimate the standing wave amplitudes in an operating receiver using the SIS junction properties. Moreover, we describe a mechanism of standing wave contribution to the final IRR. In addition, an investigation concerning IRR pattern in the ALMA Band 5 receiver will be presented.

References

1. B. Billade, O. Nyström, D. Meledin, E. Sundin, I. Lapkin, M. Fredrixon, V. Desmaris, H. Rashid, M. Strandberg, S.-E. Ferm, A. Pavolotsky and V. Belitsky, "Performance of the First ALMA Band 5 Production Cartridge", *IEEE Transactions on Terahertz Science and Technology*, 2 (2), pp. 208-214, 2012
2. A. R. Kerr, S.-K. Pan, S. M. X. Claude, P. Dindo, A. W. Lichtenberger, and E. F. Lauria, "Development of the ALMA-North America Sideband-Separating SIS Mixers", *Microwave Symposium Digest (IMS), IEEE MTT-S International*, pp. 1-4, 2013
3. D. Maier, J. Reverdy, D. Billon-Pierron, A. Barbier, "Upgrade of EMIR's Band 3 and Band 4 Mixers for the IRAM 30 m Telescope", *IEEE Transactions on Terahertz Science and Technology*, 2 (2), pp. 215 – 221, 2012
4. Y. Sekimoto, Y. Iizuka, N. Satou, T. Ito, K. Kumagai, M. Kamikura, M. Naruse, W. L. Shan, "Development of ALMA Band 8 (385-500 GHz) Cartridge", *proceedings of the 19th International Symposium on Space Terahertz Technology*, pp. 253-257, 2008
5. A. Khudchenko, R. Hesper, A. Baryshev, G. Gerlofma, P. Mena, T. Zijlstra, T. M. Klapwijk, J. W. Kooi, M. Spaans, "First Results of the Sideband-Separating Mixer for ALMA Band 9 Upgrade", *proceedings of the 21th International Symposium on Space Terahertz Technology*, 2011
6. F. P. Mena, J. W. Kooi, A. M. Baryshev, C. F. J. Lodewijk, R. Hesper, G. Gerlofsma, T. M. Klapwijk, and W. Wild, "A Sideband-separating Heterodyne Receiver for the 600–720 GHz Band", *IEEE Trans. Microwave Theory and Techniques.*, 59(1), pp. 166-177, 2011.

Improved Quadrature RF Hybrid for 2SB and Balanced THz Receivers

Hawal Rashid, Denis Meledin, Vincent Desmaris and Victor Belitsky

Abstract— We present the design and implementation of two quadrature waveguide hybrids at mm-wave frequencies with improved amplitude and phase imbalance. The measured performance of the hybrids show good agreements, with amplitude imbalance of ± 0.15 dB and a phase imbalance of ± 2.5 degrees over the 166-208 GHz frequency range.

Index Terms— Waveguide hybrid, Millimeter and sub-millimeter component, THz component, Directional coupler

I. INTRODUCTION

In recent years, 2SB and balanced receivers have proved to be a favorable option for Terahertz frontend providing suppression of the sideband noise or the LO AM noise [1-3]. Correspondingly, the performance and the design of quadrature RF hybrids has become of high relevance. The amplitude and phase imbalance of the 90° RF waveguide hybrid contribute to the degradation of the sideband rejection and noise suppression [4]. It is therefore important to minimize the imbalance of the RF hybrid for achieving ultimate performance.

The two most often used waveguide hybrids are probably the periodical and synchronous branch waveguide directional couplers. For THz frequencies, the periodical branch waveguide hybrid is the most feasible topology due to its ease of fabrication. One of the major drawbacks of the branch waveguide hybrids is that it exhibits the worst amplitude imbalance at the design center frequency, which further increases as the operational bandwidth is increased.

A typical design condition of a waveguide directional coupler is a maximized directivity / isolation. As suggested in [5], by relaxing the standard condition for maximum isolation, the classical layout of the hybrids can be modified such that interleaved ripples are introduced into S21 and S31 (cf. Fig.1 & 2), thus yielding minimum amplitude imbalance within the operating frequency band. Such a modified hybrid is a trade-off between the controllably degraded return loss and the improved amplitude imbalance.

In this paper, we present two hybrid designs, periodical and synchronous, based on the approach suggested in [5]

II. HYBRIDS DESIGN

The periodical branch waveguide hybrid design adopts the topology presented in [5] (Fig. 1).

The synchronous branch waveguide directional coupler consists of two four-branch 8.5 dB synchronous couplers,

which are cascaded with a connecting quarter wavelength impedance-mismatched waveguide (Fig. 2). The hybrids were designed to operate in frequency band 166-208 GHz. This operation band was selected in order to measure the hybrid performance with existing in-house Vector Network Analyzer (VNA) extension modules, which operate from 140 GHz to 220 GHz.

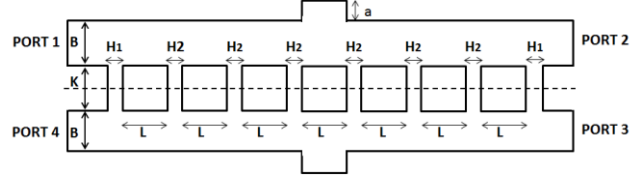


Fig.1. Cross section of the periodical eight branch waveguide hybrid in [5]. The dashed line shows the symmetry plane.

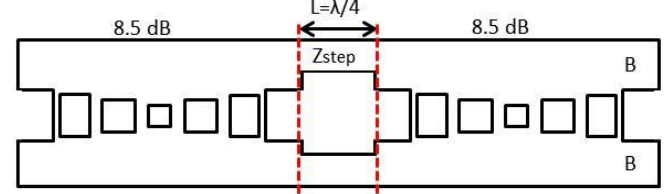


Fig.2.Cross section of two four branch 8.5 dB synchronous directional coupler with impedance mismatch at its geometrical center, which is marked with red dashed lines. The port configuration is the same as Fig.1.

III. MEASUREMENTS

The waveguide hybrid was measured with Agilent two port Vector Network Analyzer (VNA) with OML 140-220 GHz extension transmitter and receiver modules. The VNA was calibrated with the OML standard TRL waveguide calibration kit. Subsequently, Ports 1 and 3 (coupled) were connected and measured while the remaining ports are terminated. Finally, Ports 1 and 4 were connected and measured while the through and coupled ports were terminated. In order to account for the conductive loss in the leading waveguides, a two port fixture with the exact shape and length as the hybrid through path was fabricated. The S-parameters from the fixture were measured and used to de-embed the losses (0.015 dB/mm) of the leading waveguides (between the calibration planes at the output of the extension modules to the input of the hybrid structure) from the measured hybrid S-parameters. The insertion loss of the hybrid itself is approximately 0.23 dB [5].

The time gated [6] performance of the synchronous coupler shown in Fig. 3 does not agree as well with simulations due to large dimensions offsets caused by malfunction of the CNC milling machine. The depth difference between the main waveguide (**B**) and branch guide (**H**) (refereed as step) was approximately 28 μm , while the **K** and **H** values was off by approximately 10 μm . Figure 4 show the measured

All authors are with the Group of Advanced Receiver Development (GARD) at Chalmers University of Technology, Gothenburg, Sweden. (email:Hawal@chalmers.se)

performance and EM simulations for different steps. The red solid line in Fig. 4 includes the average offset in the \mathbf{K} and \mathbf{H} values of 10 μm together with the step length of 28 μm . With these values, we were able to explain the reduced agreement between simulation and measurement.

Fig. 5 and 6 show the simulated and time gated [7] measurement performance of the periodical branch waveguide hybrid manufactured with the CNC milling machine after necessary service and repair. The measured performance of the periodical hybrid demonstrates excellent agreement with the simulations.

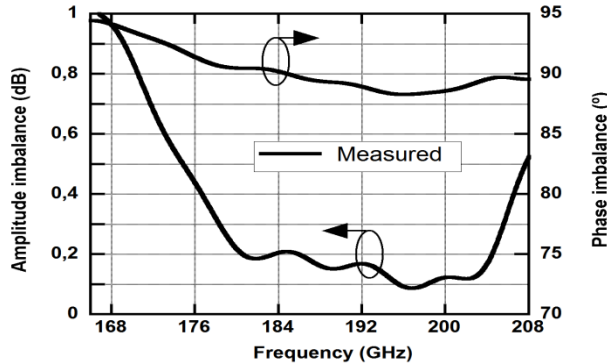


Fig. 3. Measured amplitude and phase imbalance of the synchronous hybrid shown in Fig. 2.

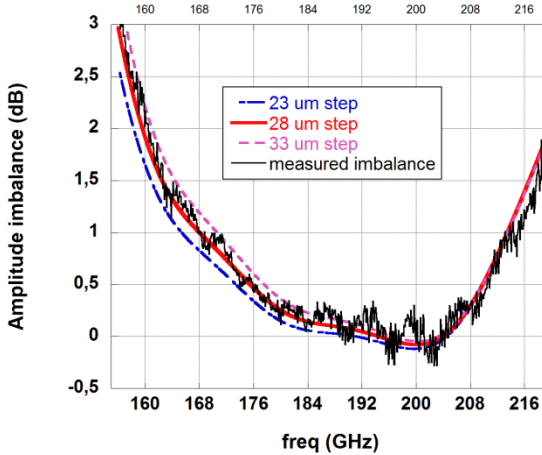


Fig. 4. Simulated performance for different step length lengths.

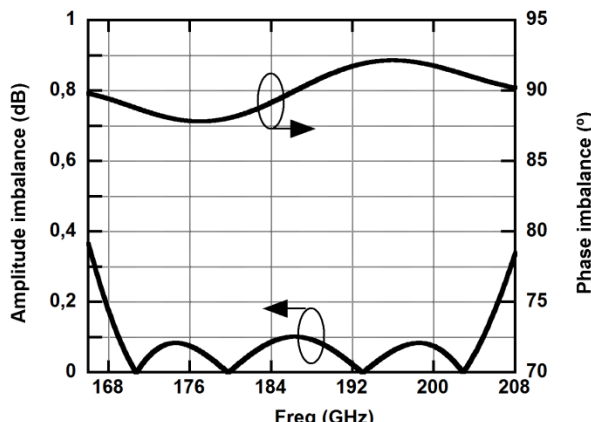


Fig. 5. Simulated through and coupled performance of the modified periodical waveguide hybrid [5].

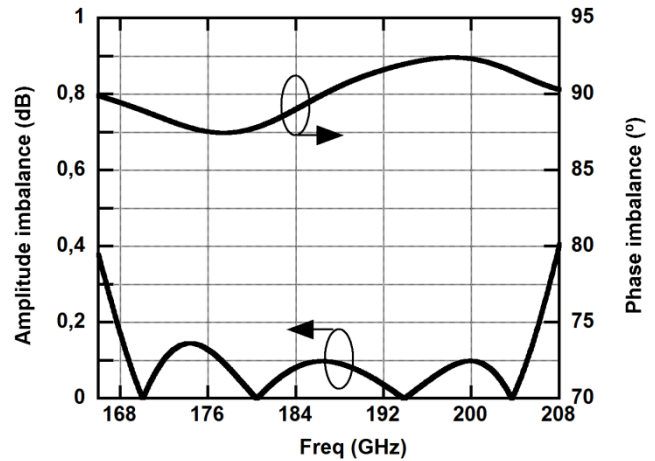


Fig. 6. Measured through and coupled performance of the modified periodical waveguide hybrid [5].

IV. CONCLUSIONS

We presented two implementation of the novel design concept for the realization of 90° synchronous waveguide hybrid for 166 – 208 GHz band. The measured performance of the periodical hybrid show excellent agreement with simulation, with amplitude imbalance of ± 0.15 dB and a phase imbalance of ± 2.5 degrees over the 166-208 GHz frequency range.

ACKNOWLEDGMENT

The authors would like to thank Alexey Pavolotsky for fruitful discussions. The authors would also like to thank Sven-Erik Ferm and Mathias Fredrixon for the hybrid fabrication.

REFERENCES

- [1] V. Belitsky, I. Lapkin, V. Vassilev, R. Monje, A. Pavolotsky, D. Meledin, *et al.*, "Facility heterodyne receiver for the Atacama Pathfinder Experiment Telescope," in *Infrared and Millimeter Waves, 2007 and the 2007 15th International Conference on Terahertz Electronics. IRMMW-THz. Joint 32nd International Conference on*, 2007, pp. 326-328.
- [2] B. Billade, O. Nystrom, D. Meledin, E. Sundin, I. Lapkin, M. Fredrixon, *et al.*, "Performance of the First ALMA Band 5 Production Cartridge," *Terahertz Science and Technology, IEEE Transactions on*, vol. 2, pp. 208-214, 2012.
- [3] D. Meledin, A. Pavolotsky, V. Desmaris, I. Lapkin, C. Risacher, V. Perez, *et al.*, "A 1.3-THz Balanced Waveguide HEB Mixer for the APEX Telescope," *Ieee Transactions on Microwave Theory and Techniques*, vol. 57, pp. 89-98, Jan 2009.
- [4] H. Rashid, D. Meledin, V. Desmaris, A. Pavolotsky, and V. Belitsky, "Superconducting 4-8 GHz Hybrid Assembly for 2SB Cryogenic THz Receivers," *Terahertz Science and Technology, IEEE Transactions on*, vol. 4, pp. 193-200, 2014.
- [5] H. Rashid, D. Meledin, V. Desmaris, and V. Belitsky, "Novel Waveguide 3 dB Hybrid With Improved Amplitude Imbalance," *Microwave and Wireless Components Letters, IEEE*, vol. 24, pp. 212-214, 2014.
- [6] Agilent, "Application notes. <http://www.agilent.com.>"
- [7] <http://www.agilent.com.>

Development of Phase Lock Loop based on Harmonic Phase Detector

Konstantin V. Kalashnikov^{1,2,*}, Andrey V. Khudchenko^{1,3}, and Valery P. Koshelets¹

¹ *The Kotel'nikov Institute of Radio Engineering and Electronics, Russian Academy of Science,
11/7 Mokhovaya St., 125009, Moscow*

² *Moscow Institute of Physics and Technology,
Institutskii per., 9, 141700 Dolgoprudny, Moscow Region, Russia*

³ *SRON Netherlands Institute for Space Research, P.O. Box 800,
9700 AV Groningen, the Netherlands*

**Email: Kalashnikov@hitech.cplire.ru*

A novel superconducting element, High-Harmonic Phase Detector (HPD), intended for phase-locking of a Flux Flow Oscillator (FFO) in a superconducting integrated receiver (SIR) has been proposed and experimentally tested. According to our concept a superconductor-insulator-superconductor (SIS) junction is implemented both for down-conversion of the FFO frequency and for phase-locking of the FFO to an external reference by applying the HPD output directly to the FFO control line. The cryogenic HPD can be placed in close vicinity to the oscillator providing extremely large synchronization bandwidth (BW). To realize efficient phase-locking of the FFO the HPD output signal should be maximized by the HPD bias voltage, frequency and power of the local oscillator (LO) and input RF signal. Calculated 3D dependences of the HPD output signal power versus bias voltage and LO power agreed well with experimental measurements.

For demonstration of the HPD operation we used additional SIS-mixer implemented for monitoring of the phase locking effect. Regulation BW of the phase-locking loop (PLL) system based on the HPD as high as 70 MHz has been experimentally achieved; that value several times exceeds BW of any other regular PLL systems used for cryogenic oscillators. Developed HPD system could synchronize up to 92% of the emitted FFO power for free running FFO line as wide as 12 MHz.

In this work we also propose new method for estimation of a synchronization efficiency based on HPD dc signal monitoring. We have developed experimental setup for measuring of the HPD output signal; it was shown that for the HPD operation the Josephson mixing regime is more efficient than quasiparticle resulting in increase of the output signal on 12 dB at moderate noise level raise on 4 dB. Detailed study of the HPD output signal on the SIS junction parameter has been performed in order to optimize the HPD operation.

The HPD PLL system is simple and compact, that is why our concept is very promising for future applications, especially for building of the multi-pixel SIR array and for phase-locking of the THz range FFO.

The work was supported by The RFBR and the Ministry of Education and Science of the Russian Federation.

1-a - THz coherent detectors: HEB

Design, fabrication and measurement of a membrane based quasi-optical THz HEB mixer

G. Gay, Y. Delorme, R. Lefèvre, A. Féret, F. Defrance, T. Vacelet, F. Dauplay, M. Ba-Trung, L. Pelay and J.-M. Krieg

*Laboratoire d'Etude du Rayonnement et de la Matière en Astrophysique (LERMA)
Observatoire de Paris, 61 Avenue de l'Observatoire, 75014 Paris, France*

Abstract—In this paper we present our recent development in quasi-optical membrane based superconducting hot electron bolometer (HEB) mixers at 0.6 THz. The phonon-cooled Niobium Nitride (NbN) HEB coupled to a double slot antenna is processed on a 1.4 μm thick stress-less $\text{Si}_3\text{N}_4/\text{SiO}_2$ membrane. The mixer block uses an off-axes mirror to focus the terahertz (THz) signal to the antenna and a back-short is placed behind the membrane to increase the gain of the antenna.

We have simulated the input impedance of the membrane based double slot antenna and the radiation properties of the quasi-optical mixer with the aid of the full wave electromagnetic solver CST Microwave Studio. Measurements have been performed to obtain the double sideband receiver noise temperature and IF bandwidth. The measurement results will be discussed and compared with those of a thick substrate based HEB mixer.

Index Terms—Heterodyne detection, hot electron bolometer, quasi-optical, membrane based HEB.

I. INTRODUCTION

THE phonon-cooled Niobium Nitride (NbN) HEB coupled with an integrated lens-antenna on thick dielectric substrate have demonstrated a high sensitivity for the THz heterodyne detection [1] – [3]. However, some losses remain inherent with this type of quasi-optical structure. The signal must pass through the dielectric material of the lens and the substrate which causes reflection and substrate modes losses. One way to avoid these problems is to use a metallic mirror to focus the signal to the antenna and reduce the substrate under the planar antenna. For a slot antenna it was shown that a dielectric thickness less than $0.04 \lambda_d$ [4] (with λ_d the wavelength into the dielectric) allows to consider the antenna as suspended in free-space, so without dielectric losses. For this reason, the antenna is deposited on a 1.4 μm thick membrane made of $\text{Si}_3\text{N}_4/\text{SiO}_2$ allowing a double slot antenna up to about 4 THz [5].

Manuscript received in June 14, 2014. This work was supported by European research project RadioNet AETHER, the French space agency (CNES) and by the "Région Ile-de-France".

G. Gay, Y. Delorme, R. Lefèvre, A. Féret, F. Defrance, T. Vacelet, F. Dauplay, M. Ba-Trung, L. Pelay and J.-M. Krieg are with the Laboratoire d'étude et du rayonnement de la matière en astrophysique (LERMA), 61 Avenue de l'Observatoire, 75014 Paris France (phone: 33-1 4051 2060; e-mail: gregory.gay@obspm.fr).

This paper will begin by presenting the concept of our quasi-optical mixer block using a mirror and a planar antenna on the stress-less membrane. Then the design of the planar antenna with CST Microwave Studio (CST MWS) will be presented. Afterward, the measurements setup employed to characterize the mixer's sensitivity and the IF gain bandwidth will be detailed. Finally, the results obtained with the membrane based structure will be discussed and compared with a HEB coupled to a double slot antenna on a thick substrate and integrated on a silicon lens in the same measurement conditions.

II. CONCEPT AND DESIGN

A. Mixer block

The quasi-optical mixer block uses an off-axis parabolic mirror to focus the radiation to the antenna (Fig. 20). The mirror has a focal length of 12.7 mm, a diameter of 25.4 mm and focuses incident signal at 90°. Under the membrane, a back-short is placed at a quarter of the wavelength to increase the gain of the planar antenna. The Back-short is a metallic plane reflector made on a silicon substrate that has been thinned to allow the reflector at the good distance behind the membrane. The intermediate frequency (IF) signal produced by the HEB is transmitted to the SMA connector by a microstrip line of 50Ω . The NbN HEB is fabricated on the membrane made of 600 nm thick of silicon nitride (Si_3N_4) and of 800 nm thick of silicon dioxide (SiO_2). All the details of the fabrication process of the membrane based HEB were explained in two previous papers [6], [7].

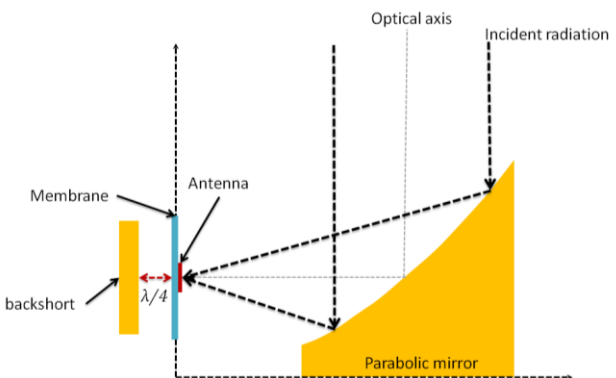


Fig. 20. Schematic view of the quasi-optical mixer block. The parabolic mirror focuses the THz signal to the antenna. The back-short placed behind the membrane increases the gain of the antenna.

B. Antenna design

Different kind of planar antennas may be selected to detect the THz radiation [8] – [11]. In this work, we have chosen a planar antenna widely used for THz heterodyne receivers: the double slot antenna (DSA). The DSA has linear polarization, good frequency selectivity and high directivity. Another advantage in our case is that the DSA can have an impedance around 75Ω [12], which is the impedance of our HEB. We used a full wave electromagnetic solver, CST Microwave Studio to simulate the impedance of the DSA on membrane and its radiation pattern.

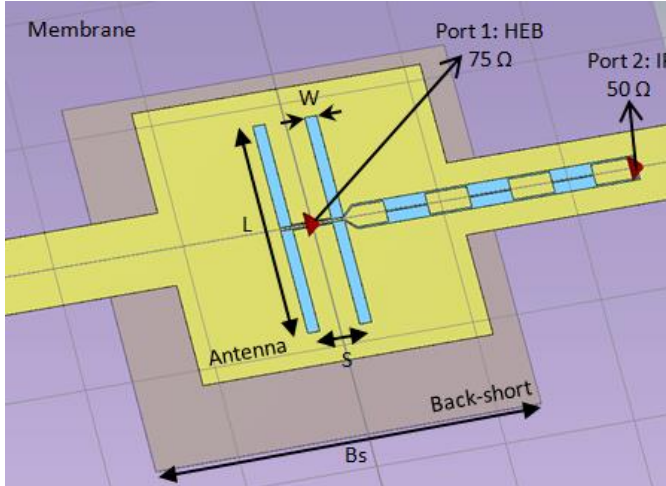


Fig. 21. Simulated structure in CST MWS. The antenna is on the membrane and the back-short is placed at a quarter of the wavelength behind the HEB. The HEB is a discrete port of 75Ω and the IF output is a discrete port of 50Ω .

A DSA can be determined by 3 parameters, the length and the width (L and W) of the slots and the separation (S) between the two slots. In a typical case the DSA is on a thick dielectric substrate and the length L is governed by the wavelength of the radiation and the material dielectric constant. In this case, the length can be written [13]:

$$L = 0.8A\lambda_0 \quad (1)$$

Here, λ_0 is the wavelength in vacuum and A is a factor that depends on the effective dielectric constant (ϵ_{eff}) and on the W/L ratio [14].

$$A = \frac{1}{\sqrt{\epsilon_{eff}} \left(1 + \frac{W}{L}\right)} \quad (2)$$

In our case, the membrane is thin enough (less than $0.04 \lambda_d$) to consider the antenna as suspended in free-space, so ϵ_{eff} tends to 1. The ratio W/L is typically chosen to be between 0.02 and 0.07. Finally, L is around $0.75 \lambda_0$ when the DSA is on a membrane, whereas it is around $0.3 \lambda_0$ for a DSA on a thick silicon substrate. This means that the DSA is larger on thin membrane, which allows an easier fabrication process for higher frequencies. Concerning the separation between the slots, S is generally chosen to be

around $0.17 \lambda_0$. These parameter values (L , W and S) are chosen as point of departure for the design of the membrane based antenna. The entire structure of the device including the DSA, the RF choker filter, the membrane and the back-short is modeled with CST MWS (

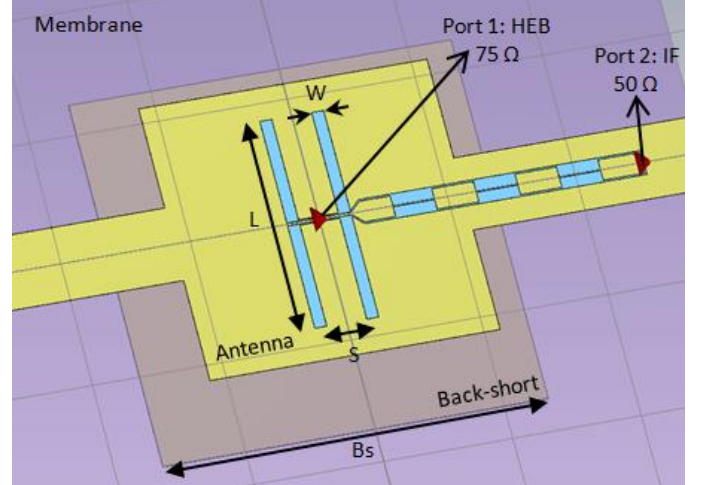


Fig. 21). For the simulation, the HEB is replaced by a discrete port of 75Ω and the IF output is represented by a port of 50Ω . Optimizations of the parameters L , W and S have been performed to minimize the return loss at the desired frequency, here 618 GHz and also to have an impedance of the antenna close to 75Ω . The size of the back-short (named Bs on the picture) has also been optimized in order to have the best radiation pattern. The optimal size was found to be $600 \times 600 \mu\text{m}^2$ resulting an antenna directivity of 9.2 dBi. The optimized parameters are listed in the table 1 and the impedance of the DSA is plotted in Fig. 22. We can notice that the antenna has an impedance very close to 75Ω near 618 GHz, allowing a good adaptation with the HEB.

TABLE 1. Parameters of the DSA and the back-short

L (μm)	S (μm)	W (μm)	Bs (μm ²)
343 (0.71 λ ₀)	80 (0.17 λ ₀)	18.7 (0.05 L)	600x600

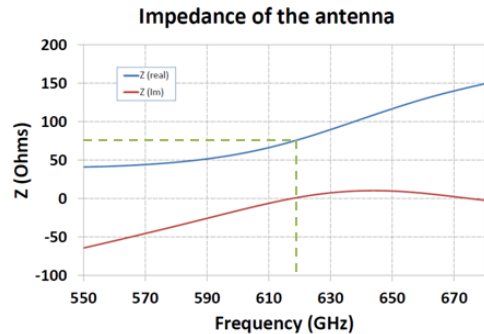


Fig. 22. Simulated impedance of the DSA. Around 618 GHz, the imaginary part (red line) is close to 0 and the real part (blue line) is very close to 75 Ohms.

The beam pattern of the membrane based DSA with the back-short has been calculated by the transient solver of

CST MWS. This method is well adapted to calculate the electromagnetic field near the antenna but is not suitable for the calculation of large structures such as the mixer block with the parabolic mirror. We thus used the Multi Level Fast Multipole Method (MLFMM) in CST MWS to simulate the beam pattern of the entire mixer block. The off-axis parabolic mirror has been modeled and the beam pattern of the membrane based antenna previously calculated has been placed in the focal plane of the mirror as an input source for the solver (Fig. 23). The result of the simulation is shown in Fig. 24. The main lobe has a magnitude of 36.5 dBi, an angular width of 1.3° at -3 dB and the side lobe level does not exceed -24.8 dB.

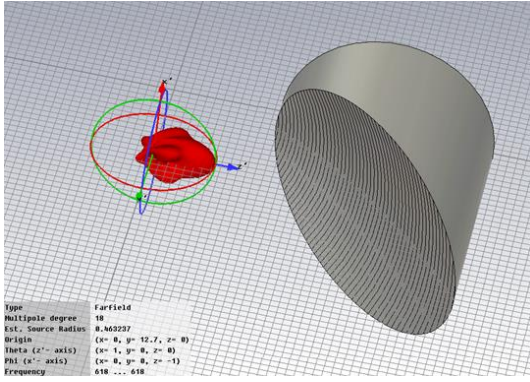


Fig. 23. The off-axis parabolic mirror is modeled to simulate the beam pattern of the entire mixer block.

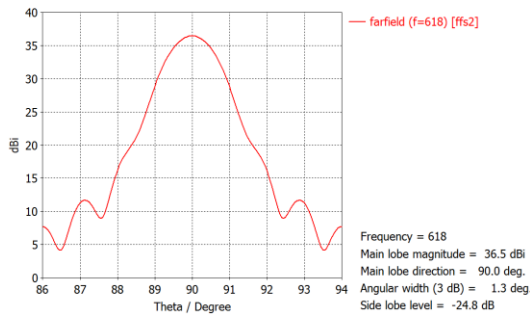


Fig. 24. Beam pattern of the mixer block.

III. MEASUREMENTS SETUP

The mixer's performance has been investigated around 600 GHz. The double side band (DSB) noise temperature and the IF gain bandwidth measurement has been performed by using two different setup.

A. DSB noise temperature measurement setup

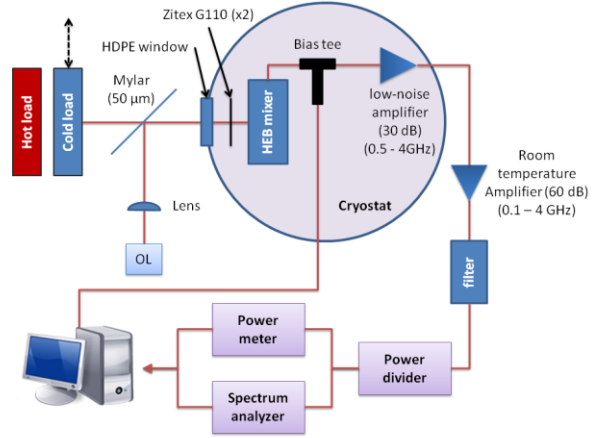


Fig. 25. Illustration of the measurement setup. The hot and cold loads are placed in front of the window of the cryostat for the Y-factor measurement.

The mixer block is mounted on the cold plate of an Infrared Labs cryostat. The RF and LO signals are sent into the cryostat by an optical access through a 1 mm thick HDPE window at room temperature. Two layers of Zitex® G110 block the infrared radiation [14], one is glued on the 4 K shield and the other one is mounted on the cold plate in front of the mixer block. A bias tee is used to feed the bias to the mixer and to transmit the IF signal to the cooled low noise amplifier (noise temperature 8 K, gain 30dB), which is a Caltech amplifier operating between 0.5 and 4 GHz. The IF signal comes out of the cryostat and is amplified by two amplifiers (2x 30 dB) at room temperature operating between 0.1 to 4 GHz. Then the output signal is filtered at 650 MHz with a bandwidth of 250 MHz.

The DSB noise temperature of the receiver is evaluated by using the Y-factor method. The LO signal, fixed at 618 GHz, is provided by an electronic source driven by a synthesizer. The LO source is placed in the focal plane of a lens to collimate the signal into the cryostat. Two black bodies made from Eccosorb are used as the hot and cold load with a temperature of 295 and 77 K respectively. The optical path between the LO source, the loads and the cryostat was not air evacuated and a 50 µm thick mylar was used as the beam splitter to combine the radiation from the hot/cold load and the LO source.

B. IF gain bandwidth measurement setup

The measurement setup is quite similar to that of the noise temperature measurement but we've taken care to suppress all the elements that could limit the IF bandwidth. The cooled low noise amplifier with a bandwidth from 0.5 to 4 GHz is removed and we don't use any filter outside the cryostat. Since the IF signal is very weak at the output of the cryostat, we amplify it with two wide band room temperature amplifiers (0.1 to 4 GHz). The output signal is read with a spectrum analyzer.

The IF signal is generated inside the HEB by mixing signals from two electronic sources, one as the LO and the other one as the RF. We start to pump the HEB with the LO around its optimal level which has been determined during the DSB noise measurement. After what, we place the second source, with a frequency very close to the LO

frequency, in front of the cryostat and we adjust carefully the RF power in order to not over pump the HEB. The RF power transmitted to the receiver is maintained unchanged all along the measurement. The scanning along the IF band is made by tuning the frequency of the LO and for each point the power is adjusted in order to keep the same pumping level of the HEB.

IV. RESULTS AND DISCUSSION

A. DSB noise temperature receiver

We measured the DSB noise temperature of the membrane based HEB in the off-axis mixer block. The HEB consist of a 2 μm wide, 0.2 μm long and 5 nm thick NbN bridge between the electrodes of the DSA designed for 618 GHz. The HEB have a room temperature resistance of 90 Ω and a critical current of 240 μA at 4.2 K (**Ошибка! Источник ссылки не найден.**). Different pumping levels have been tried to find the best region to have the minimum noise temperature of the receiver.

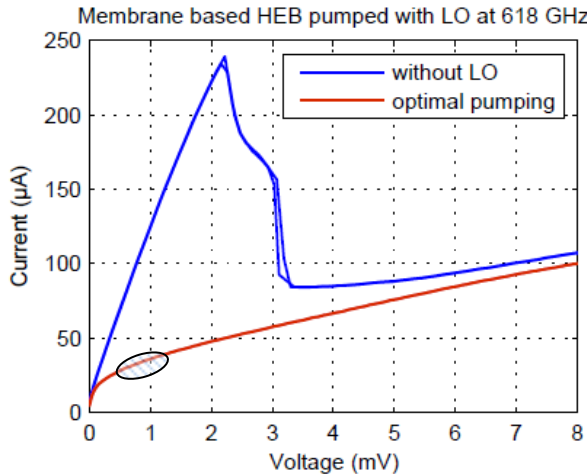


Fig. 26. I-V curves recorded at 4.2 K of the membrane based HEB without LO (blue line) and at the optimal pumping of the HEB (red line). In the circle, the optimal pumping region for the heterodyne measurement.

The IF output power of the HEB responding to the hot and cold load is recorded as a function of the bias voltage. Then, the Y-factor is calculated with: $Y = P_{\text{hot}}/P_{\text{cold}}$, and the DSB noise temperature (T_{DSB}) of the receiver can be obtained by:

$$T_{\text{DSB}} = \frac{295 - 77Y}{Y - 1} \quad (3)$$

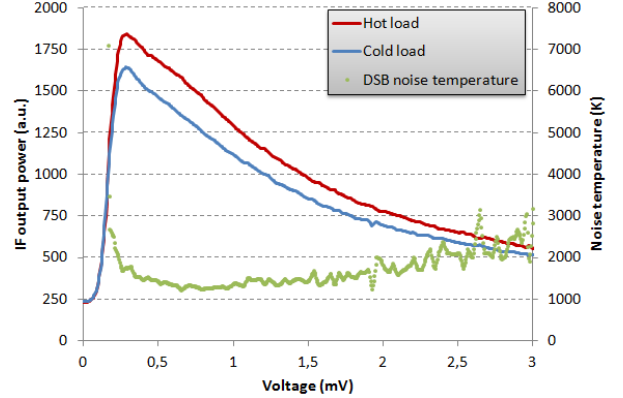


Fig. 27. DSB noise temperature measured with the membrane based mixer block. The blue and red lines represent the IF output power provided by the HEB with the cold and hot loads as a function of the bias voltage.

An uncorrected noise temperature around 1200 K was measured with the membrane based HEB (Fig. 27). In order to compare this result with a HEB on thick substrate, we used strictly the same measurement setup, only the mixer block is replaced by the one with an integrated lens-antenna and a HEB on a thick silicon substrate. This device on thick substrate is chosen for its similarity with the measured membrane based device. The HEB consist of a 2 μm wide, 0.2 μm long and 5 nm thick NbN bridge on a 350 μm thick silicon substrate. The HEB is coupled with the DSA designed for 600 GHz. It has a room temperature resistance of 83 Ω and a critical current of 210 μA at 4.2 K. With this device we measured an uncorrected noise temperature of 800 K. The measurement includes the optical losses between the beam splitter and the input of the mixer. As summarized in the table 2, the losses are estimated to be 2.85 dB. So, with an improvement of the optical path, we could hope a noise temperature below 600 K for the membrane based HEB and below 400 K for the HEB on a thick substrate.

TABLE 2. Losses in the optical elements

element	Loss (dB)
Beam splitter	1.5
HDPE window	0.45
Zitex filter (x2)	0.45 (x2)

B. IF gain bandwidth

Both membrane and thick substrate based HEB mixers are measured in the same conditions (described above) to obtain the IF gain bandwidth. As explained in the previous chapter, we tune the LO frequency to sweep the IF band between 0.2 and 5 GHz. The resulting beat signal is recorded by a spectrum analyzer for each frequency. The normalized IF output powers are presented in Fig. 28. The HEB on thick silicon substrate has an IF bandwidth at -3 dB around 3 GHz as expected and the membrane based HEB reveals an IF bandwidth much lower: around 0.9 GHz. That could be explained by the difference between the lattice

parameters of the NbN film and the substrate. In the case of the membrane based HEB, the lattice parameters of the Si_3N_4 and the NbN are quite different [15], which causes an acoustic mismatch between the NbN film and the substrate, so the relaxation time of the electron inside the superconducting film is slowed [17] while in the case of HEB on the silicon substrate, the lattice parameters of the Si and the NbN are very close [15].

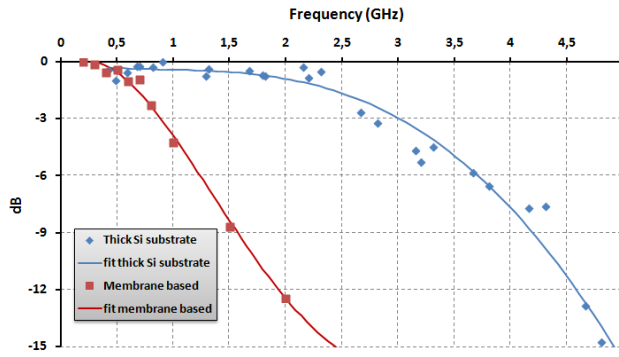


Fig. 28. IF gain bandwidth measured for a membrane based HEB (red dots) and a HEB on a thick silicon substrate (blue dots).

C. Discussion

The heterodyne measurements at 0.6 THz of the quasi-optical membrane based mixer have demonstrated promising results. Though the noise temperature is about 30% higher than that of the mixer with a HEB on a thick Si substrate which has been fabricated with the very similar process and measured in the same conditions, this work has demonstrated the feasibility of the membrane mixer concept and the fabrication process. Further improvements are needed to increase the coupling efficiency between the mirror, the antenna and the HEB. The IF gain bandwidth of the membrane based mixer seemed quite limited compared to the device on a thick silicon substrate revealing the need of a better understanding of the thermal transfer at the interface of the HEB and the $\text{Si}_3\text{N}_4/\text{SiO}_2$ membrane. Changing the layer material or adding a buffer layer could be a solution to increase the IF bandwidth.

ACKNOWLEDGMENT

We would like to thank the “laboratoire de photonique et

Nanostructure” (LPN) in France for giving us privileged access to their clean room. Thanks to David Horville from the GEPI laboratory for his help in the quasi-optical alignment.

REFERENCES

- [1] Y. Delorme, “A quasi-optical NbN HEB mixer with 800 K DSB noise temperature at 2.5 THz,” in *Proc. 22nd Int. Symp. on Space Terahertz Techn.*, Tucson, 2011.
- [2] P. Khosropanah, “Low noise NbN hot electron bolometer mixer at 4.3 THz,” *Applied Physics Letters*, 91, 2007.
- [3] J. L. Kloosterman, “Hot electron bolometer heterodyne receiver with a 4.7 THz quantum cascade laser as a local oscillator,” *Applied Physics Letters*, 102, 2013.
- [4] D.F. Filipovic, “Double-slot antennas on extended hemispherical and elliptical silicon dielectric lens,” *IEEE Trans. on Microwave Theory and Techniques*, vol 41, NO. 10, October 1993.
- [5] G. Gay, “Membrane based hot electron bolometers mixers beyond THz for the post-Herschel instrument,” PhD thesis, LERMA laboratory, Observatoire de Paris, France, 2013.
- [6] G. Gay, “Membrane based quasi-optical superconducting HEB mixers at terahertz frequencies,” *Proc. SPIE 8452, Millimeter, Submillimeter, and Far-Infrared Detectors and Instr. For Astr.* VI, 845213, 2012.
- [7] R. Lefèvre, “Terahertz NbN hot electron bolometer fabrication process with a reduced number of steps,” in *Proc. 23rd Int. Symp. on Space Terahertz Techn.*, Tokyo, 2012.
- [8] W. Zhang, “Noise temperature and beam pattern of an NbN hot electron bolometer mixer at 5.25 THz,” *Journal of Applied Physics*, 108, 2010.
- [9] W. Zhang, “Twin-slot antenna coupled NbN hot electron bolometer mixer at 2.5 THz,” *IEEE Trans. on Terahertz Sc. And Techn.*, vol. 1, NO. 2, November 2011.
- [10] Skalare, “Double dipole antenna SIS receivers at 100 and 400 GHz,” in *Proc. of 3rd ISSTT*, pp. 222-233, 1992.
- [11] Ronnung, “A nanoscale YBCO mixer optically coupled with a bow-tie antenna,” *Supercond. Sc. And Techn.*, Vol. 12, Issue 11, pp. 853-855, 1999.
- [12] V. Eleftheriades, “Self and mutual admittance of slot antennas on a dielectric half-space,” *International Journal of Infrared and Millimeter Waves*, Vol. 14, No. 10, 1993.
- [13] W. Miao, “Investigation of hot electron bolometer mixers for submillimeter multi-pixel receiver applications,” PhD thesis, LERMA laboratory, Observatoire de Paris, France, 2010.
- [14] M. Kominami, “Dipole and slot elements and arrays on semi-infinite substrate,” *IEEE Trans. on antenna and propagation*, vol. 33, pp. 600-607, 1985.
- [15] J. Benford, “Optical properties of Zitex in the infrared to submillimeter,” *Applied Optics*, vol. 42, pp. 5118-5122, 2003.
- [16] Guillet, “Influence of substrates and buffer layers on the quality of NbN ultrathin film for THz HEB,” in *Proc. of 18th ISSTT*, 2007.
- [17] S. Cherednichenko, “Gain bandwidth of NbN hot electron bolometer terahertz mixers on 1.5 μm $\text{Si}_3\text{N}_4/\text{SiO}_2$ membranes,” *Journal of Applied Physics*, vol. 101, 2007.

Wide RF band mixer -block design for waveguide-type HEB mixer

T. Soma¹, T. Sakai², Y. Watanabe¹, N. Sakai¹, L. Jiang³, H. Maezawa⁴, and S. Yamamoto¹

¹*The University of Tokyo, Hongo, Tokyo, Japan*

²*The University of Electro-Communication, Chofu, Tokyo, Japan*

³*The Nanjing Forestry University, Nanjing, Jiangsu, China*

⁴*Osaka Prefecture University, Sakai, Osaka, Japan*

Email: soma@taurus.phys.s.u-tokyo.ac.jp

A superconducting hot electron bolometer (HEB) mixer is the most sensitive heterodyne mixer above 1 THz, and it is now being used for astronomical observations thanks to various developmental efforts during the last decade. For example, it was employed for the Herschel space telescope, and was used to observe many spectral lines of various fundamental atoms, ions, and molecules in the THz band, which give us rich information about chemical and physical structures of interstellar clouds. For further observations with ground-based telescopes at a higher angular resolution, our group has been developing superconducting HEB mixers for the 0.9 and 1.3-1.5 THz band.

The HEB mixers can be classified into the two types by a coupling method to the incoming radiation; one is a waveguide type and another is a quasi-optical type. We employ the waveguide-type coupling because of its well-defined beam pattern and future extension possibilities for sophisticated receiver systems like a 2SB receiver. As a drawback, the RF bandwidth of waveguide-type mixer is generally narrower than that of quasi-optical type. In order to mitigate this weak point for the waveguide-type HEB mixer, we have tried to expand the RF bandwidth as much as possible by optimizing the mixer design.

It is thought that the HEB mixer element can be treated as a resistor for the RF signal input. Hence, the design of the waveguide mixer block and the IF matching circuit is easier than other mixer elements such as an SIS element, although actual fabrication of the THz HEB mixer is quite difficult due to very small dimensions. In order to observe the 0.9, 1.3 and 1.5 THz atmospheric windows with a single mixer, we have tried to design a mixer block which has a sensitivity in 0.9-1.5 THz range by using a computer simulation. The simulation is carried out by using the commercial software HFSS. At first, we fixed the width of waveguide so as that the basic mode can only propagate through it for the above frequency range. In order to reduce the frequency dependence of choke filters, we have adopted Hammer filters instead of conventional quarter-lambda filters. Then, I have tuned the impedance by changing the shape of the bow-tie antenna to match the impedance of the HEB element. As a result, we have found that the waveguide HEB mixer sensitive to the RF signal from 0.9 to 1.5 THz is indeed possible. Actual testing of this mixer is in progress.

Development of a 30 THz Heterodyne Receiver Based on a Hot-Electron-Bolometer Mixer

Michael Shcherbatenko^{1,2}, Yury Lobanov^{1,2*}, Matvey Finkel'¹, Sergey Maslennikov¹, Ivan Pentin¹, Alexander Semenov¹, Nadezhda Titova¹, Natalya Kaurova¹, Boris M. Voronov¹, Alexander Rodin^{2,3}, Teunis M. Klapwijk^{1,4} and Gregory N. Gol'tsman^{1,5}

¹*Moscow State Pedagogical University, Moscow*

²*Moscow Institute of Physics and Technology, Dolgoprudny*

³*Space Research Institute, RAS, Moscow*

⁴*Kavli Institute of Nanoscience, Faculty of Applied Sciences, Delft University of Technology, Delft*

⁵*National Research University Higher School of Economics, Moscow*

*Email: ylobanov@rplab.ru

We present new Hot-Electron-Bolometer (HEB) mixers designed for mid-IR spectroscopy targeting astrophysical and geophysical observations where high sensitivity and spectral resolution are required. The mixers are made of an ultrathin NbN film deposited on GaAs substrates. Two entirely different types of the devices have been fabricated. The first type is based on a direct radiation coupling concept and the mixing devices are shaped as squares of $5 \times 5 \mu\text{m}^2$ (which corresponds to the diffraction limit at the chosen wavelength) and $10 \times 10 \mu\text{m}^2$ (which was used to establish a possible influence of the contact pads on the radiation absorption). The second type utilizes a spiral antenna designed with HFSS. The fabrication and layout of the devices as well as the performance comparison will be presented.

During the experiments, the HEB mixer was installed on the cold plate of a LHe cryostat. A germanium window and an extended semi-spherical germanium lens are used to couple the radiation. The cryostat is equipped with a germanium optical filter of thickness 0.5 mm and with a center wavelength of 10.6 μm .

The incident power absorption is measured by using the isothermal method. As a Local Oscillator, a 10.6 micrometers line of a CO₂ gas laser is used. We further characterize the frequency response of the spiral antenna with a FIR-spectrometer. The noise characteristics of the mixers are determined from a room temperature cold load and a heated black body at ~ 600 K as a hot load.

2 – Direct Detectors

Development of an 8×8 Microwave Kinetic Inductance Detector Array at 850μm

J. Li^{1,2}, D. Liu^{1,2}, S. Li^{1,2}, J.P. Yang^{1,2}, Z.H. Lin^{1,2}, W. Miao^{1,2}, Z. Lou^{1,2}, S.C. Shi^{1,2*}, S. Mima³, N. Furukawa³, K. Koga³, and C. Otani³

1. Purple Mountain Observatory, CAS, China

2. Key Laboratory of Radio Astronomy, Chinese Academy of Sciences, China

3. RIKEN Center for Advanced Photonics, Wako, Saitama, Japan

* Email: scshi@pmo.ac.cn

Microwave Kinetic Inductance Detectors (MKIDs) are rather promising for astrophysical observations in the THz regime. We are developing a terahertz superconducting imaging array (TeSIA) for the DATE5 telescope to be constructed at Dome A, Antarctic. Here we report on the design, fabrication and characterization of a prototype array for TeSIA, namely an 8×8 MKIDs array at 850μm. Detailed experimental results and analysis will be presented.

Superconducting on-chip spectrometers at sub-millimeter wavelength

Masato Naruse^{*}, Hiroyuki Tanoue^{*}, Keiichi Arai^{*}, Yutaro Sekimoto^{**}, Takashi Noguchi^{**}, Tohru Taino^{*} and Hiroaki Myoren^{*}

^{*}*Department of Electrical and Electrical Systems, Saitama University*

Email: naruse@super.ees.saitama-u.ac.jp

^{**}*Advanced Technology Center, National Astronomical Observatory of Japan*

We propose an on-chip spectrometer camera for sub-millimeter astronomy. The camera will be installed to the focal plane of a telescope and be operated at 0.1 K. The camera is composed of three kinds superconducting circuits, such as wideband antennas, band pass filters (BPFs), and Microwave Kinetic Inductance Detectors (MKID) [1]. All components are fabricated on the same chip by the standard photolithographic techniques. Sub-mm photons are introduced to the chip by the antenna, are divided into three colors by three BPFs. The signal are finally measured with MKID by breaking cooper pairs in the superconducting film.

The slot log-periodic antennas and the microstrip filters are made from NbTiN films to reduce signal transmission losses from the antenna to the detectors. MKID is a half-wave resonator at microwave range (3-8 GHz) and consists of a co-planar waveguide line. With the intension to improve the optical efficiency of the camera, only the middle area of the center line of the CPW is constructed with an Al film and the other parts are manufactured by NbTiN [2].

We designed two types of BPFs. One is an open ring Chebyshev's filter which has 15 % bandwidth in 150, 220, and 440 GHz. The filters were modulated from the filter optimized for microwave signals [3]. The other is lumped element filter [4] for 0.8, 1, and 1.3 THz. The former has good tolerance for production error up to 500 GHz. The latter has 10% bandwidth suitable for the atmospheric windows.

References

1. P. Day, H. LeDuc, B. Mazin, A. Vayonakis, and J. Zmuidzinas, "A broadband superconducting detector suitable for use in large arrays," *Nature*, 425, 2003, pp. 817-821.
2. S. Yates, J. Baselmans, A. Endo, R. Janssen, L. Ferrari, P. Diener, and A. Baryshev, "Photon noise limited radiation detection with lens-antenna coupled microwave kinetic inductance detectors," *Appl. Phys. Lett.* , 99, 2011, p 073505.
3. S. Kumar, A. Vayonakis, H. LeDuc, P. Day, Peter S. Golwala, and J. Zmuidzinas, "Millimeter-wave lumped element superconducting bandpass filters for multi-color imaging," *IEEE Trans. of appl. Supercond.*, 19, 2009, pp. 924-929.
4. JS. Hong, and M. Lancaster, "Design of highly selective microstrip bandpass filters with a single pair of attenuation poles at finite frequencies," *Appl. Phys. Lett.* , 99, 2011, p 073505.

Zero bias GaAsSb/InAlAs/InGaAs tunnel diodes for MMW-THz detection

Mikhail Patrashin^{*}, Norihiko Sekine^{*}, Akifumi Kasamatsu^{*}, Issei Watanabe^{*}, Iwao Hosako^{*}, Tsuyoshi Takahashi[†], Masaru Sato[†], Yasuhiro Nakasha[†] and Naoki Hara[†]

^{*}Terahertz and Millimeter Waves ICT Laboratory

National Institute of Information and Communications Technology, Tokyo 184-0015, Japan Email:

mikhail@nict.go.jp

[†]Fujitsu Laboratories Ltd., Atsugi 243-0197, Japan

Email: takahashi.tsuyo@jp.fujitsu.com

Heterostructure tunnel diodes based on III-V compound semiconductors are the promising detector technology for MMW-THz systems. These devices demonstrate fast response, high cutoff frequencies due to small device capacitances, good sensitivity and feasibility of the monolithic integration with other semiconductor components and integrated circuits. This presentation describes on-wafer characterization of GaAsSb/InAlAs/InGaAs tunnel diodes for direct detection in 220-330GHz band.

Schematic structure of the device is shown in Fig.1. The non-linear characteristics of the detector result from the quantum-mechanical tunneling in the staggered band gap heterostructure of the device. Variable resistance of the diode produces the square-law rectification of the input signal power. Voltage sensitivity of more than 1000V/W was measured over 220-330GHz at room temperature (Fig.2). The inherent cutoff frequency of the $0.8 \mu\text{m} \times 0.8 \mu\text{m}$ mesa diode was $f_c = (2\pi R_s C_J)^{-1} = 322 \text{ GHz}$.

The devices demonstrated enhanced temperature stability of the characteristics compared to the zero-bias Schottky barrier diodes. The estimated variations of the zero-bias sensitivity at temperatures from 17K to 300K were less than 2dB.

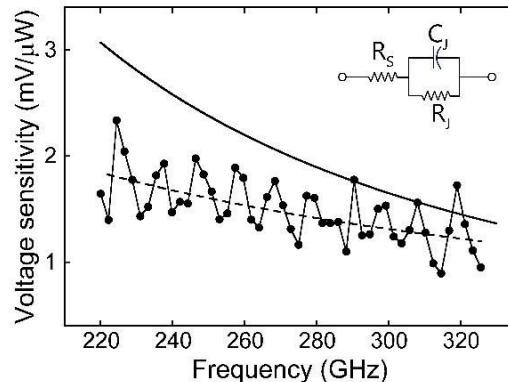
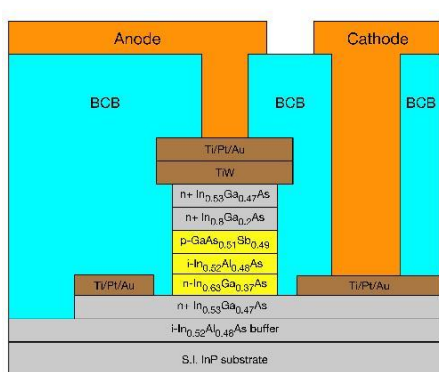


Fig. 1. Schematic cross-section of the completed tunnel diode detector after device processing (dimensions are not to scale).

Fig. 2. Measured voltage sensitivity of $0.8 \mu\text{m} \times 0.8 \mu\text{m}$ mesa diode and the theoretical values $S_V = S_{C0} / (R_s (2\pi f C_J)^2)$ corresponding to the lossless impedance match at the detector's input (solid line). Insert shows the equivalent circuit model of the device consisted of the non-linear junction resistance R_J , the parallel junction capacitance C_J , and the series resistance R_s . S_{C0} is the low-level current sensitivity at zero bias. The parameters of the model were extracted from the measurements and were equal to $S_{C0} = 11 \text{ A/W}$, $R_s = 130 \Omega$ and $C_J = 3.8 \text{ fF}$.

Characterization of Ti superconducting transition edge sensors

J.Q. Zhong^{1,2,6}, W. Miao^{1,2}, W. Zhang^{1,2}, D. Liu^{1,2}, Z. Wang^{1,2}, W.Y. Duan^{1,2}, Q.J. Yao^{1,2}, S.C. Shi^{1,2*}, T.J. Chen³, L. H. Chang³, M.J. Wang³, J. Martino⁴, F. Pajot⁴, D. Prele⁵, F. Voisin⁵, and M. Piat⁵

¹*Purple Mountain Observatory, CAS, China*

²*Key Lab of Radio Astronomy, CAS, China*

³*Institute of Astronomy and Astrophysics, Academia Sinica, Taipei*

⁴*Institut d'Astrophysique Spatiale, CNRS - Univ. Paris-Sud, France*

⁵*Laboratoire AstroParticule et Cosmologie, Univ. Paris-7, France*

⁶*University of Chinese Academy of Sciences, CAS, China*

*Contacts: scshi@mail.pmo.ac.cn, phone: +86-25-8333-2204

In this paper, we report the development of superconducting transition edge sensors (TES) based on Ti superconducting films, which are deposited on silicon substrate by DC reactive magnetron sputtering. All measurements are performed with a 0.3-K Chase He-7 cooler integrated with a two-stage 4-K Gifford-McMahon refrigerator. The critical temperature of the Ti TESs (\sim 30nm thick) is about 420 mK. Using a commercial SQUID, we measure the current-voltage (I-V) characteristics of a Ti TES device at different bath temperatures. Its thermal conductance is found to be approximately equal to 100 pW/K. The dark noise equivalent power (NEP) is about 5×10^{-17} pW/VHz in terms of the current noise measured at a bath temperature of 388 mK. Detailed design and measurement results will be presented.

Experimental study of a Josephson junction based thermometer and its possible application in bolometry

T. Faivre¹, D. Golubev & J.P. Pekola

O.V. Lounasmaa Laboratory, Aalto university.

¹*timothe.faivre@aalto.fi*

We characterise an Al/AlOx/Ti/AlOx /Al (SIS'IS) structure in terms of its zero bias slope. It shows a large temperature dependence ($\partial R_0 / \partial T \sim 10^7 \Omega/K$) close to the titanium superconducting transition. Sensitivity is measured to be $2 \mu\text{K}/\sqrt{\text{Hz}}$ rising of heterodyne measurement. Because of the low dissipation in the supercurrent branch, we discuss the structure as a bolometer. We analyse noise and dissipation in this system, allowing us to estimate the figures of merit. The electrical Noise Equivalent Power, limited by the amplifier noise, is calculated to be around $2 \cdot 10^{-16} \text{ W}/\sqrt{\text{Hz}}$. This is more than 20 times higher than the thermodynamic noise limit, leaving some room for improvement. The short relaxation time $\tau_{e-ph} \sim 1.6 \mu\text{s}$ would allow faster operation than in the currently available Ti-Transition Edge Sensor. Furthermore, the tunnel junctions allow to overcome the size limitation imposed by the proximity effect present in traditional transition edge sensors, without sacrificing the sensitivity, making the SIS'IS structure a candidate for bolometry.

A Microwave Pumped HEB Direct Detector Using a Homodyne Readout Scheme

Alexander Shurakov¹, Cheuk-yu E. Tong², Raymond Blundell² and Gregory Gol'tsman¹

¹ Moscow State Pedagogical University, 29 Malaya Pirogovskaya Street, Moscow 119992, Russia

²Harvard-Smithsonian Center for Astrophysics, 60 Garden Street, Cambridge, MA 02138, USA

Email: alexander@rplab.ru

We report the results of our study on the noise performance of a fast THz detector based on the repurpose of hot electron bolometer mixer (HEB). Instead of operating with an elevated bath temperature, microwave power is injected into the HEB device, which enhances the sensitivity of the detector and at the same time provide a mechanism for reading out impedance changes of the device induced by the modulated incident THz radiation [1]. We have demonstrated an improvement of the detector's optical noise equivalent power (NEP). Furthermore, by introducing a homodyne readout scheme based on a room temperature microwave mixer, the dynamic range of the detector is increased.

The HEB devices used in this work were made of 4 nm thick NbN film. The detector chips were installed into a waveguide mixer block fitted with a corrugated horn, mounted on the cold plate of a liquid helium cryostat. The HEBs were operated at a bath temperature of 4.2 K. The signal beam was terminated on black bodies at ambient and liquid

nitrogen temperatures. A chopper wheel placed in front of the cryostat window operating at a frequency of 1.48 kHz modulated the input load temperature of the detector. A cold mesh filter, centered at 830 GHz, was used to define the input signal power bandwidth. Microwave was injected through a broadband directional coupler inside the cryostat. Our experiments were mostly conducted at a pump frequency of 1.5 GHz. The reflected microwave power from the HEB device was fed into a cryogenic low noise amplifier (LNA). The output of the LNA was connected to the RF input port of a room temperature microwave mixer, which beat the reflected signal from the HEB using a copy of the original 1.5 GHz injection signal in a homodyne demodulation scheme. The amplitude of the detected power was measured by a lock-in amplifier, which was synchronized to the chopper frequency.

Preliminary results yield an optical NEP of $\sim 1 \text{ pW/ Hz}^{1/2}$ which corresponds to an improvement of a factor of 3 compared to [1], driven mainly by a lowering of the system noise floor. The dynamic range was also increased by similar amount.

References

1. A. Shurakov et al. "A Microwave Pumped Hot Electron Bolometric Direct Detector," submitted on Oct 18, 2013 to *Appl. Phys. Lett.*

3 – Systems & Receivers

Laboratory based terahertz spectroscopy for ice desorption studies of the interstellar medium

Olivier Auriacombe^{*}, Helen Fraser^{*}, Brian Ellison[†] and Simon Rea[†].

^{*}*Dept. of Physical Sciences*

The Open University

Email: olivier.auriacome@open.ac.uk

Email: helen.fraser@open.ac.uk

[†]*Dept. of Space Science*

STFC Rutherford Sppleton Laboratory

Email: brian.ellison@stfc.ac.uk

Email: simon.rea@stfc.ac.uk

During the process of star formation in the interstellar medium (ISM), gas molecules, such as H₂O, CO or CO₂, become trapped on the surface of dust particles (grains) and form ice layers. Within this medium, complex molecules are created by chemical reactions (e.g. HCOOH or CH₃OH). The molecules thus formed are subsequently released (desorbed) though predominantly thermal and non-thermal processes. Non-thermal desorption¹ is due to ionization of the ice by cosmic rays, UV photon absorption, collision between dust particles and chemical reactions on surface (recombination). Studying the chemistry of desorbed species via laboratory-based experiments, and which emulate the physical processes of desorption, provides valuable additional astrophysical information which potentially supports and corroborates astronomical observations and increases our understanding of the desorption mechanisms. This, in turn, increases our knowledge of star formation and star forming regions. However, the majority of ice desorption experiments use absorption spectrum analysis (reflection-absorption infrared spectroscopy); an experimental technique which does not entirely reflect the astronomical observational method, e.g. as used by the Atacama Large Millimetre and submillimetre Array (ALMA) which predominantly observes molecular species in emission. To provide a more direct comparison with observational astronomy performed via ALMA, and to independently study interstellar chemistry, we are developing a sensitive laboratory-based high-spectral-resolution terahertz spectrometer that will allow us to directly observe the spectral emission signatures of molecular species under representative environmental conditions, i.e. those found within the interstellar medium (ultra-high vacuum - <10⁻⁷ mbar and low ambient temperature – 10 K).

As a first step towards the creation of a dedicated facility, we have modified a terahertz spectrometer originally conceived for Earth atmospheric observation. The core of the instrument is a heterodyne radiometer comprising a sub-harmonically pumped image rejection Schottky diode mixer² (SHIRM), a local oscillator, and a high-speed digital spectrometer³, and which we have interfaced with a low pressure 1m gas cell. Combined together, these components provide a highly sensitive single-sideband detection system operating in the region of [320 GHz – 360 GHz] and partially mirroring the spectral range of ALMA band [275 GHz – 373 GHz]. Molecular species are viewed through the cell by the radiometer against a cold (77K) background target and a spectral resolution of 1 MHz, with an instantaneous bandwidth of 4 GHz/sideband, allows spectral profiles to be characterized. We describe the instrument concept and construction, and present preliminary spectral measurements.

References

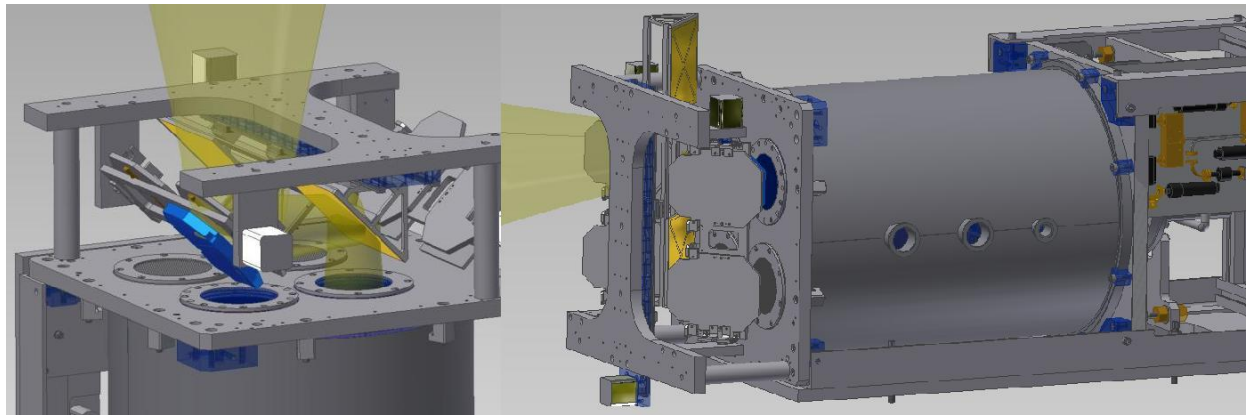
1. H. J. Faser, M. P. Collings, and M. R. S. McCoustra; Review of scientific Instrument, 73, 5 (May 2002), 263-269.
2. B. Thomas, S. Rea, B. Moyna, B. Alderman, and D. Matheson; IEE Microwave and Wireless Components Letters, vol. 19, no. 2, pp. 101-103, Feb. 2009.
3. Spectrometer developed and provided by Star Dundee, Ltd., <http://www.star-dundee.com>

Dual Band MM-Wave Receiver for Onsala 20 m Antenna

I. Lapkin¹, M. Fredrixon¹, E. Sundin¹, L. Helldner², L. Pettersson², S.-E. Ferm¹, M. Pantaleev², V. Belitsky¹

¹ Group for Advanced Receiver Development, ² Electronic Laboratory, Onsala Space Observatory, Department of Earth and Space Sciences, Chalmers University of Technology
Gothenburg, Sweden
E-mail: victor.belitsky@chalmers.se

We present the design and the first light results for the new dual band receiver (4 mm and 3 mm bands) for Onsala Observatory 20 m antenna. For single dish operation, the receiver uses innovative on-source/off-source optical switch. Within the same optical layout, the switch, in combination with additional optical components, provides 2 calibration loads and sideband measurements possibilities. The optics layout of the receiver uses offset elliptical cold mirrors for both channels whereas the on-off switch employs flat mirrors only. The 3 mm channel employs 2SB dual polarization receiver with OMT, 4-8 GHz IF, x 2pol x (USB+LSB). The cryostat has 4 optical widows made of HDPE with anti-reflection corrugations, two for the signal and two for each frequency band cold load. The cryostat employs a two stage cryocooler RDK 408D2 and uses anti-vibration suspension of the cold-head to minimize impact of the vibrations on the receiver stability. The LO system is based on Gunn oscillator with PLL and two mechanical tuners for broadband operation, providing independently tunable LO power for each polarization. At the conference, we will present details on the receiver optics, cryostat design and the result of the first on-sky observations.



Characterization of a Martin-Puplett interferometer of a 2.6THz heterodyne receiver

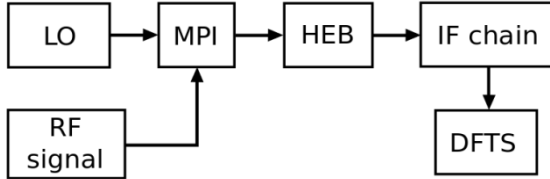
F. Defrance, M. Wiedner, Y. Delorme, M. Batrung, F. Dauplay, A. Feret, G. Gay, H. Gibson, J-M. Krieg, R. Lefèvre, L. Pelay, J. Spatazza, T. Vacelet

Abstract—In this proceeding we characterize the Martin-Puplett interferometer (MPI) of a 2.6 THz heterodyne receiver. It is used to overlay the sky and the local oscillator signal before the mixer. By measuring each component of the MPI and by calculating the atmospheric losses, we could attribute the largest losses in the MPI to the atmospheric transmission and irregular spacings of the wires in a wire grid.

Index Terms—heterodyne receiver, optics, stability, THz

I. INTRODUCTION

Several recent projects in radio astronomy are dedicated to heterodyne measurements in the THz field. For example, the GREAT instrument [1], on SOFIA, which is designed to observe some spectral lines between 1.5THz and 4.7 THz, or Millimetron [2], which is an ambitious project for a future space telescope mission aiming to observe between 0.1THz and 5THz. In order to prepare a receiver for such projects, we built a test receiver at 2.6 THz and characterized it. This heterodyne receiver is composed of a local oscillator (LO), a Martin Puplett interferometer (MPI), a Hot Electron Bolometer (HEB) mixer, an intermediate frequency (IF) chain and a digital Fourier transform spectrometer (DFTS) (see figure).



Our local oscillator is a 2.6THz multiplier-amplifier chain from VDI (Virginia Diodes, Inc) which emits a maximum of about $2\mu\text{W}$ at 2.6THz. The HEB, using a twin slot antenna and a silicon lens, was designed and produced at LERMA (Laboratoire d'Etudes du Rayonnement et de la Matière en Astrophysique et Atmosphère) and LPN (Laboratoire de Photonique et de Nanostructures) and it is optimized for 2.6THz [3]. It uses a NbN (niobium nitride) bridge on a silicon substrate and is phonon cooled. The IF chain includes one cryogenic amplifier from Caltech, two commercial warm amplifiers and a 1.5GHz low pass filter. The DFTS (Digital

Fabien Defrance is a Ph.D. student at the Observatory of Paris, 61 ave de l'Observatoire, 75014 Paris (fabien.defrance@obspm.fr).

We thank the CNES and the Observatory of Paris for providing the Ph.D. Scholarship for Fabien Defrance. The experimental equipment was financed by the CNES (Phase A study for CIDRE), by the DFG (SFB Nachwuchsgruppe) and by INSU (Banc THz, Martin-Puplett). The staff are payed by the CNRS, by the Observatory of Paris, by INSU and by Gibson Microwave Design.

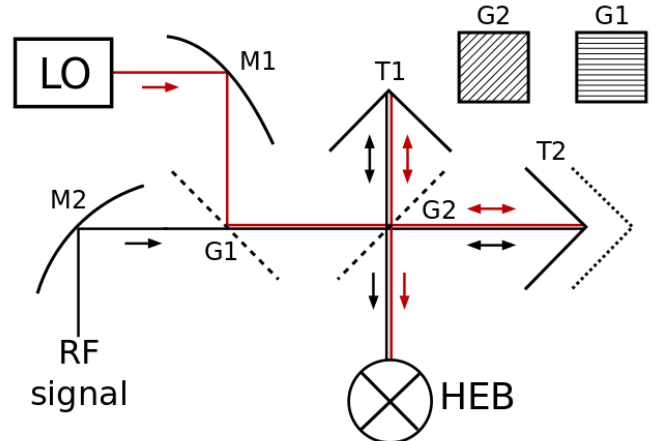
Fourier Transform Spectrometer), from RPG (Radiometer Physics GmbH), has 8192 channels and a bandwidth of 1.5GHz.

To characterize our receiver, we focused on two major points. The Martin-Puplett interferometer that assures the coupling between the local oscillator and the observed radio frequency signal (RF signal), and the stability of the receiver. Here we will describe our investigations of the Martin-Puplett interferometer.

II. MARTIN PUPPLETT INTERFEROMETER

A. Presentation of the Martin Puplett Interferometer

In heterodyne receivers the signal of the sky is mixed with the LO signal. If the mixer has only one port, the signals need to be superimposed optically before the mixer. Usually a beam splitter is used to superimpose the LO signal and the RF signal. However, 80% or 90% of the LO power is lost by the beam splitter. As we don't have a lot of LO power, we couldn't afford to lose that much power, so we decided to use a MPI instead. A MPI is a polarization rotating interferometer. An



MPI has theoretically very little loss, but is a lot more difficult to align than a beam splitter, because it is composed of several elements.

MPIs have previously been used in heterodyne receivers, such as the SMART receiver for KOSMA [4], the CONDOR P.I. receiver for APEX [5] and the GREAT receiver on SOFIA [1] besides others.

Our MPI is composed of two ellipsoidal mirrors, M1 and M2, two wire grids, G1 and G2, and two roof top mirrors, T1 and T2 (see figure). The arrows indicate the propagation of the beams in the MPI. The two squares at the top right of the schematic show the orientation of the wires for both grids. The

mirror T2 can be translated to adjust its distance to G2. A detailed description of the principles of a Martin-Puplett interferometer can be found in Martin and Puplett [6] or Goldsmith [7].

To characterize our MPI we measured the LO power at the output of the MPI with a Golay cell detector. As the measured power was below $1.0\mu\text{W}$, the Golay cell was near its detection limit. However, this experiment revealed that the MPI was losing about 40% of the LO power, without taking into account the atmospheric losses. In order to improve the MPI, we studied all the MPI's elements and characterized their losses.

B. Ellipsoidal mirrors

The two ellipsoidal mirrors were designed at LERMA and fabricated by RPG (Radiometer Physics GmbH). They were specifically designed to match the (simulated) beam pattern of the HEB at 2.6THz. As the reflection losses of an ellipsoidal mirror are not very easily measurable (the beam changes its waist and hence the coupling to the detector changes), we started by verifying the mechanical properties of the ellipsoidal mirrors. We used a profilometer to measure the rms roughness of the mirrors' surface and found 400nm rms. The roughness of the mirrors is responsible for the scattering of the beam. According to Ruze's formula [8], the corresponding directed reflection for a $115\mu\text{m}$ wavelength signal is

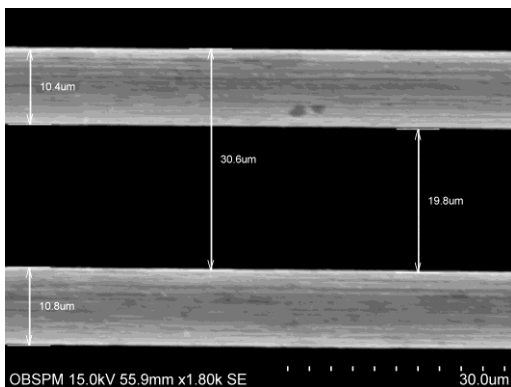
$$R = e^{-(4\pi s_{rms}/\lambda)^2} = 0.998$$

Where s_{rms} is the rms roughness.

The losses due to the mirrors' roughness can be considered as negligible. We also studied the shape of the mirrors and characterized it by measuring the depth profile along their major axis. There was less than 2.5% difference between the theoretical and experimental one. In summary, the mirror fabrication is good and the mirrors are in accordance with our requirements.

C. Wire grids

The two wire grids have been manufactured by the university of Erlangen. After measuring them with a scanning electron microscope, we could confirm that the wires' thickness was $10\mu\text{m}$, as requested (see figure).



The average spacing measured between the wires was $37\mu\text{m}$ very close to the specification of $35\mu\text{m}$. We used the formulas from P.Goldsmith's book [7] to calculate the reflection and transmission efficiencies expected for perfect grids with these parameters.

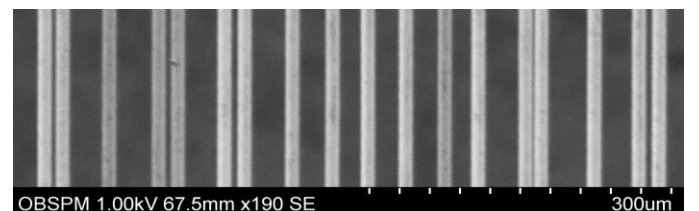
$$R = \left(\frac{1}{1 + 2Z_g/Z_{fs}} \right)^2 \quad \text{and} \quad T = \left(\frac{1}{1 + Z_{fs}/(2Z_g)} \right)^2$$

Where Z_g is the grid impedance and Z_{fs} the characteristic transmission line impedance.

$$\frac{Z_g}{Z_{fs}} = -j\omega_0 \ln \left(\frac{g}{2\pi a} \right) \left(\frac{g}{\lambda\omega_0} - \frac{\lambda\omega_0}{g} \right)^{-1}$$

Where g is the wire spacing and a , the radius of the wires, $\omega_0 \approx 0.85$ is a dimensionless number, based on measurements. It defines the location of the resonance that occurs when g is close to λ [9]. We calculated that our grids should have an efficiency of 99% for both reflection and transmission.

However, with the scanning electron microscope, we observed some important irregularities in the wire spacing (see Figure).



According to J.B. Shapiro [10], the reflection efficiency of the grids also depends on the grid spacing regularity. Shapiro defines the irregularity σ as the standard deviation of the spacings/notch. Their study showed that a value of $\sigma/\lambda = 0.085$ resulted in a reflexion efficiency of 95% (the other 5% were transmitted) and a value of $\sigma/\lambda = 0.06$ in 2% losses. Their study was carried out at lower frequencies (< 600 GHz) and for thicker wires and larger spacings, but the effects are expected to scale with wavelength. A value of $\sigma/\lambda < 0.05$ is necessary to approach the efficiency of an ideal grid [7]. From the figure above we calculated an rms variation σ of $8.2\mu\text{m}$. This corresponds to $\sigma/\lambda = 0.07$ and we would expect losses of a few percent.

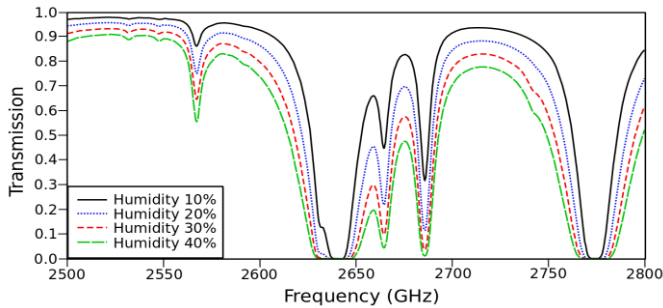
To confirm these theoretical calculations, we used the simulation software HFSS to calculate the reflection and transmission expected for the grids. Perfect grids as well as irregular grids were simulated and the results show that irregularities in the grids can cause noticeable losses (table below).

	Measured	Calculated (HFSS)	
	Real grid	Regular grid	Irregular grid
Transmission	96%	98%	98%
Reflection	80%	98%	88%

In order to measure precisely the transmission and reflection efficiency of our grids, the measurement has been performed with a set of two grids. The first grid was used to eliminate the cross polarization of the LO and the second grid was the one we wanted to characterize. The power was measured by an IR bolometer cooled with liquid helium (from IR labs). We found a transmission of 96% and a reflection of 80%. It also enabled us to measure the cross polarization of the LO, which we found to be 8%. The difference between the simulated losses and the measured losses, are due to 3 factors: 1) The simulations cannot take into account an exact copy of the grid, but works with a typical grid cell that is repeated to make up the grid. This technique is used to reduce the calculation time to less than a day. 2) A reflection angle of 90 degree has not been taken into account. 3) Misalignments of the detector can cause additional losses.

D. Air absorption

At 2.6THz, the water vapor contained in the air absorbs a part of the signal. We used the software am (atmospheric model) developed by Scott Paine [11]. For our optical path length (50cm) and ambient temperature (20°C). It gave us different values of transmission depending on the relative humidity of the air (see figure below).



As we see in the figure, for a relative humidity of 30%, which is the average value for our laboratory, we have a transmission of 80% through 0.5m of air.

III. CONCLUSION

In summary, along with the grids, the water vapor in the air seems to cause the biggest losses in our MPI. Let's estimate the total losses of the MPI. The first grid is seen in transmission for the RF signal and in reflection for the LO signal. Then, the second grid is seen in reflection and in transmission by both signals. The atmospheric absorption is the same for both signals. It gives 49% transmission for the LO signal and 59% transmission for the RF signal (or 61% and 73% not including the atmospheric absorption). It is consistent with our primary measurement, with the Golay cell detector, which was 60% transmission without taking the atmosphere into account. If we add the water vapor absorption, we find a transmission of 48% for the LO signal.

REFERENCES

- [1] Heyminck, S.; Graf, U. U.; Güsten, R.; Stutzki, J.; Hübers, H. W.; Hartogh, "GREAT: the SOFIA high-frequency heterodyne instrument" *Astronomy & Astrophysics*, Volume 542, L1, 2012
- [2] Smirnov, A. V.; Baryshev, A. M.; Pilipenko, S. V.; Myshonkova, N. V.; Bulanov, V. B.; Arkhipov, M. Y.; Vinogradov, I. S.; Likhachev, S. F.; Kardashev, N. S. "Space mission Millimetron for terahertz astronomy" SPIE meeting 2012
- [3] R. Lefèvre, Y. Jin, A. Féret, T. Vacelet, W. Miao, L. Pelay, F. Dauplay, M. Ba-Trung, J. Spatazza, J.-C. Villégier, J.-M. Krieg, Y. Delorme. Terahertz NbN hot electron bolometer fabrication process with a reduced number of steps in Proc. of the 23rd Int. Symp. on Space THz Technology, Tokyo, Japan, April 02-04, 2012
- [4] U. U. Graf, S. Heyminck, E. A. Michael, S. Stank*, C. E. Holing, K. Jacobs, R. Schieder and J. Stutzki "SMART: The KOSMA Sub-Millimeter Array Receiver for Two frequencies" in thirteenth International Symposium on Space Terahertz Technology, Harvard University, March 2002
- [5] Wiedner, M. C.; Wieching, G.; Bielau, F.; Rettenbacher, K.; Volgenau, N. H.; Emprechtinger, M.; Graf, U. U.; Honingh, C. E.; Jacobs, K.; Vowinkel, B.; Menten, K. M.; Nyman, L.-Å.; Güsten, R.; Philipp, S.; Rabanus, D.; Stutzki, J.; Wyrowski, "First observations with CONDOR, a 1.5 THz heterodyne receiver", *Astronomy and Astrophysics*, Volume 454, Issue 2, L33, 2006
- [6] Martin, D. H. and Puplett, E. "Polarised interferometric spectrometry for the millimeter and submillimeter spectrum" *Infrared Phys.*, Vol. 10, p. 105 – 109, 1970
- [7] P. Goldsmith, "Quasioptical Systems" book published by IEEE Microwave Theory and Thechnics Society, 1998
- [8] J. Ruze, "Antenna Tolerance Theory -- A Review", Proceedings of the IEEE, vol. 54, pp 633-642, 1966.
- [9] R.C. McPhedran and D. Maystre, "On the theory and solar application of inductive grids", *Appl. Phys.*, vol. 14, pp. 1-9, 1977
- [10] J.B. Shapiro and E.B. Bloemhof, "Fabrication of Wire Grid Polarizers and Dependence of Submillimeter Optical Performance on Pitch Uniformity", *International Journal of Infrared and Millimeter Waves*, Vol 11, No 8, 1990
- [11] S. Paine "The am atmospheric model", SMA memo 152, 2014 or <https://www.cfa.harvard.edu/~spaine/am/index.html>

The 220 GHz stepped-frequency Imaging Radar

Weidong Hu, Xiangxin Meng, Yu Su and Xin Lv

*Dept. of Electronics Engineering
Beijing Institute of Technology, Beijing, China
Email: hoowind@bit.edu.cn*

Terahertz imaging technology is actively being developed in response to the demand for security applications in recent years. The advance in technology of terahertz (THz) has made possible the detection of THz radiation with solid-state devices operating at room temperature. THz wave has also emerged as a more powerful tool in various areas such as medical, communication, non-destructive inspection of various pharmaceutical, agricultural, and industrial products[1-2].Terahertz imaging is being adopted for non-destructive evaluation (NDE) applications in aerospace and other government and industrial settings[3-5].

Several works have been directed for security applications. Reference “A 600 GHz imaging radar for concealed objects detection” presents the experimental results from a 600 GHz imaging radar with sub-centimeter resolution in all three spatial dimensions. The radar system used a FMCW transceiver built on a back-end of commercial microwave components-with a front-end of custom designed frequency multipliers and mixers. And the resolution is better than one centimeter in all spatial dimensions.The system uses linear sweep frequency (FMCW) across a bandwidth of 30GHz at the center of 580GHz to achieve a range resolution of about 0.5 cm has been demonstrated at Jet Propulsion Laboratory in [6]. Reference [7] also describes how a 630 GHz single-pixel scanned imager was modified to achieve a range resolution of about 2 cm at 4 m range.

All of these systems adopted the CW or FMCW terahertz signals. In the paper, the stepped frequency terahertz pulse series is provided to get the high resolution in axial spatial direction, and other two dimensions are realized. Simulation and experiment both have been finished. The bandwidth of 220GHz stepped-frequency imaging radar is 6GHz. The theoretical resolution is 2.5cm. Some microwave anechoic chamber imaging experiments have been executed. While it is applied in space detection, earth atmospheric composition, chemistry and dynamics of the troposphere, temperature and pressure distribution, dynamics, volcanic activity and ice particles in clouds, surface parameters etc. can be achieved , which will play valuable role in scientific research.

References

1. W. L. Chan, J. Deibel and D. M. Mittleman, “Imaging with terahertz radiation,” *Rep. Prog. Phys.*, Vol. 70, 2007, PP. 1325– 1379
2. J. Fitzgerald, E. Berry, et al., “An introduction to medical imaging with coherent terahertz frequency radiation,” *Phys. Med. Biol.*, Vol. 47, 2002, pp. R67–R84
3. J. V. Rudd, D. Zimdars, and M. Warmuth, “Compact fiber-pigtailed terahertz imaging system,” *Proceedings of SPIE, Commercial and Biomedical Applications of Ultrafast Lasers II*; Joseph Neev, Murray K. Reed; Eds. , San Jose, CA, 3934, (2000) p. 27-35
4. D. Zimdars, “Fiber-pigtailed terahertz time domain spectroscopy instrumentation for package inspection and security imaging,” *Proceedings of SPIE, Terahertz Military and Security Applications*, J. Hwu and D.L. Woolard, Ed., Orlando, Fla., 5070, (2003) p. 108
5. D. M. Mittleman, M. Gupta, R. Neelamani, R. G. Baraniuk, J. V. Rudd , and M. Koch, “Recent advances in terahertz imaging,” *Appl. Phys. B*, 68, (1999) p. 1085
6. K.B. Cooper, R.J. Dengler, G. Chattopadhyay, E. Schlecht, J. Gill, A.Skalare, I. Mehdi, and P.H. Siegel, “A High-Resolution Imaging Radar at 580 GHz”, *IEEE Microwave Wireless Components Letters*, vol. 18, no. 1, pp64-66, Jan. 2008
7. R.J. Dengler, K.B. Cooper, G. Chattopadhyay, I. Mehdi, E. Schlecht, A. Skalare, C. Chen, and P.H. Siegel, “600 GHz imaging radar with 2 cm range resolution,” in *IEEE MTT-S Int. Dig., Honolulu, HI*, Jun. 2007, pp. 1371–1374

Search for New Sites for THz Observations in Eurasia

Grigoriy M. Bubnov^{* †}, Vyacheslav F. Vdovin^{* †} Igor I. Zinchenko^{*}, Vladimir I. Nosov^{*},
Evgeniy B. Abashin^{*}, Oleg S. Bolshakov^{* †} and Stepan Yu. Dryagin^{* †}

^{*}*Dept. of radio receiving equipment and millimeter astronomy
Institute of Applied Physics RAS*

Email: payalnik89@gmail.com

[†]*Laboratory of Cryogenic Nanoelectronics
NNSTU n.a. R.E. Alekseev*

For the ground support of the planned submillimeter wave space VLBI mission (“Millimetron”) an extended network of ground-based facilities operating in this band is needed. Nowadays the number of such observatories is scarce and our goal is to search for appropriate sites in Eurasia. For this purpose during the last two years we performed measurements of atmospheric transparency at millimeter waves at several promising sites. The main measurement tool was the mm-wave radiometric “tau-meter” developed at IAP RAS. It determines the total absorption of millimeter waves at zenith by using the atmospheric dip method. [1]

The first expedition for the astroclimate exploration took place in July 2012. The absorption was measured at the foot of the glacier Mus-Khaya at an altitude of 2000 meters above sea level. The value of absorption amounted to about 0.09 Nep for a few hours, that corresponds to about 5 mm of precipitated water vapor (PWV). Probably in the winter at -50°C the absorption should be substantially lower.

In the central part of Russia, on the contrary, the absorption value does not drop below 0.12 Nep even in the clear frosty day. The unsuitability of this climate zone for mm-wave observations was shown by measurements in Pushchino in March 1013. [2]

Then we explored the site of the RT-70 radio telescope construction on the Suffa plateau in Uzbekistan at the altitude of about 2400 m. The similar radiometric system, but functioning in dual-band (2 and 3 mm) mode, was commissioned in the Suffa observatory in October 2013. The preliminary measurements in mid-November have shown the values of about 0.1 Nep, that corresponds to about 4 mm PWV at an altitude of the Suffa plateau. The results of long-term astroclimate monitoring are expected.

One of the promising locations for mm-waves observations is North Caucasus near the Special Astrophysical Observatory. There are several areas in highland located higher than 2700 meters above sea level with a potentially good astroclimate. The preliminary measurements during several days in December at different altitudes (2000-2700m) have shown stable values of absorption and low amount of water. The regular astroclimate monitoring occurs at the moment.

Furthermore the seasonal variations of PWV were approximately calculated for every place we traveled. Knowing the PWV, the forecast of total absorption for other atmospheric windows (2.0; 1.3 and 0.87 mm) was calculated. Using available information about measured absorption, PWV, height, etc., we can make conclusions about the suitability of the place to locate mm- and sub mm- wave range observatory.

This work was partially supported by a grant of Ministry of Education by order of the Government of the Russian Federation (contract number 11.G34.31.0029).

References

1. I. I. Zinchenko, V. I. Nosov, P. L. Nikiforov, L. I. Fedoseev, A. A. Shvetsov, O. S. Bolshakov. // Proceedings of the Institute of Applied Astronomy RAS, issue 24, pp. 194-198, 2012.
2. E.B. Abashin, G.M. Bubnov, V.F. Vdovin, I.I. Galanin, S. Yu. Dryagin, I. I. Zinchenko, V. I. Nosov / Exploration of atmospheric transparency at millimeter waves in in eastern Yakutia and the central part of Russia // Proceedings of the XVII Scientific Conference on Radiophysics, NNSU, pp 68-70, 2013.

4 – NbN Film Technology

Deposition of high-quality ultra-thin NbN films at ambient temperatures

S. Krause, V. Desmaris, D. Meledin, V. Belitsky *Senior Member IEEE*, M. Rudzinski, E. Pippel

Abstract—This paper discusses the possibility of growing NbN ultra-thin films on Si-substrates and Al_xGa_{1-x}N buffer-layers by means of DC magnetron sputtering without intentional substrate heating. Resistance-temperature measurements were carried out and the superconducting properties such as T_c, ΔT_c and R_□ were deduced while HRTEM gave insight into the crystal structure and film thickness. The adjustment of the partial pressure of argon and nitrogen was found to be critical in establishing a reliable deposition process. The quality of the interface between the NbN film and the substrate was improved by optimizing the total pressure while sputtering, and is therefore particularly valuable for phonon-cooled HEB heterodyne receivers. NbN films of 5 nm thickness were obtained and exhibited a T_c from 8 K on Si-substrates, and up to 10.5 K on the GaN buffer-layers. This result is significant since the absence of a high-temperature environment permits the establishment of more complex fabrication processes for intricate thin-film structures without compromising the overall integrity of e.g. dielectric layers, or hybrid circuitries with e.g. SIS junctions.

Index Terms— NbN ultra-thin films, HEB, epitaxial growth

I. INTRODUCTION

ULTRA sensitive receivers based on superconducting materials provide the basis for the detection of terahertz radiation, both for ground-based and space-born radio astronomical observations [1-2]. For more than two decades, NbN has been used as material for hot electron bolometers (HEB) due to its large energy gap and short electron-electron and electron-phonon interaction times, which yield a decent IF bandwidth of typically 4 GHz [3]. Ultra-thin NbN films with thicknesses 3.5 to 6 nm are usually required and are typically grown by means of DC magnetron sputtering at elevated substrate temperatures in a reactive argon/nitrogen gas mixture. This process is dependent on numerous parameters and has been investigated with the purpose to maintain the quality of the NbN films while reducing their thickness. However, only a few studies exist to date on the investigation of

deposition techniques which do not require high substrate temperatures. More complex processing techniques could be applied by addressing this issue, hence enabling NbN to be e.g. used in other receiver technologies such as SIS junctions [4] or in general multilayer structures based on superconducting materials.

This paper demonstrates the deposition of 5 nm NbN films on Si-substrates and AlGaN layers with excellent crystallographic properties on the GaN epi-layer, confirmed by HRTEM microscopy. The suitability to grow NbN on GaN buffer-layer, was recently demonstrated at elevated temperatures [5] and is here applied for ambient temperature depositions. Superconducting properties of the ultra-thin films were determined by resistance-temperature measurements and T_c, ΔT_c and R_□ were deduced. Furthermore, micro-bridges with dimensions ranging from 4*4 μm to 4*20 μm were fabricated and characterized. The results of the NbN/GaN compound strongly point towards prospective applications in THz electronics, taking advantage of the enhanced superconducting properties of epitaxially grown NbN films combined with the favorable non-heat growth environment.

II. EXPERIMENT

A. Substrates

AlGaN epi-layers were grown by means of MOCVD on sapphire substrates (0002) and exhibited a hexagonal crystal structure. The Al content in the compound was gradually increased in order to investigate the influence of changing lattice parameter within the range of GaN and AlN. The epi-layers exhibited similar thicknesses of approximately 1.2 μm. Furthermore, bare silicon substrates with native oxide layer served as a reference. All substrates were ultra-sonically cleaned in acetone prior to loading, and treated in an argon-plasma before the sputtering of NbN.

B. Deposition

The deposition was carried out in an AJA Orion-6UD DC magnetron sputtering tool. Particular attention was paid to achieving optimal adjustment of the partial argon/nitrogen pressure, and the total pressure while sputtering from the Nb target. The optimal partial pressure is dependent on the total pressure and had to be adjusted accordingly.

Manuscript submitted: 2014-06-10

S. Krause, V. Desmaris, D. Meledin, V. Belitsky are with the Group for Advanced Receiver Development (GARD) at Chalmers University of Technology, Gothenburg, Sweden; e-mail: sascha.krause@chalmers.se

Mariusz Rudzinski was with the Institute of Electronic Materials Technology (ITME), Warsaw, Poland.

E. Pippel is with the Max Planck Institute of Microstructure Physics, Halle/Saale, Germany.

C. Characterization

All films were first characterized by R(T) measurements in a dedicated four-point-probe measurement set-up. The best films on silicon substrates and GaN buffer-layer were used to fabricate micro-bridges using photo-lithography techniques and dry etching in CF_4 to pattern the bridges. Investigation of the structural properties and the confirmation of the targeted thickness was conducted by HRTEM.

III. RESULTS

A. $R(T)$ measurement

Characteristic properties of the deposited films were extracted from resistance versus temperature measurements. **Ошибка! Источник ссылки не найден.** depicts the evolution of T_c for different Al content in the AlGaN compound and relates it to the film properties on bare silicon. A high T_c of 10.5 K has been obtained for low Al content of up to 20 % in the AlGaN layer. Above this, the T_c slowly deteriorated and approached the value of bare silicon.

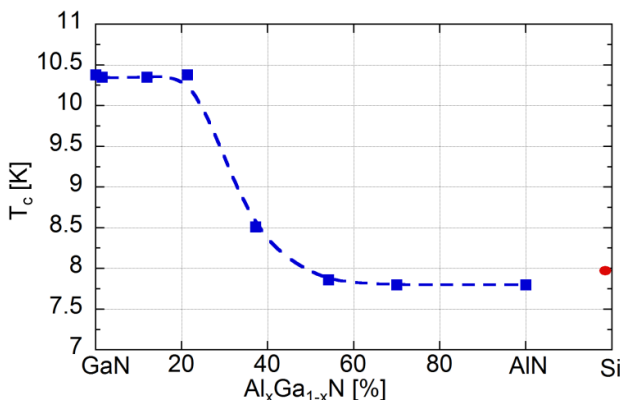


Fig. 29. Critical temperature versus Al content on AlGaN and Si substrates deposited at room temperature

B. Structural properties - HRTEM

After their electrical characterization, specimens of the NbN films were prepared both on the Si-substrate and the GaN epi-layer. Therefore, a thin Ti/Au layer was evaporated on the silicon substrates and a Nb-layer on the GaN sample in order to provide sufficient contrast.

The NbN film on silicon exhibits a poly-crystalline structure, and is arranged in differently sized grains. The ultra-thin NbN grown onto the GaN buffer-layer on the other hand, features epitaxial growth, as seen in **Ошибка! Источник ссылки не найден..**

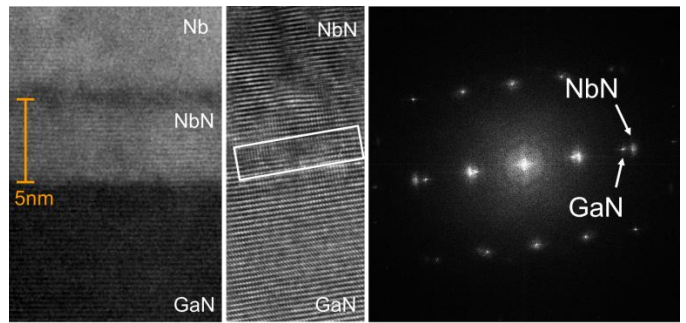


Fig. 30. Epitaxially grown NbN films of 5 nm thickness. Indicated interface with very few defects. The Fourier transformed diffraction pattern supports the lattice match to the underlying GaN buffer-layer.

The left-hand side confirms the thickness of 5 nm, whereas the interface between the GaN layer and NbN match perfectly within one atomic layer. Furthermore, analysis of segments within the NbN and GaN layer yield the Fourier transformed diffraction pattern which supports the epitaxial nature of the NbN and its high quality.

IV. CONCLUSION

The presented properties of 5 nm thick NbN films grown at ambient temperatures on GaN buffer-layer are in accordance with the results from [5], presenting the growth at elevated temperature above 525 °C on GaN buffer-layers. A critical temperature of 10.5 K was achieved on AlGaN layer with Al content of up to 20 % and is therefore comparable with other lattice matched substrates, such as MgO [6]. Apart from its advantageous processibility over MgO, is it resistance to chemicals. Optimization of both the total pressure and the partial pressure of argon and nitrogen can improve the quality of the interface to NbN, thus, may benefit the phonon-escape in HEBs. The demonstration of the possibility to grow NbN without intentional substrate heating on AlGaN layer in high quality may pave the way for the integration of NbN in more complex multi-layer structures.

REFERENCES

- [1] C. Kulesa, "Terahertz Spectroscopy for Astronomy: From Comets to Cosmology" in *IEEE Transactions on Terahertz Science and Technology*, vol.1, no. 1, 2011.
- [2] D. Meledin et al. "A 1.3THz Balanced Waveguide HEB Mixer for the APEX Telescope", *IEEE Trans. Microw. Theory Tech.*, vol. 57, p. 89, 2009.
- [3] S. Cherednichenko, V. Drakinskiy, J. Baubert, J.-M. Krieg, B. Voronov, G. Goltsman and V. Desmaris, "Gain bandwidth of NbN hot-electron bolometer terahertz mixers on 1.5μm Si3N4/SiO2 membranes", *J. Appl. Phys.* 101, 124508, 2007.
- [4] Belitsky, V. et al. "Design and performance of ALMA band 5 receiver cartridge", *35th International Conference on Infrared Millimeter and Terahertz Waves (IRMMW-THz)*, 2010.
- [5] S. Krause et al., "Epitaxial growth of ultra-thin NbN films on $\text{Al}_x\text{Ga}_{1-x}\text{N}$ buffer-layers" in *Supercond. Sci. Technol.*, vol. 27, no. 6, 065009, Mar. 2014.
- [6] A. Kawakami, "Design and Fabrication of NbN terahertz hot electronolometer mixer", *24th Int. Symp. on Space Terahertz Technology*, 2013.

Study of NbN ultra-thin films for THz hot-electron bolometers

Victor P. Afanas'ev, Sascha Krause, Alexander V. Lubchenko, Alexander A. Batrakov,
Vincent Desmaris, Alexey B. Pavolotsky, Victor Belitsky

Abstract— Hot-electron bolometer (HEB) mixers based on superconducting ultra-thin NbN films are largely used for THz spectroscopy for space and ground-based observations. Performance of the HEB mixers directly depends on the details of the structure and composition of thin film surface, as well as the nitrogen composition and its depth distribution. In this work, we present the study of the composition and the surface oxidation state of NbN films grown at two different temperatures and of 5 and 10 nm thickness.

Index Terms—Hot-electron bolometers, NbN, surface analysis, thin films

I. INTRODUCTION

HOT-ELECTRON bolometer (HEB) mixers based on superconducting ultra-thin NbN films are largely used for THz spectroscopy for space and ground-based observations [1], [2], [3]. The performance of the HEB mixers directly depends on the details of the structure and composition of the thin-film surface, as well as the nitrogen composition and its depth distribution.

The composition of the NbN film affects its superconducting transition critical temperature and width of the transition. Besides the effect on the superconducting critical temperature itself, deviation from the stoichiometric NbN composition causes an increase of the normal resistivity of the film, as well as the precipitation of the second phases. At its interface with the substrate, the NbN film composition can be affected by the substrate material. It is natural to expect the effect of the substrate material to be dependent on the temperature, at which the NbN film was grown. Keeping in mind that the NbN films are ultra-thin, typically 5 nm thick, one could expect that, if present, the effect of the substrate material on the NbN stoichiometry manifests differently for films with different thicknesses. From the other side, at the outer surface of the film, a natural oxide layer is unavoidable when films are exposed to air. The latter eventually provides additional and unwanted series resistance to the bolometer

device, thus, the knowledge about the thickness and composition of the natural oxide layer over the NbN film is much desired.

In this work, we present the study of the composition and the surface oxidation state of NbN films grown at two different temperatures and of 5 and 10 nm thickness.

II. EXPERIMENT

The NbN ultra-thin films were deposited on (100)-Si substrates by means of DC magnetron reactive sputtering of Nb in the N₂-containing atmosphere using an AJA Orion-6UD sputtering system. The system is evacuated by a turbo pump and equipped with a load-lock thus achieving base pressure of $< 2 \times 10^{-8}$ Torr. The 99.95% Nb 2-inch diameter magnetron is placed about 10 cm away from the substrate and slightly off-centered and tilted from the normal to the substrate table [4], allowing highly uniform, $< 2\%$ variation, deposition rate across the 4-inch substrate table. The substrate holder was pre-heated to either 650°C and maintained at this temperature during the sputtering (further referred as hot deposition) or kept at ambient temperature during the deposition (further referred as cold deposition). The deposition rate was kept about 1.2 Å/s. The further details on the deposition process are reported in [5], [6].

Thin film were analysed with a help of X-ray Photoelectron Spectroscopy (XPS) and Reflected Electron Energy Loss Spectroscopy (REELS). For the studies, the sources of primary electrons (Kimball Physics EMG 4212 with BaO cathodes), and X-rays (SPECS XR-50) were employed. Electron energy spectra have been recorded using semi-spherical energy analyzer SPECS Phoibos 225 with absolute energy resolution of 0.3 eV within 0-15 keV range. The NbN films have been studied by means of X-ray Photoelectron Spectroscopy (XPS) and Reflected Electron Energy Loss Spectroscopy (REELS).

III. RESULTS AND DISCUSSION

With XPS, we studied the oxidized layers at the NbN films surface; the sort of the oxides and their thicknesses were identified. Fig. 1 presents XPS spectra recorded on the studied NbN films. The recorded spectra are represented as a superposition of the peaks of Nb 3p3/2, Nb-O and Nb-N bonds. From that, one can conclude that metallic niobium is not present in the NbN film samples. The eventually residual

Manuscript received June 13, 2014.

V. P. Afanas'ev, A. V. Lubchenko, A. A. Batrakov are with the Department of General Physics and Nuclear Fusion, National Research University "Moscow Power Engineering Institute", Moscow, 111250 Russia (e-mail: LubchenkoAV@mpei.ru).

S. Krause, V. Desmaris, A. B. Pavolotsky, V. Belitsky are with the Group of Advanced receiver Development (GARD), Chalmers University of Technology, Gothenburg, 41296, Sweden (e-mail: Alexey.Pavolotsky@chalmers.se).

Nb 3p3/2 peak seen for the 5nm film deposited on the hot substrate (Fig. 1a) is likely an artefact of the CasaXPS software extracting individual peaks out of the measured superimposed spectrum [7].

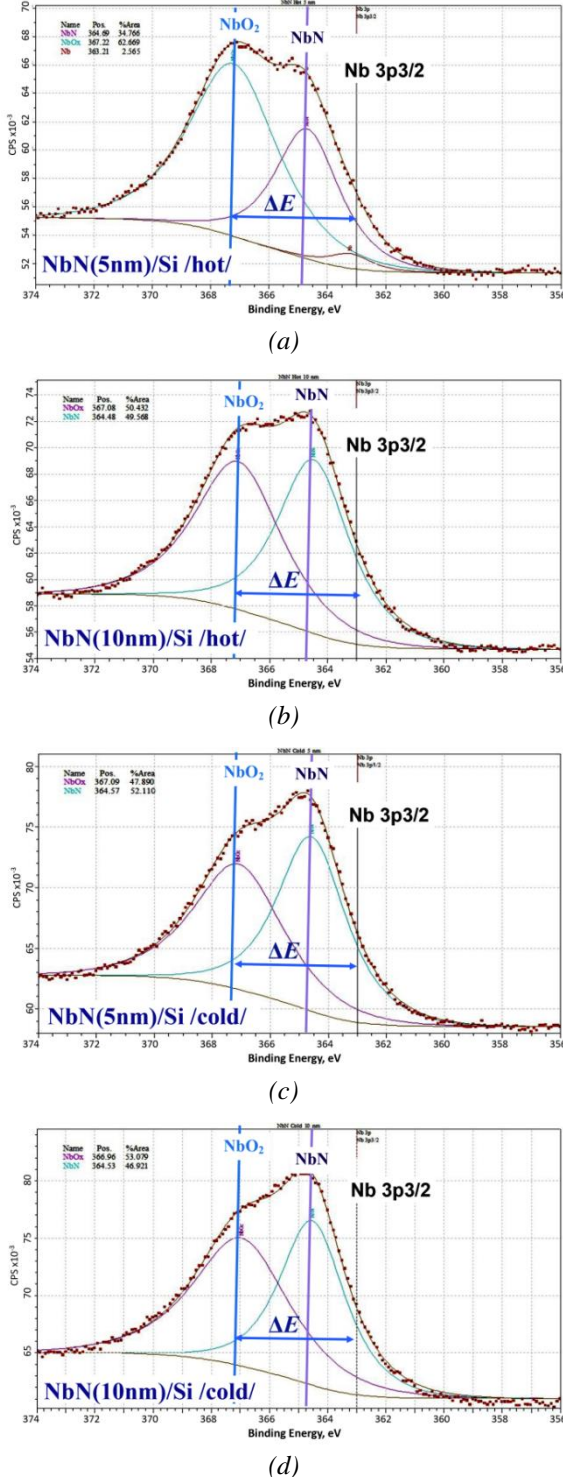


Fig. 1. XPS spectra, recorded on the *NbN* films. Dots represent experimental data; solid lines show results of representation of the spectrum as a superposition of the peaks of *Nb* 3p3/2, *Nb-O* and *Nb-N* bonds (CasaXPS software). (a) – 5 nm *NbN* film deposited on the hot substrate; (b) – 10 nm *NbN* film deposited on the hot substrate; (c) – 5 nm *NbN* film deposited on the cold substrate; (d) – 10 nm *NbN* film deposited on the cold substrate.

The shift ΔE (Fig 1a-d) of the *Nb-O* peak position in respect to the position of the *Nb* 3p3/2 peak gives the stoichiometry of the natural oxide [8] at the *NbN* film surface. The observed identical position of the *Nb-O* peaks for all four films indicates the identical composition of the natural oxide films on top of the *NbN*.

Accounting for the peak intensity ratio for *NbN* and *Nb-O*, I_{Nb-O}/I_{Nb-N} , allows the evaluation of the oxide film thickness:

$$d_{NbO_x} = \cos(\gamma) \lambda_{in_{NbO_2}} \ln \left(\frac{I_{NbO_2}}{I_{NbN}} \frac{\lambda_{in_{NbN}}}{\lambda_{in_{NbO_2}}} + 1 \right),$$

where λ_{in} is inelastic mean free path (IMFP) calculated following [9], $\gamma = 54.74^\circ$ angle between the X-ray beam and the direction towards the energy analyzer. The data on the stoichiometry and thickness of the natural oxide films are summarized in the Table I.

TABLE I STOICHIOMETRY AND THICKNESS OF NbO_x FILMS

Sample	ΔE , eV	Oxide composition	Oxide Thickness, nm
Nb	4.9	Nb_2O_5	1.5
<i>NbN</i> 5 nm, cold substrate	4.1	NbO_2	0.9
<i>NbN</i> 5 nm, hot substrate	4.0	NbO_2	0.6
<i>NbN</i> 10 nm, cold substrate	4.1	NbO_2	0.5
<i>NbN</i> 10 nm, hot substrate	4.1	NbO_2	0.6

Fig. 2 presents the REELS spectra recorded for *NbN* films, as well as for thick *Nb* film and reference spectra from [10]. Comparing the REELS spectra for the *NbN* films of different thickness and grown on hot and cold substrates, one can see that the *NbN* plasmon peaks appear at the same electron energy loss. This confirms that the stoichiometry for all *NbN* films is identical for all deposition conditions. One can also extract concentration of the valent electron n_e from REELS data. Energy of electron plasmon oscillation ε_p is defined by the concentration of valent electrons n_e :

$$\varepsilon_p = \hbar e \sqrt{\frac{n_e}{m_e \epsilon_0}}$$

where m_e – electron mass, \hbar - Planck constant, ϵ_0 - permittivity of free space.

The extracted valent electrons concentration in the studied *NbN* films and thick *Nb* film as reference, as well as in their natural surface oxides are summarized in the Table II.

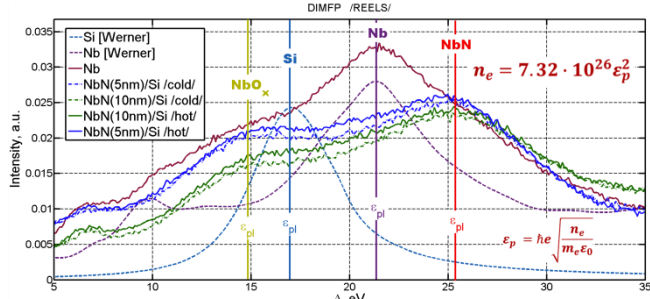


Fig. 2. Differential inelastic scattering cross sections (differential inverse mean free path, DIMFP) extracted by Tougaard method [11].

TABLE II CONCENTRATION OF VALENT ELECTRONS IN Nb, NbN FILMS AND THEIR SURFACE OXIDES

Sample	$n_e, 10^{29} \text{ m}^{-3}$		
	Nb	NbN	NbO_x
Nb	3.38 ± 0.16	-	1.4 ± 0.6
NbN 5nm, cold substrate	-	4.7 ± 0.4	1.6 ± 0.6
NbN 5nm, hot substrate	-	4.7 ± 0.4	1.6 ± 0.6
NbN 10nm, cold substrate	-	4.7 ± 0.4	1.5 ± 0.6
NbN 10nm, hot substrate	-	4.7 ± 0.4	1.5 ± 0.6

IV. CONCLUSION

We have studied the composition and the surface oxidation state of NbN films grown at elevated and ambient temperatures and of 5 and 10 nm thickness. We have found that all the studied films have identical stoichiometry, with no dependence on layer thickness. All studied films do not contain metallic Nb , so the nitridation is complete; no evidence of any second phase has been found. Stoichiometric composition and thickness of oxidized surface layer has been

identified. For all NbN films, the natural oxide layer consists of Nb_2O_5 , in contrast to the one formed on Nb film, which contains Nb_2O_3 oxide. The concentration of valent electrons in NbN films and their oxide layers have been extracted from REELS data.

REFERENCES

- [1] E. Gershenson, G. Gol'tsman, I. Gogidze, Y. Gusev, A. Elantiev, B. Karasik and A. Semenov, *Sov. Phys.—Supercond.*, vol. A3, p. 1582, 1990.
- [2] V. Belitsky, I. Lapkin, V. Vassilev, R. Monje, A. Pavolotsky, D. Meledin, D. Henke, O. Nyström, V. Desmaris, C. Risacher, M. Svensson, M. Olberg, E. Sundin, M. Fredrixon, D. Dochev, S.-E. Ferm and H. Olofsson, in *Infrared and Millimeter Waves, 2007 and the 2007 15th International Conference on Terahertz Electronics. IRMMW-THz, 2-9 Sept. 2007, Cardiff, 2007*.
- [3] D. Meledin, A. Pavolotsky, V. Desmaris, I. Lapkin, C. Risacher, V. Perez, D. Henke, O. Nyström, E. Sundin, D. Dochev, M. Pantaleev, M. Fredrixon, M. Strandberg, B. Voronov, G. Goltsman and V. Belitsky, *IEEE Trans. Microw. Theory Tech.*, vol. 57, p. 89, 2009.
- [4] AJA International Inc., P.O.Box 246, N. Scituate, MA 02066, USA, "<http://www.ajaint.com/>," [Online].
- [5] S. Krause, D. Meledin, V. Desmaris, A. Pavolotsky, V. Belitsky, M. Rudziński and E. Pippel, *Supercond. Sci. Technol.*, vol. 27, p. 065009, 2014.
- [6] S. Krause, V. Desmaris, D. Meledin, V. Belitsky, M. Rudzinski and E. Pippel, in *The 25th International Symposium on Space Terahertz Technology, 27-30 April 2014, Moscow, 2014*.
- [7] N. Fairley, CasaXPS Manual 2.3.15 Spectroscopy, TeignmouthDevon: Casa Software Ltd, 2009.
- [8] M. V. Kuznetsov, A. S. Razinkin and A. Ivanovskii, *Phys. Usp.*, vol. 53, p. 995, 2010.
- [9] S. Tanuma, C. J. Powell and D. R. Penn, *Surf. Interf. Anal.*, vol. 20, p. 77, 1993.
- [10] S. M. Werner, "Database for electron spectroscopy," [Online]. Available: <http://eapclu.iap.tuwien.ac.at/~werner/data.html>.
- [11] S. Tougaard and I. Chorkendorff, *Phys. Rev. B*, vol. 35, p. 6570, 1987.

5 – THz Sources

Terahertz Emission from Silicon Nanostructures Heavily Doped with Boron

Nikolay T. Bagraev*, Andrey .K. Kaveev†, Leonid E. Klyachkin*, Anna M. Malyarenko*, Vladimir A. Mashkov*,
Dmitrii I. Tsypishka†, and Ilya A. Vinerov†

* *Ioffe Physical Technical Institute, St. Petersburg, Russia*

Email: impurity dipole@mail.ioffe.ru

† *TYDEX, LLC., Domostroitelnaya str. 16, 194292 St. Petersburg, Russia*

Email: andreykaveev@tydex.ru

The THz emission from the microcavities embedded in silicon nanostructures appears to be revealed by measuring with the Bruker-Physik VERTEX 70 FT-IR spectrometer.

The device has been prepared on the n-type Si (100) surface within frameworks silicon planar technology. Making a mask and performing photolithography after preliminary oxidation, the short time diffusion of boron was used to obtain the ultra-shallow p+-n junctions [1]. The cyclotron resonance measurements as well as the infrared and local tunneling spectroscopy data have shown that the p+-boron diffusion profile represent the ultra-narrow p-type silicon quantum well (Si-QW), 2 nm, confined by the δ-barriers, 3 nm, heavily doped with boron, $N(B)=5\cdot10^{21}\text{cm}^{-3}$ on the n-type Si (100) surface. The SIMS and STM studies have shown that the δ-barriers represent really alternating arrays of silicon empty and doped dots, with dimensions restricted to 2 nm. This extremely high concentration of boron seems to indicate that each doped dot located between empty dots contains two impurity atoms of boron. The EPR studies show that these boron pairs are the trigonal dipole centers, B(+) - B(-), that contain the pairs of holes, which result from the negative-U reconstruction of the shallow boron acceptors, $2B(0)\Rightarrow B(+) + B(-)$.

This device appears to allow the THz emission of the dipole boron centers inside the δ-barriers which is caused by the stabilized drain-source current along the Si-QW plane. The corresponding series of the electroluminescence (EL) spectral lines are in an agreement with the values of the negative-U energy gap, 0.044 eV, and the excited states of trigonal boron dipole centers [1]. This THz emission lines, 1.35, 2.9, 3.4, 5.3 and 10.6 THz, are found to be enhanced by inserting the corresponding planar cavities, 4, 8 and 16 microns.

Besides, the 0093 THz and 0.129 THz emission spectral lines caused by also the radiation of the dipole boron centers are revealed by measuring the Shapiro and Fiske steps, which are identified also as the modulation frequency of the black body radiation of the device [2]. These findings seem to be due to the oscillations of the heat capacity that are induced by the THz emission of the dipole boron centers inside the δ-barriers confining the Si-QW. Finally, by varying the values of the drain-source current and the lateral voltage applied in the Si-QW plane, the phase shifts of the THz modulation of the black body radiation appear to be observed as a result of the negative-U properties of the dipole boron centers.

References

1. N.T. Bagraev, E.Yu Danilovsky., D.S. Gets, W. Gehlhoff, L.E. Klyachkin, A.A. Kudryavtsev, R.V. Kuzmin, A.M. Malyarenko, V.V. Romanov, Journal of Modern Physics, 2, 256 (2011)
2. S. Shapiro, A.R. Janus, S. Holly, Rev. Mod. Phys., 36, 223 (1964)

Monolithically integrated 440 GHz doubler using Film-Diode (FD) technology

I.Oprea¹, H.J. Gibson^{2,3}, O. Cojocari¹ A. Walber³ and T. Narhi⁴

¹ACST GmbH, Hanau, Germany

Email: oprea@acst.de

²Gibson Microwave Design EURL, Antony, France

Email : gibson@radiometer-physics.de

³RPG Radiometer Physics, Meckenheim, Germany

⁴ESA/ESTEC Noordwijk, Netherlands

This work presents results of a recently developed frequency doubler at 440 GHz. The doubler is realized using a balanced planar MMIC doubler approach with only one high breakdown-voltage varactor diode per arm. The diodes are connected in anti-series (DC) and are suspended on thick beamleads directly in the input waveguide. This approach allows a simple but very effective thermal coupling of the anode mesa trough massive metallic beamleads to the WG-block, providing good heatsink for the dissipated power.

The doubler showed peak efficiency exceeding 21% and (simultaneously) an output power of nearly 12 mW at 440GHz. Of particular interest is the quality of the varactor, with near ideal breakdown voltage, very low RF series resistance and optimal doping density, allowing a simple, well-heatsunk 2-diode design to be used.

This power and efficiency represents European state-of-the-art performance in this frequency range and is comparable to the highest efficiency and power for a single device worldwide.

A Schottky Diode Frequency Multiplier Chain at 380 GHz for a gyro-TWA Application

Zhe Chen^{*†}, Hui Wang[†], Byron Alderman[†], Peter Huggard[†], Bo Zhang^{*} and Yong Fan^{*}

^{*}School of Electronic Engineering

University of Electronic Science and Technology of China, Chengdu, China

[†]Science and Technology Facilities Council, Rutherford Appleton Laboratory, Didcot, UK

In this paper, we report on the design of a Schottky diode doubler chain to generate 10 mW over 360-395 GHz to drive a gyrotron travelling wave amplifier (gyro-TWA). This chain consists of two frequency doublers; the first stage is required to handle an input power of 200 mW at W-band. The doubler chain could potentially act as a source to drive subsequent frequency multipliers to produce output power at terahertz (THz) frequencies; this is highly attractive to meet the increasing demand on the local oscillator (LO) systems of THz heterodyne receivers.

The circuit topology of both doublers is based on a balanced configuration [1]. The physical and geometrical parameters of the diodes in both doublers were optimized to ensure reasonable conversion efficiency and sufficient output power at each stage. For the first stage, the diode chip with 6 anodes was designed to be soldered onto a 50 μm thick aluminum nitride (AlN) substrate, which provides better heat spreading than quartz due to its higher thermal conductivity. As shown in Fig.2, with an input of 200 mW the first stage doubler can produce around 50 mW of power to drive the second stage. The second doubler is an integrated structure on 12 μm thick GaAs with two diodes in an anti-series configuration. The fabrication is currently on-going and the measurements results will be presented at the conference.

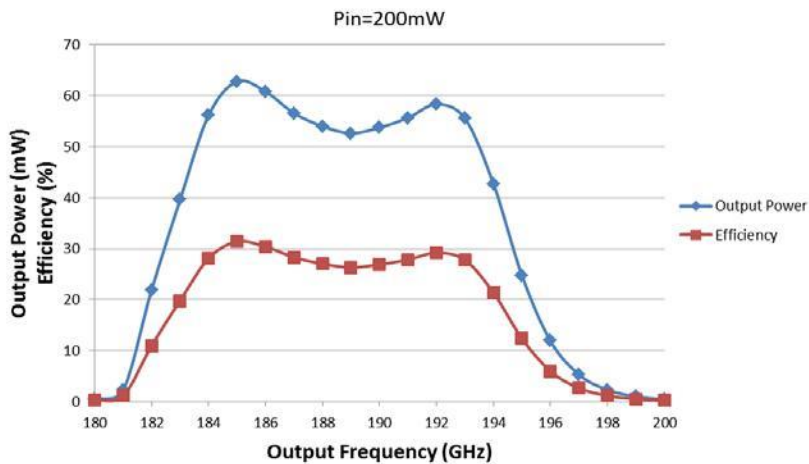


Fig.1 Predicted performance of the first stage doubler.

This work is carried out at the STFC-Rutherford Appleton Laboratory and is supported by the Engineering and Physical Sciences Research Council (EPSRC), UK.

References

1. N. Erickson, "High efficiency submillimeter frequency multipliers," in IEEE MTT-S Int. Microwave Symp. Dig., 1990, pp. 1301–1304.

Phase-locking of a 3.1THz quantum cascade laser to terahertz reference generated by a frequency comb

Yoshihisa Irimajiri, Motohiro Kumagai, Isao Morohashi, Akira Kawakami, Norihiko Sekine, Shigeo Nagano, Satoshi Ochiai, Shukichi Tanaka, Yuko Hanado, Yoshinori Uzawa, and Iwao Hosako

National Institute of Information and Communications Technology, Koganei, Tokyo, Japan*

* Contact: irimaji@nict.go.jp, phone +81-42-327-6089

Abstract— We are developing a low noise heterodyne receiver at 3THz band for applications of atmospheric and astronomical research and for application of wireless communications. We have developed a phase-locking system of a terahertz quantum cascade laser (THz-QCL) by using a hot electron bolometer mixer. The THz-QCL was locked to terahertz reference generated by an optical frequency comb and a photo mixer. The beat signal with IF frequency of 230MHz was compared with a microwave reference, and the error signal was applied to a loop filter with feedback to the bias current of the THz-QCL. The line width of the phase-locked beat signal of narrower than 1Hz which is limited by the resolution bandwidth of a spectrum analyzer was achieved.

I. INTRODUCTION

We are developing a HEBM (Hot Electron Bolometer Mixer) using a THz-QCL (quantum Cascade Laser) as a local oscillator for atmospheric or astronomical observations. For these applications, it's important to reduce the line width and the phase noise of the THz local oscillator and to give it the absolute frequency. Although the FWHM of free running THz-QCL is around 20kHz within the short-period (several milliseconds) [1], [2], it's around 10MHz in the longer integration time due to the instability of the temperature and the bias [2].

Several reports have been published for phase-locking of the THz-QCL. They are phase-locking of THz-QCL by using a harmonic mixer [3], [4], [5], that of 1.5THz QCL to solid state oscillator and frequency multiplier chains [6], that of 2.7THz QCL to the 15th harmonic generated by a semiconductor superlattice nonlinear devices [7], that using a free-space THz-comb and HEBM [8], that using a PCA (Photo Conductive Antenna) and a frequency comb [9], and that using a EO sampling by ZnTe crystal and a frequency comb [10]. Frequency-locking of 2.55 THz-QCL to absorption line of methanol gas was also reported [11].

We have developed a phase-locking system of a THz-QCL using a HEBM to detect a beat signal between a THz-QCL and a THz reference. THz reference signal was generated by photomixing two optical modes of a frequency comb.

II. PHASE-LOCKING SYSTEM OF A THz-QCL

Figure 1 shows a system block diagram of a phase-locking system of a THz-QCL. A beat signal detected by a HEBM with IF frequency of 230MHz was compared with a microwave reference, and the error signal was applied to a loop filter with feedback to the bias current of the THz-QCL.

THz-CW signal was generated by photomixing two optical modes of a frequency comb. Figure 2 shows a system block diagram of the THz-CW source. The CW-THz source is composed of a Mach-Zehnder-modulator (MZM)-based flat comb generator (MZ-FCG), a nonlinear (NL) fiber, band pass filters, and a photo mixer [12]. Figure 3 shows a detailed system block diagram and photographs of a phase-locking system of the THz-QCL.

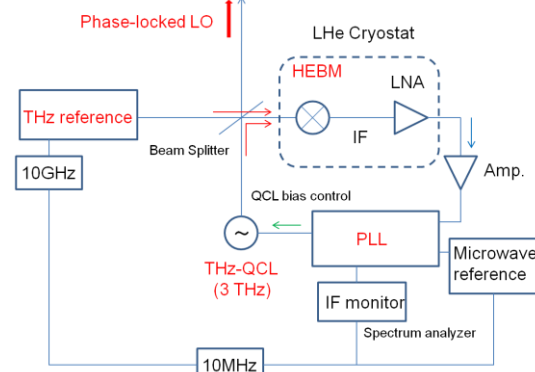


Fig. 1. A System block diagram of a phase-locking system.

As for the THz-QCL, metal-metal type waveguide type THz-QCL was fabricated in our clean room. The size of waveguide structure is 40 μ m in width and 1.5 mm in length. Figure 4 shows a measured voltage and laser power characteristics as a function of current. The operation current and voltage is around 133mA and 11.4V, respectively. Therefore, the electric power consumption is about 1.5W. The laser output power is about 100 μ W at a heat sink temperature of 15K in CW mode. Figure 5 shows a measured spectrum using a Fourier transform spectrometer. The longitudinal mode oscillating frequencies for the main modes are 3.07 THz and 3.09 THz. Frequency tuning sensitivities by the bias current is ~30MHz/mA.

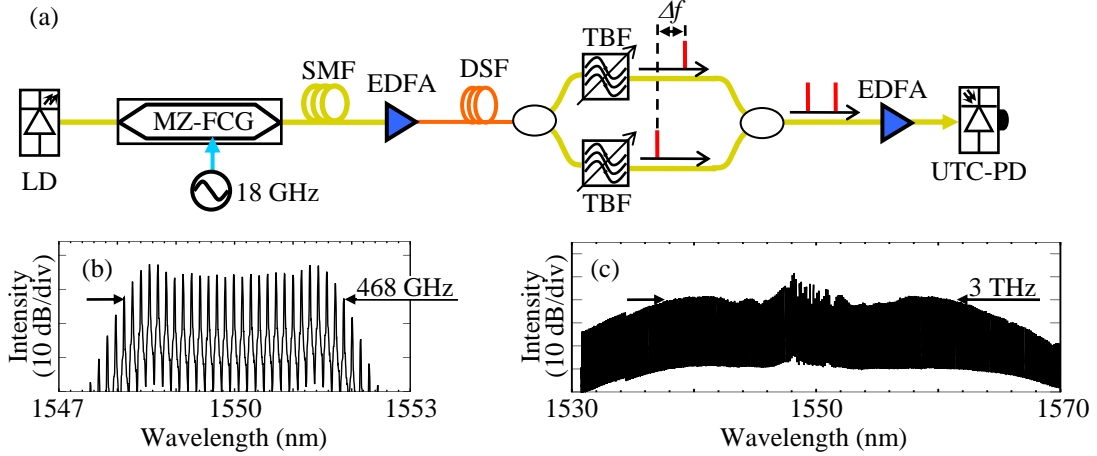


Fig. 2. (a) System block diagram of a CW-THz source composed of a modulator-based comb source. Broadband optical combs were generated by a combination of a Mach-Zehnder-modulator-based flat comb generator (MZ-FCG) and a dispersion-shifted fiber (DSF). Optical two-mode signals were extracted from the comb by using a pair of tunable bandpass filters (TBFS), and CW-THz signals were generated by a unitraveling carrier photodiode (UTC-PD). LD: laser diode, SMF: single-mode fiber, EDFA: erbium-doped fiber amplifier. Spectra of comb signals (a) generated by the MZ-FCG and (c) broadened by the DSF.

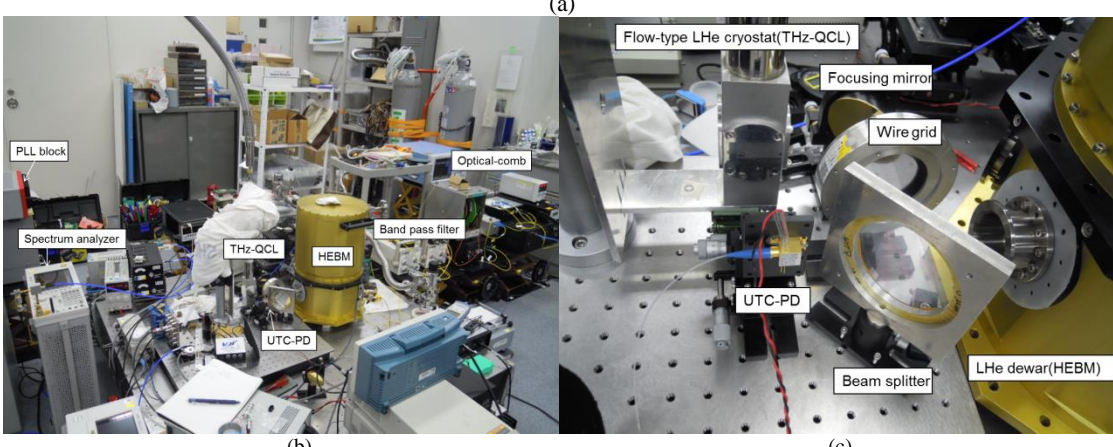
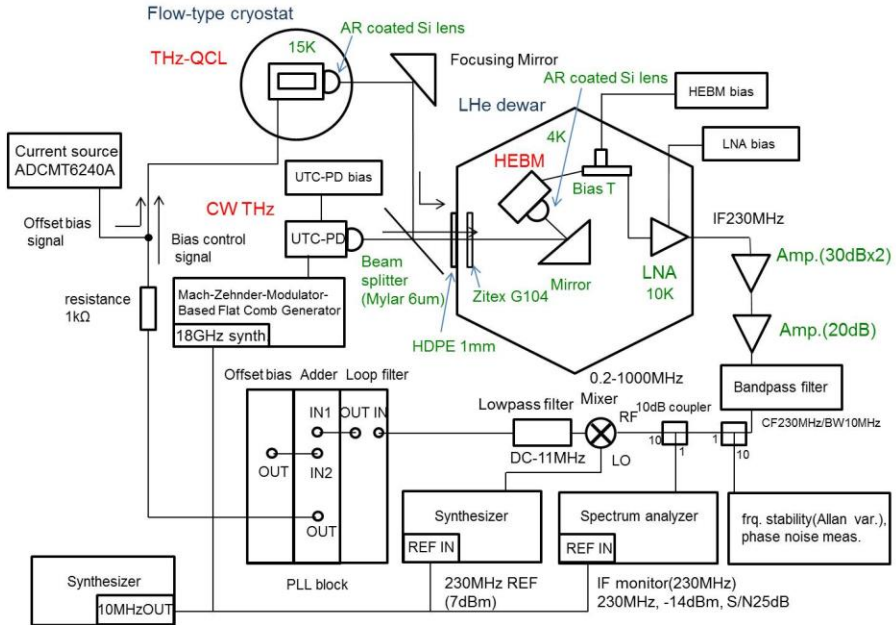


Fig. 3. A detailed system block diagram (a) and photographs (b), (c) of a phase-locking system of the THz-QCL.

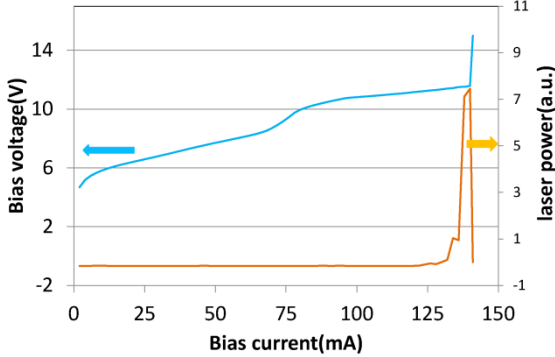


Fig. 4. Measured current vs voltage (I-V) curve (blue line) and current vs laser power characteristics (red line) at heat sink temperature of 15K. The maximum laser power is $\sim 100\mu\text{W}$ in CW mode.

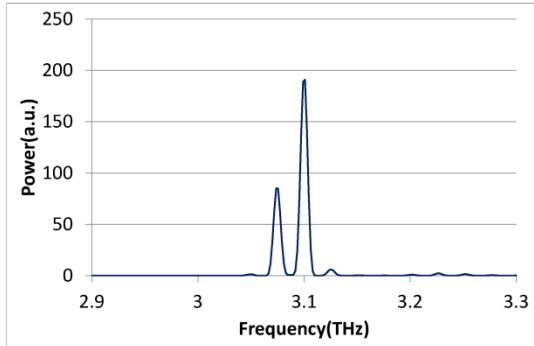
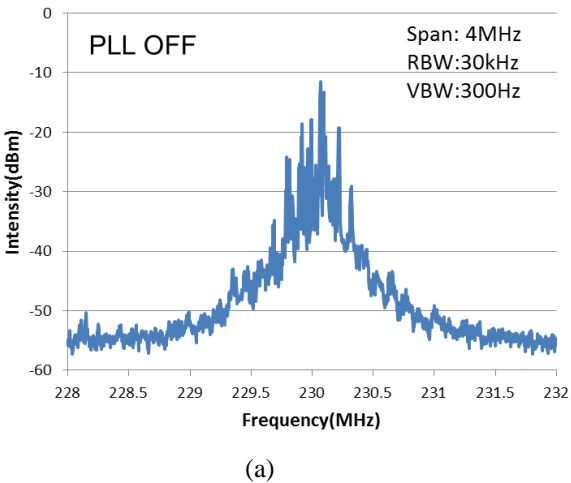


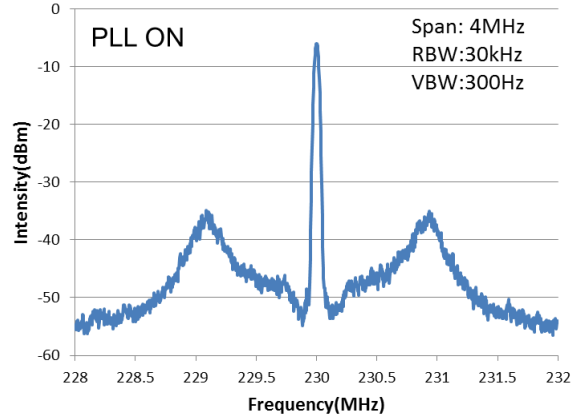
Fig. 5. Measured frequency spectrum of the THz-QCL operated in CW mode by using a FTIR. The longitudinal mode oscillating frequencies for the main modes are 3.07 THz and 3.09 THz.

III. RESULTS

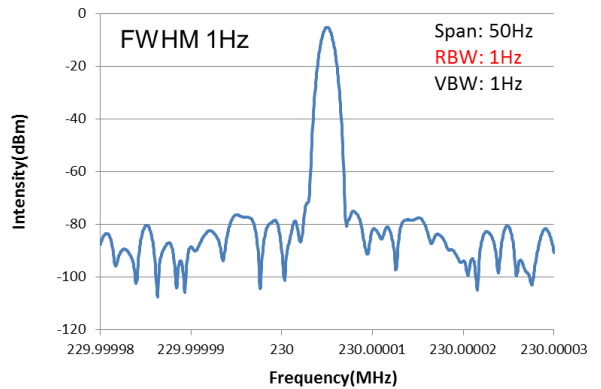
Figure 6 (a) and (b) show measured beat signals for PLL OFF and PLL ON (span: 4MHz, RBW: 30kHz, VBW: 300Hz). The signal to noise ratio for phase locked signal is more than 40dB. Figure 6(c) shows the phase locked beat signal with resolution band width of 1Hz. The FWHM (Full Width Half Maximum) is better than the limit of the resolution of the spectrum analyzer of 1Hz.



(a)



(b)



(c)

Fig. 6. Measured beat signals for PLL OFF (a) and PLL ON (span: 4MHz, RBW: 30kHz, VBW: 300Hz) (b). The SN ratio for phase locked signal is more than 40dB. Figure 6(c) shows the phase locked beat signal with resolution band width of 1Hz. The FWHM is better than the limit of the resolution of the spectrum analyzer of 1Hz.

As the next step, we actually used the phase-locked THz-QCL as a local oscillator for a heterodyne receiver. Another HEBM was installed in the same LHe dewar and a portion of the THz-QCL radiation was coupled in to the HEBM. We prepared a VDI 3THz CW source as a test signal and confirmed that the heterodyne receiver with the phase-locked THz-QCL worked properly. We will further investigate the performance of the phase-locked THz-QCL in terms of residual phase noise and frequency stability. Figure 7 shows a system block diagram and a photograph.

IV. SUMMARY

We have developed a phase-locking system of a THz-QCL by using a HEBM as a detector and a THz-CW generated by photomixing two optical modes of a frequency comb. The FWHM of the phase locked beat signal is better than 1Hz which is the limit of the resolution band width of the spectrometer. The performance of the heterodyne receiver using the HEBM and the phase-locked THz QCL was preliminary evaluated. For future application, low power consumption, reduction in size and weight etc. are important issues.

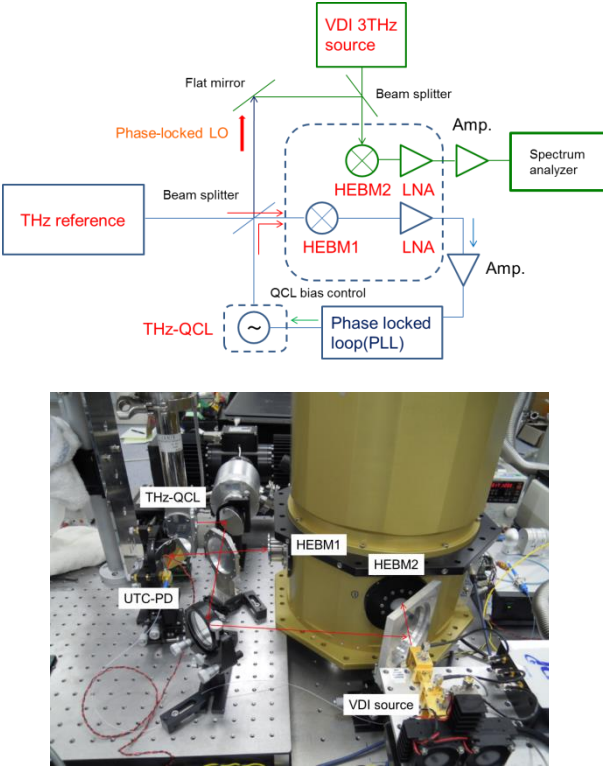


Fig. 7. The phase-locked THz signal is used as a local oscillator for another HEBM installed in the same LHe dewar. The beat signal using a VDI 3THz CW source was measured with FWHM of less than 1Hz same as the phase-locked LO source.

REFERENCES

- [1] H.-W. Hubers, S. G. Pavlov, A. D. Semenov, R. Kohler, L. Mahler, D. A. Ritchie, and E. H. Linfield, "Terahertz quantum cascade laser as local oscillator in a heterodyne receiver," Opt. Express, vol.13, no.15, 2005.
- [2] A. Barkan, F. K. Tittel, and D. M. Mittleman, R. Dengler and P. H. Siegel, G. Scalari, L. Ajili, and J. Faist, H. E. Beere, E. H. Linfield, A. G. Davies, and D. A. Ritchie, "Linewidth and tuning characteristics of terahertz quantum cascade lasers," Opt. Lett., vol.29, no.6, pp.575-577, 2004.
- [3] N.R. Erickson, A.A. Danylov, A.R. Light, J. Waldman, X. Qian, W.D.Goodhue , "Frequency Locking of a QCL at 2.3 THz using a Harmonic Mixer", ISSTT2013 proceedings, 2013.
- [4] A. Khudchenko, D. J. Hayton, D. Paveliev, J. N. Hovenier, A. Baryshev, J. R. Gao, T-Y. Kao, Q. Hu, J.L. Reno, and V. Vaks, "Phase-locking of a 3.4-THz quantum cascade laser using a harmonic super-lattice mixer", ISSTT2013, proceedings, 2013.
- [5] D. J. Hayton, A. Khudchenko, D.G. Paveliev, J.N. Hovenier, A. Baryshev1, J. R. Gao1, T.Y. Kao4, Q. Hu, J.L. Reno and V. Vaks, "Phase-locking of a 4.7 THz quantum cascade lasers based on a harmonic super-lattice mixer", ISSTT, Moscow, 2014.
- [6] D. Rabanus, U. U. Graf, M. Philipp, O. Ricken, J. Stutzki, B. Vowinkel, M. C. Wiegner, C. Walther, M. Fischer, and J. Faist, "Phase locking of a 1.5 Terahertz quantum cascade laser and use as a local oscillator in a heterodyne HEB receiver," Opt. Express, vol.17, no.3, pp.1159-1168, 2009.
- [7] P. Khosropanah, A. Baryshev, W. Zhang, W. Jellema, J. N. Hovenier, J. R. Gao, T. M. Klapwijk, D. G. Paveliev, B. S. Williams, S. Kumar, Q. Hu, J. L. Reno, B. Klein, and J. L. Hesler, "Phase locking of a 2.7THz quantum cascade laser to a microwave reference," Opt. Lett., vol.34, no.19, pp.2958-2960, 2009.
- [8] L. Consolino, A. Taschin, P. Bartolini, s. Bartalini1, P. Cancio, A. Tredicucci, H. E. Beere, D. A. Ritchie, R. Torre, m. s. Vitiello, and P. De natale, "Phase-locking to a free-space terahertz comb for metrological-grade terahertz lasers", Nature Communications, 3:1040, DOI: 10.1038/ncomms2048.
- [9] M. Ravaro, C. Manquest, C. Sirtori, S. Barbieri, G. Santarelli, K. Blary, J.-F. Lampin, S. P. Khanna, and E. H. Linfield, "Phase-locking of a 2.5 THz quantum cascade laser to a frequency comb using a GaAs photomixer", Opt. Lett., vol.36, no.20, 2011.
- [10] M. Ravaro, P. Gellie, G. Santarelli, C. Manquest, P. Filloux, C. Sirtori, J.-F. Lampin, G. Ferrari, S. P. Khanna, E. H. Linfield, H. E. Beere, D. A. Ritchie, and S. Barbieri, "Stabilization and Mode Locking of Terahertz Quantum Cascade Lasers", IEEE J. Sel. Top. Quant. Electron., vol. 19, no.1, 2013.
- [11] H. Richter, S. G. Pavlov, A. D. Semenov, L. Mahler, A. Tredicucci, H. E. Beere, D. A. Ritchie, and H.-W. Hubers, "Submegahertz frequency stabilization of a terahertz quantum cascade laser to a molecular absorption line," Appl. Phys. Lett., 96, 071112, 2010.
- [12] I. Morohashi, Y. Irimajiri, T. Sakamoto, T. Kawanishi, M. Yasui, and I. Hosako, "Generation of Millimeter Waves with Fine Frequency Tunability Using Mach-Zehnder-Modulator-Based Flat Comb Generator", IEICE Trans. Electron., vol. E96-C, no. 2, pp.192-196, 2013.

6 – THz Optics

Spline Feed Horns for the STEAMR Instrument

Arvid Hammar^{*†}, Yogesh Karandikar^{*}, Per Forsberg^{*}, Anders Emrich^{*} and Jan Stake[†]

^{*} Omnisys Instruments AB

August Barks gata 6B, SE-42132 Västra Frölunda, Sweden Email: arvid.hammar@omnisys.se

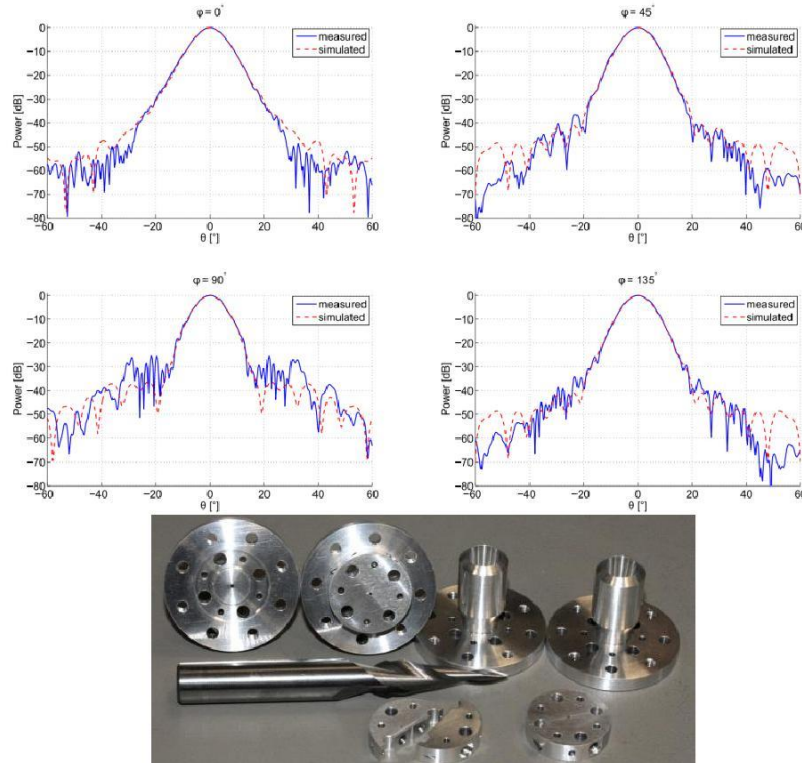
[†]Terahertz and Millimetre Wave Laboratory

Department of Microtechnology and Nanoscience – MC2

Chalmers University of Technology, Göteborg, Sweden

A smooth walled spline feed horn antenna at 340 GHz for STEAMR [1] has been designed, manufactured and measured using a planar near-field scanner. The design was based on a method which, for a certain desired beam waist, can be used to optimize the horn profile for high Gaussicity and ultra-low sidelobes. A beam waist of 1.9 mm over the band 323-357 GHz with Gaussian coupling efficiency exceeding 98% and cross-polar sidelobe levels below -28 dB was achieved in the simulations. In order to avoid de-focusing losses, the horn design was optimized so that variations of the waist location inside the horn aperture were minimized. Simulations reveal a variation less than 0.8 mm over the operating frequency band. The feed horns were manufactured by drilling out the spline profile from a solid metal block using a custom-made broach. This method is cost effective and ensures high repeatability.

Phase and amplitude of the feed horns were measured in a plane located approximately 70 mm from the horn aperture. The results show a Gaussicity of approximately 97% and a waist radius of 1.9 mm located 11.8 mm inside the antenna aperture.



Figures showing beam patterns in four different cuts from measurements (solid lines) and simulations (dashed lines) and a photo of four prototype feeds, rectangular to quadratic waveguide transitions and the custom-made broach used for manufacturing the feeds.

References

1. K. Kerridge, M. Hegglin, J. McConnell, D. Murtagh, J. Orphal, V. Peuch, M. Riese, and M. v. W. (2012, feb), Report for mission selection: Premier, esa sp-1324/3. [Online]. Available: http://esamultimedia.esa.int/docs/EarthObservation/SP1324-3_PREMIER.pdf

1.9-2.5 THz and 4.7 THz electroformed smooth-wall spline feedhorns for the HEB mixers of the upGREAT instrument onboard SOFIA aircraft

B. Thomas¹, H. Gibson¹, P. Krahe¹, S. Hees¹, A. Walber¹, P. Pütz², and C. Risacher³

¹Radiometer Physics GmbH, Birkenmaastrasse 10, 53340 Meckenheim, Germany

Email: thomas@radiometer-physics.de

²KOSMA, Universität zu Köln, Zülpicher Str. 77, 50937 Köln, Germany

Email: puetz@ph1.uni-koeln.de

³Max-Planck-Institut für Radioastronomie, Auf dem Hügel 69, 53121 Bonn, Germany

Email: crisache@mpifr-bonn.mpg.de

The upGREAT instrument is the second generation of receivers currently being built for the GREAT project [1]. upGREAT will extend the single pixel GREAT receivers to 14-pixel 1.9-2.5 THz (LFA) and 7-pixel 4.7 THz (HFA) focal plane arrays for much increased mapping efficiency. In order to couple the incoming beam from the main reflector into the waveguide based HEB mixers from KOSMA, it was decided to use smooth-wall spline feed horn antennas similar to [2] and redesigned to match the upGREAT optical requirements. This type of horns has performance comparable to corrugated feedhorn antennas in terms of directivity, return losses, side lobe and cross-polarization levels, but are significantly easier to manufacture using conventional electroforming techniques, as they have smooth side walls. The main challenge comes from the extremely small rectangular waveguide size interface between the horn and the mixers (96 um x 48 um cross-section for the LFA horn, and 48 um x 24 um for the HFA horn). RPG has manufactured high precision mandrels featuring the smooth-wall spline profile horn antenna and circular-to-rectangular transition with micron accuracy using beryllium-copper milling. The mandrels have then been electroplated and etched in order to make the horn antenna. The post-machining tolerance measurements are in-line with the requirements. The underlying design for both feedhorns is similar and for the LFA frequencies a verification of the beam pattern is planned by MPIfR/KOSMA. If proven successful, this will be, to the authors' knowledge, the highest frequency for a electroformed feedhorn manufacturing with performance comparable to that of a corrugated one.

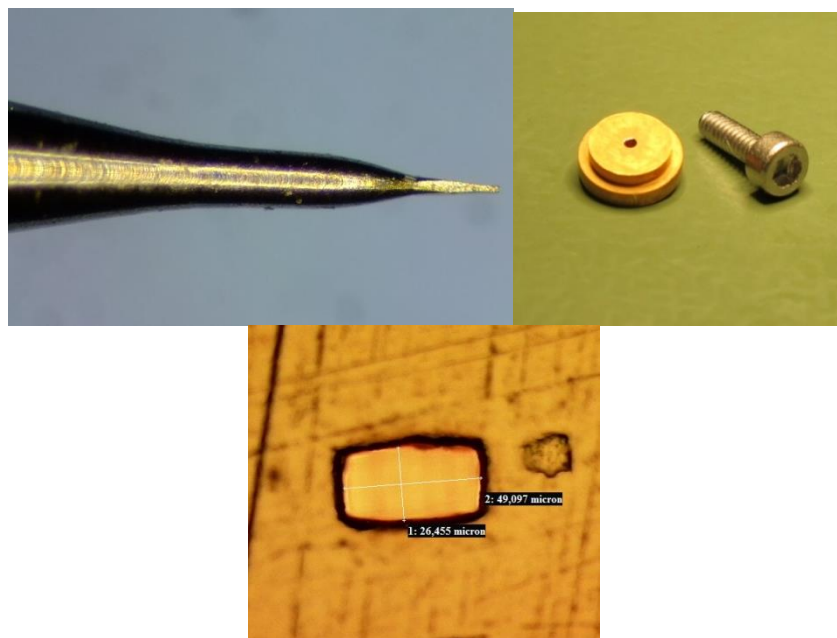


Fig. 1. Left: mandrel for the 4.7 THz horn. Right: delivered 4.7 THz horn antenna.

References

1. upGREAT website at MPI: <http://www3.mpifr-bonn.mpg.de/div/submmtech/>
2. "A smooth-walled spline-profile horn as an alternative to the corrugated horn for wide band millimeter-wave applications", C. Granet et al., IEEE Trans. on Antenna and Propagation, Vol.52, No.3, March 2004

Condition of Optical systems Independent of Frequency for Wide Field-of-View Radio Telescope

Hiroaki Imada, Makoto Nagai, Masumichi Seta, Masaru Kino, Shun Ishii and Naomasa Nakai

Abstract—We present a condition of optical systems independent of frequency. We have known the condition independent of frequency in case of a single Gaussian beam on an optical axis, but have not known one in case of a beam propagated off the axis or tilted beam, which appears in a wide field-of-view telescope. We first show relations between an arbitrary electric field on an object and induced one after passing through a lens with calculating Fresnel diffraction. If the lens formula is met, there is a one-to-one correspondence between points on the object and image plane. This result shows we can use methods of the geometrical optics. The condition and relations derived here are confirmed by simulation. We also apply them to a wide field-of-view telescope.

Index Terms—Physical theory of diffraction

I. INTRODUCTION

WIDE field-of-view (FOV) telescopes for observing in sub-mm or THz region have been and are being developed, e.g. SPT [1], ACT [2] and CCAT [3]. In optical and infrared region, telescopes with FOV of more than 1 degree were developed e.g. Schmidt telescopes or designed using geometrical optics, e.g. [4].

There are a few characteristics of a wide field of view. First, in general, wide FOV systems have many mirrors to cancel the aberrations, not only to transmit beams. Second, we can now use a free-form surface e.g. [5], which allows us to have more choice in designing optical systems. Finally, beams propagate various paths, i.e. most of them are kept away from and tilted against the optical axis. It means that a concept of “pupil” grows greatly important.

We now focus on influence of diffraction seen in a wide FOV system. It has not been studied sufficiently in both radio and optical regions. In case of the Gaussian beam, according to [6], the beam radius at specific positions does not depend on frequency in case that the Gaussian beam propagates on the optical axis. The conditions showed in [6] are not sufficient when we apply them to a wide FOV system due to the characteristics above. We have to find applicable conditions of

a wide FOV system.

Reference [7] calculated an electric field induced by an arbitrary electric field expanded into a summation of fundamental and higher order mode Gaussian-Hermite beams. Using beam-mode transfer matrices of quadratic surface mirrors (lens), [7] showed that the distribution on the image plane can be calculated by scaling or magnifying that on the object plane without depending on frequency in case that the two planes met the lens formula. Relation of wavefront between the object and image plane, however, cannot be acquired unless the electric field is expanded into a summation of Gaussian-Hermite beams.

We can use the Fresnel diffraction integral instead of expansion of the electric field and using beam-mode transfer matrices. Reference [8] showed the calculation of the Fresnel integral but did not integrate on the object plane or take into consideration finally quadratic terms present in the phase terms.

We would like conditions, relations or equations applicable to a wide FOV system as simply as possible. It is shown that an electric field on the image plane is calculated by Fresnel diffraction integral on a single lens and the object plane and that the relation is investigated between the object and image plane in Section II. Relations between the Geometrical optics and the derivation in Section II are treated briefly in Section III. Numerical simulations verify the condition and equation derived here in Section IV and shows in Section V that we can apply them to a wide FOV telescope.

II. CALCULATING FRESNEL DIFFRACTION INTEGRAL

Fig. 1 represents the model for calculating the Fresnel diffraction integral. The xyz -coordinate is set as shown in Fig. 1 and an electromagnetic wave with a wavenumber of k propagates from the negative region of z to the positive. There is an axially symmetric lens at $z = 0$ with a radius of R , a focal length of $f > 0$ and no aberrations. We refer to the plane at $z = a$ as an object plane and to the plane at $z = b$ as an image plane, respectively. We now consider only in case of $a < 0$ and $b > 0$. (ξ_1, η_1) and (ξ_2, η_2) represent the coordinate on the object and image plane, respectively. $E_{\text{obj}}(\xi_1, \eta_1)$, $E_{\text{lens}}(x, y)$ and $E_{\text{img}}(\xi_2, \eta_2)$ are the field expressed by a complex number on the object plane, lens and image plane, respectively. The time dependence is assumed as $\exp(-i\omega t)$, where $i = \sqrt{-1}$.

Manuscript received 1 June 2014

H. Imada, M. Nagai, M. Seta and N. Nakai are with University of Tsukuba, Tsukuba, Ibaraki 305-8571 Japan (corresponding author to provide phone: +81-29-853-5600 (ext.8299); e-mail: s1330093@u.tsukuba.ac.jp).

M. Kino is with Kyoto University, Kyoto, Kyoto 606-8502 Japan.

S. Ishii was with University of Tsukuba. He is now with the University of Tokyo, Mitaka, Tokyo 181-0015 Japan

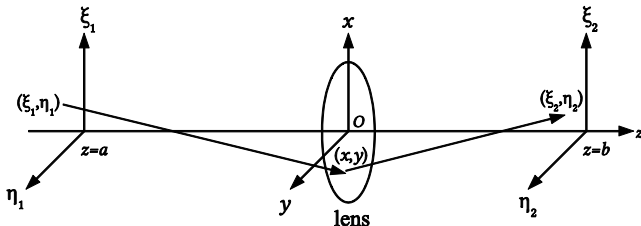


Fig. 1. Model for calculating the Fresnel diffraction integral. There is a lens with a focal length of f at $z = 0$. The plane at $z = a$ and $z = b$ is called “object plane” and “image plane”, respectively. The coordinates (x, y) , (ξ_1, η_1) and (ξ_2, η_2) are defined as shown.

Assuming the paraxial approximation which means $1/k \ll x, y, \xi, \eta, R \ll a, b, f$, paying attention to the phase transformation at the lens and using the Fresnel diffraction integral, we express the fields as follows.

$$\begin{aligned} E_{\text{img}}(\xi_2, \eta_2) &= \frac{k^2}{4\pi^2 ab} \exp\left(ik(b-a) + ik \frac{\xi_2^2 + \eta_2^2}{2b}\right) \\ &\times \int d\xi_1 \int d\eta_1 E_{\text{obj}}(\xi_1, \eta_1) \exp\left(-ik \frac{\xi_1^2 + \eta_1^2}{2a}\right) \\ &\times \int dx \int dy \exp\left[-ik \frac{x^2 + y^2}{2} \left(\frac{1}{f} + \frac{1}{a} - \frac{1}{b}\right) + ikx \left(\frac{\xi_1}{a} - \frac{\xi_2}{b}\right) \right. \\ &\quad \left. + iky \left(\frac{\eta_1}{a} - \frac{\eta_2}{b}\right)\right] \end{aligned} \quad (1)$$

Equation (1) shows that the field distribution $E_{\text{obj}}(\xi_1, \eta_1)$ on the object plane and the wavenumber k define the distribution $E_{\text{img}}(\xi_2, \eta_2)$ on the image plane. We seek conditions which make the distribution $E_{\text{img}}(\xi_2, \eta_2)$ independent of the wavenumber k , that is,

$$E_{\text{img}}(\xi_2, \eta_2) = C(a, b) E_{\text{obj}}(\alpha\xi_2, \alpha\eta_2) \exp(ik\Delta), \quad (2)$$

where $C(a, b)$ and Δ are real coefficients. Evaluating the integral, we acquire

$$\frac{1}{f} + \frac{1}{a} - \frac{1}{b} = 0, \quad (3)$$

otherwise we cannot obtain the relation like (2). Equation (3) represents the lens formula. Thus, the relation is acquired, $E_{\text{img}}(\xi_2, \eta_2)$

$$= \frac{a}{b} E_{\text{obj}}\left(\frac{a\xi_2}{b}, \frac{a\eta_2}{b}\right) \exp\left(ik(b-a) + ik \frac{a\xi_2^2 + \eta_2^2}{2f}\right). \quad (4)$$

In case of any sign of a, b and f , (4) holds when the position a and b meet the lens formula.

III. RELATION TO GEOMETRICAL OPTICS

When we have a closer look at (4), there is a one-to-one correspondence between the points $(\xi_1, \eta_1) = (a\xi_2/b, a\eta_2/b)$ and (ξ_2, η_2) . It means that we can treat the field distribution with the geometrical optics on the plane, where the lens formula holds. Equation (4) saves us a lot of time to apply the equations introduced in [6] and [7] to a wide FOV system with many mirrors because geometrical optics allows us to know the equivalent single lens system of it which is obtained by a ray tracing simulation or by the formula combining two focal lengths of f_1, f_2 .

$$\frac{1}{f_{\text{comb}}} = \frac{1}{f_1} + \frac{1}{f_2} - \frac{d}{f_1 f_2}, \quad (5)$$

where f_{comb} is the equivalent focal length and d is the distance between the two lenses. In addition, we can apply to a complicated system with free-form surfaces whenever the ray tracing simulation tells us where the object and image plane is.

The “pupil” is one of the most important concepts in the geometrical optics. In general, various beams each propagate on their own paths in a wide FOV system except for the pupil, where all of them are piled up on the same position. The lens formula always holds on all of the pupils because they are images of one another. In addition, it is most important that the entrance pupil (Fig. 6) defines beam patterns of a telescope. When we set an electric field distribution on a specific pupil unrelated to propagating directions and apply (4) to it and the entrance (exit) pupil, the electric field distributions of all the beams are the same one and always independent of frequencies on them. Thus, a frequency-independent system is simply obtained. All we have to do is investigate where the entrance and exit pupil are with a ray tracing simulation or (5), and to determine beam parameters on the pupil.

IV. VERIFICATION OF THE RELATION

In this section, we verify the relation of (4). We apply to one spherical mirror system with a focal length $f = -150$ mm. We run an electromagnetic simulation by Grasp8 and compare simulation results with the expected one by (4). Fig 2 shows the one mirror system. Three Gaussian beams enter the mirror, on- and off-axis with a frequency of 500 GHz and off-axis with a frequency of 1 THz. The beam waists of the 500 GHz beams are located at $z = 450$ mm in Fig 2. We first investigate the field distribution of the incident beams on the plane named obj1, obj2 and obj3 at $z = 200, 300$ and 600 mm, respectively. The beams reflect and then we calculate the distribution of the reflected beams on the plane named img1, img2 and img3 at $z = 600, 300$ and 200 mm, respectively, by Grasp8 and substituting the distribution on the obj1, obj2 and obj3 for (4). Finally we compare the distribution by Grasp8 and (4).

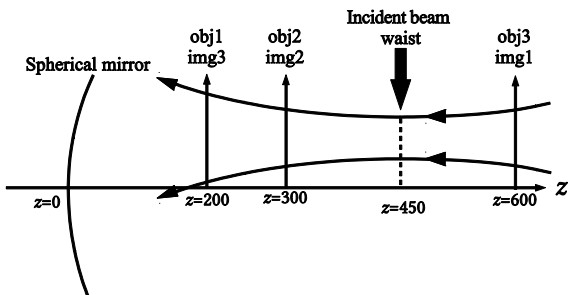


Fig. 2. One mirror simulation model. A beam propagates from the positive z axis and reflects to the same positive region.

Fig. 3 and Fig. 4 show the results for the 500 GHz beams. The electric distributions expected by (4) agree with that calculated by Grasp8 very well. The finite size of the spherical mirror affects the distribution distant from the center. The

results of calculating the phase by (4) also agree with that by Grasp8 near the center.

We also confirm whether or not the electric distributions and phase on specific position are independent of the beam frequencies. The 500 GHz off-axis beam and 1THz off-axis

beam have the same distribution and phase at the obj2. The results are shown in Fig. 5. Expect for the region where the effect of the finite mirror size exists, the distribution and phase of both frequencies at the img2 shows the same shape.

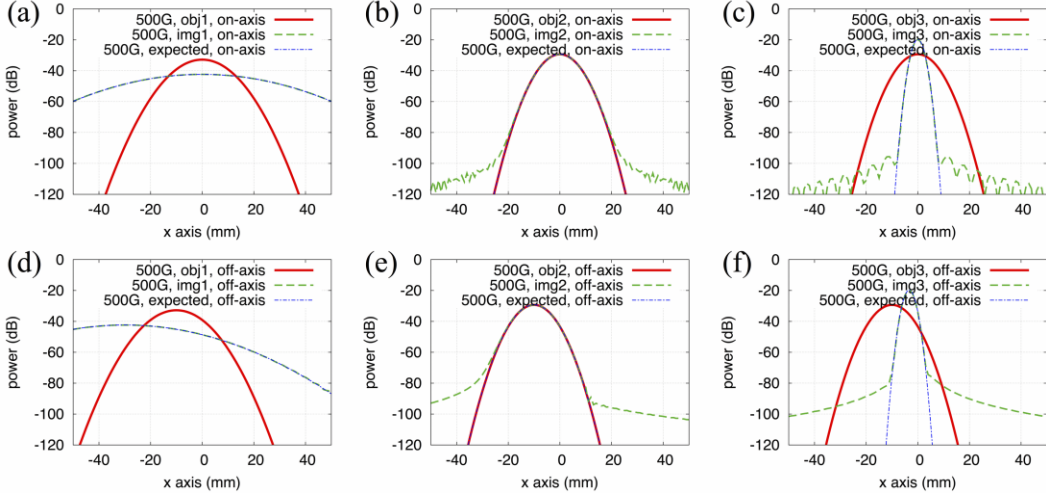


Fig. 3. Calculated electric fields on the obj and img shown in Fig. 2. The red (solid) line is the incident beam, the green (dashed) line is the reflected beam by Grasp8. The blue (dashed-dotted) line is the expected distribution by (4) based on the incident beam distribution (the red-solid line). (a) 500 GHz on-axis beam investigated on the obj1 and img1. (b) 500 GHz on-axis beam investigated on the obj2 and img2. (c) 500 GHz on-axis beam investigated on the obj3 and img3. (d) 500 GHz off-axis beam investigated on the obj1 and img1. (e) 500 GHz off-axis beam investigated on the obj2 and img2. (f) 500 GHz off-axis beam investigated on the obj3 and img3.

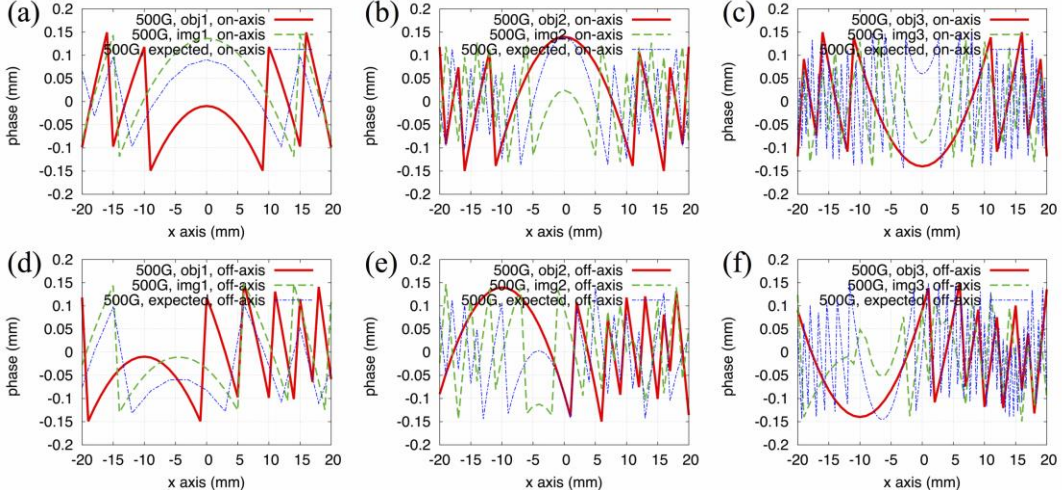


Fig. 4. Calculated phase of the electric fields on the obj and img shown in Fig. 2. The red (solid) line is the incident beam, the green (dashed) line is the reflected beam by Grasp8. The blue (dashed-dotted) line is the expected distribution by (4) based on the incident beam distribution (the red-solid line). (a) 500 GHz on-axis beam investigated on the obj1 and img1. (b) 500 GHz on-axis beam investigated on the obj2 and img2. (c) 500 GHz on-axis beam investigated on the obj3 and img3. (d) 500 GHz off-axis beam investigated on the obj1 and img1. (e) 500 GHz off-axis beam investigated on the obj2 and img2. (f) 500 GHz off-axis beam investigated on the obj3 and img3.

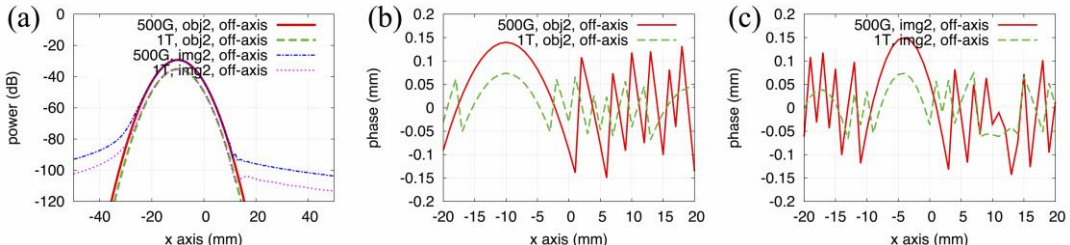


Fig. 5. The distribution and phase on the obj2 and img2. (a) The red (solid) line and green (dashed) line represent the distribution of the 500 GHz and 1THz off-axis incident beam, respectively. They are similar one. The blue (dashed-dotted) line and magenta (dotted) line is 500 GHz and 1THz off-axis reflected beam distribution, respectively. (b) The red (solid) line and green (dashed) line represent the phase of the 500 GHz and 1THz off-axis incident beam, respectively. (c) The red (solid) line and green (dashed) line represent the phase of the 500 GHz and 1THz off-axis reflected beam, respectively. They have the same shape.

V. APPLYING TO THREE MIRROR TELESCOPE

We apply (4) to the three mirror telescope as shown in Fig. 6. The primary mirror is an off-axis paraboloid with a diameter of 300 mm. The secondary mirror is an off-axis ellipsoid. The tertiary mirror is an off-axis hyperboloid. The telescope has a focal length of about -1663 mm. This telescope has a wide FOV of 1 degree at 1 THz without vignetting. There are three pupils in this system. One of them is located at the secondary. The others are images of the secondary, the entrance and exit pupil in Fig. 6. The lens formula holds on the entrance and exit pupil because they are the images of the secondary.

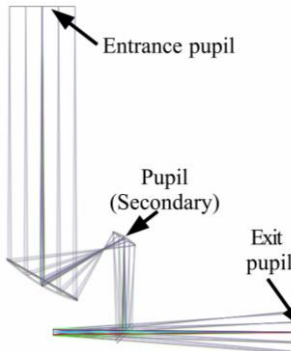


Fig. 6. Three pupils. One of them is located at the secondary.

We carry out calculations with Grasp8. Four beams pass through the telescope from the focal plane. One of them is a 500 GHz on-axis beam, the second is a 500 GHz off-axis apart from the center of the FOV, the others are the same beams as the 500 GHz ones, except for the frequency of 1 THz. An edge taper is set to be 15 dB at the secondary. According to (4), a beam radius is estimated in order to meet 15 dB at the edge of the exit pupil. A radius of curvature of wavefront is estimated from a distance between the focal plane and the exit pupil.

Fig. 7 shows the distributions on the exit and entrance pupil of the telescope. The 500 GHz and 1 THz distributions are similar on the exit pupil and keep their own shape on the entrance pupil. The fine dotted lines in Fig. 7 represent the expected distribution by (4). In this case, an equivalent a and b are -4248 mm and -1664 mm, respectively. It is shown that the field distributions on the entrance pupil do not depend on the beam frequencies. We also confirm beam patterns of this telescope. Fig. 8 shows beam patterns of the four beams in Fig. 7 on the celestial sphere. They are axially symmetric beams and have beam sizes expected from the diameter of the entrance pupil.

References

- [1] J. E. Carlstrom, P. A. R. Ade, K. A. Aird, B. A. Benson, L. E. Bleem, S. Busetti, et al., "The 10 meter south pole telescope," *Publications of the Astronomical Society of the Pacific*, vol. 123, no. 903, pp. 568–581, May 2011.
- [2] J. W. Fowler, M. D. Niemack, S. R. Dicker, A. M. Aboobaker, P. A. R. Ade, E. S. Battistelli, et al., "Optical design of the Atacama Cosmology Telescope and the Millimeter Bolometric Array Camera," *Applied Optics*, vol. 46, no. 17, pp. 3444–3454, Jun. 2007.
- [3] S. Padin, M. Hollister, S. Radford, J. Sayers, D. Woody, J. Zmuidzinas, et al., "CCAT Optics," *Proc. SPIE*, vol. 7733, 77334Y, 2010

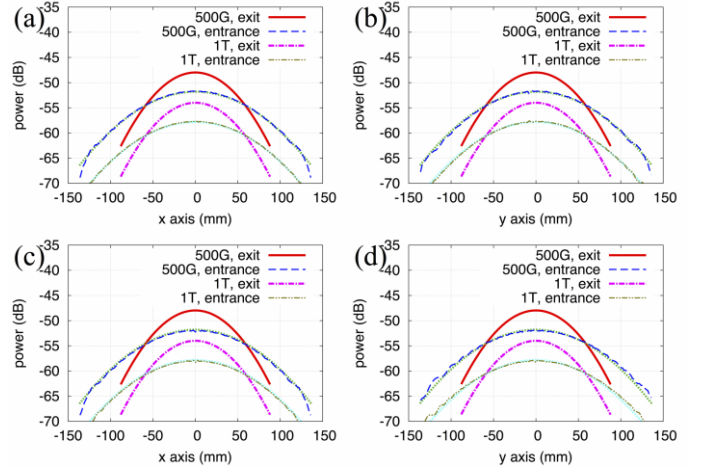


Fig. 7. Field distributions on the entrance and exit pupil. The red (solid) line is the distribution of the 500 GHz beam at the exit pupil, the blue (dashed) line is that at the entrance pupil. The magenta (dash-dotted) and greenish brown (dashed-dotted-dotted) represents the distribution of the 1 THz beam at the entrance and exit pupil, respectively. The cyan and green (fine dotted) lines are expected from the distribution on the exit pupil. (a) The distribution along x axis of on-axis beams. (b) The distribution along y axis of on-axis beams. (c) The distribution along x axis of off-axis beams. (d) The distribution along y axis of off-axis beams.

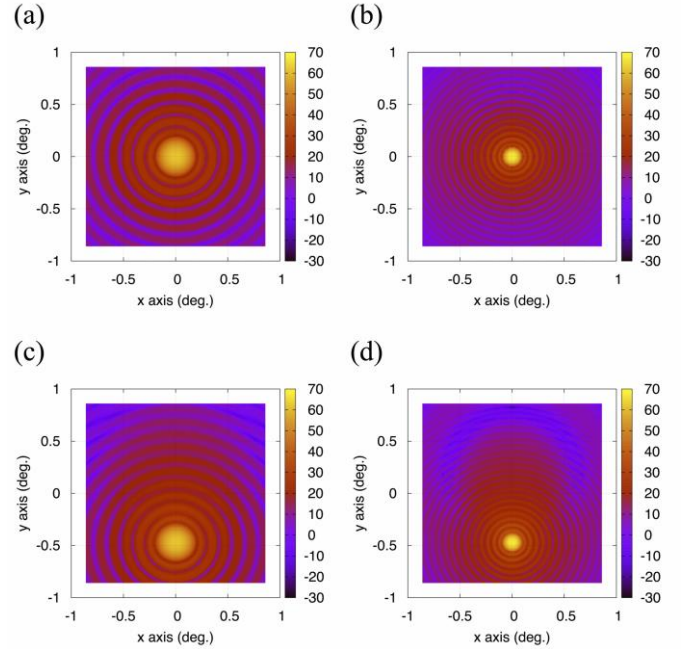


Fig. 8. Beam patterns of the telescope. (a) The 500 GHz on-axis beam. (b) The 1 THz on-axis beam. (c) The 500 GHz off-axis beam. (d) The 1 THz off-axis beam

- [4] V. Y. Terebikh, "A Purely Reflective Large Wide-Field Telescope," *Bulletin of the Crimean Astrophysical Observatory*, vol. 104, pp. 179–186, 2008
- [5] H. Kataza, T. Wada, I. Sakon, N. Kobayashi, Y. Sarugaku, N. Fujishiro, et al., "Mid-infrared Camera and Spectrometer on board SPICA," *Proc. SPIE*, vol. 8442 84420Q, 2012
- [6] T. Chu, "An Imaging Beam Waveguide Feed," *IEEE Trans. Antennas Propagat.*, vol. 31, no. 4, pp. 614–619, Jul. 1983.
- [7] D. H. Martin and J. W. Bowen, "Long-Wave Optics," *IEEE Trans. Microwave Theory and Techniques*, vol. 41, no. 10, pp. 1676–1690, Oct. 1983.
- [8] J. W. Goodman, *Introduction to Fourier Optics*. New York: McGraw-Hill, 1968

Design and Loss Measurement of Substrate Integrated Waveguides at Terahertz Frequencies

Takafumi Kojima, Alvaro Gonzalez, and Yoshinori Uzawa.

Advanced Technology Center

National Astronomical Observatory of Japan

Email: t.kojima@nao.ac.jp

At Terahertz frequencies, integration is a key aspect in the development of the next generation of high-sensitivity receivers, for example, for multibeam receivers. In order to integrate superconductor- and/or semiconductor-based devices, receivers will require low-loss waveguides and passive components integrated on a substrate. Substrate integrated waveguides (SIWs) are a suitable candidate for new THz receivers, because of the easy transition to two-dimensional circuits (e.g. CPW, microstrip lines) and because they have the same fundamental propagation mode TE_{10} as a rectangular waveguide. In this frequency range, although SIW can be fabricated, it is difficult to characterize their electrical performance. Therefore, the design of a test fixture is necessary in addition to the design of the SIW.

We have designed a THz SIW and a test fixture to evaluate it. The SIW was designed using a 76- μm -thick quartz substrate with permittivity of 3.8 and loss tangent of 0.003 at 0.9 THz at room temperature. For the SIW, the diameter of all the plated-through holes was set to 45 μm and their spacing was chosen as 60 μm . The distance between the holes used as sidewalls is 187 μm . These agree with the design rule described in [1]. 2- μm -thick aluminum has been used for the top and bottom metallization of the substrate. The test fixture for the mount and evaluation of the SIW consists of waveguide flanges, impedance transformers, and waveguide to SIW transitions. In order to tolerate a small H-plane gap when the SIW is mounted on the test fixture, a groove gap waveguide was used as the transmission line of the test fixture [2]. The size of the waveguide is the same as WR-1.2 (0.304 mm x 0.152 mm), but the side wall is composed of periodically-placed metal pins.

We evaluated the SIW using a vector network analyzer in the frequency range of 0.8 to 0.9 THz with a dynamic range of more than 60 dB [3]. The test fixture including the SIW is put between the transmitter and the receiver and the insertion loss is measured. Three SIWs with lengths of 5.0, 8.7, and 11.6 mm were evaluated to determine the associated insertion loss. Results showed waveguide loss of about 3 dB/mm at room temperature. The loss is attributed to the imperfect shape of the through holes. Proper fabrication will improve the loss.

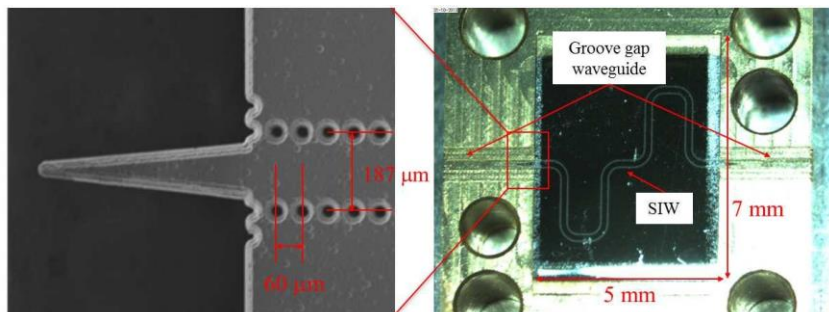


Fig. 1 A scanning electron microscope image of the SIW and optical microscope image of the test fixture including the SIW.

References

1. D. Deslandes et al., "Accurate Modeling, Wave Mechanisms, and Design Considerations of a Substrate Integrated Waveguide," *IEEE Transactions on Microwave Theory and Techniques*, Vol. 54, No. 6, pp 2516-2526, 2006.
2. E. Rajo-Iglesias et al., "Groove gap waveguide: A rectangular waveguide between contactless metal plates enabled by parallel-plate cut-off," *Proceedings of the Fourth European Conference on Antennas and Propagation (EuCAP) 2010*, pp.1-4, 12-16 April 2010.
3. T. Kojima et al., "A Low-Noise Terahertz SIS Mixer Incorporating a Waveguide Directional Coupler for LO Injection," *Journal of Infrared, Millimeter, and Terahertz Waves*, Vol. 31, Issue 11, pp. 1321-1330, November 2010.

7 - Back-ends: readout & signal processing

The operation of SIS mixer as up- and down-converter at low frequencies for frequency multiplexing

Anton A. Artanov^{1,2,*}, Konstantin V. Kalashnikov^{1,2}, Gert de Lange³, Valery P. Koshelets¹

¹ *The Kotel'nikov Institute of Radio Engineering and Electronics, Russian Academy of Science,
11/7 Mokhovaya St., 125009, Moscow*

² *Moscow Institute of Physics and Technology,
Institutskii per., 9, 141700 Dolgoprudny, Moscow Region, Russia*

³ *SRON Netherlands Institute for Space Research, P.O. Box 800,
9700 AV Groningen, the Netherlands*

*Email: artanov@hitech.cplire.ru

A feasibility study of a frequency multiplexed read-out scheme for large number Transition Edge Sensor arrays is described in paper [1]. The read-out makes use of frequency up- and down-conversion with Superconducting-Insulator-Superconducting (SIS) tunnel junctions operating at GHz frequencies, in combination with an existing frequency multiplexed read-out at MHz frequencies. Such read-out scheme can drastically reduce the wiring from room temperature to the cryogenic detectors.

Experimental measurements of a SIS tunnel junction operating as frequency up- and down-convertors at low frequencies (< 10 GHz) were carried out. A possibility to implement a “traditional” SIS-mixer for down- and up-conversion with acceptable conversion loss (well below 15 dB) has been demonstrated. Dependencies of the conversion efficiency on the SIS-junction parameters, local oscillator (LO) power and SIS-bias have been measured and compared with theoretical estimations. The best conditions for the SIS-mixer operation at low LO frequencies have been determined. The transitions between different regimes of operations (quantum and classical; quasiparticle and Josephson) have been studied in a wide bath temperature range by using specially designed circuits with an integrated control line for the Josephson effect suppression. Preliminary conclusions on the feasibility of the frequency-multiplexed TES read-out using superconducting tunnel junctions will be presented.

The work was supported by The RFBR and the Ministry of Education and Science of the Russian Federation.

References

1. G. de Lange «Feasibility of a frequency-multiplexed TES read-out using superconducting tunnel junctions», Journal of Low Temperature Physics, special issue LTD 15.

Development of Superconducting Low Pass Filter for Ultra Low Noise Measurement System of Microwave Kinetic Inductance Detector

K. Karatsu^{*}, T. Kojima^{*}, Y. Sekimoto^{*}, T. Nitta^{**}, M. Sekine^{***}, S. Sekiguchi^{***}, T. Okada^{***}, S. Sibo^{***}, T. Noguchi^{*}, Y. Uzawa^{*}, H. Matsuo^{*}, H. Kiuchi^{*}, and M. Naruse^{****}

^{*}*Advanced Technology Center, National Astronomical Observatory of Japan*

Email: kenichi.karatsu@nao.ac.jp

^{**}*Institute of Astronomy, University of Tsukuba*

^{***}*Department of Astronomy, The University of Tokyo*

^{****}*Department of Electrical and Electronic Systems, Saitama University*

Microwave Kinetic Inductance Detector (MKID) is a cooper pair breaking superconducting detector [1]. MKID consists of a superconducting resonance circuit which resonance frequency is typically designed around 2-8 GHz where a HEMT low noise amplifier can be used for readout. MKID is a promising technology for multiplexing, which can contribute to produce high-sensitive large-scale camera array for radio astronomy.

We developed MKID camera for astronomical observations such as CMB B-mode search or Antarctica telescope. MKID performances were measured with 100 mK dilution refrigerator and the best Noise Equivalent Power (NEP) we got was 6e-18 W/sqrt(Hz) [2]. However, this is slightly low-performance compared to the world best NEP of MKID [3]. The sensitivity is probably limited by our measurement system. In particular, the system is weak against stray light (or thermal radiation) coming through signal cables from higher temperature stages of the refrigerator, as we have not installed any low pass filter before the 100 mK stage. The thermal radiation coming through signal cables might generate excess quasi-particles on MKID causing the reduction of the sensitivity.

In order to suppress such stray light, wide-band low pass filter is required and should be placed right before the MKID device (i.e. on 100 mK stage). We developed superconducting low pass filter which can suppress microwave in 10-100 GHz band down to more than 30 dB, while the insertion loss in 1-10 GHz range is smaller than 1 dB. It consists of various sizes of microstrip stub filters. The material of these filters is niobium (Nb) on silicon (Si) substrate and chassis, made of gold plated copper, acts as the ground plane of the microstrip structure. The design of stub filters and chassis has been optimized using 3D electromagnetic simulator, HFSS.

We would like to present the design specifications and performance assessments of the developed superconducting low pass filter. The effect of the filter on the noise performance of MKID will be also discussed.

References

1. P. K. Day et al., Nature, 425, 817-821, (2003); J. Zmuidzinas, Annu. Rev. Cond. Mat. Phys., 3, 169-214, (2012)
2. M. Naruse et al., J. Low Temp. Phys. 167, 373-378 (2012)
3. P. J. de Visser et al., J. Low Temp. Phys. 167, 335-340 (2012)

8 - Novel devices & measurements

A Superconducting Millimetre Switch with Multiple Nano-Bridges

Boon-Kok Tan, Ghassan Yassin, Leonid Kuzmin, Ernst Otto, Hocine Merabet, and Chris North

Abstract—In this paper, we describe the design of a planar superconducting on/off switch comprising a high normal resistance nano-bridge deposited across a slotline transmission line. We present preliminary experimental results measured at 220 GHz range, and we discuss in detail the various parameters that affect the performance of the planar on/off switch, including the optimum thickness required for the nano-bridge to achieve high dynamic range and low transmission loss. The analysis is done by combining the accurate superconducting surface impedance description with rigorous electromagnetic simulations, and comparing the simulated results with the measured performance of a previously fabricated on/off switch fed by a back-to-back unilateral finline taper. Finally, we propose an improved method to further increase the dynamic range of the switch, by introducing a multi-bridge design to tune out the residual inductance of the nano-bridges.

Index Terms—Superconducting integrated circuits, system-on-a-chip, submillimeter wave devices, superconducting switches, phase modulation.

I. INTRODUCTION

AN important component for constructing an ultra-sensitive polarimeter is the fast modulating of the input signal's polarisation state. It shifts the signal frequency away from the $1/f$ noise, and separates the polarised signals from the unpolarised foreground. More importantly, it allows the measurement of both Q and U Stoke's parameters without moving the polarimeter components [1]. Several technologies have been considered for modulating the polarization signal from the sky in various astronomical instruments, including rotating quasioptical or waveguide half-wave plates and Faraday rotators [2]. However, these techniques involve the employment of moving parts, or require varying magnetic fields.

A planar phase shift circuit that can translate the rapid on/off switching mechanism into phase modulation is potentially a much more efficient and elegant solution. A planar design allows the switch to be easily integrated into the detector circuit and eventually the realisation of a fully planar receiver. Figure 1 shows how a planar phase shift circuit can be incorporated into a pseudo-correlator system to measure the polar-

B-K. Tan and G. Yassin are with the Department of Physics (Astrophysics), University of Oxford, Denys Wilkinson Building, Keble Road, OX1 3RH, Oxford, UK. E-mail: tanbk@astro.ox.ac.uk

B-K. Tan is also with the Institute for Research and Innovation, Wawasan Open University, 54 Jalan Sultan Ahmad Shah, 10050 Penang, Malaysia.

L. Kuzmin and E. Otto are with the Department of Microtechnology and Nanoscience, Chalmers University of Technology, S-41296 Gothenburg, Sweden.

H. Merabet is with the Mathematics, Statistics and Physics, Qatar University, P.O. Box 2713 Doha, Qatar.

C. North is now with the Cardiff School of Physics and Astronomy, Cardiff University, Queen's Buildings, The Parade, Cardiff CF24 3AA.

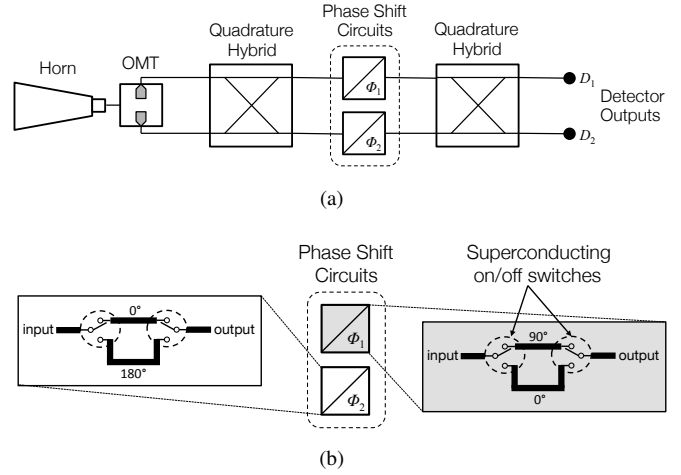


Fig. 1. (a) Schematic of a pseudo-correlator using phase shift circuits. The incoming radiation is split into two linear polarizations by the OMT, which are then combined using a quadrature hybrid to produce two circular polarizations. A phase shift circuit is used to produce a phase difference of $\Delta\phi = |\phi_1 - \phi_2|$ between the circular polarised signals, before they are recombined through another quadrature hybrid to produce two orthogonal linear polarisations, and fed to the detectors D_1 and D_2 . (b) Schematic drawing showing how a phase switch circuit can be constructed using two delay lines. Two on/off switches alternating in sync are utilised to select which delay line the RF signal will pass through.

ization of the sky signal. The incoming signal is split into two linear polarisations by the orthogonal mode transducer (OMT) and converted into circular polarisations via the quadrature hybrid. The two polarised signals are phase modulated with respect to each other using the phase shift circuits, before they are recombined through another quadrature hybrid to produce two orthogonal linear polarisations, and fed to the detectors D_1 and D_2 . If the input RF signal is described by the Stoke's parameters I , Q , and U , it can be shown that the outputs of the two detectors D_1 and D_2 are [3]:

$$D_1 = I - Q \cos \Delta\phi - U \sin \Delta\phi, \quad \text{and} \quad (1a)$$

$$D_2 = I + Q \cos \Delta\phi + U \sin \Delta\phi. \quad (1b)$$

When the first phase shift circuit is set to modulate between $\phi_1 = 90^\circ$ and 0° , and the second phase shift circuit modulating between $\phi_2 = 0^\circ$ and 180° , the synchronous modulation produces a phase difference of $\Delta\phi = |\phi_1 - \phi_2| = 90^\circ$ during the first half of the duty cycle and $\Delta\phi = |\phi_1 - \phi_2| = 180^\circ$ during the second half. Therefore, by taking the difference of the detector outputs $D_1 - D_2$, the linear polarisation parameters Q and U can be determine simultaneously for a single sky pixel.

Figure 1 (b) shows a conceptual sketch of a phase shift

circuit where two delay lines of different lengths are used to bridge the input and the output line. To select the desired phase delay, two on/off switches that alternate in sync between the two delay lines is required. The on/off switch can be realised by depositing a narrow strip of high residual resistance ratio (RRR) superconductor, such as Niobium Nitride (NbN) or Niobium Titanium Nitride (NbTiN), across a slotline. By changing the impedance of this nano-bridge from superconducting to normal state (and vice versa), the RF signal can be directed to either branches of the phase shift circuit. In each case, the RF signal sees two substantially different complex impedance states, hence switched from one delay line branch to another. The detail design of a planar superconducting on/off switch operating at millimetre wavelengths can be found in [4], [5] and [6]. In this paper, we focus on discussing the preliminary experimental results and the various parameters that affect the performance of the switch, including the optimum thickness required for the nano-bridge to achieve high dynamic range and low transmission loss. All the analysis presented below is done by combining the accurate superconducting surface impedance description with High Frequency Structure Simulator (HFSS).

II. PRELIMINARY EXPERIMENTAL RESULTS

Our superconducting on/off switch comprises a 22 nm thick and 0.5 μm wide NbN nano-bridge deposited across a 5 μm wide slotline, corresponding to a characteristic impedance of 69 Ω . The RF signal is fed to the slotline via a unilateral finline taper, and re-radiated back to the output port via another finline, as shown in Figure 2. Both the finline taper and the nano-bridge are made out of the same superconducting

material, NbN, with resistivity $\rho = 200 \mu\Omega\text{cm}$, critical current density $J_{crit} \approx 15 \text{kA}\mu\text{m}^{-2}$, and the London penetration depth $\lambda_L = 200 \text{ nm}$. The NbN finline taper was overlaid with a thin layer of gold for bonding purposes and the whole structure is supported by a 200 μm quartz substrate. The reader is referred to [5] for the detailed description of the fabrication process.

The finline chip is positioned at the E-plane of a rectangular waveguide, and a superconductor-insulator-superconductor (SIS) device designed to operate at the frequency range of 180–260 GHz is placed after the finline chip to read the transmitted RF power. Both the finline and the SIS detector chips are housed within a split aluminium block, along the waveguide connected to a millimetre horn to couple the local oscillator (LO) signal to the finline chip, as shown in Figure 3. The nano-bridge is modulated between the superconducting (on) and the normal (off) states by applying a bias current along the nano-bridge, causing it to become normal when the bias current exceeds the critical current value. By measuring the tunnelling current across the SIS device, we can therefore obtain the response of the nano-bridge (as a switch) to the LO signal. Figure 4 shows a typical DC IV curve measured from the SIS devices, with and without the illumination of the LO signal at 207 GHz. The difference between the pumping level when the nano-bridge is biased above and below the critical current is clearly seen in the inset of Figure 4. This demonstrates that the nano-bridge is in fact acting as a switch, attenuating the LO signal coupled to the SIS detector, when the nano-bridge is in the superconducting state.

In order to reduce the $1/f$ noise, we modulated the LO signal entering the millimetre horn using a chopper wheel, and employed a lock-in amplifier to measure the output from the SIS detector. Figure 5 shows the lock-in timestream data of the SIS device output and the demodulated switching signal, at 234 GHz and 247 GHz. The nano-bridge is switched at 8.137 Hz, and the LO signal was chopped at 120 Hz. As can be seen, the response of the SIS devices is clearly corresponding to the switching of the nano-bridge. Interestingly though, the switching behaviour changes over the range of frequencies, as shown in Figure 6 (a). At some frequencies, the switching is inverted. Contrary to expectation, the power transmitted to the SIS device is lower when the nano-bridge is at normal state compared to the superconducting state i.e., $\Delta_T = S_{12,on}/S_{12,off} > 0 \text{ dB}$. An example of this is shown in Figure 5 (b) where a clear inversion effect is observed at 247 GHz. Simulation done using HFSS¹ shows the exact same effect, although in this case, the inversion occurs around 230 GHz instead of 247 GHz. Moreover, the HFSS simulation predicts a dynamic range Δ_T of around $\pm 0.5 \text{ dB}$, which is very close to the measured dynamic range of the fabricated nano-bridge device.

It is obvious from Figure 6 (a) that the main reason the tested design has a low dynamic range is because when the nano-bridge is in superconducting, it does not reject the LO signal efficiently. When the switch is off (normal state), it transmits approximately -0.5 dB of power through as ex-

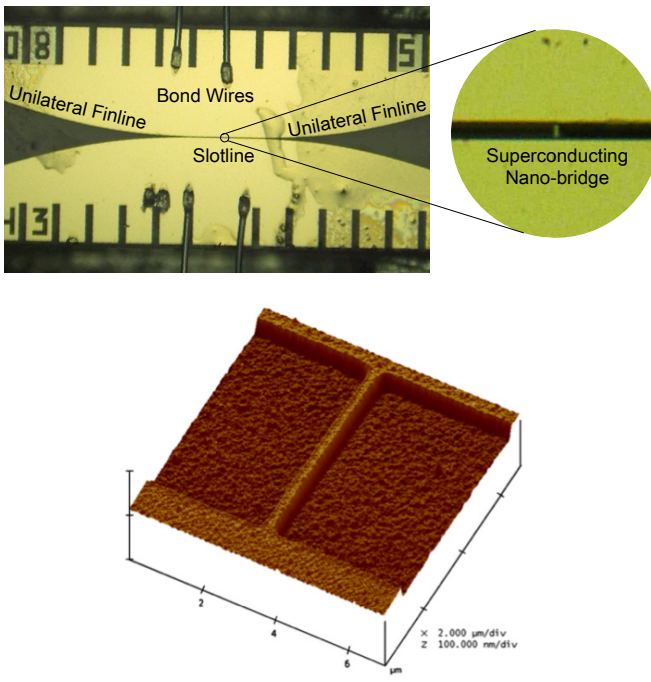


Fig. 2. A planar superconducting on/off switch comprising a superconducting nano-bridge deposited across the slotline section of a back-to-back unilateral finline taper.

¹The nano-bridge is represented as a lumped element with surface impedance of both normal and superconducting states calculated using Equation 2.

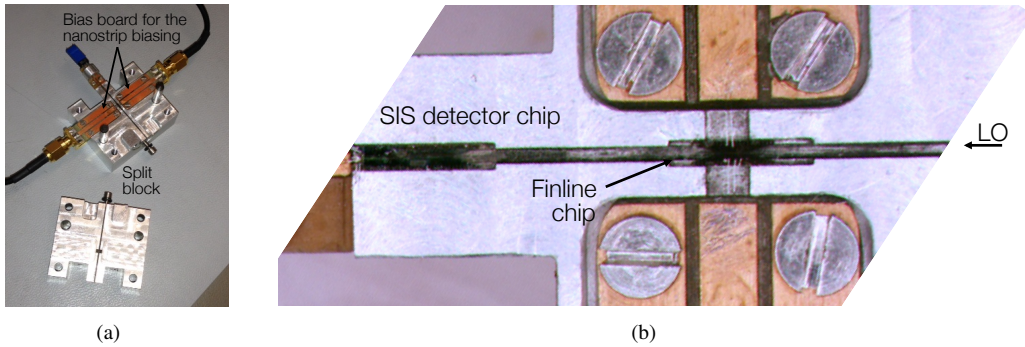


Fig. 3. (a) A split aluminium block housing both the finline and the SIS detector chips. (b) Both the SIS detector chip and the finline chip are suspended across the E-plane of a rectangular waveguide via the deep grooves in the waveguide wall. Two coplanar waveguide transmission lines are used to supply the bias current to switch the nano-bridge from superconducting to normal state. The LO signal from the left is coupled to the slotline section with the nano-bridge, and re-radiated towards the SIS detector chip via a back-to-back finline taper.

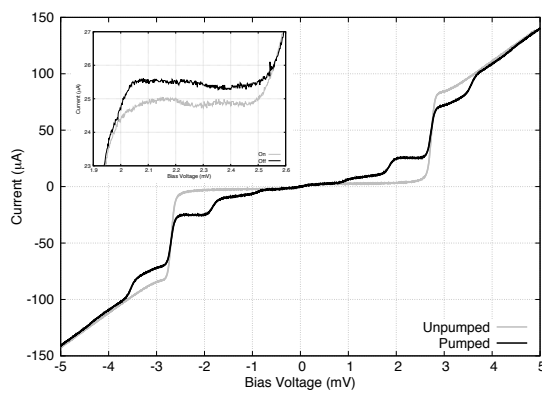


Fig. 4. An example of the DC pumped and unpumped I-V curves of the SIS device. The inset shows the changes in the tunnelling current across the first photon step, when the nano-bridge is being switched from normal to superconducting state, therefore attenuating the LO power coupled to the tunnel junction.

pected, where a negligible part of the LO power was rejected due to the finite impedance of the nano-bridge. Therefore, the main issue here is why the superconducting nano-bridge presents a relatively large impedance value that does not short the transmission line. Furthermore, at certain frequencies, the impedance presented by the nano-bridge must be higher at the superconducting state, compared to the normal state, causing the inversion effect.

The impedance of a superconducting strip is determined by the resistive part of its surface impedance R_{surf} ; the geometric inductance L_{geo} , and the kinetic inductance L_{kin} . The later inductance has a significant value only in the superconducting state, whereas $R_{surf} = R_N$, its thin film normal resistance in the normal state, and $R_{surf} \approx 0$ in the superconducting state. The value of these parameters are given by [3]:

$$R_N = \rho l / w t, \quad (2a)$$

$$L_{geo} = 0.2l \left[\frac{1}{2} + \ln \left(\frac{2l}{w+t} \right) + 0.11 \left(\frac{w+t}{l} \right) \right] \mu\text{H}, \quad (2b)$$

$$L_{kin} = \mu_0 \frac{l \lambda_L}{w} \coth \frac{t}{\lambda_L}, \quad (2c)$$

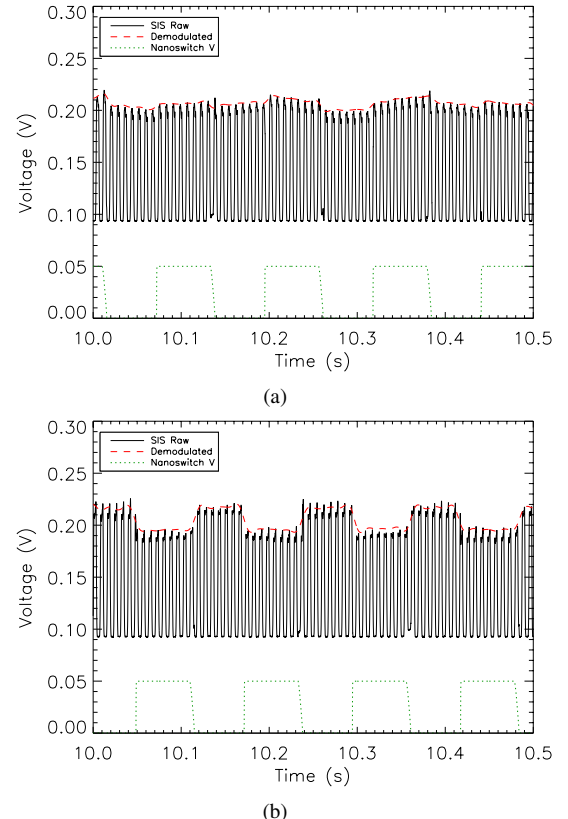


Fig. 5. Zoom in timestreams of a nano-bridge device with illumination from the LO at two frequencies: 234 GHz (top) and 247 GHz (bottom). The SIS tunnelling current is plotted as black, solid line, while the demodulated switching signal is plotted as red, dashed line. The voltage across the nanoswitch is the green line at the bottom. The switching is in opposite senses at these two LO frequencies, being inverted at 247 GHz.

where ρ is the resistivity of the superconductor, λ_L is the London penetration depth, and w, l and t is the width, length and thickness of the superconducting strip respectively. For an RF/LO signal at an angular frequency of $\omega = 2\pi f$, the two impedance states are thus given by [3]:

$$Z_{strip,on} = i\omega(L_{kin} + L_{geo}) \quad (3a)$$

$$Z_{strip,off} = R_N + i\omega L_{geo}. \quad (3b)$$

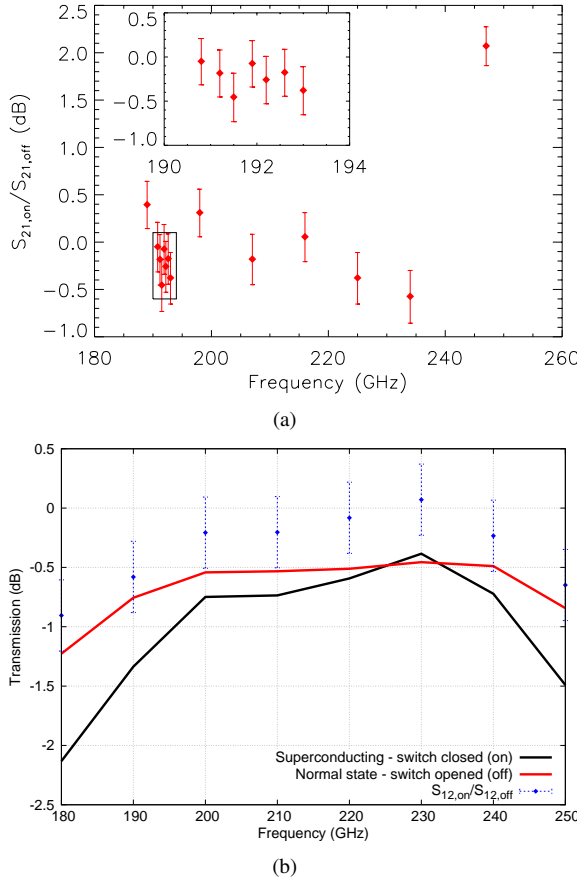


Fig. 6. (a) The power transmission ratio of the nano-bridge device between the two states across the operating frequency range. The inset is a zoom of the ratio at a narrow frequency range. (b) HFSS simulated response of the same nano-bridge device, showing similar dynamic range and switching behaviour as the measured results. The inversion in response is observed at 230 GHz, instead of the measured 247 GHz.

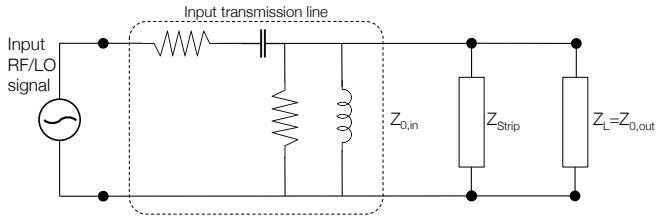


Fig. 7. Circuit diagram representing the input and output transmission line, connected with a nano-bridge across the slotline, represented by Z_{strip} .

For an ideal switch: in the superconducting ('switch-on' or closed) state, the nano-bridge has an impedance of $Z_{\text{strip},\text{on}} \ll Z_0$, the characteristic impedance of the slotline as shown in Figure 7. In this state, the load acts as a short, and any waves propagating along the transmission line are reflected, therefore no power is transmitted to the output line. In the normal ('switch-off' or opened) state, the surface impedance is much higher ($\approx R_N$) and the nano-bridge has an impedance of $Z_{\text{strip},\text{off}} \gg Z_0$. This act as an open in the circuit term, and the RF/LO signal will pass through the transmission line with minimum loss.

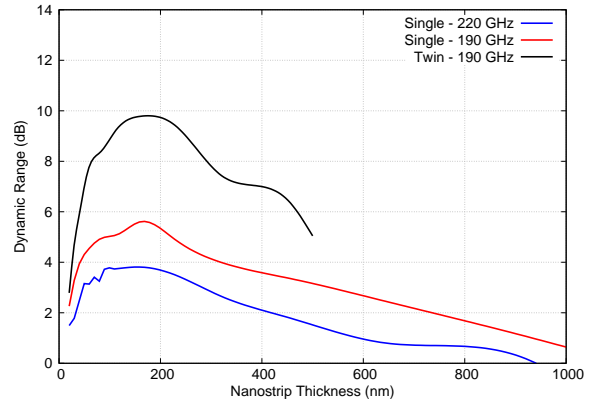


Fig. 8. The effects of the nano-bridge thickness on the dynamic range of the on/off switch.

The successful operation of the nano-bridge as a superconducting on/off switch relies on the fact that $Z_{\text{strip},\text{on}}$ is significantly smaller than $Z_{\text{strip},\text{off}}$. From Equation 3, one can see that this relation does not always hold true. Under certain circumstances, $i\omega L_{\text{kin}}$ could be larger or approaching R_N , causing $Z_{\text{strip},\text{on}} \geq Z_{\text{strip},\text{off}}$, and hence the inversion effect. From Equation 2, we can see that L_{kin} is greatly dependent on the term t/λ_L due to the exponential function in the equation. Small value of t/λ_L give rise to a large value of $\coth(t/\lambda_L)$. Therefore, we believe that the main reason the current design have a small dynamic range, and sometimes incurs the inversion effect, is because the fabricated nano-bridge is too thin, compared to the London penetration depth in the NbN thin film. This effect is especially noticeable at high frequencies, as shown in Figure 6. Take for example, the nano-bridge with the dimension of $w, l, t = 0.5 \times 5 \times 0.022 \mu\text{m}$ and $\rho = 200 \mu\Omega\text{cm}$ would have a value of $R_N \approx 9 \Omega$. At 240 GHz, and assuming $\lambda_L = 200 \text{ nm}$, $\coth(t/\lambda_L) = \coth 0.11 \approx 9$. This would give a value of $i\omega L_{\text{kin}} = 34.6 \Omega$, four times higher than R_N . In fact, as shown in Figure 8, the dynamic range of the nano-bridge as an on/off switch improves significantly when the thickness of the nano-bridge approaches $\lambda_L = 200 \text{ nm}$.

III. MULTIPLE NANO-BRIDGES DESIGN

It is obvious that the next generation of the on/off switch design must employed a thicker NbN nano-bridge to reduce the surface impedance in the superconducting state. However, as shown in Figure 8, the dynamic range of a $t \rightarrow \lambda_L$ nano-bridge is still limited to around 5 dB. The dynamic range of the planar superconducting on/off switch can be improved by depositing multiple nano-bridges along the slotline. The utilisation of the multi-bridge design have a two fold effects. First, the length of the transmission line between the nano-bridges can be optimised so that the complex impedance of one nano-bridge is transformed to the complex conjugate impedance of the other nano-bridge, and therefore to tune out the residual kinetic inductance of the nano-bridges. This is largely similar to the twin-junction tuning network used for cancelling out the junction capacitance of an SIS mixer [7], [8]. As shown in Figure 8, by employing two nano-bridges

separated by 50 μm slotline, we can double the dynamic range of the switch to about 10 dB.

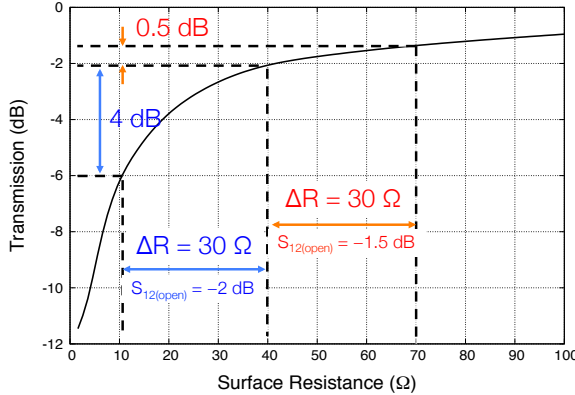


Fig. 9. The non-linear relation between the surface impedance of the nano-bridge and the power transmission. The was simulated using the HFSS model of a single $l, w, t = 5 \times 0.5 \times 0.02 \mu\text{m}$ nano-bridge as the switch.

Secondly, by using a multi-bridge scheme, the total impedance of the switch seen by the RF/LO signal at both states, $Z_{\text{strip},\text{on}}$ and $Z_{\text{strip},\text{off}}$, can be altered, giving a degree of freedom for selecting the optimum operating point of the switch. As shown in Figure 9, the power transmission allowed by the switch depends on the impedance of the nano-bridge/s, and the relation is non-linear. This indicates that the dynamic range of the switch relies heavily on the difference of the nano-bridges resistances between the two switching states. From the plot, it is clear that the dynamic range improves with the lower impedance values, but this also results in lower power transmission when the switch is in the normal state ('switch-off'). For example, if the difference in impedance between the superconducting and the normal state are $\Delta_R = |R_{\text{normal}} - R_{\text{super}}| = 30 \Omega$, where R_{normal} is 40 Ω and R_{super} is 10 Ω , the dynamic range is about 4 dB. However, in this scenario, when the switch is off, it only allows -2 dB of power transmission. In order to improve the power transmission at the switch-off state, we can operate the switch at say 70 Ω , giving a transmission of approximately -1.5 dB. However, if we retain the same $\Delta_R = 30 \Omega$ difference², one notice immediately that the dynamic range drops by 8-folds. Therefore, there is an unavoidable compromise between the optimum dynamic range achievable and the allowed power transmission when the switch is off.

Figure 10 shows a HFSS simulated model of two and three nano-bridges deposited to form the on/off switch. Each nano-bridge is 0.5 μm wide, 5 μm long and is formed using a 50 nm thick NbN film. The nano-bridges are separated by a 50 μm long slotline, and fed by a back-to-back unilateral finline taper as described before. Figure 10 (c) shows the HFSS predicted power transmission and dynamic range behaviour of the on/off switch with one, two and three nano-bridge/s. As can be seen, the dynamic range improves almost linearly with the number

²The reason behind this is that if R_N is increased to give a higher R_{normal} value by say making the nano-bridge longer, it will inevitably increase the value of L_{kin} as well, thus higher value of R_{super} . Therefore, Δ_R always remain almost the same regardless of the switch-off impedance operating point of the switch.

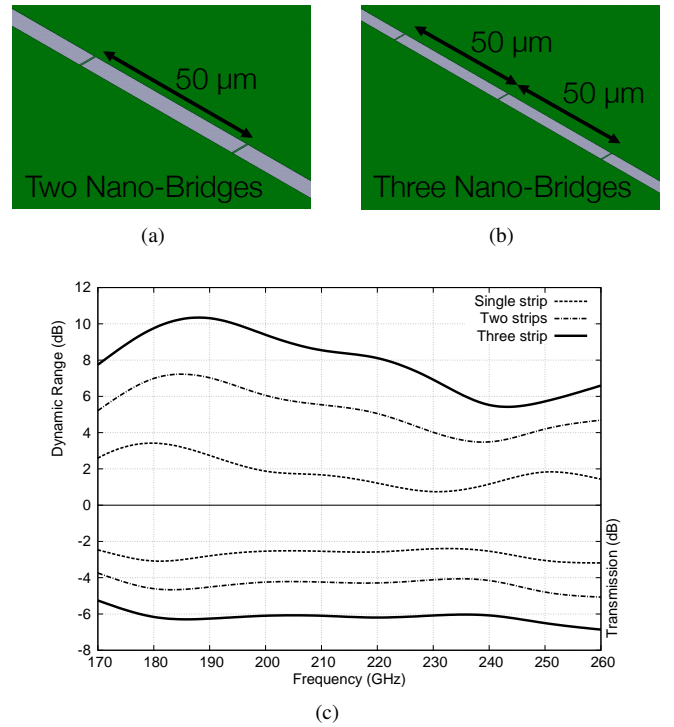


Fig. 10. (a) & (b) Examples of the multi-bridge design, where two and three nano-bridges are deposited along the transmission line, separated by a 50 μm long slotline. The nano-bridges are 0.5 μm wide, 5 μm long and 50 nm thick. (c) The power transmission allowed by the multi-bridge switch during the switch-off state, and the dynamic range, of the one-, two- and three-bridges design.

of nano-bridges, but at the same times, the transmission in the off-state drops almost proportionally as well. Hence, for a specific application, the designer should carefully chosen the number of nano-bridges and the dimension of the nano-bridge, to find a balance between the dynamic range required and the transmission loss.

IV. CONCLUSION

We have presented a design of a planar superconducting on/off switch utilising a nano-bridge connecting the two electrodes of a slotline. The preliminary experimental results have been presented and discussed in detail, especially the various parameters that affect the performance of the switch. The most important result from the discussion is that the tested nano-bridge is too thin, therefore preventing the nano-bridge to present low impedance when it is biased below the critical current value. In this paper, we have also proposed a new design that can improve the dynamic range of the switch, by utilising multiple nano-bridges along the same slotline. We have shown that by carefully choosing the separation distance between the nano-bridges, we can improve the dynamic range by two fold. We are currently in the process of fabricating a new batch of superconducting on/off switch using the new multi-bridge design with a thicker NbN film, and the experimentally obtained results from testing these devices will be reported.

REFERENCES

- [1] C. North, “Observations of the cosmic microwave background polarization with *clover*,” Ph.D. dissertation, University of Oxford, Oxford, United Kingdom, 2010.
- [2] P. A. R. Ade, D. T. Chuss, S. Hanany, V. Haynes, B. G. Keating, A. Kogut, J. E. Ruhl, G. Pisano, G. Savini, and E. J. Wollack, “Polarization modulators for CMBPol,” *Journal of Physics Conference Series*, vol. 155, no. 1, p. 012006, Mar. 2009.
- [3] G. Yassin, P. Kittara, A. Jiralucksanawong, S. Wangsuya, J. Leech, and M. Jones, “A High Performance Horn for Large Format Focal Plane Arrays,” in *Proceedings of the Eighteenth International Symposium on Space Terahertz Technology*, 2007, pp. 199–+.
- [4] P. K. Grimes, G. Yassin, L. S. Kuzmin, P. D. Mauskopf, E. Otto, M. E. Jones, and C. E. North, “Investigation of planar switches for large format CMB polarization instruments,” in *Society of Photo-Optical Instrumentation Engineers (SPIE) Conference Series*, ser. Society of Photo-Optical Instrumentation Engineers (SPIE) Conference Series, vol. 6275, Jul. 2006.
- [5] G. Yassin, L. S. Kuzmin, P. K. Grimes, M. Tarasov, E. Otto, and P. D. Mauskopf, “An integrated superconducting phase switch for cosmology instruments,” *Physica C Superconductivity*, vol. 466, pp. 115–123, Nov. 2007.
- [6] L. Kuzmin, M. Tarasov, É. Otto, A. Kalabukhov, G. Yassin, P. Grimes, and P. Mauskopf, “Superconducting subterahertz fast nanoswitch,” *Soviet Journal of Experimental and Theoretical Physics Letters*, vol. 86, pp. 275–277, Oct. 2007.
- [7] V. I. Belitskii, M. A. Tarasov, S. A. Kovtoniuk, L. V. Filippenko, and O. V. Kaplunenko, “Low noise completely quasioptical SIS receiver for radioastronomy at 115 GHz,” *International Journal of Infrared and Millimeter Waves*, vol. 13, pp. 389–396, Apr. 1992.
- [8] P. Grimes, “Design and analysis of 700 GHz Finline Mixers,” Ph.D. dissertation, University of Cambridge, United Kingdom, 2006.

A Digital Terahertz Power Meter Based on an NbN Thin Film

C. Edward Tong^{*}, Andrey Trifonov^{*}, Raymond Blundell^{*}, Alexander Shurakov[†] and Gregory Gol'tsman[†]

^{*}
Harvard-Smithsonian Center for Astrophysics, Cambridge, MA, USA

Email: etong@cfa.harvard.edu, avtrifonov@cfa.harvard.edu, rblundell@cfa.harvard.edu

[†]
Moscow State Pedagogical University, Moscow, Russia.

Email : alexandrus1986@gmail.com, goltsman@rplab.ru

We have further studied the effect of subjecting a superconducting Hot Electron Bolometer (HEB) element made from an NbN thin film to microwave radiation. Since the photon energy is weak, the microwave radiation does not simply heat the film, but generates a bi-static state, switching between the superconducting and normal states, upon the application of a small voltage bias. Indeed, a relaxation oscillation of a few MHz has previously been reported in this regime [1]. Switching between the superconducting and normal states modulates the reflected microwave pump power from the device. A simple homodyne setup readily recovers the spontaneous switching waveform in the time domain. The switching frequency is a function of both the bias voltage (DC heating) and the applied microwave power.

In this work, we use a 0.8 THz HEB waveguide mixer for the purpose of demonstration. The applied microwave pump, coupled through a directional coupler, is at 1 GHz. Since the pump power is of the order of a few μ W, a room temperature amplifier is sufficient to amplify the reflected pump power from the HEB mixer, which beats with the microwave source in a homodyne set-up. After further amplification, the switching waveform is passed onto a frequency counter. The typical frequency of the switching pulses is 3-5 MHz. It is found that the digital frequency count increases with higher microwave pump power. When the HEB mixer is subjected to additional optical power at 0.8 THz, the frequency count also increases. When we vary the incident optical power by using a wire grid attenuator, a linear relationship is observed between the frequency count and the applied optical power, over at least an order of magnitude of power.

This phenomenon can be exploited to develop a digital power meter, using a very simple electronics setup. Further experiments are under way to determine the range of linearity and the accuracy of calibration transfer from the microwave to the THz regime.

References

1. Y. Zhuang, and S. Yngvesson, "Detection and interpretation of bistatic effects in NbN HEB devices," *Proc. 13th Int. Symp. Space THz Tech.*, 2002, pp. 463–472.

REGISTERED PARTICIPANTS

First name	Last name	Organization	Country	e-mail
Nikolay	Abramov	NUST MISIS	Russia	n-abram-n@yandex.ru
Ivan	Andreev	Terasense, LLC	Russia	ivan.andreev@rerasense.ru
Anton	Artanov	The Kotel'nikov Institute of Radio Engineering and Electronics, Russian Academy of Science	Russia	artanov@hitech.cplire.ru
Olivier	Auriacombe	The Open University	UK	olivier.auriaccombe@open.ac.uk
Andrey	Baryshev	SRON/Kapteyn Astronomical Institute	The Netherlands	a.m.baryshev@sron.nl
Jochem	Baselmans	SRON Netherlands Institute for Space Research	The Netherlands	J.Baselmans@sron.nl
Alena	Belitskaya	SRON Netherlands Institute for Space Research	The Netherlands	a.belitskaya@sron.nl
Victor	Belitsky	GARD, Chalmers University of Technology	Sweden	victor.belitsky@chalmers.se
Mostafa	Benzazaa	Radiometer Physics GmbH	Germany	benzazaa@radiometer-physics.de
Stella	Bevilacqua	Chalmers University of Technology	Sweden	stellab@chalmers.se
Bhushan	Billade	Chalmers University	Sweden	bhushan.billade@chalmers.se
Raymond	Blundell	Smithsonian Astrophysical Observatory	USA	rblundell@cfa.harvard.edu
Grigoriy	Bubnov	IAP RAS, LCN NSTU	Russia	payalnik89@gmail.com
Denis	Büchel	KOSMA, 1. Physikalische Institut, Universitaet zu Koeln	Germany	buechel@ph1.uni-koeln.de
Goutam	Chattopadhyay	NASA-JPL/Caltech	USA	goutam@jpl.nasa.gov
Artem	Chekushkin	V.Kotelnikov Institute of Radio Engineering and Electronics	Russia	boudko@gmail.com
Zhe	Chen	STFC-RAL/UESTC	UK	zhechen_uestc@126.com
Jian	Chen	Research Institute of Superconductor Electronics (RISE) Nanjing University	China	chenj63@nju.edu.cn
Sergey	Cherednichenko	Chalmers University of Technology	Sweden	serguei@chalmers.se
Oleg	Cojocari	ACST GmbH	Germany	oleg.cojocari@acst.de
Daniel	Cunnane	Jet Propulsion Laboratory	USA	Daniel.P.Cunnane@jpl.nasa.gov
Thijs	de Graauw	ASC-LPI	Russia	tdegraau@alma.cl
Gerhard	de Lange	SRON Netherlands Institute for Space Research	the Netherlands	gert@sron.nl
Emile	de Rijk	SWISSTo12	Switzerland	e.derijk@swissto12.ch

First name	Last name	Organization	Country	e-mail
Fabien	Defrance	LERMA	France	fabien.defrance@obspm.fr
Vincent	Desmaris	Chalmers University of Technology	Sweden	vincent.desmaris@chalmers.se
Simon	Doyle	Cardiff University	UK	simon.doyle@astro.cf.ac.uk
Andrey	Ermakov	IRE RAS	Russia	ermakov@hitech.cplire.ru
Timothe	Faivre	Aalto University	Finland	timothe.faivre@aalto.fi
Georgy	Fedorov	Moscow State Pedagogical University	Russia	gefedorov@mail.ru
Jian-Rong	Gao	SRON/TU Delft	The netherlands	j.r.gao@tudelft.nl
Lina	Gatilova	Observatoire de Paris - LERMA	France	lina.gatilova@lpn.cnrs.fr
Gregory	Gay	Observatoire de Paris - LERMA	France	gregory.gay@obspm.fr
Hugh	Gibson	RPG Radiometer Physics / Gibson Microwave Design EURL	France	gibson@radiometer-physics.de
Gregory	Gol'tsman	Moscow State Pedagogical University	Russia	goltsman@rplab.ru
Frederic	Gueth	IRAM	France	gueth@iram.fr
Arvid	Hammar	Omnisys Instruments and Chalmers University of Technology	Sweden	ah@omnisys.se
Paul	Hartogh	Max Planck Institute for Solar System Research	Germany	hartogh@mps.mpg.de
Darren	Hayton	SRON	Netherlands	d.j.hayton@sron.nl
Jeffrey	Hesler	Virginia Diodes Inc	United States	hesler@vadiodes.com
Ronald	Hesper	Kapteyn Astronomical Institute, University of Groningen	The Netherlands	r.hesper@sron.nl
Weidong	Hu	Beijing Institute of Technology	China	hoowind@bit.edu.cn
Norma	Hurtado	I. Physikalisches Institut, University of Cologne	Germany	hurtado@ph1.uni-koeln.de
Hiroaki	Imada	University of Tsukuba	Japan	s1330093@u.tsukuba.ac.jp
Yoshihisa	Irimajiri	National Institute of Information and Communications Technology (NICT)	Japan	irimaji@nict.go.jp
Konstantin	Kalashnikov	Kotel'nikov Institute of Radio Engineering and Electronics RAS	Russia	kalashnikov@hitech.cplire.ru
Boris	Karasik	Jet Propulsion Laboratory, California Institute of Technology	USA	boris.s.karasik@jpl.nasa.gov
Kenichi	Karatsu	National Astronomical Observatory of Japan	Japan	kenichi.karatsu@nao.ac.jp
Anna	Kardarova	Moscow State Pedagogical University	Russia	anna_kardakova@mail.ru
Pierre	Kaufmann	McGill University	Brasil	pierrekau@gmail.com

First name	Last name	Organization	Country	e-mail
Andrey	Kaveev	Tydex, LLC	Russia	andreykaveev@tydex.ru
Andrey	Khudchenko	SRON	Netherlands	A.Khudchenko@sron.nl
Nickolay	Kinev	Kotel'nikov Institute of Radio-engineering and Electronics of RAS	Russia	nickolay@hitech.cplire.ru
Teunis M.	Klapwijk	Delft University of Technology, Moscow State Pedagogical University	the Netherlands	t.m.klapwijk@tudelft.nl
Takafumi	Kojima	National Astronomical Observatory of Japan	Japan	t.kojima@nao.ac.jp
Alexander	Korneev	Moscow State Pedagogical University	Russia	akorneev@rplab.ru
Yuliya	Korneeva	Moscow State Pedagogical University	Russia	korneeva_yuliya@mail.ru
Valery	Koshelets	Kotel'nikov Institute of Radio Engineering and Electronics RAS	Russia	valery@hitech.cplire.ru
Yury	Kovalev	Astro Space Center of P.N. Lebedev Physical Institute	Russia	yyk@asc.rssi.ru
Sascha	Krause	GARD (Group for Advanced Receiver Development) Chalmers University of Technology	Sweden	sascha.krause@chalmers.se
Artem	Kuzmin	IMS KIT	Germany	artem.kuzmin@kit.edu
Leonid	Kuzmin	Chalmers University	Sweden	kuzmin@chalmers.se
Igor	Lapkin	Chalmers University of Technology; Institute of Applied Physics of the Russian Academy of Sciences	Sweden, Russia	lapkin@chalmers.se
Jung-Won	Lee	Korea Astronomy and Space Science Institute	South Korea	jwl@kasi.re.kr
Jing	Li	Purple Mountain Observatory,CAS	China	lijing@pmo.ac.cn
Yury	Lobanov	Moscow State Pedagogical University	Russia	ylobanov@rplab.ru
Doris	Maier	Institut de RadioAstronomie Millimetrique	France	maier@iram.fr
Hiroshi	Matsuo	National Astronomical Observatory of Japan	Japan	h.matsuo@nao.ac.jp
Imran	Mehdi	Jet Propulsion Laboratory	USA	imran.mehdi@jpl.nasa.gov
Hocine	Merabet	Qatar University	Qatar	merabet@qu.edu.qa
Amna	Mir	Beijing university of posts and telecommunications	China	amna_mir@hotmail.com
Viacheslav	Murav'ev	Terasense, LLC	Russia	viacheslav.muravev@terasense.ru
Masato	Naruse	Saitama University	Japan	naruse@super.ees.saitama-u.ac.jp
Evgenii	Novoselov	Chalmers University of Technology	Sweden	evgenii@chalmers.se

First name	Last name	Organization	Country	e-mail
Ion	Oprea	ACST GmbH	Germany	oprea@acst.de
Roman	Ozhegov	SCONTEL	Russia	ozhegov@rplab.ru
Mikhail	Patrashin	National Institute of Information and Communications Technology	Japan	mikhail@nict.go.jp
Dmitry	Pavelyev	Lobachevsky State University of Nizhni Novgorod	Russia	pavelev@rf.unn.ru
Alexey	Pavolotsky	Chalmers University of Technology	Sweden	alexey.pavolotsky@chalmers.se
Patrick	Pütz	KOSMA, 1. Physikalisches Institut, Universität zu Köln	Germany	puetz@ph1.uni-koeln.de
Dmitry	Radchenko	Astro Space Center of P.N. Lebedev Physical Institute	Russia	radchenkod@asc.rssi.ru
Hawal	Rashid	Group for Advanced Receiver Development, Chalmers University of Technology	Sweden	hawal@chalmers.se
Simon	Rea	STFC Rutherford Appleton Laboratory	United Kingdom	simon.rea@stfc.ac.uk
Heiko	Richter	Institute of Planetary Research, DLR	Germany	heiko.richter@dlr.de
Christoph e	Risacher	Max Planck Insitut für Radioastronomie	Germany	crisache@mpifr-bonn.mpg.de
Peter	Roelfsema	SRON Netherlands Institute fro Space Research	The Netherlands	P.R.Roelfsema@sron.nl
Shigeyuki	Sekiguchi	Department of Astronomy in School of Science, the University of Tokyo / National Astronomical Observatory of Japan	Japan	shigeyuki.sekiguchi@nao.ac.jp
Yutaro	Sekimoto	National Astronomical Observatory of Japan	Japan	sekimoto.yutaro@nao.ac.jp
Sergey	Seliverstov	Moscow State Pedagogical University	Russian Federation	seliverstovsv@mail.ru
Alexej	Semenov	DLR, German Aerospace Center	Germany	alexei.semenov@dlr.de
Evgeny	Serov	Institute of Applied Physics of RAS	Russia	serov@appl.sci-nnov.ru
Patrice	Serres	IRAM	France	serres@iram.fr
Wenlei	Shan	Purple Mountain Observatory, Chinese Academy of Sciences	China	shan@pmo.ac.cn
Michael	Shcherbatenko	Moscow State Pedagogical University	Russia	mishasoutherner@gmail.com
Sheng-Cai	Shi	Purple Mountain Observatory,CAS	China	scshi@pmo.ac.cn
Alexander	Shurakov	Moscow State Pedagogical University	Russia	alexander@rplab.ru
Jose V.	Siles	NASA Jet Propulsion Laboratory	USA	Jose.V.Siles@jpl.nasa.gov
Andrey	Smirnov	Astro Space Center of P.N. Lebedev Physical Institute	Russia	asmirn@asc.rssi.ru

First name	Last name	Organization	Country	e-mail
Konstantin	Smirnov	SCONTEL	Russia	smirnov@scontel.ru
Alexander	Sobolev	Kotel'nikov Institute of Radio Engineering and Electronics RAS; Moscow Institute of Physics and Technology	Russia	sobolev@hitech.cplire.ru
Nataliya	Solovieva	SCONTEL	Russia	natalya.solovyeva@scontel.ru
Tatsuya	Soma	The University of Tokyo	Japan	soma@taurus.phys.s.u-tokyo.ac.jp
Boon Kok	Tan	Department of Physics (Astrophysics), University of Oxford	United Kingdom	tanbk@astro.ox.ac.uk
Mikhail	Tarasov	V.Kotelnikov Institute of Radio Engineering and Electronics	Russia	tarasov@hitech.cplire.ru
Bertrand	Thomas	Radiometer Physics GmbH	Germany	thomas@radiometer-physics.de
Edward	Tong	Harvard-Smithsonian Center for Astrophysics	USA	etong@cfa.harvard.edu
Ivan	Tretyakov	Moscow State Pedagogical University	Russia	ivan.tretyakov@mail.ru
Ekaterina	Tsygankova	Tydex, LLC	Russia	EkaterinaTsygankova@tydex.ru
Alexey	Ustinov	Karlsruhe Institute of Technology	Germany	ustinov@kit.edu
Yury	Vachtomin	SCONTEL	Russia	vakhtomin@scontel.ru
Dariya	Vachtomina	SCONTEL	Russia	DVahtomina@yandex.ru
Nathan	Vercruyssen	TU Delft	The Netherlands	N.vercruyssen@tudelft.nl
Hui	Wang	STFC - Rutherford Appleton Laboratory	UK	hui.wang@stfc.ac.uk
Martina	Wiedner	LERMA2, Observatory of Paris	France	martina.wiedner@obspm.fr
Wolfgang	Wild	ESO	Germany	wwild@eso.org
Parisa	Yadranjee Aghdam	Chalmers university of technology	Sweden	parisa.aghdam@chalmers.se
Qijun	Yao	Purple Mountain Observatory	China	yqj@mwlab.pmo.ac.cn
Ghassan	Yassin	University of Oxford	United Kingdom	g.yassin1@physics.ox.ac.uk
Wen	Zhang	Purple Mountain Observatory	China	wzhang@pmo.ac.cn
Igor	Zinchenko	Institute of Applied Physics of the Russian Academy of Sciences	Russia	zin@appl.sci-nnov.ru